DEVELOPMENT OF GAS DETECTORS & STUDIES OF ONE-AND TWO-NUCLEON TRANSFER REACTIONS AT SUB-BARRIER ENERGIES FOR S + Ni SYSTEMS

by

P.P.SHAKKEEB, MSc, BEd.
Nuclear Spectroscopy Laboratory
Department of Physics
University of Calicut
Thenhippalam-673 635, Malappuram (Dist)
KERALA, INDIA

THESIS SUBMITTED TO THE UNIVERSITY OF CALICUT IN PARTIAL FULFILLMENT OF THE REQUIREMENTS FOR THE AWARD OF THE

DEGREE OF

DOCTOR OF PHILOSOPHY IN PHYSICS

2002

CERTIFICATE

This is to certify that the thesis entitled "**DEVELOPMENT OF GAS DETECTORS & STUDIES OF ONE- AND TWO-NUCLEON TRANSFER REACTIONS AT SUB-BARRIER ENERGIES FOR S + Ni SYSTEMS** " which is being submitted by Mr. P.P.Shakkeeb in partial fulfillment of the **Doctor of Philosophy in Physics of Calicut University**, is a record of his own research work carried out by him. He has carried out his investigations for the last eight years on the subject matter of the thesis under my guidance. The matter embodied in the thesis has not been submitted for the award of any other degree by him or anybody else.

K. M. Varier

University of Calicut,
Date : 22-05-02

Prof. K.M. VARIER
(RESEARCH SUPERVISOR)

DECLARATION

I hereby declare that this thesis entitled **"DEVELOPMENT OF GAS DETECTORS & STUDIES OF ONE- AND TWO-NUCLEON TRANSFER REACTIONS AT SUB-BARRIER ENERGIES FOR S + Ni SYSTEMS "** is a bona-fide record of the original research work carried out by me at the Nuclear spectroscopy laboratory of the Department of Physics, University of Calicut as well as at the Nuclear Science Centre, New Delhi, under the supervision of Prof. K. Muraleedhara Varier. I also declare that this work or any part of it, has not been submitted for the award of a degree either in this University or in any other Universities.

University of Calicut,
Date: 22.05.2002

P. P. SHAKKEEB

ACKNOWLEDGEMENTS

I would like to gratefully express my sincere appreciation to my thesis supervisor Prof. K. M. Varier for his valuable guidance, advice and help during my doctoral work. Appreciation is also due to Dr.A.K. Sinha, NSC for his valuable discussions and guidance. I am grateful to the former Head of the Department, Prof. V.K. Thankappan and present Head of the Department, Prof. K. Neelakandan for providing me all facilities in the Department of Physics, University of Calicut for my research work. I am thankful to all teaching and non-teaching staff (present and former) of the Department of Physics, for all their help during my work. I would like to thank Dr.B.R.S. Babu for his valuable advices.

I have no words to express my thanks to the authorities of Nuclear Science Centre, New Delhi, especially Prof. G.K. Mehta, for providing me an opportunity to work in the excellent atmosphere to test our detectors and to do the experiment at HIRA using the pelletron accelerator. I am highly grateful to Dr. R.K. Bhowmwik, Dr. S.K. Datta, Dr. Amit Roy and Dr. K. Asokan for their support. I have benefited a lot from the advices and informations concerning the detectors provided by the NSC Scientists Mr. D.O. Kataria and Mr. P. Sugathan and like to express my sincere appreciation to them. I am thankful to Mr. Joby Antony for his company and help during the development and testing of MWPC and during my stay at NSC. I am remembering with deep sense of gratitude about Mr. N. Madhavan and Mr.J.J. Das and Mr. N.V.S.V. Prasad for their help during the experiment.

The help extended by Mr.A.M. Vinod Kumar, Lagy and M.J.Singh also require special mention. I gratefully acknowledge Bivash, Chayya, Mallikarjuna Rao and Madhusoodhana Rao for their help during my stay at NSC. I would like to thank all academic, scientific, technical and administrative personnels of Nuclear Science Centre for their support in various ways during my work and stay at NSC. I am thankful to all research students whom I have acquainted with at NSC for their kind helps in one way or other. I am gratefully remembering Prof. M.C. Radhakrishna, Prof. N.G. Puttaswamy, Prof. D.L. Sastry, Prof. R.Singh and Dr.N.M. Badiger for their support and advice.

Advice and encouragement from Prof. Kuruvilla Eapen (Late) and Prof. T.N. Vasudevan is deeply acknowledged. I am highly thankful to Dr. Antony Joseph, Dr. M.P. Unnikrishnan, Dr. Ravikrishna Menon, Mr. Anto, Mr. Kunhikrishnan and Dr. Pankajakshan for their company and help during the early days of my work. I extend my thanks to Mr. Karunakaran, Mr.Ramachandran, Sister Lilly, Deepak , Prasad and Shaji for their helps. I would like to acknowledge the administrative and examination staff of the University of Calicut for their valuable services during my research work.

The financial support from UGC (through NSC), CSIR (through Dr. Rakesh Sharma), DST(through Dr. Praveer Asthana) and DAE (through IIT, Kanpur) is gratefully acknowledged without which I would not have been able to survive during my PhD days. Also I like to thank the present and former staff of Govt. Polytechnic, Palakkad and Institute of Printing Technology and Govt. Polytechnic, Shoranur for their kind help and suggestions. The encouragement from Dr. Elizabeth John, Mr.P.Dileep, Mr.Biju, Mr.Ashokan (IPT&GPT, Shoranur), Mrs.Seema and Mr.P.U.Abdul Rahim (GPT, Palakkad) is deeply acknowledged. Lastly, and most deeply I would like to thank my parents, wife, other family members, friends, relatives and all well wishers without whose constant support and encouragement this work would not have been finished.

University of Calicut,
Date : 22.05.2002

P. P. SHAKKEEB

Contents

List of Publications

I. Journals

1. Position Sensitive Parallel Plate Avalanche Detectors with tilted electrodes.

   P.P. Shakkeeb, Antony Joseph, A.M. Vinod Kumar, K.M. Varier.

   Indian J. Pure & Appl. Phys. **33**(1995)317.

2. Gas Amplification in isobutane and P10 gas counters.

   P.P. Shakkeeb, A. Joseph, A.M. Vinod Kumar, K.M. Varier, B.R.S. Babu.

   Nucl. Instr. and Meth. **A366**(1995)320.

3. Sub-barrier few nucleon transfer reaction and channel coupling effects in heavy ion fusion.

   A.K.Sinha, L.T.Baby, N. Badiger, J.J. Das, S.K Hui, D.O. Kataria, R.G.Kulkarni, N. Madhavan, P.V. Madhusudhana Rao, I. Mazumdar, M.C. Radhakrishna, N.V.S.V. Prasad, N.G. Puttaswamy, **P.P. Shakkeeb**, R. Singh, D.L. Sastry, P. Sugathan, V.Tripathi, K.M. Varier, A.M. Vinod Kumar.

   Jour. Phys. G. Nucl. Part. Phys. **23**(1997)1331.

II. Symposia

1. First Townsend Coefficients in P10 and isobutane using SWPC.

   K.M.Varier, B.R.S.Babu, Antony Joseph, A.M. Vinod Kumar, **P.P.Shakkeeb**

   Procedings of DAE Symposium on Nuclear Physics **35B**(1992)430.

2. Comparison of Townsend Coefficients in isobutene measured using SWPC and PPAC

   P.P.Shakkeeb, Antony Joseph, A.M. Vinod Kumar, K.M. Varier, and B.R.S. Babu.

   Procedings of DAE Symposium on Nuclear Physics **36B**(1993)450.

3. A comparative study of near barrier fusion of $^{46}Ti+^{64}Ni$ and $^{50}Ti+^{60}Ni$ systems

N.V.S.V. Prasad, A.M.Vinod Kumar, K.M.Varier, J.Antony, **P.P.Shakkeeb**, D.L. Sastry, I. Mazumdar, N. Madhavan, P.Sugathan, D.O. Kataria, J.J.Das and A.K. Sinha.

Procedings of DAE Symposium on Nuclear Physics **36B**(1993)208.

4. Position Sensitive PPAC detector with non-uniform electrode spacing

P.P.Shakkeeb, K.M.Varier, A.M.Vinod Kumar and Antony Joseph.

Procedings of DAE Symposium on Nuclear Physics **37B**(1994)449.

5. A CAMAC Nuclear ADC.

Joby Antony, E.T.Subrahmanian and **P.P.Shakkeeb.**

Procedings of DAE Symposium on Nuclear Physics **38B**(1995)

6. A deep ionization detector with enhanced capabilities for the HIRA focal plane.

D.O. Kataria, M.J.Singh, J.J.Das, N.Madhavan, P.Sugathan, S.K.Hui, **P.P.Shakkeeb**, A.M.Vinod Kumar, N.V.S.V. Prasad, I. Mazumdar, L.T. Baby and A.K.Sinha.

Procedings of DAE Symposium on Nuclear Physics **38B**(1995)I-54.

7. Sub-barrier transfer studies for the $^{32}S+^{60,64}Ni$ systems.

P.P.Shakkeeb, A.M.Vinod Kumar, K.M. Varier, N.V.S.V. Prasad, R. Singh, A.K. Sinha, N. Madhavan, P. Sugathan, D.O.Kataria and Lagy.T.Baby.

Procedings of DAE Symposium on Nuclear Physics **38B**(1995)B-39.

III. Workshop

1. Fusion Studies for Ti+Ni systems at near and sub-barrier energies.

   A.M.Vinod Kumar, N.V.S.V. Prasad, K.M. Varier, D.L. Sastry, B.R.S. Babu

   P.P.Shakkeeb, J. Antony, I. Mazumdar, N. Madhavan, P. Sugathan, J.J. Das,

   D.O. Kataria and A.K. Sinha.

   Workshop on Heavy Ion Physics, Padova, Italy (1994).

IV. Reports

1. Sub-barrier fusion measurements on Ti+Ni system.

   A.M.Vinod Kumar, K.M. Varier, B.R.S. Babu, J. Antony, **P.P.Shakkeeb**,

   N.V.S.V. Prasad, D.L. Sastry, A.K. Sinha, N. Madhavan, P. Sugathan,

   D.O. Kataria and J.J. Das.

   Nuclear Science Centre-Annual Report (1993)50

2. $^{32}S+^{48}Ti$ fusion at sub-barrier energies.

   R. Singh, J.J. Das, D.O. Kataria, N. Madhavan, I. Mazumdar, A.K. Sinha, P.

   Sugathan, L.T. Baby, M.M. Musthafa, R. Prasad, B.P. Singh, N.V.S.V. Prasad,

   A.M. Vinod Kumar, **P.P. Shakkeeb**, M.J. Singh.

   Nuclear Science Centre-Annual Report (1994)52.

3. Few nucleon transfer studies for 32S+60,64Ni systems using kinematic coincidence method with HIRA.

   P.P. Shakkeeb, A.M.Vinod Kumar, K.M. Varier, N.V.S.V. Prasad, A.K. Sinha,

   N. Madhavan, P. Sugathan, D.O. Kataria and L.T. Baby.

   Nuclear Science Centre-Annual Report (1995)78

4. Development of Gas Detectors for Heavy Ions.

   K.M.Varier, B.R.S. Babu, Antony Joseph, **P.P. Shakkeeb.**

   DST Project completion Report (1995)

Chapter 1

Introduction

Nuclear reaction is a wide branch of physics which is an effective tool that can be used to understand the properties of atomic nucleii and their interactions. In modern nuclear physics studies, nuclear reactions are used for the production of super heavy elements ($Z \leq 112$ and $A \leq 277$). Based on the incident particle energy, nuclear physics can be broadly classified as low energy nuclear physics, intermediate energy nuclear physics and high energy nuclear physics. The studies discussed in this thesis are related to intermediate energy nuclear reactions. The nuclei involved normally in this type of reactions are called heavy ions. Heavy ions are charged particles having excess positive or negative charge which can be accelerated to high energies by the application of external electric fields. The collection of heavy ions with high kinetic energy with a small energy spread moving almost in the same direction is called heavy ion beam, which can be produced using particle accelerators. Heavy ion beam can be used for nuclear reaction experiments with foil or gas targets. The reaction products can be separated from the beam particles by using Recoil Mass Separators (RMS) and detected at the focal plane of RMS using suitable gas detectors. The data obtained can be analyzed to get useful information about the physics of nuclear reaction, such as reaction dynamics and structural properties of nucleus.

In a heavy ion collision two massive nuclear matter possessing large kinetic energy and angular momentum interact with each other, resulting in compound nucleus formation, deep inelastic reactions etc. The extra conditions of spin and temperature can be studied by observing the compound nucleus possessing high excitation energy and large angular momentum. When the projectile-target nuclei are in sufficient contact, they share large fraction of the kinetic energy and undergo internal excitation by the heating up of the nuclei which results in the deep inelastic breakup reaction by forming nuclear fragments with nearly equal mass. The transfer of few nucleons result in peripheral collisions or direct reactions. At large impact parameters the reaction will be pure elastic scattering. The

other reaction channels are incomplete fusion, quasi-fission, quasi-elastic etc. The boundaries between these various process are neither distinct nor well defined. Studies of various systems [1] showed that inelastic scattering and quasi-elastic transfer models exhibit larger cross section and contribute more to the total reaction cross section with increasing mass of the system. With lighter projectiles fusion is more dominant and with heavier projectiles quasi-elastic transfer is more obvious. Inelastic scattering is mainly due to the coulomb and nuclear excitation, where coulomb excitation takes place mainly at large inter nuclear distances with partial waves which are not involved in nuclear reactions. Around the coulomb barrier quasi-elastic transfer reaction channel is more important and at lower energies quasi-elastic transfer plus inelastic scattering shows dominance. Figure1.1 shows the fractionation of angular momentum and time scale for nuclear reactions. The various reaction mechanisms due to the fractionation of partial waves in shown in this figure. The compound nucleus (CN) and fission-like (FL) reaction occur at distance of closest approach smaller than the interaction radius where target and projectile interact completely. The identity of the entrance channel is completely dissolved, kinetic energy is totally damped and interaction time is too long. The lowest ℓ-values lead to compound nucleus fusion and its evaporation. But highest ℓ-values lead to fission after attaining equilibrium. Other reaction modes are damped (DA), quasi-elastic (QE), elastic (EL) and coulomb excitation (CE). In the case elastic and coulomb excitation there is no mass transfer at all. Energy and mass of the ions define the properties of non-elastic events. That means, for heavier systems major fraction of the reaction cross section is contributed by deep inelastic channel where as the fusion is dominated for central collisions of light and medium heavy systems.Classical considerations can be given to the trajectories because of the smaller de Broglie wavelength associated with relative motion of heavy ions, which can be used for studying nuclear properties. The finite probability for each exit channel depends on the incident energy and the properties of the interacting nuclei. Actually different reaction channels are mutually dependant and the enhancement in each channel is due to the coupling between different interaction channels. However heavy ion nuclear reactions can be broadly classified by considering impact parameter 'b' as a variable as shown in figure 1.2. For distant collision with large 'b' the reaction is a combination of Rutherford elastic scattering and Coulomb excitation. At large distances of closest approach

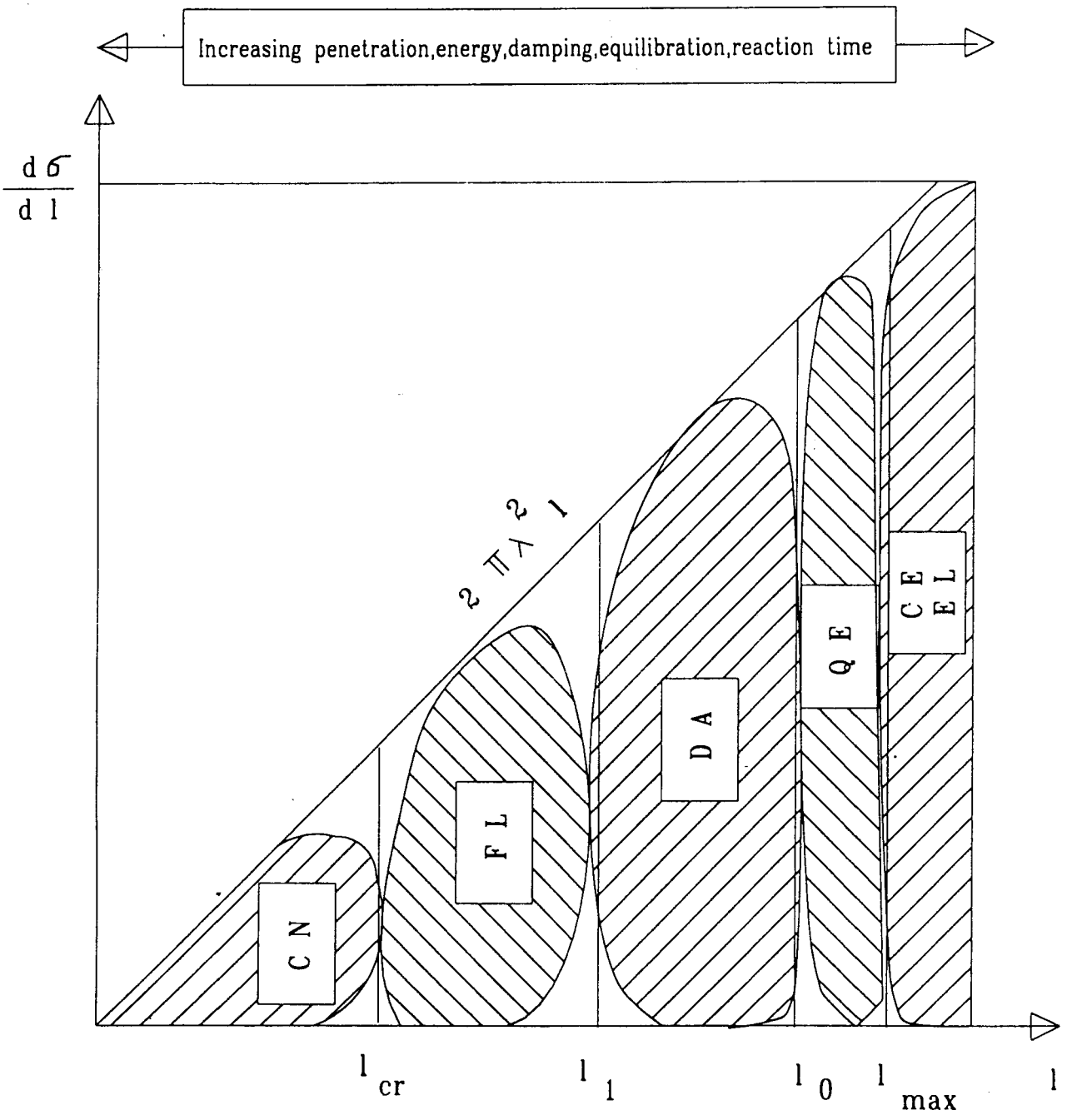

Figure : 1.1 Fractionation of Angular Momentum and time scale for nuclear reactions.

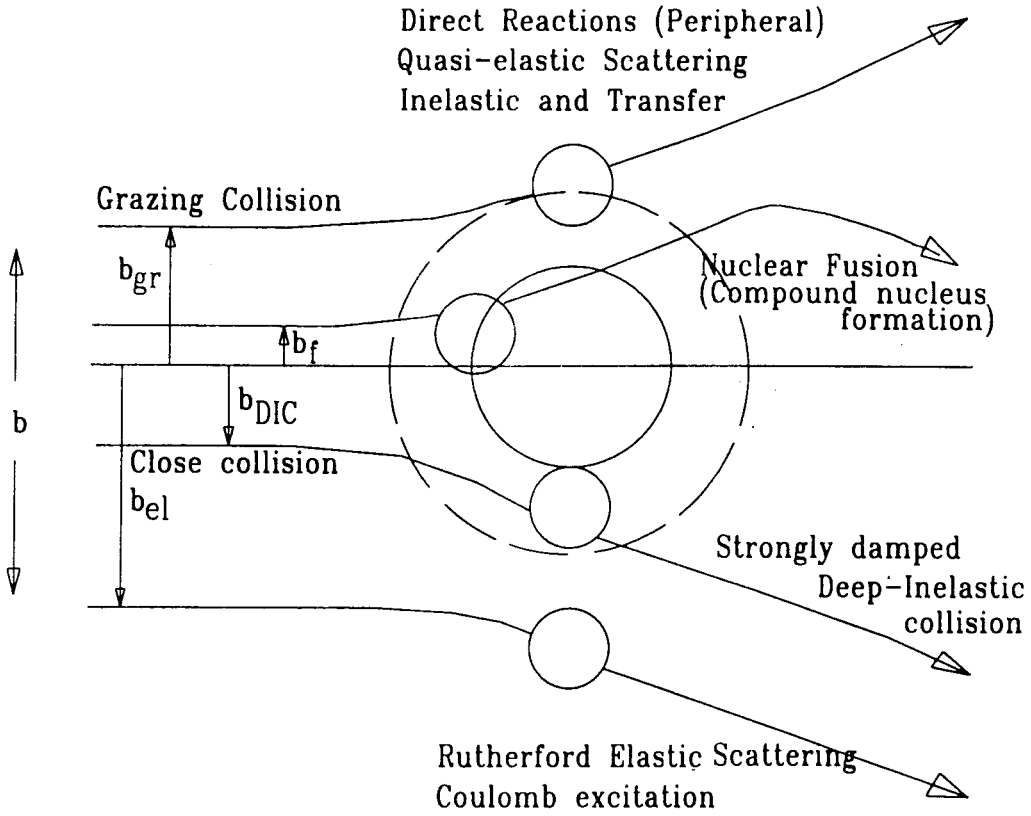

Figure : 1.2 General Classification of nuclear reactions according to impact parameter (b)

($b>b_{gr}$), the projectile-target ions do not experience the nuclear force, but they interact via coulomb field and undergo excitation. The interaction is dominated by electromagnetic forces and resulting in coulomb excitation or Rutherford elastic scattering. For grazing type collisions the reaction results in quasi-elastic scattering or direct reactions or direct reactions involving peripheral inelastic scattering and nucleon transfer. In these collisions $b \approx b_{gr} = R\sqrt{(1-V_b/E)}$ and projectile spends less time in the target and the ions experience the nuclear field. The interaction can be represented by a complete potential. In the case of close collisions strongly damped deep inelastic reaction is dominant. For close collisions at small distances of closest approach ($b<b_{gr}$) the projectile and target ions undergo very strong interaction resulting in small changes in A and Z. Considerable amount of incident kinetic energy is utilized for internal modes of excitation. This reaction mechanism is called strongly damped deep inelastic collision which lies between the quasi-elastic and compound nuclear formation.

For quasi-elastic reactions the energy loss, charge and mass transfer is comparatively less than that of deep inelastic reactions. A clear well defined distinction between quasi-elastic and deep inelastic reactions in terms of energy loss, charge and mass transfer does not exist such that deep inelastic reactions evolve gradually from quasi-elastic reactions. In the case of quasi-elastic reactions only a slight change in mass, charge and energy results. Fusion and fission of the compound nucleus occurs for very low impact parameters. For fusion and deep inelastic reactions the change in mass, charge and energy will be considerably large. At impact parameters nearly equal to zero ($b<<b_{gr}$), the projectile spends more time in the target leading to fusion of the two nuclei. The scattering angle $\theta >> \theta_{gr}$ and a large amount of energy and angular momentum of the relative motion is transferred to the internal degrees of freedom of the compound nuclear system. Since the centrifugal barriers favor the emission of low energy light particles ($\ell=0$) such as n, p, α, etc., the compound nuclei evaporate to give de excited evaporation residues which in turn decay to the ground state by gamma-ray emission. The total fusion cross section is measured as $\sigma_f = \sigma_{ER} + \sigma_{fusion\text{-}fission}$ where the last term is dominant for compound nucleus of $A \geq 240$, but negligible for $A \leq 120$. Recently the interest in the heavy ion physics has been turned towards the study of heavy ion fusion dynamics around and below the

coulomb barrier. Fusion takes place when the ions pass over or penetrate through the barrier-the maximum potential at which long range repulsive coulomb force and the short range attractive nuclear force just balance each other. By assuming the nuclei as spherical and by using a one-dimensional coulomb and nuclear potential, the fusion cross section can be calculated according to one-dimensional barrier penetration model-1DBPM [2]. The experimentally measured heavy ion induced fusion cross section shows large deviation from theoretical predictions of macroscopic semi-classical 1DBPM at energies around and below the coulomb barrier. The experimentally observed fusion cross section at above barrier energies can be well reproduced by 1DBPM theoretical calculations. The mechanism of the enhancement of sub-barrier fusion cross section is not well understood. This well known enhancement of sub-barrier fusion cross section is an exciting phenomenon that got special attention of researchers some 20 years or so ago. Several extensive theoretical and experimental investigations have been carried out in this field and several articles can be found in literature [3,4]. Developments of theoretical explanations such as the macroscopic liquid drop model to the microscopic channel coupling treatments are milestones in sub-barrier fusion research. Other models used for the explanation of the observed enhancement are based on the deformation of the participating nuclei, vibrational effects of nucleons, neutron transfer and neck formation between colliding partners. Among these models, the Coupled Channel (CC) approach [5,6] is found to be the most suitable model for explaining sub-barrier fusion enhancement. In this approach, the coupling effects of the other degrees of freedom to the entrance channel is taken into account. Inelastic scattering and quasi-elastic transfer channels are mainly responsible for the enhancement of sub-barrier fusion cross section and they have to be included in coupled channel calculations. But the inclusion of low lying collective states (inelastic) of the projectile and target ions is not sufficient to explain all features of sub-barrier fusion reaction such as neutron number dependence of fusion yields. Dasso et. al.,[5,7] reported about a simplified coupled channel calculation including inelastic states (2^+,3^-) of projectile and target. At energies below barrier and with more neutron rich targets, the fusion yield exhibit high enhancement. This phenomenon can be well explained by considering two-neutron transfer process with positive ground state Q-value where the energy gain can increase the fusion probability considerably at below barrier energies. The above mentioned Dasso

formalism was modified by Broglia et. al.,[8,9] by including transfer coupling. In these two calculations the nuclear surface modes were considered as independent harmonic oscillators at one phonon level. The separation between 1DBPM and CC cross section will give the asymptotic barrier shift (lowering of barrier) ΔB. The inelastic coupling is responsible for only part of the asymptotic barrier shift in the sub- barrier fusion cross section and can not explain isotopic effects [10,11] mentioned above. The study of the enhancement of fusion cross section is not an isolated process any more and involve the other reaction channels which influence each other such as inelastic scattering, quasi-elastic transfer etc. Recent studies including two and higher order phonon coupling have been reported else where [12] where extensive calculations have been carried out for second and multiphonon coupling. These studies showed that the low lying collective states are not sufficient for understanding the enhancement but the higher states should also need to be considered for coupling.

From the measured transfer cross sections the form factors can be extracted and used in CC calculations. But a few experimental data is available to extract the coupling strengths from transfer probability. Therefore measurement of transfer probabilities at sub-barrier energies is indeed essential for performing a more complete CC calculation. Semi-classical methods [13] can be used to extract the coupling strength and form factor from transfer probabilities. These methods are easy to use in practical applications and give a physical insight to the problem by relating the wave properties and particle properties of the ions. The transfer probability at below barrier energies is peaking at 180° in centre-of-mass system, a back angle measurement is required to calculate the form factor in the semi-classical methods. The measurement of 180° back angle cross section is quite tedious and hence the forward going target-like particles in coincidence with the back scattered projectiles are detected by recoil mass separators. This technique is called kinematic coincidence technique. The lack of experimental data for nucleon transfer reaction at and below coulomb barrier is one of the main motivation of the transfer measurement. Only a few reports have been published about 2 nucleon and multinucleon transfer and the importance of these channels as a link between entrance channel and final compound nucleus formation (fusion) is not yet explored deeply. Like inelastic scattering transfer

reaction is also an important doorway to fusion reactions which must be included in any theoretical analysis of sub-barrier fusion reactions and deserve special attention.

One nucleon (neutron) transfer reaction have largest cross section among quasi-elastic processes, next to inelastic scattering. Experimental investigations have shown that like inelastic scattering transfer reactions can also influence other reaction modes such as elastic scattering and fusion reactions which require to measure the transfer yield. Another goal of the experiment was to make qualitative comparison between fusion and transfer. Quasi-elastic transfer reactions contribute largest fraction to the total heavy ion reaction cross section at energies below coulomb barrier. Only a few experimental data is available at such low energies on heavy ion induced transfer reaction compared to inelastic scattering where transfer takes place at large inter nuclear distances. The reason for the lack of data is due to the experimental difficulties in identifying the transfer products at sub-barrier energies for the systems where the projectile has a significant fraction of the target mass. The usual measurement techniques are not so effective in such cases because of the small cross sections and the low energy of the back scattered projectile-like fragments. The above mentioned difficulties can be overcome by performing inverse kinematic reactions or by the measurements of angular distributions at near barrier energies. In the case of angular distributions the distances of closest approach depends on the angle in centre-of-mass which probes the transfer at varying inter nuclear distances.

The transfer measurements in the sub-barrier region for many heavy ion systems are still to be explored completely. But fusion studies for those systems are almost well performed. The exact role of transfer in the observed enhancement effects for those systems still not completely asserted. Since neutrons are charge less particles the transfer strength is more for the neutron transfer than protons and contribute more to the fusion enhancement. Transfer channels with positive Q-values also contribute more to the enhancement. A detailed study of both of these cases require special consideration. Even though the inelastic couplings are responsible for only part of the asymptotic barrier shifts ΔB in the sub-barrier fusion cross sections, it can not explain the isotopic effects. This necessitates the coupling of quasi-elastic transfer channels to give rather good

description for the asymptotic shift ΔB. The need for the transfer measurements on $^{32}S+ ^{60,64}Ni$ systems is given in the following explanations.

The closed proton shell Z = 28 and the proximity to the neutron shell closure and N = 28 make nickel isotopes an interesting set of targets for neutron transfer measurements from the point of view of the sub-barrier fusion enhancements. It is also interesting to study the mass asymmetry in the entrance channel and its effects on sub- barrier fusion enhancement. Napoli et. al., [14] - LNL group - already carried out the fusion and transfer measurements for $^{32}S+^{58,64}Ni$ systems. But their attempts for 2- nucleon transfer measurements are not successful. Saha et al., [15] reports the one- and two-neutron transfer measurements on $^{32}S+^{64}Ni$ system at near barrier energies by adopting a coincidence technique between the projectile-like ions and the prominent gamma radiations from the residual nuclei.

Our Calicut-NSC group carried out an experiment on $^{32}S+^{60,64}Ni$ systems which was mainly aimed to study the one- and two-nucleon transfer more systematically using the recent technique of kinematic coincidence to have an investigation on transfer reaction for a detailed understanding of fusion enhancement. This technique is helpful in solving the complex problem of the identification of the transfer products of smaller cross section compared to inelastic channel. It is a coincidence measurement between the low energy back scattered projectile-like fragment and the corresponding target-like fragment recoiling in the forward angle with a large fraction of the incident energy. Napoli et. al.,[14] reports the same technique for the $^{32}S + ^{64}Ni$ system but it was not succeeded in resolving the m/q ambiguity for identifying the 2N transfer channel. This was due to the focusing of particles of the same m/q value to the same focal plane position. This was the reason why we have studied the same system using the same technique of kinematic coincidence and it was quite successful in resolving the m/q ambiguity from the TOF information. This made the identification of different channels of $^{32}S+ ^{60,64}Ni$ system easier. The elastic scattering of $^{32}S+^{64}Ni$ angular distributions have been measured at several energies around coulomb barrier by Stefanini et. al.,[16]. They have analyzed the data using optical model and found remarkable energy dependence of the potentials at strong absorption radius. Among

the different systems they studied $^{32}S+^{64}Ni$ system shows unique properties and larger effects - larger transfer cross section and stronger inelastic excitation - than the other systems. The largest sub-barrier fusion enhancement and threshold anomaly of $^{32}S+^{64}Ni$ system observed by previous studies motivated our group to a detailed study of transfer reaction of the same system. No considerable reports have come about the transfer measurement of $^{32}S+^{60}Ni$ system. That is why we have performed the measurement of that system also. The S+Ni system was chosen because of the positive Q-values for the -2p (0.216 MeV) and +2n (3.563 MeV) channels which were expected to play a significant role in the sub-barrier fusion enhancement. The higher order phonon coupling effects in the sub-barrier fusion of medium mass nuclei with Z_pZ_t in the range 350 to 1100 for nearly symmetric and asymmetric systems also require special attention. The $^{32}S+^{60,64}Ni$ transfer experiment was carried out using the 15UD Pelletron accelerator and the RMS - Heavy Ion Reaction Analyzer (HIRA) - at Nuclear Science Centre (NSC), New Delhi, the national inter University research facility under the University Grants Commission (UGC). This experiment was done to study about the enhancement of fusion cross section below barrier by coupling the inelastic, transfer and phonon 2^+, 3^- states to 1DBPM.

Nuclear radiation detectors from an important and integral part of any nuclear physics experimental set up. Some introductory discussion on heavy ion detection is given below. A fast charged particle traversing through a gaseous or condensed medium interact with the medium in different ways. Out of all possible interactions, only the electromagnetic one is used as the basis for radiation detection. This is because electromagnetic interaction is mainly orders of magnitude more probable than weak and strong interactions which can yield information even from a thin sample of material. The highly probable incoherent coulomb interaction between the electromagnetic fields of incoming charged particle and of the medium results in both excitation and ionization of the atoms of the medium. The contribution of the other electromagnetic process such as bremssstrahlung, cerenkov and transition radiation to the total energy loss is negligibly small in gas detectors. The average differential energy loss per unit length due to the coulomb interaction has been obtained by Bethe [17] and Bloch [18] in the frame work of relativistic quantum mechanics.

The differential energy loss depends only on the projectile velocity and not on it's mass. At higher velocities energy loss reaches a constant value called the minimum ionizing region. At energies above a few hundred MeV all particles are at the minimum ionization and loose same amount of energy per unit length. The electromagnetic energy loss [19] is the result of small number of discrete interactions and therefore has the characteristic of a statistical average. Individual events can be grouped into two classes as close collisions and distant collisions. In close collision large energy transfer takes place which results in the liberation of electronic charge (ionization). In distant collisions energy transfer is small which results in both ionization and excitation.

As the design and development of new accelerators progressed heavier projectiles and higher bombarding energies became available. This resulted in the dramatic increase of reaction products, which could be identified only by time-of-flight (TOF) techniques. Coincidence experiments were performed for the particle identification in the case of many body problems. This technique require large area detectors because of small cross sections for each individual channel. Earlier solid state detectors were affected by material damage by the high energy intense heavy ion beams. These reasons revived the development of particle identification systems based on new type of gaseous detectors including energy loss, time-of-flight, magnetic analysis, and kinematic coincidence technique. The experience gained in medium and high energy physics experiments with position sensitive detectors together with that gained in handling large amounts of data has figured largely in this new development of gas detectors. A number of techniques remain unique to the field of heavy ion detection. As a result of these efforts large area ionization chambers, parallel plate counters, multi wire position sensitive detectors and light particle or gamma-ray multiplicity detector systems are used in heavy ion experiments. Fast response, high counting rate capability, good resolution, low cost, high radiation resistance, high efficiency, easiness to handle, low back ground sensitivity, etc. are some of the merits of gas detectors. Also the geometry can be varied to any desired dimension. The lack of commercial availability of gas detectors motivated our group to develop heavy ion detectors according to our requirements. The various detectors developed by our group are single wire proportional counter (SWPC), parallel plate avalanche counter (PPAC), multi wire

proportional counter (MWPC) etc. [20,21]. These detectors were tested at the nuclear spectroscopy lab at the Calicut University as well as at Nuclear Science Centre (NSC), New Delhi. The detector development project was funded by the Department of Science and Technology (DST), Govt. of India through a project entitled "Development of gas detectors for heavy ions". The transfer experiment was funded through a UGC-NSC project.

Chapter 2 contains a detailed discussion of the theoretical models and various experimental methods used for sub-barrier fusion studies. A review about the theories and experimental techniques of transfer measurements is given in Chapter 3. Theoretical aspects of gas detectors is given in Chapter 4. Details of fabrication, testing and experimental investigations with these detectors are explained in Chapter 5. A foil stretching unit and wire stretching unit were used for the development of the above detectors. A vacuum system and gas handling system were used for testing the detectors. Amerecium, Polonium and Californium α-sources were used for testing. The SWPC and PPAC data were used for finding the first Townsend and for the comparison of the first Townsend coefficients between SWPC and PPAC for different fill gases. A study of gas amplification by measuring the Aoyama, Diethorn and Zastawny parameters were also carried out. This is because their operating voltage and gas pressure corresponds to the proportionality region where gas amplification takes place. The experimental techniques and data analysis of the transfer measurement on $^{32}S+ {}^{60,64}Ni$ systems is given in Chapter 6. The 7^{th} Chapter includes the results and discussions of the transfer measurement on S+Ni systems. This chapter also includes the results of CC calculations and the summary of the measurements and the conclusions of the thesis.

References

[1](a) M. Beckermann, Rep. Prog. Phys. **51**(1988)1047.

(b) R.G. Stokstad and E.E. Cross, Phys. Rev. **C23**(1981)281.

[2] T.D.Thomas, Ann. Rev. of Nucl. Sci.**18**(1968)343.

[3] A.M. Stefanini, G. Fortuna, R. Pengo, W. Meczynski, G. Montagnoli, L. Corradi, A. Tivelli, S. Beghini, C. Signorini, S. Lunardi, M. Morando and F. Soramel, Nucl. Phys. A **456**(1986)509.

[4] M. Beckermann, M. Salomaa, A. Sperduto, J.D. Molitoris, Di Rienzo Phys. Rev.C **25**(1982)837.

[5] C.H. Dasso, S. Landowne, A. Winther, Nucl. Phys.A **405**(1983)381.

[6] R.A. Broglia, C.H. Dasso, S. Landowne and A. Winther, Phys. Rev.**C27**(1983)2433.

[7] C.H. Dasso, S. Landowne, A. Winther, Nucl. Phys.A **407**(1983)221.

[8] R.A. Broglia, C.H. Dasso, S. Landowne, G. Pollarolo, Phys. Lett. **133** B(1983)34.

[9] R.A. Broglia, C.H. Dasso, S. Landowne, Phys. Rev. C **32**(1985)1426.

[10] (a) M. Beckerman, M. Salomaa, A. Sperduto, J.D. Molitoris, Phys. Rev.**C25** (1983)339.

(b)M. Beckerman, M. Salomaa, A. Sperduto, J.D. Molitoris, Phys. Rev.**C25** (1982)1581.

[11] (a) W. Reisdorf, F.P. Hessberger, K.D. Hildenbrand, S. Hofmann, G. Muenzenberg, K.H. Schmidt, J.H.R. Schneider, W.F.M. Schneider, K. Suemmerer, G. Wirth, J.V. Kratz, and K. Sclitt, Phys. Rev. Lett. **49**(1982)1811 and

(b) W. Reisdorf, F.P. Hessberger, K.D. Hildenbrand, S. Hofmann, G. Muenzenberg, K.H. Schmidt, J.H.R. Schneider, W.F.M. Schneider, K. Suemmerer, G. Wirth, J.V. Kratz, and K. Sclitt, Nucl. Phys. **A438**(1985)212.

[12] K. Hagino, N. Takigawa, M. Dasgupta, D.J. Hinde and J.R. Leigh, Phys. Rev. **C55**(1997)276.

[13] R.A. Broglia and A. Winther, Heavy Ion Reactions, Vol.1, Lecture Notes, Addison Wesley, Redwood City (1991).

[14] D.R. Napoli, A.M. Stefanini, H. Moreno Gonzale, B. Million, G.Prete, P. Spolaore, M. Narayanasamy, Zi Chang Li, Nucl. Phys. A **559**(1993)443.

[15] (a) S. Saha and Y.K. Agarwal, Nucl. Phys. **A601**(1996)251 and
(b) S. Saha, Y.K.Agarwal and C.V.K. Baba, Phys. Rev. **C49**(1994)2578.

[16] A.M. Stefanini, A.Tivelli, G. Montagnoli, D.R. Napoli, D. Bonamini, S. Bhegini, F. Scarlassara, F. Soramel, C. Signorini, A. De Rosa, G. Inglima, M. Sandoli, G. Cardella, M. Papa and F. Rizzo, Phys. Rev. C **41**(1990)1018.

[17] H.A. Bethe, Ann. Phys.**5**(1930)325.

[18] F. Bloch, Ann. Phys. **16**(1933)287.

[19] W. Heitler, "The Quantum Theory of Radiation", Oxford University Press, London (1944).

[20] P.P. Shakkeeb, A. Joseph, A.M. Vinod umar, K.M. Varier, and B.R.S. Babu, Nucl. Instr. And Meth A **366**(1995)320.

[21] K.M. Varier, B.R.S. Babu, Antony Joseph and P.P. Shakkeeb, DST Project Completion Report (1995).

Chapter 2

Sub-Barrier Fusion - A Review

For two colliding heavy nuclei there exists a small but measurable cross section for fusion at energies below the coulomb barrier. This sub-barrier fusion has been attributed to the probability of quantum tunneling through a potential barrier. Experimental investigations illustrated that the probability of heavy ion fusion at energbies below barrier exceeds by several orders of magnitude, the predictions of the One Dimensional Barrier Penetration Model - 1DBPM [1]. The heavy ion interaction process depends not only on the inter nuclear distance between projectile and target nuclei, but also on other some important degrees of freedom. The identification and understanding of these additional degrees of freedom is a major and hot problem in heavy ion nuclear fusion Physics. The various mechanisms suggested by the experimental studies on fusion for the last two decades are orientation and vibration of nucleons, static and dynamic deformation of the participating nuclei, coupling of the inelastic and transfer channels, threshold variation of nuclear potential etc. Neck formation between colliding partners, zero point motion of the nuclear shape nature of the nuclei such as the permanant deformation etc., are mechanisms which influence fusion by splitting and lowering the coulomb barrier. It is a very complicated and inconvienient task to seperate the effects of each individual degree of freedom, though the role of static deformation has been well established. Another exciting phenomenon is the broadness of the measured partial wave distribution compared to the predictions of 1DBPM. The theoretical approaches to understand sub-barrier fusion and angular momentum distribution are mainly the following - Coupled Channel (CC) Model due to Dasso-Broglia [2,3], Stelson's neutron flow and neck formation model [4,5] and Satcheler's energy and ℓ-dependant optical potential model [6]. A descrete number of barriers is considered in CC calculation where as a continuum of barriers is used in neuton flow model. The fusion excitation function and moments of angular momentum distribution in fusion are related to each other. The enhancement of sub-barrier fusion cross section is due to the coupling of various internal degrees of freedom to the relative motion. CC calcutions can qualitatively and quantitatively describe the enhancement effects. A clear understanding and identification of the channels, which act as a main door way to fusion

is a severe problem. Even though the fusion excitation function are considered as featureless, the extraction of barrier distribution [7] from experimental excitation function data reveals the characteristic features of the type of coupling involved. Over the past few years a new dynamical picture of sub-barrier fusion has emerged as a consequence of the considerable theoretical efforts of various authors [8,9] for explaining the experimentally observed sub-barrier fusion enhancements. According to this new picture additional degrees of freedom besides the one corresponding to the relative motion of the colliding nuclei are necessary and relevant components of the interation potential that governs the fusion process at sub-barrier energies.These internal degrees of freedom produce a strong influence by nuclear structure effects on nuclear reaction dynamics. The nature of the interaction can be determined from the nuclear structure of the colliding nuclei or conversely nuclear structure information can be extracted from sub-barrier fusion data. The various models that have been proposed for explaining the sub-barrier fusion process are briefly discussed in the following sections. A brief review of the experimental investigations by different groups on various projectile-target combinations in the sub-barrier fusion measurements is also given.

2.1 Fusion Probability

Energy E and angular momentum ℓ-dependant futions probability is defined as [10]

$$P(E,\ell) = 1/(\pi R_b^2)\,[(E-E_{rot})\, d\sigma_{fus}/dE\,|_{(E-Erot)} + \sigma_{fus}\,(E-E_{rot})] \qquad (2.1)$$

where $$E_{rot} = (\hbar^2/2I)\, J\,(J+1) \qquad (2.2)$$

with the rigid moment of inertia, $I = 2mr^2/5$

Fusion cross section can be written using $P(E,\ell)$ as [11]

$$\sigma_{fus} = \pi\lambda\!\!\!^{-2} \sum_{\ell=0}^{\infty} (2\ell+1)\, P(E,\ell) \qquad (2.3)$$

For a compound nucleus of excitation energy E* formed through a reaction of Q-value Q, the neutron evaporation residue cross section is related to the probability of the compound nucleus to end up in neutron evaporation residues W(E*,l)

$$\Sigma_x\sigma_{xn}\,(E^*) = \pi\lambda\!\!\!^{-2} \sum_{\ell=0}^{\infty} (2\ell+1)\, P(E^*-Q, \ell)\, W(E^*,\ell) \qquad (2.4)$$

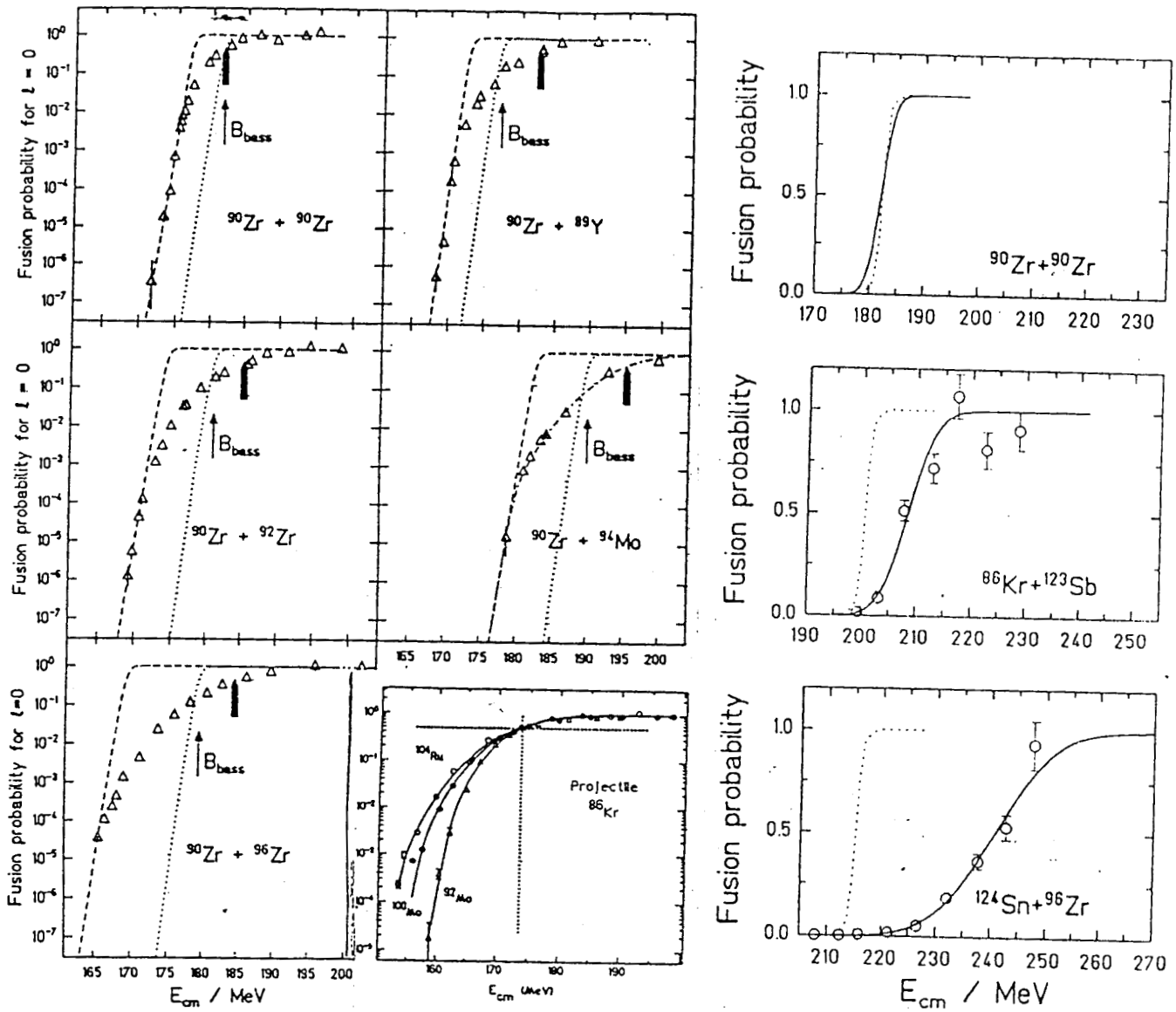

Figure 2.1 : Fusion probability for different systems as a function of centre-of-mass energy.

The angular momentum weighted average of the fusion probability <P(E,l)>is given as

$$\langle P(E,\ell)\rangle = \Sigma_x \sigma_{xn}(E^*) / \{ \pi\lambda^2 \sum_{\ell=0}^{\infty} (2\ell+1)\, W(E^*,\ell)\} \quad (2.5)$$

$$= \{\pi\lambda^2 \Sigma (2\ell+1)\, P(E^*,\ell)\, W(E^*,\ell)\} / \{\pi\lambda^2 \Sigma (2\ell+1)\, W(E^*,\ell)\} \quad (2.6)$$

Figure 2.1 shows the fusion probability measured for various systems reproduced from different authors. The dotted lines are one dimensioned fusion model/WKB calculations using Bass potential barrier. The solid curves in the right most figures show the fusion probability for ℓ=0 determined from a fit of a 1DBPM with barrier fluctuations to evaporation residue measurements. Dashed curves shows fusion probability with barriers shifted to low energy data. Triangles represents experimental excitation function and circles experimentally measured fusion probability.

2.2 Spin Angular Momentum Distributions in the Compound Nucleus

The various moments of the spin angular momentum distribution is defined as

$$\langle \ell^n \rangle = \sum_{\ell=0}^{\infty} (\ell^n \sigma_\ell) / \sum_{\ell=0}^{\infty} \sigma_\ell \equiv \int_0^{\infty} ((\ell^n \sigma_\ell d\ell) / \int_0^{\infty} \sigma_\ell d\ell \quad (2.7)$$

where n = 0,1,2,3,..... and the fusion cross section σ_ℓ for the ℓ^{th} partial wave at the centre of mass energy E is expressed as the zeroth moment of ℓ-distribution.

$$\sigma_\ell(E) = \pi\lambda^2(2\ell+1)\, T_\ell(E) \quad (2.8)$$

with $\lambda = \hbar/\sqrt{2\mu E}$ where μ is the reduced mass and transmission coefficients for ℓ^{th} partial wave

$$T_\ell(E) = \Sigma_\alpha |U_{\alpha 0}|^2 [1+\exp\{2\pi/\hbar\omega\, (v_{b\ell}+\lambda_\infty-E)\}]^{-1} \quad (2.9)$$

The angular momentum distribution depends on the coupling interaction strength V_{cpl} and energy E. For lower energies $E < V_{b\ell}-V_{cpl}$ the angular momentum distribution has a quantal limit and independent of the coupling strength and bombarding energy given as [12]

$$P(\ell) \cong - d/d\ell \exp[-(l/a)^2] \quad (2.10)$$

where $a^2 = 2\mu R_b^2 \varepsilon/\hbar^2$ and $\varepsilon = \hbar\omega/2\pi$

For higher energies $E > V_{b\ell}+V_{cpl}$ and the spin distribution approaches a triangular form. At intermediate energies coupling interaction is effective and $V_{b\ell}-V_{cpl} < E < V_{b\ell}+V_{cpl}$ which certifies about the importance of the effect of coupling strength. Angular momentum distribution can not be measured directly like the experimental measurement of fusion cross section, but can only be derived from different experimental methods such as :

1) Relative yields of the various evaporation resides (partial fusion cross section ratio) formed in the decay of compound nucleus using statistical methods.
2) Fission fragment angular distributions.
3) Gamma–ray multiplicity measurements.
4) Isomer ratios.

These methods are also used for measuring the average angular momentum (ℓ) of the compound nucleus system which is the first momentum considered as a measure of the centroid of the spin distribution.

2.3 Methods for Determining ℓ–distribution (Partial Fusion Cross Section Method)

The relative yield of various evaporation residues at a given excitation energy of the compound nucleus depends on the angular momentum distribution, density of the final states, barrier penetration factors etc. This ratio of partial fusion cross section for different evaporation residues (ER) can be obtained from statistical model calculations for a given angular momentum with which the compound nucleus is formed [13]. The fractional yields of the ERs have to be folded with the ℓ-distribution with which the compound nucleus is formed. A comparison between the statistical model calculations –CASCADE- [14] with experimental results is given by Dasgupta et al., [15] for 3N/4N and 4N/5N ER ratio. The angular momentum dependance of the fractional evaporation cross section for 2N/3N channels had been well investigated by Hasse et al. [16]. The average angular momentum extracted by this method was found to depend on the statistical model parameters such as level density parameter 'a' [17]. Vinod Kumar et al., [18] derived the average angular momentum for the $^{48}Ti + ^{58,60,64}Ni$ systems by this method and compared with CASCADE predictions.

2.4 Average Angular Momentum <ℓ>

As a function of energy mean angular momentum exhibits mainly three features in the frame work of CC formalism [12,19]. For energies well below the barrier the shape of σ_ℓ becomes Gaussian and does not change with energy. Above the coulomb barrier σ_ℓ has a triangular shape and <ℓ> varies quickly with energy. Around the barrier <ℓ> depends on the coupling strengths and enhanced to form a bump corresponding to the strong coupling region [12]. The average angular momentum attains a constant value for below barrier energies which can be represented as

$$<\ell> \cong 2/3 \sqrt{((2\mu R_b^2(2\varepsilon))/\hbar^2)} \qquad (2.11)$$

For above barrier energies average angular momentum is given by a classical limit

$$<\ell> \cong 2/3 \sqrt{((2\mu R_b^2(\varepsilon - Vb))/\hbar^2)} \qquad (2.12)$$

At the intermediate energy region around the barrier <ℓ> can be roughly estimated as

$$<\ell> \cong 2/3 \sqrt{((2\mu R_b^2(V_{cpl}))/\hbar^2)} \qquad (2.13)$$

The coupling interaction have no significant effect on <ℓ> for energies well below and well above the coulomb barrier which can be illustrated from the similar results of <ℓ> values obtained by coupled channel calculation and 1DBPM predictions for these energy regions. Balantekin et al., [20,21] reported an expression for deriving average angular momentum for fusion excitation function, by numerical integration using interpolated and extrapolated values of σ_f .In the case of deformed target an R_b is associated with each orientation, a weighted average of R_b has been used .

$$<\ell> = (1/E\sigma(E))(2\hbar^2/\mu R_b^2)^{1/2} \int_{-\infty}^{E} \sigma(E_\ell) E_\ell \, dE_\ell \; / (E-E_\ell)^{1/2} \qquad (2.14)$$

$$\text{where } E_\ell = E - \ell(\ell+1)\hbar^2/2\mu R_b^2 \qquad (2.15)$$

This method was used by Ackermen et al., [10] and Dasgupta et al., [13] and found that values of <ℓ> obtained was well with in the experimental uncertainities. Vinod Kumar et al., [18] also followed the same method for extracting <ℓ> from experimental

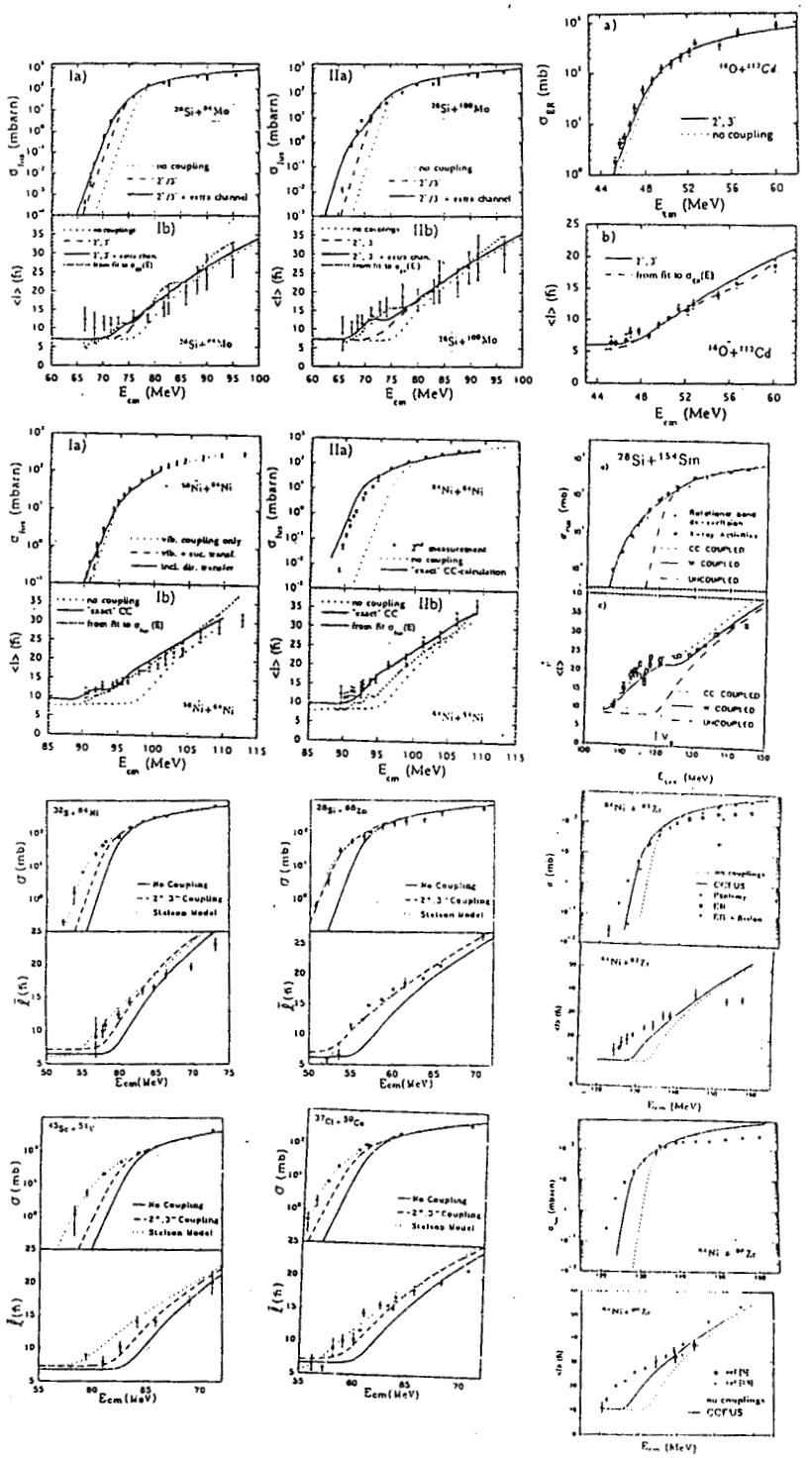

Figure 2.2 : Typical fusion excitation functions and average angular momenta for different systems.

fusion excitation function for the $^{48}Ti+ ^{58,60,64}Ni$ systems. Dasso et.al., [22] also suggested that fusion cross sections and angular momentum are not independent quantities and angular momentum can be obtained from measured fusion excitation function using some simple assumptions about fusion process. Figure 2.2 shows a comparison of fusion cross section and average angular momentum for different systems.

2.5 Cross section and Critical Angular Momentum

The maximum angular momentum above which the possibility of formation of a compound nucleus would disappear is called critical angular momentum (ℓ_{cr}). For low energy light ion reactions the direct reaction cross section and compound nuclear (CN) cross section are almost equal. $\sigma_R \cong \sigma_{CN} = \pi R_b^2 (1-V_b/E)$ where R_b is the barrier radius and V_b is the interaction barrier and E incident energy. But for high energy heavy ion reactions $\sigma_{CN}<\sigma_R$ and $\sigma_{CN} = \pi R_{cr}^2(1-V_{cr}/E)$ where R_{cr} and V_{cr} are the critical values. The simplest classical summation formulation of partial waves for CN cross section is

$$\sigma_{CN} = \pi\lambda\!\!\!^{-2} \sum_{0}^{\infty} (2\ell+1)\, P_\ell \qquad (2.16)$$

where P_ℓ is the product of the transmission coefficient T_ℓ and probability $P_\ell(CN)$ for the ℓ-wave to end up in the compound system. For highest ℓ-values $T_\ell < 1$ and $P_\ell(CN) = 0$. Therefore

$$\sigma_{CN} = \pi\lambda\!\!\!^{-2} \sum_{0}^{\ell cr} (2\ell+1) P_\ell(CN) \qquad (2.17)$$

where $\ell_{cr}\hbar$ is the limit above which $P_\ell(CN) = 0$. At the sharp cut off $P_\ell(CN) = 1$ to $P_\ell(CN) = 0$

$$\sigma_{CN} = \pi\lambda\!\!\!^{-2}(\ell_{cr}+1)^2 \qquad (2.18)$$

The total reaction cross section is given as

$$\sigma_R = \pi\lambda\!\!\!^{-2}[\ell_g^2 + \sum_{\ell_g}^{\infty} (2\ell+1)T_\ell] \qquad (2.19)$$

wher the grazing collisions are summed up above ℓ_g, damped collisions are summed up between ℓ_{cr} and ℓ_g with $T_\ell = 1$ and $P_\ell(CN) = 0$ and the compound nucleus collisions are summed up between $\ell=0$ and ℓ_{cr}. At the sharp cut off where T_ℓ decreases from 1 to 0 the

diffuse edge region can be replaced by a step function at a cut off value $\ell_{CT(max)}$. Then the total reaction cross section $\sigma_R = \pi\lambda^2\Sigma_0^{\infty}(2\ell+1)T_\ell$ becomes $\sigma_R = \pi\lambda^2(\ell_{CT(max)}+1)^2$. For larger ℓ values $\sigma_{CN}/\sigma_R = \ell_{cr}^2/\ell_{CT(max)}^2$. The experimental measurement of σ_{CN} are expressed in terms of the critical angular moments $\ell_{cr}\hbar$. Another parametrization for fusion cross section reported by Prasad et. al.,[23] which can be written as

$$\sigma_{red} = \ln [1+ \exp 2\pi E_{red}] \qquad (2.20)$$

where $\sigma_{red}=2\sigma_{fus} E_{cm} / R_b^2\hbar\omega$, $E_{red} = E_{cm} - V_b/\hbar\omega$, $\hbar\omega$ = barrier curvature, R_b = Radius Parameter, V_b = Coulomb barier height and E_{cm} = Incident energy in CM system. The parameter V_b, R_b and $\hbar\omega$ can be obtained by using Akyuz-Winther (AW) potential.Therefore fusion cross section becomes

$$\sigma_{fus} = R_b^2 \hbar\omega /2E_{cm} \ln[1+\exp (2\pi E_{cm}-V_b/\hbar\omega)] \qquad (2.21)$$

The classical sharp cut off model based expression for fusion cross section for energeis above barrier ($E > V_b$) is $\sigma_{fus} = \pi R_b^2(1-V_b/E_{cm})$

2.6 Interaction Potentials

The interaction potential for a projectile-target system is given as

$$V_\ell(r) = V_n(r) + V_c(r) + V_{cent} \qquad (2.22)$$

where V_n is the nuclear potential, V_c is the Coulomb potential and the last term is the centrifugal potential.. The nuclear potential is normally of the Akyuz-Winther form with Woods-Saxon parameterization having real and imaginary parts.

$$V_n(r) = -V_0/\{1+\exp[(r-R_v)/a_v]\} + i\ W_0/\{1+\exp[(r-R_w)/a_w]\} \qquad (2.23)$$

Here 'R' stands for the core radius, 'a' represents the diffuseness parameter and V_0 and W_0 represents the depths of nuclear potential. Assuming the nuclei as uniformly charged spheres of radius $R_c = r_c(A_p^{1/3} + A_t^{1/3})$ with r_c=1.3 fermi. For systems $A_p < A_t$, the Coulomb potential can be represented as

$$\begin{aligned} V_c(r) &= [Z_p Z_t e^2]\{3-(R/R_c)^2\}/2R_c \quad \text{for } r<R_c \\ &= Z_p Z_t e^2 /r \quad \text{for } r>R_c \end{aligned} \qquad (2.24)$$

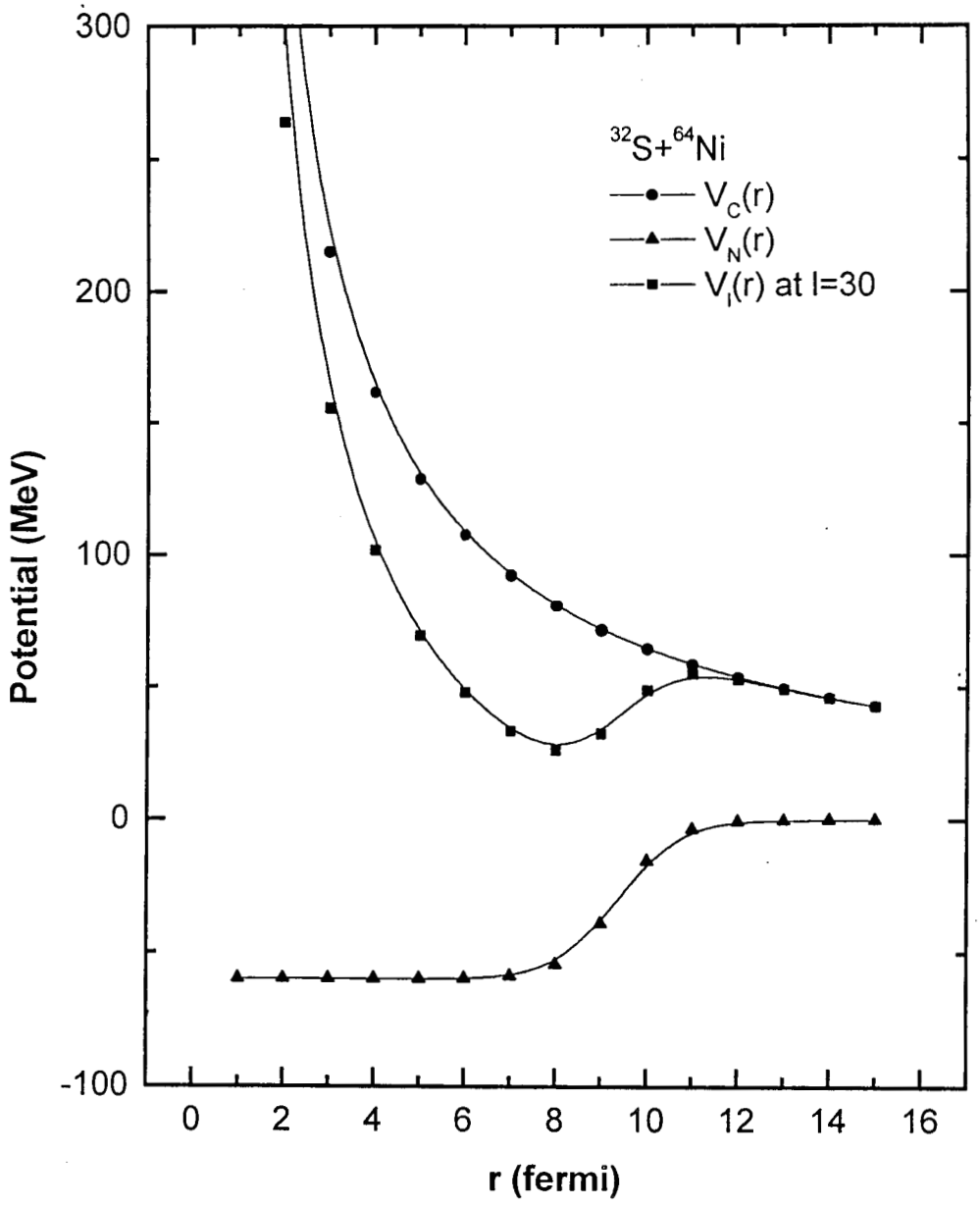

Figure 2.3 : The interaction potential for $^{32}S+^{64}Ni$ system having the nuclear and coulomb parts as a function of the relative separation between the projectile and target nuclei. The coulomb barrier is also shown.

The centrifugal potential is given as

$$V_{cent} = \ell(\ell+1)\hbar^2/2\mu r^2 \qquad (2.25)$$

where μ is the reduced mass of the system and ℓ is the relative angular momentum quantum number. Figure 2.3 represents the interaction potential $V_\ell(r)$ for $\ell = 30\hbar$ for the typical nuclear system $^{32}S+^{64}Ni$ which shows the above components $V_c(r)$, $V_n(r)$ and the coulomb barrier V_b. The macroscopic estimation of nuclear potential is carried out by folding methods, energy density methods and proximity methods [24].

2.7 Theoretical models for sub-barrier fusion

Different nuclear models are integral part of the development of nuclear physics and highly useful for understanding various nuclear phenomena. These models are applicable in the systematic interpretation of the large volume of experimental data available so far for large number of projectile-target combinations at different incident energies. These models are used to predict elastic cross sections, reaction cross sections, inelastic scattering to various excited states and the population of other individual channels with sufficiently good accuracy for any interacting system. Optical model is a versatile tool in nuclear physics which forms the starting point of various other models.

2.7.1 One Dimensional Barrier Penetration Model (1DBPM)

In nucleus-nucleus collision, when the centre of mass energy of the partners is larger than the barrier height they overcome the barrier and may lose some of the relative energy through friction to get trapped in the pocket and ultimately it will lead to the formation of a compound nucleus. The partial cross section for formation of compound nucleus of total angular momentum J and parity π from a projectile nucleus with spin I_p, parity π_p and target nucleus with spin I_t and parity π_t is given by Thomas [1]

$$\sigma(E,J) = \pi\lambda^2 (2J+1) / (2I_p+1)(2I_t+1) \sum_{s_1}^{s_2} \sum_{L_1}^{L_2} T_\ell(E) \qquad (2.28)$$

where J is the resultant of the incoming angular momentum ℓ and the channel spin S having the limits $L_1=|J-S|$, $L_2=|J+S|$, $s_1=|I_p-I_t|$ and $s_2=|I_p+I_t|$. Parity of the compound nucleus $\pi_{CN} = \pi_p\pi_t(-1)^{\ell}$ and de Broglie wave length of relative motion $\lambda(E) = (\hbar^2/2\mu E_\ell)^{1/2}$. The transmission coefficients $T_\ell(E)$ for the two nuclei depends mainly on angular momentum ℓ and energy E. The transmission coefficient for the potential $V_\ell(r)$ at energy E for heavy ion collision leading to compound nucleus formation due to strong absorption can be obtained as a simple Fermi's function of angular momentum.

$$T_\ell(E) = 1/(1+\exp[-(\ell-\ell_g)/d]) \qquad (2.29)$$

where ℓ_g is the grazing angular momentum and 'd' is the diffuseness parameter, which can be obtained from systematics and comparisons to optical model parameter. For even projectile and target nuclei spin I=0 and equation (2.28) reduces to the partial cross section expression as :

$$\sigma_\ell^R(E) = \pi\lambda^2(2\ell+1)T_\ell(E) \qquad (2.30)$$

where $\lambda = \sqrt{\hbar^2/2\mu E}$ is the asymptotic wave length and μ is the reduced mass of the system. If $P_\ell(E)$ is the probability for the system to fuse after passing through coulomb barrier, we can write the partial cross section as

$$\sigma_\ell^{fus}(E) = \pi\lambda^2 (2\ell+1)T_\ell(E)P_\ell(E) \qquad (2.31)$$

The cross section for complete fusion can be obtained by summing the above cross section in equation (2.31) for all partial waves which contribute to fusion as

$$\sigma^{fus}(E) = \sum_{\ell=0}^{\ell=\infty} \pi\lambda^2 (2\ell+1)T_\ell(E)P_\ell(E) \qquad (2.32)$$

When fusion reactions are described in the one dimensional model the effective potential is assumed to be a function of only the relative separation of the colliding nuclei. In such a model, for not too massive systems and near barrier energies it is assumed that nuclei which overcome the barriers will fuse to give rise to a probability of fusion equal to one. The total reaction cross section becomes

$$\sigma^R(E) = \sum_\ell \sigma(E) = \pi\lambda^2 \sum_{\ell=0}^{\infty} (2\ell+1)T_\ell(E) \qquad (2.33)$$

Many possible reaction mechanisms are involved in $\sigma^R(E)$. The relative importance of each process will depend on the energy, angular momentum and type of nuclei involved. The transmission coefficient for angular momentum ℓ at energy E depends on the total nucleus-nucleus potential V_ℓ. A knowledge of the potential is essential for undestanding the nuclear reaction mechanism. The nucleon-nucleon interaction, properties of the nuclear matter, distribution of the nucleons can be understood from the interaction potential. WKB approximation is used for the penetration through the barrier to determine the transmission coefficient. This problem can be simplified by approximating the interaction potential around the barrier by an inverted parabola of height V_ℓ and radius of curvature $\hbar\omega_\ell$. The Hill-Wheeler [25] expression for transmission coefficient T_ℓ under this approximation is given as a special case of WKB approach

$$T_\ell(E) = [1+ \exp((2\pi/\hbar\omega_\ell)(B_\ell-E))]^{-1} \qquad (2.34)$$

Where B_ℓ is the barrier height in Mev for angular momentum ℓ and ω_ℓ is the vibrational frequency of the harmonic oscillator in the parabolic potential

$$\hbar\omega_\ell = \left|(\hbar^2/2\mu)(d^2V_\ell/dr^2)\right| r=R_{b\ell} \qquad (2.35)$$

If the barrier curvature and barrier radius are independent of angular momentum ℓ and equal to S-wave values $\hbar\omega_\ell = \hbar\omega$ and $R_{b\ell} = R_b$. Therefore

$$\sigma_\ell = \pi\lambda\!\!\!^{-2}(2\ell+1)[1+\exp((2\pi/\hbar\omega)(B_\ell-E))]^{-1} \qquad (2.36)$$

Total fusion cross section

$$\sigma_{fus}(E) = \pi\lambda\!\!\!^{-2} \sum_{\ell=0}^{\ell=\ell c} (2\ell+1)\, T_\ell(E) \qquad (2.37)$$

Wong formula [26] for fusion cross section for a quantal system of single barrier

$$\sigma_{fus}(E) = R_b^2\hbar\omega_0/2E \ln[1+\exp[2\pi/\hbar\omega_0(E - V_b)] \qquad (2.38)$$

where V_b is the S-wave barrier height in the region $\ell=0$, R_b is the potential barrier radius for the S-wave and ω_0 is the oscillator frequency corresponding to the barrier top $V_{b\ell} = V_b+\hbar^2\ell(\ell+1)/2\mu R_b^2$. The above equation (2.38) shows that the fusion cross section increases exponentially with $(E - V_b)$ for sub-barrier energies. This model could explain the cross section for light ions but under estimates the experimental cross sections for reactions

with heavier systems at sub-barrier energies. In classical approximation, the penetrabilities are completely determined by the height $V_{b\ell}$ of the barrier in the potential.

$$T_\ell(E) = \begin{cases} 1 & \text{for } E > V_{b\ell} \text{ and } \ell < \ell_c \\ 0 & \text{for } E < V_{b\ell} \text{ and } \ell > \ell_c \end{cases} \qquad (2.39)$$

Here ℓ_c is the highest partial wave for which $E > V_{b\ell}$. This is the sharp cut off model. With this assumption for fusion equation can be written for a barrier radius $R_{b\ell}$ not depending on orbital angular momentum ℓ and $\ell_c >> 1$

$$\sigma_{fus} = \pi\lambda\!\!\!^{-2}(\ell_c+1)^2 \cong \pi\lambda\!\!\!^{-2}\ell_c^2 = \pi\lambda\!\!\!^{-2}\left[\frac{2\mu R_b\sqrt{(E-V_b)}}{\hbar}\right]^2 \qquad (2.40)$$

$$\text{For } E > V_b, \quad \sigma_f(E) = \pi R_b^2(1-V_b/E) \qquad (2.41)$$

$$\text{For } E < V_b, \quad \sigma_f(E) = \frac{R_b^2\,\hbar\omega_0}{2E}\exp[2\pi/\hbar\,(E-V_b)] \qquad (2.42)$$

Equation (2.41) gives a linear dependance between $\sigma_f(E)$ and 1/E for above barrier energies. For lower energies a clear departure from linearity is observed which indicates that the classical expression is no longer valid. Then the barrier penetration probabilities have to be calculated using quantum mechanical methods like the WKB approximation.

2.7.2 Coupled Channel (CC) Model

The coupling of the channels such as transfer, inelastic etc., to the incident channel suggested by Dasso [2] and Broglia [3] can modify the barriers leading to the enchancement of fusion cross section at below barrier energies. The schrodinger equation for the coupled channels to be solved as given by Dasgupta et al .,[13] is

$$[(-\hbar^2/2\mu)(d^2/dr^2)+V_\ell(r)-E]\psi_\alpha(r) = -\Sigma_\beta \langle \alpha | H_0+V_{coup}(r,\xi) | \beta \rangle \psi_\beta(r) \qquad (2.43)$$

where H_0 is the intrinsic Hamiltonian, $|\alpha\rangle$ are the associated eigen vectors ,$\psi_\alpha(r)$ is the relative motion wave function, 'r' is the seperation between the centres of mass of the two nuclei, ξ represents intrinsic variables, μ is the reduced mass which can be assumed as same for all channels. By splitting the coupling interaction $V(r,\xi)$ into relative part $F(r)$ and an intrinsic part $G(\xi)$, the above set of coupled channel equations can be simplified.

Under this assumption, the coupling matrix becomes

$$M_{\alpha\beta} = < \alpha|H_0 + V_{coupl}|\beta > = \delta_{\alpha\beta}\, \varepsilon_\beta + F(r) < \alpha|G(\xi)|\beta > \qquad (2.44)$$

As per the constant coupling approximation, F(r) can be considered to be spatially constant around coulomb barrier and can be represented by F_0. The above approximations decouple the above mentioned coupled channel equation as

$$[(-\hbar^2/2\mu)\, d^2/dr^2 + V_\ell(r) + \lambda_\alpha(R_b)]\, \Sigma_\beta U_{\alpha\beta}\, \psi_\beta(r) = 0 \qquad (2.45)$$

where the unitary matrix $U_{\alpha\beta}$ diagonalizes the coupling matrix $M_{\alpha\beta}$ to give a set of eigen values λ_α . The single barrier will be replaced by a set of barriers $V_\ell(R_b) + \lambda_\alpha(R_b)$ due to coupling effects . The summation of the transmission coefficient for individual barriers in the spectrum weighted by overlap factor $|U_{\alpha 0}|^2$ gives the total transmission coefficient at the energy E for the ℓ-wave

$$T_\ell(E) = \Sigma_\alpha\, |U_{\alpha 0}|^2\; T_{\ell 0}\, [E, V_\ell(r) + \lambda_\alpha(R_b)] \qquad (2.46)$$

where the weight factor $U_{\alpha 0}$ is the overlap probability of the entrance channel with the corresponding eigen factor, λ_α is the eigen value of the coupling matrix relative to α-channel and $T_{\ell 0}$ is the transmission coefficient at energy E - λ_α which can be calculated by WKB parabolic approximation for below barrier energies. For strong coupling low energy fusion cases, the coupled system has to be diagonalised in the vicinity of coulomb barrier to obtain the eigen values and eigen vectors as a function of 'r'.

The barrier position for each channel can be obtained by finding the value of 'r' for which the quantity $V_\ell(r) + \lambda_\alpha(r)$ is an extremum (maximum) and hence the barrier height $V_\ell(R_{b\alpha}) + \lambda(R_{b\alpha})$ and the curvature $\hbar\omega_\alpha$ can be obtained. The transmission coefficient can be obtained by the modified expression :

$$T_\ell(E) = \Sigma_\alpha\, |\, U_{\alpha 0}(R)|^2\, T_\ell\, [(E, V_\ell(r) + \lambda_\alpha(r)] \qquad (2.47)$$

here $|U_{\alpha 0}(R)|^2$ is the weight factors fixed at distance R which is the position of the unperturbed barrier or the average position of the eiegn barriers and 0 in $U_{\alpha 0}$ represents the entrance channel. The coupling strength for inelastic excitations for low lying collective states can be obtained as

$$F_k(r) = \frac{\beta_{\lambda k}}{\sqrt{4\pi}} \left[-R_k \frac{dV_n(r)}{dr} + \frac{3 Z_p Z_t e^2 R_k^{\lambda}}{(2\lambda+1) R_b^{\lambda+1}} \right] \qquad (2.48)$$

where λ is the multipolarity of the transition k represents the excited nuclei, R_k is the radius of the excited nuclei, and V_n is the nuclear potential $\beta_{\lambda k}$ is the input nuclear and coulomb deformation parameter is given as

$$\beta_{\lambda k} = \frac{4\pi}{3ZR^{\lambda}_{k}} [B_k (E\lambda)/e^2]^{1/2} \text{ with } R_k = 1.2\ A_k^{1/3} \qquad (2.49)$$

The fusion cross section is given as

$$\sigma_{fus}(E) = \pi\lambda^2 \sum_{\ell} (2\ell+1)T_{\ell}(E) \qquad (2.50)$$

Figure 2.4 shows the splitting of the barrier for different partial waves for a typical Titanium-Nickel nuclear system extrapolated from Vinod Kumar et al.[18].

2.7.3 Stelson's Neutron flow model

Stelson [4] developed a successful and compact parametrization for heavy-ion fusion cross section. In this model a distribution of barriers extending below the classical barrier is considered and the integration of the classical expression for the fusion of the two charged spheres over the distribution of barrier will give a detailed explanation for fusion. Stelson used mainly four parameters for developing the model. These are the nucleus-nucleus potential barrier B, the barrier radius R, threshold barrier T where the distribution of barriers cuts off and the width ω of the Gaussian modulation of this cut off threshold. By examining the threshold barrier obtained for different isotope series Stelson observed that the position of the threshold barrier correlated well with the binding energy of the valence neutrons of the nuclei in the entrance channel. On the basis of this observation Stelson suggested that neutron flow between the nuclei sets in at large inter nuclear distance leading to the neck formation and acts as an agent for lowering the barrier there by enhancing the heavy ion fusion probability. As the projectile approches target nuclei, the nuclear surfaces overlap each other and gradually the barrier for neutron flow across the nuclei vanishes results in the neck formation and fusion. The correlation between the neutron flow and experimental data of sub-barrier fusion, role of neutron binding in the entrance channel and maintanance of neutron flow after the first neutron transfer are the questions yet to be answered in Stelson model [4].

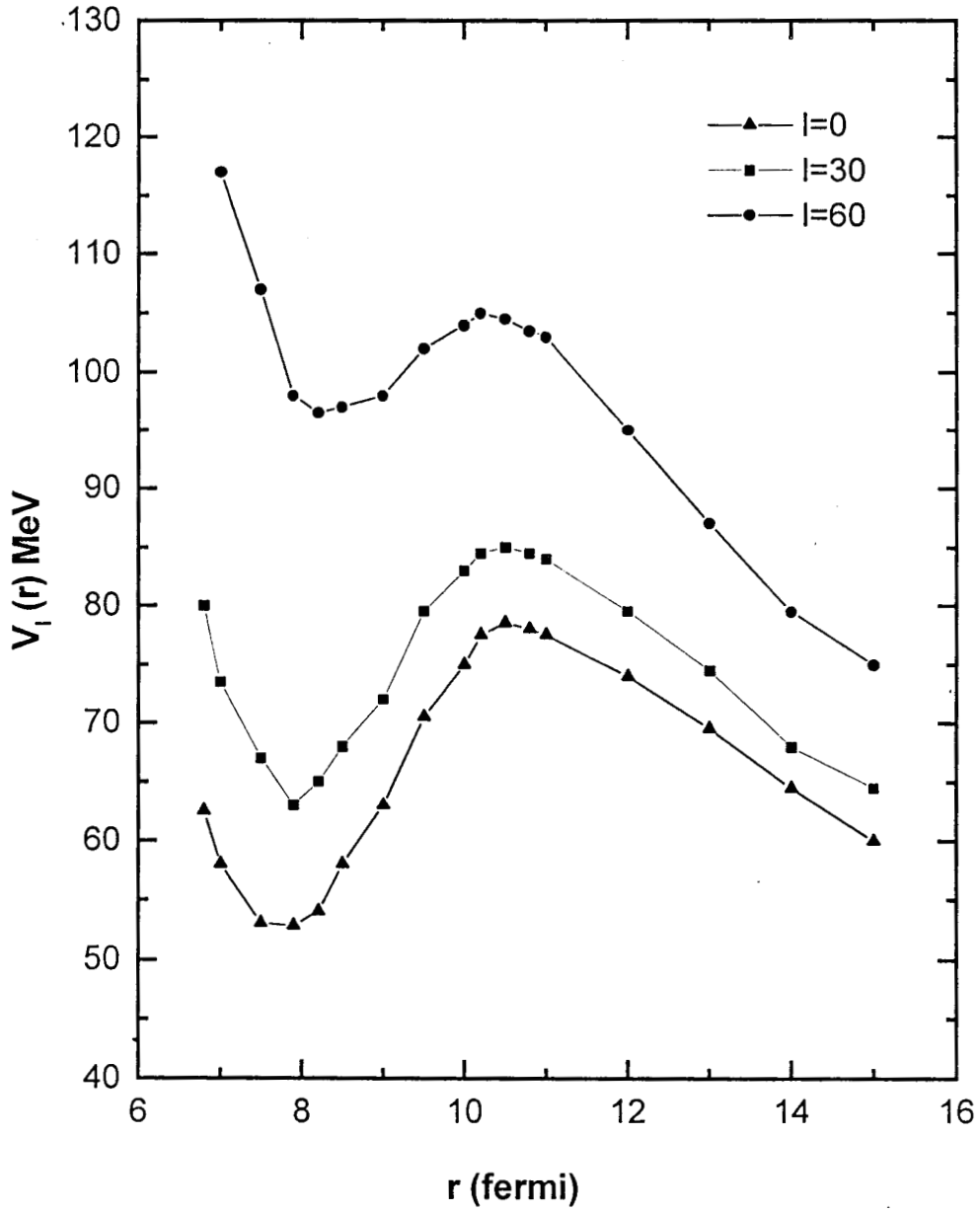

Figure 2.4 : Splitting of coulomb barrier for a typical nuclear system (^{48}Ti+^{58}Ni). The data have been extrapolated from Vinod Kumar et al.[18].

According to Stelson's neutron flow model a distribution of barrier fit the experimental cross section at sub-barrier energies. The fusion cross section at energy E is given as :

$$\sigma(E) = \int_0^\infty \sigma(E,B)\, D(B)\, dB \qquad (2.51)$$

where $\sigma(E,B) = \pi R_b^2(1-B/E)$ and $\int D(B)\, dB = 1$. By fitting the above equation (2.51) for $\sigma(E)$ to the experimental cross section, the distribution of barriers D(B) can be deduced. Best fits are expected for a flat distribution about the mean barrier B_M with a sharp cut off at the low energy. Barrier distribution is defined as

$$D(B) = \begin{cases} \frac{1}{2}(B-T) & \text{for } T \le E \le 2(B-T) \\ 0 & \text{else where} \end{cases} \qquad (2.52)$$

B-T is the half width of the distribution. The classical expression for calculating the fusion cross section proposed by Stelson et. al., [4] are: $\sigma_f = \pi R_b^2 [1-B/E]$ for $E > B$ where σ lies in the range 200 mb $< \sigma <$ 400 mb and $\sigma_f = \pi R^2(E-T)^2 / 4(B-T)E$ for $E < B$, the value of σ lies within the range 10 mb $< \sigma <$200 mb. Here R is the barrier radius, T is the sharp lower cut off threshold, B is the mean of the symmetric flat distribution of barriers D(B) in the absence of fluctuation. Below T the nuclear surfaces can not come sufficiently close to cause neutron flow. So classically fusion can not be expected for energies below the threshold barrier. A very good correlation between T and inter surface distance has been observed [27] for a large number of systems after including the zero point motion of collective surface vibrations of the colliding nuclei, using the Stelson's neutron flow model. Shapira and Stelson [28] studied about the role of neutron flow in the enhancement of heavy ion fusion at sub-barrier energies for several systems. Theoretically T corresponds to the inter nuclear distance required for the overlap of neutron wells to depress the barrier between them more than 1 MeV below the neutron binding energy in the nucleus.

2.7.4 Interacting Boson Model

Various nuclear structure models can be tested by the effects of sub-barrier fusion enhancement by the experimental determination of the average angular momentum and the barrier distributions in the fusion reactions. Balantekin et. al.,[29] reported a model for sub-barrier fusion incorporating the interacting boson model (IBM). In this model the S and d bosons describe the nuclear structure effects of the low lying states of the collective nuclei. The coupling of nuclear multipole interactions to all orders beyond the linear coupling approximation was done using Green's function technique. Barrier distributions determined directly from fusion data are sensitive to the nuclear structure effects and can provide good test for various sub-barrier fusion models. The extra degrees of freedom coupled to the simple barrier penetration model of two colliding spherical nuclei yield the distribution of barriers and so enhance the fusion cross section below the barrier. Balentekin et. al.,[30] calculated the fusion cross section and barrier distribution using their formalism of linear and higher order coupling and compared with the experimental results. They have calculated the fusion cross section using the expression for partial wave expansion in the barrier penetration picture.

$$\sigma_{fus}(E) = [\pi\hbar^2/2\mu E] \sum_{\ell}^{\infty} (2\ell+1)T_{\ell}(E) \qquad (2.53)$$

The penetration probabilities for different partial waves were calculated numerically using a uniform WKB approximation valid for energies both above and below barrier.

2.7.5 Satchler's Energy and ℓ-dependant Optical Potential Model

The optical model [6] is used to calculate both elastic and non-elastic scattering or reaction by defining a one body complex potential. Due to the complexity of solving the Schorodinger equation for realistic forms of the potential the connection between the properties of the potential and features of the reaction cross section is rather indirect. Optical model is based on an analogy with optics where a complex index of refraction fulfils the function of scattering potential for light waves in the presence of absorption. The generalised optical potential operator which is introduced in the place of the potential in

Schrödinger equation for elastic scattering takes account of the effect of the coupling to all other non-elastic channels. The elastic scattering amplitude calculated from generalized optical potential (GOP) generally has a complicated energy dependance which can be decomposed into an energy averaged part and a flucturing part. The phenomenological optical model potential is the above energy averaged part. When a nucleon of mass m_n labelled by index O is transferred into a target of mass number A, the space of reaction states for the A+1 nucleon system is spanned by eigen states of the shell model Hamiltonian.

$$H_S = \sum_{i=0}^{A} T(i) + V_S(i) \qquad (2.54)$$

where the potential V_S is the shell model potential which binds or scatter the nucleons.

2.8 Statistical Model

Niels Bohr [31] proposed the Statistical model theory of nuclear fusion to form the compound nucleus. The excited compound nucleus attains thermal equilibrium, forgets about its mode of formation and then decays through the evaporation procedure. Depending on the excitation energy the compound nucleus may undergo fission or emits heavy or light ions and then come to the complete deexcitation by the emission of gamma rays. This theory is developed by incorporating the energy and angular distributions of the emitting particles with special consideration to the parity and angular momentum effects. By considering the probability for the fusion of projectile and target and the probability for the decay of the compound nucleus, the transmission coefficient is derived. The probability for any mode of decay is inversely proportional to the total number of exit decay channels. The decay probability is related to level density of the residual nucleus, angular momentum and transmission coefficient T_ℓ of the emitted particles. If ℓ is the orbital angular momentum, ε is the kinetic energy and B_i is the binding energy of the emitted nucleon, then the energy and angular momentum is conserved as $E = E_f + \varepsilon + B_i$ and $J = I + \ell + J_f$. The partial cross section for compound nucleus with total angular momentum J and parity π is given by equation (2.28). The total reaction cross section includes contributions from various exit channels as given in equation (2.33).

2.8.1 Statistical Model Codes

The decay scheme of compound nucleus by emitting fission fragments,α,p,n,γ etc. can be studied using the statistical model codes. This calculations consider various decay modes by calculating the energy and angular momentum distributions. Two methods are normally followed in this model and on the basis of this methods, two types of codes are popular. They are discussed in the following sections.

1) CASCADE : This is a multistep gridded calculation by considering a grid of various decay modes to various residual nuclei. It was developed by Pühlhofer [14] to perform the evaporation calculations based on the statistical theory of compound nucleus. CASCADE require two input data files-one mass table (EBTABLE.DAT) and a table of transmission coefficients(TLCALC.DAT). Optical model potential (Woods-Saxon) are to be used for generating TLCALC.DAT. This code can be used for calculating the partial fusion cross section and mean angular momentum as a function of level density parameters. Gamma decay widths also have to be considered for the predictions of the decay of the compound nucleus through the gamma ray emission. Another parameter to be used in CASCADE is the diffuseness parameter. A detailed study of the extraction of partial fusion cross section and average angular momentum for various systems were carried out by Prasad et. al.,[23] and Vinod Kumar et. al.,[18] using this code. They have given a comparison with experimental results.

2) PACE : This is a multistep Monte Carlo code. PACE2 is a modified version of PACE which calculates the first transmission coefficient $T_\ell(z)$ and interpolates the rest of the $T_\ell(z)$. The mode of decay is chosen through the Monte Carlo technique from the available decay probabilities for different daughter channels. The computing time is longer due to step by step nature of PACE2. The input parameters are some what similar to that of CASCADE. PACE2 can not be used for calculations below the barrier because it does not include the tunneling effects. PACE2 is used for calculating energy and angular momentum of evaporated particles besides the predictions of the decay scheme of compound nucleus.

2.9 Distribution of Barriers

The sub-barrier fusion process can be explained using the theoretical models of coupled channel calculations approach and Stelson's neutron flow model. The CC model proposes a discrete set of barrier distribution where as Stelson's model proposes a continuous distribution of barriers. In the expression for fusion cross section at energy E given by equation (2.51), the value of D(B) is

$$D(B) = \sum U_\alpha \ \delta(B-B_\alpha) \tag{2.55}$$

a descrete distribution in CC model and a smooth flat distribution function in Stelson's model as given in equation (2.52). The distribution of barriers D(B) can be obtained by fitting the experimental cross section. The classical fusion cross section can be written as

$$\sigma(E,B) = \pi R_b^2(1-B/E) \ \text{for } E > B \ \text{and} \ \sigma(E,B) = 0 \quad \text{for } E > B \tag{2.56}$$

Taking the derivatives of $E\,\sigma(E,B)$ with respect to E

$$\frac{d}{dE}[E\sigma(E,B)] = \pi R_b^2 \ \text{for } E > B \tag{2.57}$$
$$= 0 \quad \text{for } E < B$$

The second derivative of the above function becomes

$$\frac{d^2}{dE^2}[E\sigma(E,B)] = \pi R_b^2 \delta(E-B) \tag{2.58}$$

Using this relation in equation (2.51) becomes

$$\frac{d^2}{dE^2}(E\sigma) = \pi R_b^2 D(E) \tag{2.59}$$

$$1/(\pi R_b^2) \ \frac{d^2}{dE^2}(E\sigma) = D(E) \tag{2.60}$$

where D(E) is the distribution of barriers which can be obtained from the experimental fusion cross section around the barrier. In CC model the above quantity is related to the descrete set of barrier as

$$\frac{1}{\pi R_b^2} \frac{d^2}{dE^2}(E\sigma) = \Sigma_\alpha \left| U_{\alpha 0}(R_b) \right|^2 G(x_\alpha) \tag{2.61}$$

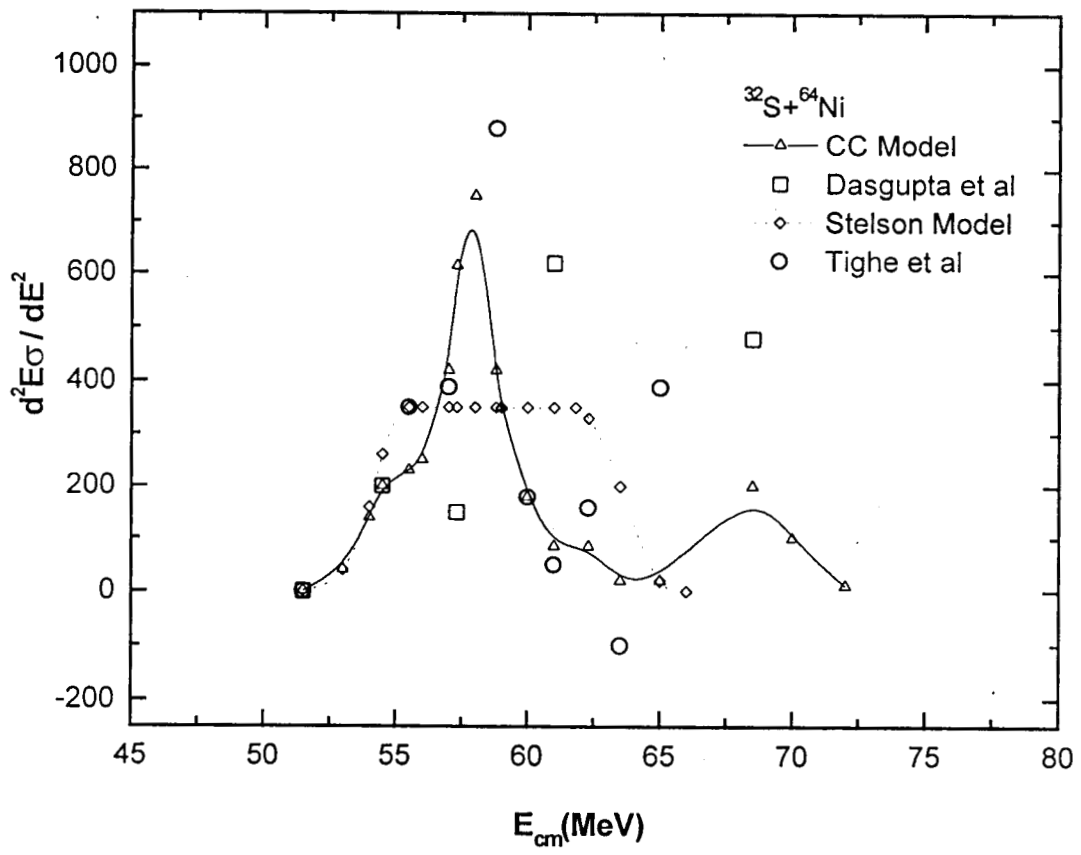

Figure 2.5 : A comparison of the barrier distributions for $^{32}S+^{64}Ni$ system by the experimental measurements with theoretical calculations based on Stelson model. The results of Coupled Channel calculations also given. The data have been extrapolated from Dasgupta et al.[13].

where $$G(x_\alpha) = \frac{2\pi\, e^{x_\alpha}}{\hbar\omega_\alpha(1+e^{x_\alpha})^2} \qquad (2.62)$$

with $x_\alpha = 2\pi / \hbar\omega_\alpha$ ($E-B_\alpha$) and $B = V(R_{b\alpha}) - \lambda_\alpha$. The analytical relation in Stelson's model is given as

$$\frac{1}{\pi R_b^2}\,\frac{d^2}{dE^2}(E\sigma) = \int_0^\infty D(B)\, G(x)\, dB = D(E) \qquad (2.63)$$

The second derivative of the experimental data is related to the barrier distribution smoothed with the function G(x)

$$\text{where } G(x) = \frac{2\pi\, e^{x}}{\hbar\omega(1+e^{x})^2} \quad \text{and} \quad x = \frac{2\pi(E-B)}{\hbar\omega} \qquad (2.64)$$

Here ω is the oscillator frequency corresponding to the barrier top. The function G satisfies the condition $\int G(x)dx = 1$ and becomes a delta function in the limit $\hbar\omega \rightarrow 0$. Figure 2.5 shows a comparison of the experimental values of $d^2(E\sigma)/dE^2$ for $^{32}S + ^{64}Ni$ system with the predictions of CC model and Stelson's model extrapolated from Dasgupta et al. [13].

2.10 Experimental Techniques for the Measurement of Fusion cross section

A review of the basic experimental techniques for the measurement of fusion cross section is given by Beckermann [32]. The methods can be generally classified into direct methods and indirect methods. The direct method is mainly the measurement of fusion evaporation residue by recoil mass spectrometers. The indirect methods are gama-ray yield measurement and X-ray yield measurement. Reisdorf [33] presented a review article on various experimental techniques.

2.10.1 Evaporation residue detection method

They are the devices used to focus the desired particles of the reaction products emitted in to a given solid angle on to a position sensitive detector and dispersed in terms of mass, energy, momentum or velocity. A good resolution can be obtained by the combination of high dispersion and high quality of focus with minimum ion-optical aberrations. The aberrations are strong functions of the solid angle of acceptance of the device and hence a compromise between high yield and good resolution is required. The energy dispersion is achieved through high electric fields and momentum dispersion through magnetic fields. Good mass resolution and the capability of operating at zero degree to the beam direction are the main features of a RMS. The path of an ion in an electromagnetic field is determined by the parameters such as mass, velocity and charge. The radius of curvature depends on E/q for electric field and mv/q for magnetic field. The fields are set for a velocity v = E/B in a velocity selector. The requirements of using RMS is due to the following reasons.

i) The availability of accelerated beams of heavier mass and higher recoil velocities of reaction products made the identification of Z, A and E quite cumbersome. This problem

can be solved by using on line RMS for measuring TOF(T), energy loss(ΔE) and residual energy (E) using ΔE-E telescope.

ii) The intensity of the beam is 10^{12} times higher than the intensity of the desired recoil nuclei. The recoils of fusion and transfer reactions of interest emitted in the forward direction have to be physically separated from the beam or from the intense background of elastically scattered particles at zero degree.

iii) Identification of the charge state q : Electric and magnetic deflectors sense only q, not Z. So for Z identification focal plane detectors are required.

There are at present a large number of recoil mass separators (RMS) used world wide. The FMA at Argone, RMS at LNL and HIRA at NSC are the latest devices in this series. The beam is well focussed and positioned at the center of the target by varying the electric and magnetic fields along the beam line after proper tuning by observing at the two beam profile monitors located along the beam line.

The evaporation residues with optimum m/q were selected by varying the RMS fields at the center of the focal plane, detected by the focal plane detectors (ΔE-E telescope). This data is used for determining the evaporation residue cross section. The mass (m/q) spectrum obtained from the banana gated projection of the 2D spectrum (MWPC-ΔE versus focal plane X-position) and from the m/q calibration, the mass peaks are identified and fitted with multiple/single Gaussian. If σ_i is the evaporation residue cross section for the i^{th} channel determined from the yield Y_i of the i^{th} channel, the total fusion cross section can be obtained from the partial ER cross section as $\sigma_{fus} = \sum\sigma_i$. The efficiency of the RMS can be obtained by the γ-coincidence method as the ratio of the number of gamma rays detected in coincidence with ER and the number of gamma rays detected at the scattering chamber using High Purity Germanium (HPGe) detector. That is $\varepsilon_{RMS} = N_{coinc}/N_{Ge}$.

2.10.2 Gamma-ray yield measurement

In this method [34] online or offline measurements are carried out on the charecteristic gamma-rays emitted by the excited residual nuclei or its daughter after the radioactive decay of ER. The gamma-rays are detected by HPGe detectors. The partial fusion cross section can be measured from the intensity of gamma lines. The catcher foil method is used for the offline measurement of the delayed gamma-rays produced in the reaction. This method requires a thorough knowledge about the decay scheme of the compound nucleus. An online measurement of gamma rays from the compound nucleus (CN) formed by the following reactions $^{28}Si+^{68}Zn$, $^{32}S+^{64}Ni$, $^{37}Cl+^{59}Co$ and $^{45}Sc+^{51}V$ is reported by Dasgupta et al.[13]. For the measurement they have used efficiency calibrated 110 cm^3 HPGe detector at about 5 cm from the target at an angle around 55° w.r.to the beam direction. Short lived ($T_{1/2}$ < 10 min) activities were measured with same detector after switching off the beam and the long lived activities with a similar detector after removing the target to a different location. They also used a gold catcher foil to measure the offline activities. The γ-ray yields for different channels such as pn, 2n, 2pn, 2p2n etc. were measured and determined the corresponding ER cross sections and hence the fusion cross section.

2.10.3 X-ray yield measurement

By placing carbon catcher foils of thickness about 1000 $\mu g/cm^2$ a few mm behind the target the evaporation residues are collected and offline measurements are carried out on the X-rays emitted by the decay of the compound nucleus and their daughters. After an irradiation for a time of half to one hour the catcher foil is taken out of the scattering chamber and the X-rays are detected using intrinsic Ge detectors at various time intervals until no further activity is detected. From the measured time dependance of the X-ray yield of the parent and daughter nuclei the individual contribution by neighbouring elements can be determined. The main decay scheme of the radioactive compound nuclei and their daughters are electron capture, internal conversion and the K_α X-ray emission. The absolute fusion cross section can be evaluated from the Rutherford cross section, monitor

counts, measured X-ray intensity, absolute intensity in photons per decay, relative counting rates for elastically scattered projectile ions etc. Necessary corrections should be applied for summing the coincident radiations. Gomes et. al.,[35] reported about the X-ray yield method for the measurement of fusion cross section for the $^{32}S+^{154}Sm$ system. They have used aluminium catcher foils for irradiation for the K X-ray yield. After each irradiation the catcher foil was removed from scattering chamber and placed in front of germanium detector and X-ray spectra were recorded at different intervals. Yield of low cross section were detected with detectors of high efficiency and low resolution. The evaporation residue cross sections were obtained as an adjustable parameter by a least squares fit of the X-ray activities as a function of time interval for different atomic numbers.

2.11 Previous Experimental Methods

A number of projectile-target systems have so far been subjected to detailed investigation with regard to fusion at sub-barrier energies. A few of the important ones are described below.

2.11.1 Sulphur - Nickel Systems

A detailed investigation of fusion for these systems have been carried out by Stefanini et al. [36]. Fusion evaporation residue (ER) cross sections for all these systems were measured for centre-of-mass energy ranging from 55.9 Mev to 97.2 Mev for $^{32}S+^{58}Ni$ system, 52.7 Mev to 100.4 Mev for $^{32}S+^{64}Ni$ system, 55.8 Mev to 71.8 Mev for $^{34}S+^{58}Ni$ system, 53.9 Mev to 74.2 Mev for $^{34}S+^{64}Ni$ system, 54.0 Mev to 68.4 Mev for $^{36}S+^{58}Ni$ system, and 53.5 Mev to 88.9 Mev for the $^{36}S+^{64}Ni$ system. These systems with the product Z_pZ_t = 448 are heavy enough and significant effects in sub-barrier region has been reported. Positive Q-values exists for the +2n channels of $^{32,34}S+^{64}Ni$ systems and for the –2n channel of $^{34,36}S+^{58}Ni$ systems, where ^{36}S is a magic nucleus with N= 20. The various Ni targets have similar level structure at low excitation but different number of valence neutrons out side the closed N = 28 shell. The ERs which are separated from the beam particles by using electrostatic deflector because of their different electric rigidity, the ratio of which between beam and ERs nearly equal to 5 were detected within the angular range 0° to 9° by time-of-flight (TOF) technique. The start signal for zero time is

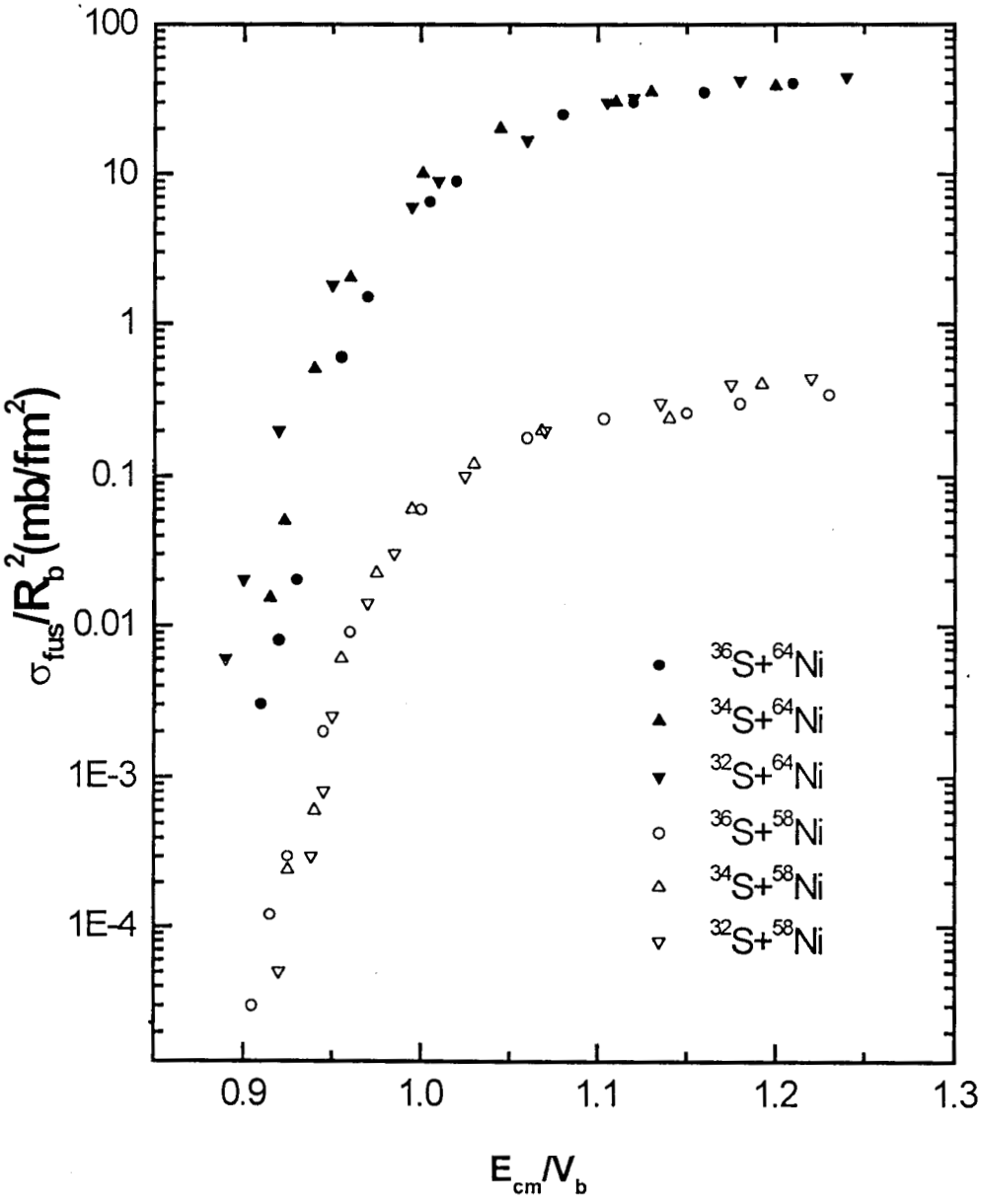

Figure 2.6 : Reduced fusion cross sections as a function E_{cm}/V_b for the various S+Ni systems reported by Stefanini et al.[36].

taken from microchannel plate (MCP) detector and stop signal from silicon surface barrier detector (SBD) kept 30 cm away from MCP. The angular distributions were measured at some selected energies. The barrier parameters such as height (V_b), Radius (R_b) and the

parameter $\hbar\omega$ which is an inverse measure of barrier thickness in the parabolic approximation of the barriers were determined by fitting the data and also from the proximity potential and systematics. The fitted values are less than the predictions by proximity potential, while those from the empirical systematics were greater than the proximity values. Figure 2.6 shows the reduced fusion cross sections versus energies scaled by the barrier height for various S+Ni systems extrapolated from Stefanini et. al.[36]. They have taken the barrier parameters from Vaz systematics.

Fusion of $^{32}S+^{64}Ni$ system has also been studied by other groups. Dasgupta et al., carried out investigations [13] using the 14UD pelletron at the TIFR-BARC accelerator research facility, Bombay for energies below and above barrier. The target thicknesses were measured using X-ray fluorescence and PIXE technique. HPGe detectors were used at 5 cm from the target at 55° w.r.to the beam direction. The online and offline detection of the γ-rays emitted from CN by radioactive decay were done with these detectors. The evaporation residues were identified from their charecteristic γ-rays and ER cross section were obtained from the γ-ray yields which was estimated up to 85% of the fusion cross section. The experimental fusion cross sections were compared with the predictions of the statistical model code CASCADE. A comparison of the fusion cross section with the results obtained by Stefanini et al.,[36] shows disagreement by a factor 3 at 4 MeV below barrier. But the same shows agreement within the experimental uncertainities with the cross section obtained by Tighe et al.[37]. The results of $^{32}S+^{64}Ni$ have also been compared with other systems such as $^{28}Si+^{68}Zn$, $^{37}Cl+^{59}Co$ and $^{45}Sc+^{51}V$. The sub barrier fusion enhancement is larger for $^{32}S+^{64}Ni$ compared to other systems which supports Stelson's proposal of neutron flow as a main mechanism for the fusion enhancement.

Author	V_b	R_b	$\hbar\omega$
Stefanini et al.	58.1±0.7	8.8±0.5	4.1±0.2
Dasgupta et al.	59.0	10.4	3.2

Table 2.1: Barrier parameters for $^{32}S+^{64}Ni$ system

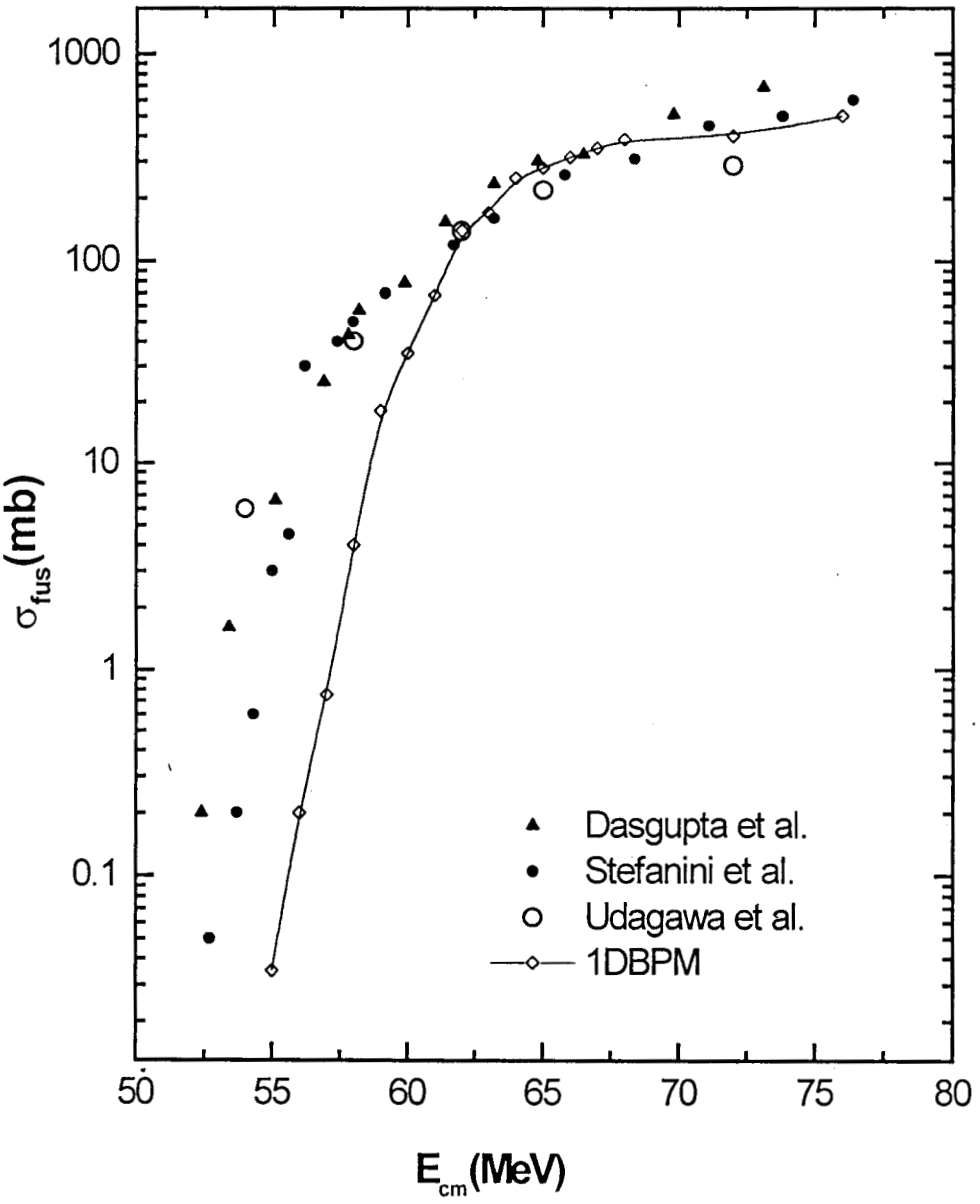

Figure 2.7 : Fusion excitation function for $^{32}S+^{64}Ni$ system-A comparison between different experimental measurements.

The experimental barrier parameters reported by Stefanini et al., and Dasgupta et al. for the $^{32}S+^{64}Ni$ system is given in table 2.1. The fusion cross sections measured by Stefanini et al.,[36] Dasgupta et al.,[38] and Udagawa et al.,[39] is compared with 1DBPM predictions in figure 2.7. Udagawa et al., carried out a theoretical study of fusion and elastic scattering of $^{32}S+^{58,64}Ni$ systems within the frame work of direct reaction theory using optical model.

2.11.2 Nickel - Nickel Systems

A precision experiment on $^{58}Ni+^{60}Ni$ system for measuring fusion excitation function and experimental fusion barrier distributions D(B) was performed by Stefanini et al.,[40] in the energy range around the coulomb barrier. D(B) was around 13 MeV wide which displays structure charecteristic of strong phonon couplings with two large well resolved peaks and a smaller peak at low energies. The smaller peak is essential for fitting the low energy cross section. This was obtained only when the target and projectile double phonon excitations are taken into account. Such a study of the above system to identify the complex vibrations is a first report in this field. ^{58}Ni beam in the energy range 182-222 MeV with intensities 2 to 5 pnA from LNL - XTU Tandem accelerator was used for the experiment on ^{60}Ni target having thickness of 100 $\mu g/cm^2$ and isotopic abundance 99.8%, evaporated on carbon backing. The RMS separates the forward recoiling ERs from beam particles and detected and identified using TOF-E telescope. An excellent beam rejection of more than 10^7 was obtained by the electrostatic deflector. Monitor detectors placed at $\pm 25^\circ$ w.r.to the beam direction was used for relative normalization between various runs and for the corrections due to beam direction. The total fusion evaporation cross section were determined from integration of the ER angular distribution measured in the range -7° to $+7^\circ$ at energies 196,208 and 220 MeV. The energy scale is corrected for the target half thickness energy loss (HTEL) and for target isotopic impurities. The statistical and systematic errors was estimated up to ±15%. The second derivative or the experimental barrier distribution $d^2(E\sigma)/dE^2$ has been extracted using a point difference formula proposed by Wei et al.[41]. The results are compared with the measurements carried out on $^{58}Ni+^{58}Ni$ system by Beckermann et al. [32]. The relative cross section enhancement for

^{58}Ni+^{60}Ni observed only at low energies is a qualitative indication of the prominence of neutron transfer well below the barrier. Measurement of ^{58}Ni+^{64}Ni fusion excitation function was reported by Esbensen et al. [42]. A systematic comparison of the experimental data to the various coupling schemes to the 1DBPM to explain sub-barrier fusion enhancement is given by the author. The coupling schemes includes inelastic excitations and one- and two-neutron transfer. A measurement of the elastic scattering angular distributions on the same system was performed by Stefanini et al.[43]. A comparison of the fusion cross section for ^{58}Ni+^{64}Ni with the measurements of Beckermann et al., on ^{58}Ni+^{58}Ni and ^{64}Ni+^{64}Ni is reported by Stefanini [44]. Fusion evaporation excitation function and mean angular momenta for the ^{58,64}Ni+^{64}Ni systems were measured by Ackermann et al.[10]. The data was compared with CC calculations. The mean angular momenta are compared with the curves obtained by the first derivative of fusion excitation function. The small humps observed at the lowest energies for ^{58}Ni+^{64}Ni is due to the direct 2 neutron transfer included in CC calculations. In the case of ^{64}Ni+^{64}Ni the theoretical predictions over estimate the experimental fusion cross section.

2.11.3 Titanium - Nickel systems

The enhancement of fusion cross section in the sub-barrier region have been investigated for the ^{46,48,50}Ti+^{58,60,64}Ni systems by Vinod Kumar et al., [18] and Prasad et al.,[45] using 15UD Pelletron accelerator at NSC, New Delhi with beam energies ranging from 126 to 168 MeV. The self supporting and enriched targets used were of thickness 240 $\mu g/cm^2$ to 330 $\mu g/cm^2$. The forward recoiling ERs were separated from the beam background using the RMS – Heavy Ion Reaction Analyser(HIRA). The ERs are also transported and space and energy focused with mass (m/q) dispersion at the focal plane by means of HIRA. The absolute efficiency of ER detection by HIRA has been determined by mounting a HPGe detector through the 90° port of the sliding seal chamber. Two Silicon surface barrier detectors were mounted at ±30° inside the sliding seal chamber symmetrically w.r.to the beam direction for beam flux normalization. Angular distribution of the evaporation residues were detected at various angles –6° to 12°. Charge state distributions also measured with and without charge reset foil after the target. Fusion

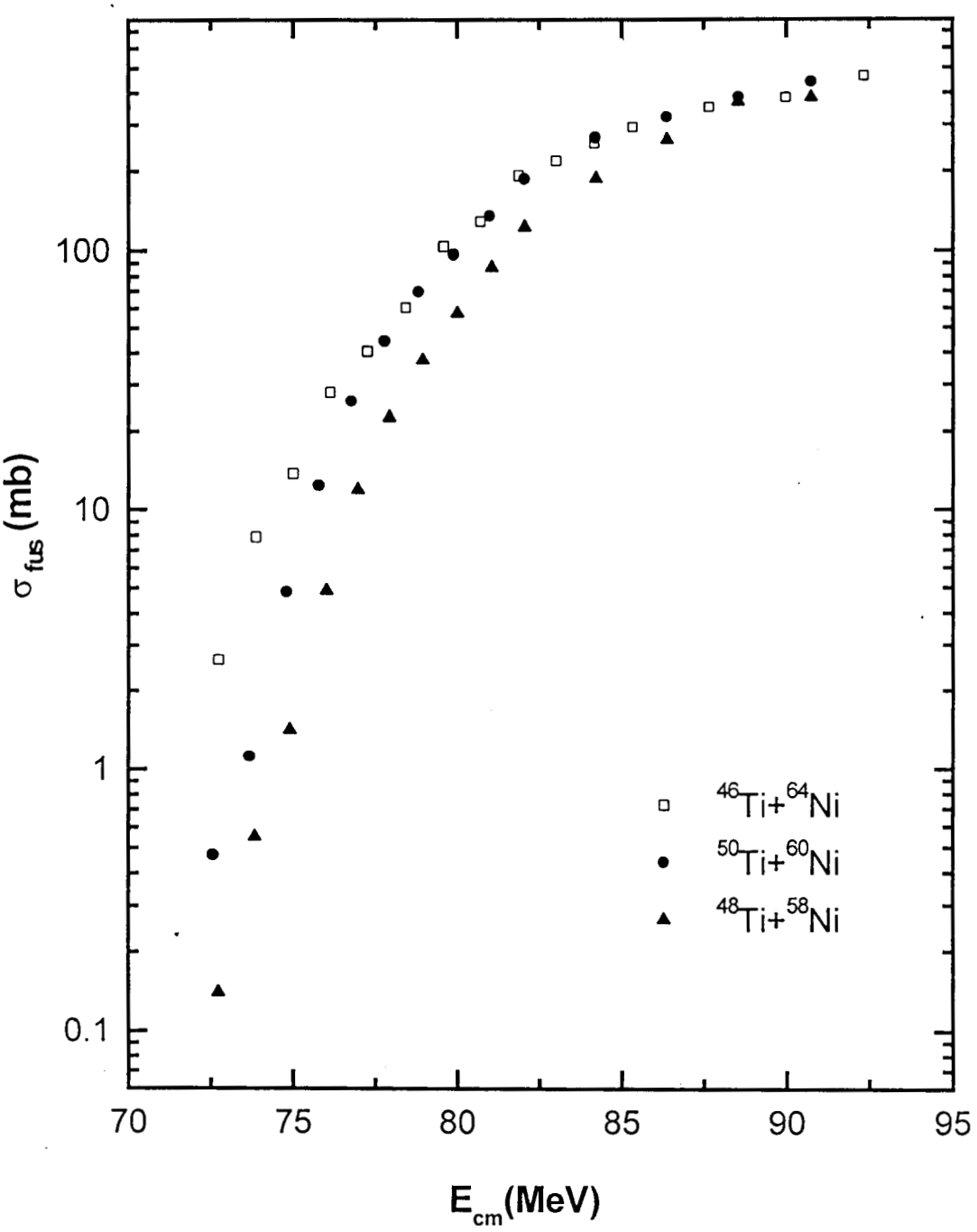

Figure 2.8 : Results of Excitation function measurements for different Ti+Ni systems carried out at NSC.

excitation functions for the above systems were determined by considering different aspects such as beam energy loss in target and energy dependance of Rutherford cross section during normalization. Spin distributions predicted for these systems were also extracted within the frame work of CC formalism. The measured fusion excitation function for these systems were compared with the predictions of 1DBPM without any renormalization. By fitting the fusion cross section σ versus $1/E_{cm}$ for above barrier energies, the one dimensional barrier parameters V_b, R_b and $\hbar\omega$ were also been determined experimentally and compared with standard potential calculations proposed by various authors. An excellent matching between theory and experimental data were obtained well within the probable errors. A significant enhancement of σ_f w.r.to 1DBPM predictions were observed for almost all the systems. They also carried out simplified CC calculations by coupling the lowest lying collective 2^+ and 3^- states of target and projectile nuclei using the computer code CCFUS. They found considerable improvement in matching between theory and experiment by coupling inelastic channel, but it was not alone sufficient to explain experimentally observed enhancement. The authors also studied about the role of neutron flow [27] in the enhancement of sub-barrier fusion cross section for the various Ti+Ni systems. The one neutron separation energies for the ^{46,48}Ti+^{64}Ni systems are lower than other systems. The absolute average angular momentum and angular momentum distribution were deduced from the measured fusion cross sections. Barrier distributions were also determined from fusion excitation function and compared with 1DBPM and CC predictions. Figure 2.8 shows some of the results of their measurements [18].

2.11.4 Silicon - Nickel Systems

Fusion cross sections for the ^{28,30}Si+^{58,62,64}Ni systems were measured at energies 68.4 to 94 MeV by the Legnaro group, Stefanini et al., [36] using the LNL - XTU Tandem accelerator. They have corrected the measured cross section for target impurities and target energy losses. A TOF telescope was used for detecting the ERs at 0^o to 9^o angular range by rotating the whole setup in the horizontal plane to measure the angular distributions for the systems other than ^{28}Si+^{62}Ni. Excellent beam rejection were obtained by the electric rigidity E/q selection method. The TOF information has been extracted using microchannel plates as the time zero detector and silicon SBD as the stop detector for a flight path of

30 cm and the ERs were identified by mass as separate islands in the TOF-E 2D histogram. They have also studied the $^{28}Si+^{58}Ni$ system by inverse kinematics using ^{58}Ni beam on self supporting $^{28}SiO_2$ target of 220 $\mu g/cm^2$ with a longer flight path of 100 cm for much faster ER. The inverse reaction was helpful to check the absolute cross section, scale and the accuracy of ER identification method against the oxygen and carbon contamination in the target. The actual experimental voltage to be applied to the high voltage (HV) plates to detect 0° ER at a given beam energy was determined by measuring the ER yield as a function of the voltage. The selected voltage maximizing the yield was matching with the simple estimation based on the realistic assumptions of ER electric rigidities and electric field distribution in the separator. The monitor counter placed in the target chamber at 15° w.r.to the incident beam was used for normalization between different runs. The evaporation residue angular distributions also measured for the above systems at different incident energies.

2.11.5 Sulphur - Samarium Systems

Fusion process at sub-barrier energies for the $^{32}S+^{154}Sm$ system has been well investigated by Gomes et al.[35]. The fusion ER cross sections for the reaction induced by ^{32}S on the deformed ^{154}Sm were measured by the offline detection of K X- rays emitted by the radioactive decay of the residual nuclei via electron capture and internal conversion. The sulphur beam at energies 122.5 to 155 MeV from the 20UD Tandem accelerator at the TANDAR lab in Buenos and the Sm target of thickness 183 $\mu g/cm^2$ and 98% isotopic enrichment on carbon backing was utilized for the experiment. Aluminium catcher foils of thickness 1.6 to 2.6 $\mu g/cm^2$ were placed behind the target to collect ERs. Two SBD monitors were used at angles ±30° for normalizing the cross sections to absolute values. The catcher foils were irradiated for a period of about 120 min, removed from the scattering chamber and the X-ray spectra were recorded automatically for different intervals using a Ge detector. By least square fitting the X-ray activities as a function of time for different atomic numbers, the ER cross section σ_A were obtained with possible errors between 10 to 20%. The results are compared with the behaviour of the fusion excitation functions for systems with different projectiles on the same deformed target.

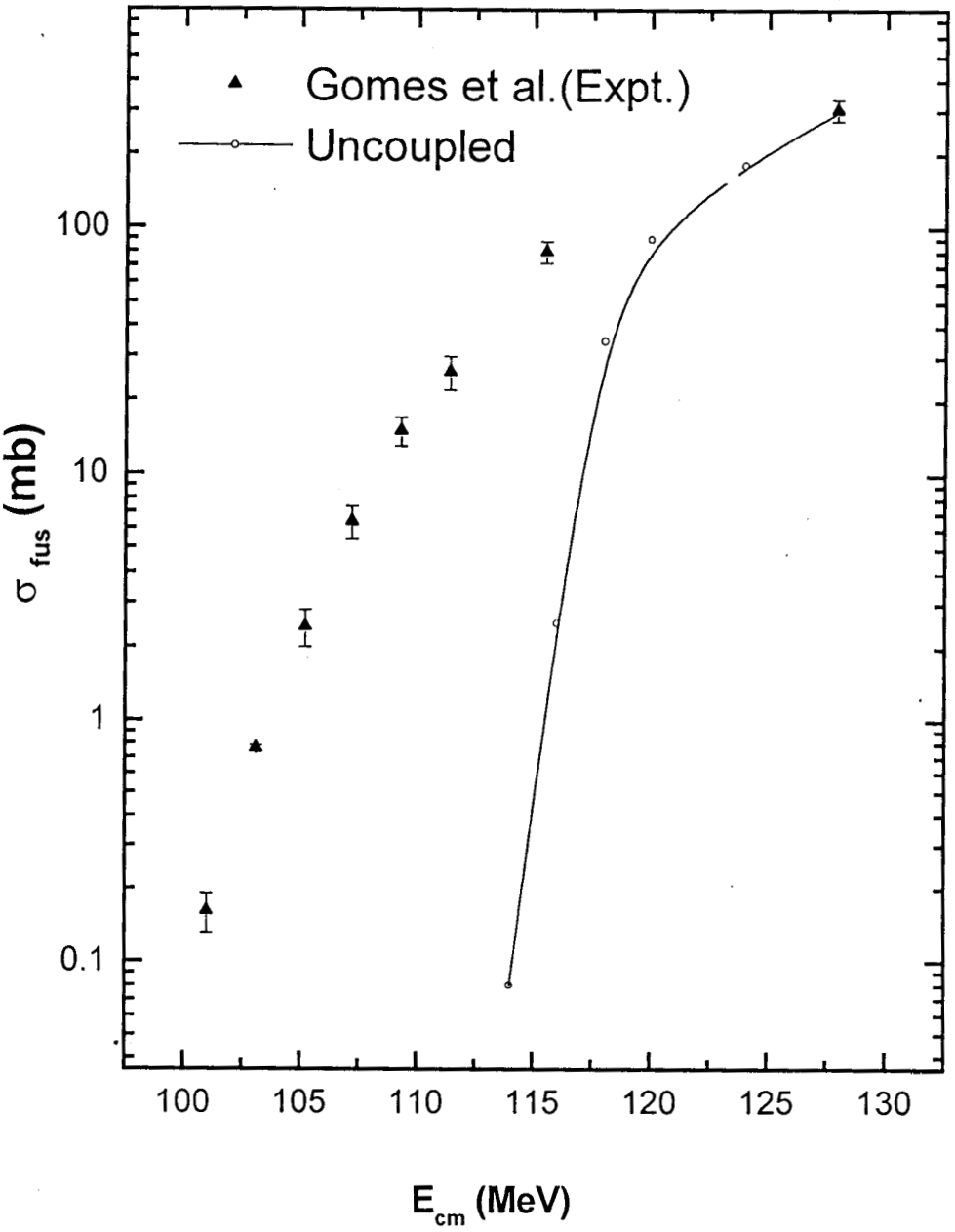

Figure 2.9 : Experimental fusion excitation function versus the centre-of-mass energy for the S+Sm system. Results of uncoupled calculations is also given.

The enhancement of sub-barrier fusion by the large static deformation of the target nuclei, the permanent quadrapole and hextapole deformation of the target and quadrapole oscillations of the projectiles using CC calculations were well established. Figure 2.9 shows the fusion cross sections for the $^{32}S+^{154}Sm$ at various energies extrapolated from Gomes et al.[35].

2.11.6 Calcium - Osmium and Calcium - Platinum Systems

An extensive measurement of the fusion excitation function for the $^{40}Ca+^{192}Os$ and $^{40}Ca+^{194}Pt$ systems were reported by Bierman et al.[46,47]. ^{192}Os is prolate deformed where as ^{194}Pt is oblate deformed. They have extracted the fusion barrier distributions from the excitation function. A CC calculation using the computer code CCDEF was also performed for a comparison with the above experimental results. The calculations included the effects of the static target nuclear deformation(quadrupole and hextadecapole), coupling to the inelastic projectile state (octupole) and coupling to the very positive Q-value transfer of 2-neutron from target to projectile ground state. The comparison showed good agreement between calculation and experimental barrier distribution shapes. But there was a mismatch in the case of fusion cross section between calculation and experimental results. Also calculation had failed to reproduce the deepness of the valley between the two peaks for the ^{194}Pt target. The resolution was better in the case of experimental data for Platinum target. The discrepancy of the calculation was due to the differentiating step size and quantal tunneling. The differentiating step size can be made identical for the two distributions. Then the smearing due to the tunneling in the calculations depends on the nuclear diffuseness parameter. By increasing this parameter they have suggested that the curvature of the barrier can be reduced to make it less penetrable for reducing the smearing of the barrier distribution. This also lower the fusion cross section above the barrier. They have attempted this technique by varying the diffuseness parameter and by considering the transfer to the projectile first excited state. The results showed good agreement between theoretical calculation and experimental data. The barrier region of osmium ranges between 180 to 230 MeV and platinum between 190 to 240 MeV. The experiment was performed at the Nuclear Physics Laboratory using the Tandem Van-de-Graaff accelerator in conjunction with the superconducting LINAC.

2.11.7 Oxygen – Silicon System

A comprehensive CC analysis of the $^{16}O+^{28}Si$ reaction near the coulomb barrier had been reported by Bragin et al.[48]. They have used the real part of the optical potential for describing the above interaction. One nucleon transfer process and the effects of the collective excitation of the deformed target nucleus were considered for performing the CC calculations. This approach was used to the static deformation of the silicon target nucleus for the explicit treatment of the collective excitation. By assuming a static quadrupole deformation for the target nucleus, its rotation was described in the frame work of the collective rotation model. They have experimentally measured the elastic and inelastic scattering differential cross sections and fusion excitation function for the $^{16}O+^{28}Si$ for the incident energy range for the elastic channel 21 to 38 MeV. They have calculated the excitation function for the elastic and inelastic scattering and compared with experimental results of Braun-Munzinger et al.[49]. The fusion cross sections for the $^{16}O+^{28}Si$ system were also calculated by Bragin et al., for the energy range 21 to 40 MeV and compared with the experimental data obtained by Jordan et al.[50]. Bragin et al., had obtained excellent fits to all available experimental data on the $^{16}O+^{28}Si$ system for scattering and fusion in the incident energy range 21 to 38 MeV with a deformed optical potential consistent with nuclear structure information. They have concluded that an explicit treatment of the coupling effects is necessary to obtain an authentic explanation of the anomalous large angle scattering (ALAS) phenomenon in the collisions of strongly deformed heavy ions in the vicinity of coulomb barrier.

2.11.8 Oxygen - Samarium Systems

The fusion excitation functions for the system $^{16}O+^{154}Sm$ have been measured experimentally with a precision ~ 1% [41,51,52]. By varying the quadrupole and hexadecapole deormation parameters β_2 and β_4, the data for ^{154}Sm were fitted and best fit was obtained for the corresponding deformation parameters obtained from inelastic α-particle scattering and coulomb excitation. Using the established deformation parameters and including the weak couplings to the vibrational states the ^{154}Sm data was found to be reproducible. They have extracted the fusion barrier distributions from the fusion cross

sections and found that the barrier distributions were not well defined at higher energies. This was due to the increase in experimental uncertainity in proportion to the cross section with the increase in energy. So there was a scope for an alternative method for extracting the barrier distributions at higher energies for the above system. The above scope for a new approach was utilized by Timmers et al.,[53] by developing a suitable technique for extracting a representation of the fusion barrier distributions from quasi-elastic back scattering excitation functions. They have carried out a systematic investigation on $^{16,17}O+^{144,154}Sm$ using the 14UD pelletron accelerator at ANU in the energy range E_{lab} = 53 to 75 MeV. The results were compared with barrier distributions obtained from fusion data and with CC calculations. The barrier distribution obtained from fusion data shows a distinct peak about 5 MeV above the main barrier for the ^{144}Sm target, but a second peak was absent in the case of that obtained from quasi-elastic scattering.

They have used the ECIS calculations for $^{16}O+^{144}Sm$ system to understand the above disagreement between D(B) measured from fusion and quasi-elastic scattering. They arrive at the conclusion that this discrepancy is due to the effect of transfer process. Stockstad et al.,[54,55] also carried out extensive measurements of fusion cross section for the $^{16}O+^{148,150,152,154}Sm$ systems at near barrier energies by using X-ray method. The ERs were collected in a carbon catcher foil and the off line X-rays were detected using Ge detectors. The absolute cross section were evaluated from Rutherford cross section, the monitor counts, X-ray intensity and the absolute intensity of various radioactive products in the catcher foil. Measured cross sections were found increasing with the target mass.

References

[1] T.D. Thomas, Ann. Rev. of Nucl. Sci. **18**(1968)343.

[2] (a)C.H. Dasso, S. Landowne and A. Winther, Nucl.Phys.**A407**(1983)221;

(b)C.H. Dasso, S. Landowne and A.Winther, Nucl.Phys.**A405**(1983)381.

[3] R.A. Broglia, C.H. Dasso, S. Landowne and A. Winther, Phys.Rev.**C27**(1983)2433.

[4] P.H. Stelson, H.J. Kim, M. Beckerman, D. Shapira and R.L. Robinson, Phys. Rev.**C41**(1990)1584.

[5] P.H. Stelson, Phys. Lett. **B205**(1988)190.

[6] G.R. Satchler, M.A. Nagarajan, J.S. Lilley and I .J. Thompson, Ann. of Phy.**178**(1987)110.

[7] N. Rowley, Nucl. Phys. **A538**(1992)205c.

[8] W. Reisdorf , F.P. Hessberger, K.D. Hildebrand, S. Hofmann, G. Münzenberg, K.H. Schmidt, J.H.R. Schneider, W.F.W. Schneider, K. Sümmerer, G. Wirth, J.V. Kartz and K. Schlitt, Phys. Rev. Lett.**49**(1982)1811.

[9] M. Beckerman, J. Ball, H. Enge, M. Salomaa, A. Sperduto, S. Gazes, A.Dirienzo and J.D. Molitoris, Phys. Rev.**C23**(1981)1581.

[10] D. Ackermann, F. Scarlassara, P. Bendnarczyk, S. Beghini, L. Corradi, G. Montagnoli, L. Muller, D.R. Napoli, C.M. Petrache, K.M. Varier, F. Soramel, P. Spolaore, A.M. Stefanini, G.F. Segato, C. Signorini and H. Zhang, Nucl. Phys. **A 583**(1995)129.

[11] C.C.Sahm, H.G.Clerc, K.H. Schmidt, W. Reisdorf, P. Armbruster, F.P.He Bberger, J. G. Keller, G. Munzenberg and D.Vermeulen, Z. Phys.**A319**(1984)113.

[12] C.H. Dasso and S. Landowne, Phys.Rev.**C32**(1985)1094.

[13] M. Dasgupta, A. Navin, Y.K. Agarwal, C.V.K. Baba, H.C. Jain, M.L.Jhingan and A. Roy, Nucl. Phys. **A539**(1992)351.

[14] F. Pühlhofer, Nucl. Phys. **A280**(1977)267.

[15] M. Dasgupta, A. Navin, Y.K. Agarwal, C.V.K. Baba, H.C. Jain, M.L. Jhingan and A. Roy, Phys. Rev. Lett. **66**(1991)1414.

[16] R. Hasse and P. Schuck, Phys. Lett. **B189**(1986)313.

[17] A. Navin, PhD Thesis, Bombay Univ.(1996) unpublished.

[18] A.M. Vinod Kumar, PhD Thesis, calicut Univ.(1996) unpublished.

[19] C.H. Dasso and S. Landowne, Comput. Phys. Commun. **46**(1987)187.

[20] A.B. Balantakin and P.E. Reimer, Phys. Rev. **C33**(1986)379.

[21] A.B. Balantakin, S.E. Koonin and J.W. Negele, Phys. Rev. **C28**(1983)1565.

[22] C.H. Dasso, H. Esbenson and S. Landowne, Phys. Rev. Lett.**57**(1986)1498.

[23] N.V.S.V. Prasad, PhD Thesis, Anthra Univ.(1996) unpublished.

[24] J.Blocki, J. Randrup, W.J. Swiatecki and C.F. Tsang, Ann. Phys. N.Y) **105**(1977)427.

[25] D.I. Hill and J.A. Wheeler, Phys. Rev.**89**(1953)1102.

[26] C.Y. Wong, Phys.Rev. Lett. **31**(1973)766.

[27] A.M.Vinod Kumar, A.K. Sinha, N.V.S.V. Prasad and K.M. Varier, Phys. Rev. **C 54**(1996)1.

[28] D. Shapira and P.H. Stelson, Phys. Rev. **C47**(1993)1666.

[29] A.B. Balantekin, J.R. Bennett and S. Kuyucak, Phys. Rev.**C49**(1994)1294.

[30] A. Balantekin, J.R. Bennett and S. Kuyucak, Phys. Rev. **C48**(1993)1269.

[31] N. Bohr, Nature **137**(1936)344.

[32] M. Beckerman, Rep. Prog. Phys.**51**(1988)1047.

[33] W. Reisdorf, J. Phys.**G20**(1994)1297.

[34] M. Dasgupta, PhD Thesis, Bombay Univ.(1991)unpublished.

[35] P.R.S. Gomes, I.C. Charret, R. Wanis, G.M.Sigaud, V.R. Vanin, R. Liguori Neto, D. Abriola, O.A.Capurro, D.E. Digregorio, M. di Tada, G. Duchena, M. Elgue, A. Etchegoyen, J.O.Fernandez Niello, A.M.J. Ferrero, S.Gil, A.O. Machiavelli, A.J. Pacheco and J.E. Testoni, Phys. Rev. **C49**(1994)245.

[36] A.M. Stefanini, G. Fortuna, R. Pengo, W. Meczynski, G. Montagnoli, L. Corradi, A. Tivelli, S. Beghini, C. Signorini, S. Lunardi, M. Morando and F. Soramel, Nucl. Phys. **A456**(1986)509.

[37] R.J. Tighe, J.J. Vega, E. Aguilera, G.B. Liu, A. Morsad, J.J. Kolata, S.H. Fricke, H. Esbensen and S. Landowne, Phys. Rev. **C42**(1990)1530.

[38] T. Udagawa and T. Tamura, Phys. Rev. **C39**(1989)1840.

[39] T. Udagawa and T. Tamura, Phys. Rev.**C29**(1984)1922.

[40] A.M. Stefanini, D. Ackermann, L. Corradi, D.R. Napoli, C. Petrache, P. Spolaore, P. Bednarczyk, H.Q. Zhang, S. Beghini, G. Montagnoli, L. Muller, F. Scarlassara, G.F. Segato, F. Soramel and N. Rowley, Phys. Rev. Lett. **74**(1995)864.

[41] J.X.Wei, J.R. Leigh, D.J. Hinde, J .O. Newton, R.C. Lemmon, S. Elfstrom, J.X. Chen and N. Rowley, Phys. Rev. Lett. **67**(1991)3368.

[42] H. Esbenson and S. Landowne, Nucl. Phys. **A492**(1989a)473.

[43] A.M. Stefanini et al., Phys. Lett. **B240**(1990a)306.

[44] A.M. Stefanini, J.Phys.G.Nucl. Part. Phys.**17**(1991)S453.

[45] N.V.S.V. Prasad, A.M. Vinod Kumar, A.K. Sinha, K.M. Varier, D.L. Sastry, N. Madhavan, P. Sugathan, D.O. Kataria, J.J. Das, Nucl. Phys. **A603**(1996)176.

[46] J.D. Bierman, P. Chang, J.F. Liang, M.P. Kelly, A.A. Sonzogni and R. Vadenbosch, Phys. Rev. **C54**(1996)3068.

[47] J.D. Bierman, P. Chan, J.F. Liang, M.P. Kelly, A.A. Sonzogni and R. Vadenbosch, Phys. Rev. Lett. **76**(1996)1587.

[48] V.N. Bragin, G. Pollarolo and A.Winther, Nucl. Phys. **A 456**(1986)475.

[49] P. Braun-Munzinger, G.M. Berkowski, M. Gai,C.M. Jachcinski, T.R. Renner, C.D. Uhlhorn, J. Barrette and M.J. Le Vine, Phys. Rev.**C24**(1981)1010.

[50] W.J. Jordan, J.V. Maher and J.C. Peng, Phys. Lett. **87B**(1979)38.

[51] R.C.Lemmon, J.R. Leigh, J.X. Wei, C.R. Morton, D.J. Hinde, J.O. Newton, J.C. Mein, M. Dasgupta and Rowley, Phys. Lett.**B316**(1993)32.

[52] J.R.Leigh, N. Rowley, R.C. Lemmon, D.J. Hinde, J.O. Newton, .X. Wei, J.C. Mein, C.R. Morton, S. Kuyucak and A.T. Kruppa, Phys. Rev.**C47**(1993)R437.

[53] H.Timmers, J.R. Leigh, M. Dasgupta, D.J. Hinde, R.C. Lemmon, J.C. Mein, C.R. Morton, J.O. Newton and N. Rowley, Nucl. Phys. **A584**(1995)190.

[54] R.G.Stockstad, W. Reisdorf, K.D. Hildenbrand, J.V. Kratz, G. Wirth, R. Lucas and J. Poiou, Z. Phys. **A295**(1980)269.

[55] R.G.Stockstad, Y. Einsen, S. Kaplanis, D. Palte, U. Smilansky and I. Tserruya, Phys. Rev. Lett. **41**(1978)465.

Chapter 3

Review of Transfer Reaction Studies

The role of transfer reaction channels in the enhancement of sub-barrier fusion cross section is well established by theoretical studies based mainly on the CC approach [1,2,3]. Even though theoretical predictions exist for a wide variety of nuclear systems, experimental data is not available for all of those systems. Consequently there has been a continuous interest especially in experimental area over the past 20 years in transfer reaction studies. This interest in the sub-barrier region is due to the experimentally observed discrepancy between the measured fusion cross sections and the theoretical predictions of 1DBPM. The above mentioned CC approach requires information on the form factors for the transfer channels in order to extract fusion cross section, barrier and spin distributions and so on. Theoretical calculations of the transfer form factors are often tedious and cumbersome. These theoretically estimated transfer form factors often vary considerably and are inconclusive. Consequently form factors have to be determined from transfer probability experimentally to study the role of transfer reaction channels on sub-barrier fusion. The transfer coupling strength can be obtained from theoretical shell model calculations of the bound state form factors. A semi-classical formalism is normally used for extracting the coupling strengths of transfer form factors from measured transfer probabilities. In the semi-classical approach the relative motion between projectile and target is expressed classically using real and complex trajectories and the transition amplitudes are treated quantum mechanically. This implies that elastic scattering can be described semi-classically and transfer can be treated as a perturbation to elastic scattering. At energies well below the barrier the above semi-classical approach fails to describe transfer reactions and one has to depend on quantum mechanical approximation to understand the experimental observation of transfer process. This chapter includes a detailed discussion of the semi-classical methods, quantum mechanical models, slope anomaly, CC calculations and a review on the experimental methods.

3.1 Fusion and Transfer Process

In general a large number of degrees of freedom are evolved during the complex nuclear rearrangement process occurring during and after fusion of two heavy nuclei. The fusion process can be easily understood by investigations in sub-barrier region. This is because only a few reaction channels are open in this region. The enhancement of sub-barrier fusion cross section w.r.to the 1DBPM can be well understood by considering the low lying surface excitations ($2^+$and 3^-) due to the significant contribution of the inelastic channel. In some cases coupling of multiphonon states and few nucleon transfer channels can form a significant part of the sub-barrier reaction cross section.

System	Transfer Channel	Q-value(MeV)	Reference
$^{50}Ti+^{60}Ni$	+2p	1.67	[5]
$^{48}Ti+^{64}Ni$	+2n	2.58	[6]
$^{46}Ti+^{64}Ni$	+2n	4.01	[5,6]
$^{19}F+^{93}Nb$	+1p	6.81	[5,6]
$^{19}F+^{93}Nb$	-1p	0.50	[5,6]
$^{28}Si+^{68}Zn$	+2n	1.83	[7,8]
$^{28}Si+^{68}Zn$	+2p2n	1.62	[7,8]
$^{32}S+^{64}Ni$	+2n	3.56	[7,8,9,10]
$^{32}S+^{64}Ni$	-2p	0.22	[7,8,9,10]
$^{28}Si+^{64}Ni$	+2n	2.74	[10]
$^{32}S+^{100}Ru$	-2p	4.41	[11]
$^{32}S+^{100}Ru$	+2n	3.30	[11]
$^{32}S+^{100}Ru$	-2p-2n	2.52	[11]
$^{32}S+^{101}Ru$	+1n	2.03	[11]
$^{32}S+^{101}Ru$	-2p	5.19	[11]
$^{32}S+^{101}Ru$	-2p-1n	4.39	[11]
$^{32}S+^{101}Ru$	+2n	3.96	[11]
$^{32}S+^{101}Ru$	-2p-2n	2.77	[11]
$^{28}Si+^{93}Nb$	+2n	2.37	[12]
$^{48}Ti+^{58}Ni$	+2p	2.14	
$^{18}O+^{58}Ni$	-2n	8.20	[13]
$^{18}O+^{60}Ni$	-2n	6.23	

Table 3.1 : Some nuclear systems with positive Q-values.

Only a few cases have been reported about the experimental studies to illustrate the importance of transfer channel in sub barrier fusion enhancement. Dasso et al.,[1,4] theoretically predicted that transfer channels with +ve Q-values play a major role in sub-barrier fusion enhancement besides the coupling of surface excitation modes. It is also required to extract the relevant form factors from transfer probabilities to perform the CC calculations. Table 3.1 lists a few systems with +ve Q-values. In cases where transfer measurements have been carried out the references have been mentioned.

3.2 Semi-classical theory of nucleon transfer

For energies close to and below the barrier region, heavy ion transfer reaction can be described by the well known theory of semi-classical approximation. According to this theory the transfer process is described as the tunneling of nucleons through a potential barrier. Semi-classically the nuclear potential between the two interacting nuclei describes the classical trajectory along which the centers of the two nuclei are moving. The transition amplitude for transfer is treated quantum mechanically. The semi-classical methods related to elastic scattering can be explained using phase shift method, classical deflection function and complex trajectory method.

3.2.1 Phase Shift Method

The complex WKB phase shifts for the turning points for various ℓ values can be written as

$$\eta_\ell = \pi T_\theta - T_r(+\infty) Z_0 + 2\int_{Z_0}^{\infty} T_r - T_r(+\infty) dz \qquad (3.1)$$

where $T_r = \sqrt{2\mu E - V}$, $T_\theta = \hbar(\ell + 1/2)$ and $Z_0(\ell)$ are complex turning points. By solving the following equation $Z_0(\ell)$ can be obtained.

$$E - V_c(Z) + V_n(Z) + W_n(Z) + \frac{\hbar\,\ell(\ell+1)}{2\mu Z^2} = 0 \qquad (3.2)$$

Here E = the incident beam energy, $V_c(Z)$ = coulomb potential, $V_n(Z)$ = real part of the optical potential and $W_n(Z)$ = the imaginary part of the optical potential. The real and

imaginary parts of the turning points for each ℓ can be obtained from the solution of the above equation (3.2). Similarly the real and imaginary parts of the phase shifts can be obtained from numerical integration of equation (3.1) with appropriate limits.

3.2.2 Classical Deflection Function

The relation between centre of mass scattering angle θ_{cm} and the impact parameter 'b' or angular momentum ℓ is called classical deflection function. The effective scattering potential is given by the relation

$$U_{eff}(b,r) = V_c(r) + V_n(r) + b^2E/r^2 \qquad (3.3)$$

where E is the incident energy and 'r' is the radial distance.

The expressions for the nuclear and coulomb potentials are given in previous chapter. The expression for the classical deflection function is related to the effective scattering potential as

$$\theta(b,E) = \pi - 2b\int_{r_{min}}^{+\infty} [1 - U_{eff}(b,r)/E]^{-1/2} dr/r^2 \qquad (3.4)$$

where r_{min} is the outermost turning point which can be obtained from the solution of the equation

$$E_{cm} - \{V_c(r) + V_n(r) + b^2E/r^2\} = 0 \qquad (3.5)$$

Since the distance of closest approach or apsidal distance D is related to 'b' or ℓ, the D- θ_{cm} relation is also known as deflection function.

$$\theta(D,E) = \pi - 2L(E,D)\int_{r_m}^{+\infty} [E - V_n - V_c - V_L]^{-1/2} dr/r^2 \qquad (3.6)$$

From the conservation of energy and angular momentum [14] the deflection function can be defined in terms of the classical turning point R_{min} and real part of the optical potential U(R) as

$$\theta(L,E) = \pi - 2\int_{R_{min}}^{+\infty} [2\mu E/\hbar^2 - U(R) - L^2/R^2]^{-1/2} L dR/R^2 \qquad (3.7)$$

So whatever be the nature of the potentials used a deflection function can be derived from that. For large impact parameters the coulomb potential dominates the scattering and deflection function decreases with the increasing of L. Thus large impact parameter trajectories correspond to forward angle scattering. The strong attractive nuclear potential bend the trajectories around the target nucleus. Back scattering is caused for small L values by repulsive coulomb core. Consequently at some bombarding energies two or more trajectories well separated in L may scatter into same angle. Classical trajectories with a scattering angle may scatter into indistinguishable angles quantum mechanically resulting in wave mechanical interferences. This phenomenon has been observed in nucleon transfer reactions [14]. When considering the coulomb and nuclear branches of deflection function, the quasi-elastic scattering amplitude can be expressed as [7]

$$A_{QE} = A_{QE}(coul) + A_{QE}(nucl) \tag{3.8}$$

The quasi-elastic cross section becomes $\sigma_{QE} = | A_{QE} |^2$. The transfer cross section can be given as

$$\sigma_{tr} = \sigma_{QE}(D_{coul})P_{tr}(D_{coul}) + \sigma_{QE}(D_{nucl})P_{tr}(D_{nucl}) \tag{3.9}$$

From this the transfer probability becomes

$$P_{tr}(D) = [\sigma_{QE}(D_{coul})P_{tr}(D_{coul}) + \sigma_{QE}(D_{nucl})P_{tr}(D_{nucl}]/ \sigma_{QE} \tag{3.10}$$

Since $D_{nucl} < D_{coul}$, $P_{tr}(D_{nucl}) >> P_{tr}(D_{coul})$ for two-nucleon transfer reactions due to large value of α_{2N}.

3.2.3 Method of complex trajectories

According to single reflection approximation the impact parameter is given as

$$b = r_0 n(r_0) = r_0[1-V(r_0)/E]^{1/2} \tag{3.11}$$

where r_0 is the turning point such that a wave reflected at one turning point will not get reflected at another turning point. For complex trajectories turning point r_0 and deflection angle θ can be complex and they are related to each other as

$$\theta = \pi - 2 \int_0^{+\infty} r_0 n(r_0)\, dr / r[n^2(r)r^2 - n_0^2 r_0^2]^{1/2} \tag{3.12}$$

The method of complex trajectories are used in Fresnel, Fraunhoffer diffraction as well as in CC calculations for direct reactions.

3.3 Distance of Closest approach

Since the influence of nuclear potential is small at large distances, the distance of closest approach 'd_0' can be obtained from the distance parameter D using the pure Rutherford classical approximation [15] expression for a scattering angle θ_{cm} of the back scattered projectile-like particles as

$$D = a\,[1+1/\mathrm{Sin}(\theta_{cm}/2)] \qquad (3.13)$$

where $a = Z_pZ_te^2/2E_{cm}$, Z_p is the projectile atomic number, Z_t is the target atomic number and E_{cm} is the incident energy in centre-of-mass. In the case excited nuclei E_{cm} should be replaced by $E_{cm}+Q$ where Q is the Q-value of the reaction channel.

For a given system D can be varied by changing the incident energy by locating the detector at a fixed angle θ or by varying the scattering angle θ at a fixed bombarding energy. The first technique is called excitation function measurement and second one is called angular distribution measurement. The important point to be considered in these measurements is that the above equation for D is valid only at distances where the effects of nuclear potential are negligible. At smaller inter nuclear distances, the influence of the nuclear potential has to be considered for the calculation of distance parameter D. This is due to the larger nuclear overlap of wave functions which makes the imaginary part of the wave function as repulsive and hence the actual distance is larger than the Rutherford value. Corresponding to the coulomb trajectory the distance of closest approach is given as

$$d_0 = D/\,(A_p^{1/3} + A_t^{1/3}) \qquad (3.14)$$

where A_p is the projectile mass number and A_t is the target mass number. So the reduced overlap distance parameter D_0 can be obtained as $D_0 = d_0\,(A_p^{1/3} + A_t^{1/3})$, where $d_0 = 1.44$ fermi. Pure Rutherford coulomb trajectory is a reasonable approximation in the calculation of d_0. Figure 3.1 shows the definition of various parameters used in transfer measurement.

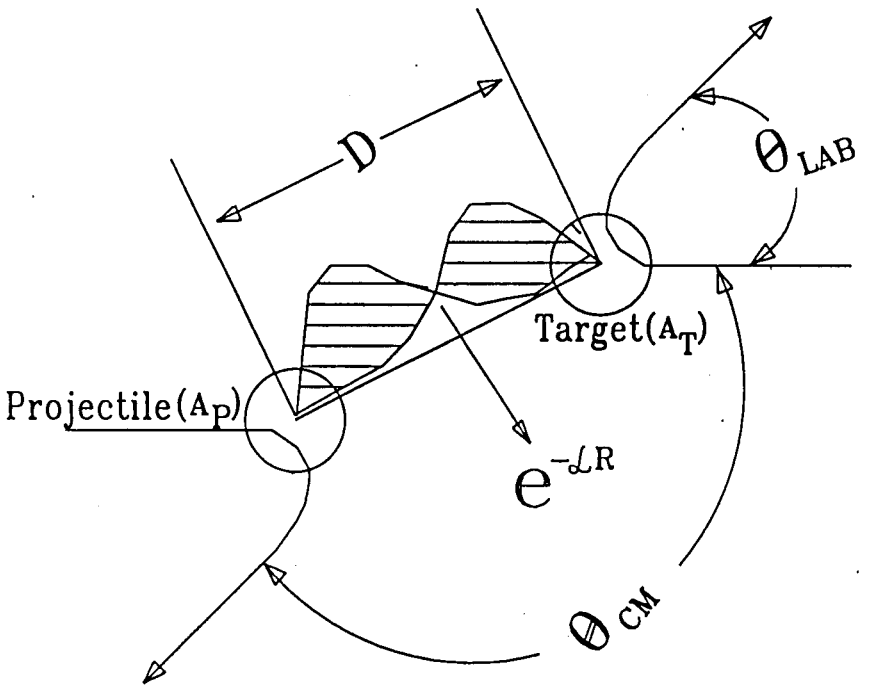

Figure : 3.1 Definition of the reaction angle θ_{CM} and distance of closest approach D close to the Coulomb barrier (reproduced from C.S.Wu et.al)

3.4 Theories of Transfer probability

According to semi-classical theory the transfer probability at large inter nuclear reaction distances is given by the Hankel function approximation [8] for the small overlap between the wave functions of projectile and target nuclei.

$$P_{tr}(D) = P_{tr}(D_0) \exp [-2\alpha(D-D_0)] \quad (3.15)$$

From the above expression (3.15) the slope parameter 'α' can be obtained by the relation

$$2.3 \log P_1/P_2 = +2\ \alpha\ (d_2-d_1)\ (A_p^{1/3} + A_t^{1/3}) \quad (3.16)$$

where 'P_1' is the transfer probability for a distance of closest approach 'd_1' and 'P_2' is the transfer probability for a distance of closest approach 'd_2'. The classical definition [16] for transfer probability is

$$P_{tr} = d\sigma_{tr}/2\pi bdb \quad (3.17)$$

where $d\sigma_{tr}$ is the transfer cross section at a given scattering angle 'θ' and 'b' is the impact parameter associated with this scattering angle. This expression can be modified using the Rutherford values of 'b' as [17]

$$P_{tr} = \frac{d\sigma_{tr}/d\Omega}{d\sigma_{Ruth}/d\Omega} = \frac{d\sigma_{tr}}{d\sigma_{Ruth}} \quad (3.18)$$

Another classical expression for transfer probability using elastic scattering cross section is

$$P_{tr} = \frac{d\sigma_{tr}}{d\sigma_{el}} \quad (3.19)$$

The main drawback of the above expression considering elastic channel is that $d\sigma_{el}$ includes inelastic channels that affect the slope parameter extracted from the data at smaller distances. Also the distance of closest approach d can not calculate at small inter nuclear distances because of the large nuclear overlap of wave functions using Rutherford classical expression. The differential transfer cross section at below barrier energies can be obtained [18] by semi-classical theory from the differential Rutherford scattering cross section and transfer probability as

$$d\sigma_{tr}/d\Omega = P_{tr}(\theta)\ d\sigma_{coul}/d\Omega \quad (3.20)$$

where the transfer probability expected for nucleon tunneling between two potential wells as a function of the scattering angle 'θ' is related to the amplitude parameter A_{pt} as

$$P_{tr}(\theta) = [\pi\alpha / 2\eta k]\ A_{pt}\ \mathrm{Sin}\ (\theta/2) \exp [-2\ \alpha\ d(\theta)] \qquad (3.21)$$

the slope parameter $\alpha = [\sqrt{2\mu E_B}]/\hbar$ (3.22)

which is the propagation number, E_B is the binding energy of the transferred particle corrected for coulomb effects of the transferred nucleons in projectile and target. A_{pt} depends on the initial and final states and on the kinematics of the reaction, k is the asymptotic wave function number, η is the Sommerfield parameter of the relative motion, and μ is the reduced mass of the system. The parameter $d(\theta)$ is the effective distance between nuclear surfaces relevant for transfer process given by the relation $d_0 = D - R_c$ where D is the distance parameter and the interaction radius $R_c = 1.54(A_p^{1/3} + A_t^{1/3})$. Integration of equation (3.20) over Ω gives the transfer probability as a function of energy integrated distance of closest approach d_0 which is related to the total transfer cross section as [18]

$$P_{tr}(d_0) = \sigma_{tr}\ 2\alpha/\pi(d_0 + R_c) = \sigma_{tr} \div \pi a/\alpha \qquad (3.23)$$

That is the transfer probability is the ratio between transfer cross section and the effective peripheral area ($\pi a/\alpha$). This $P_{tr} - d_0$ variation can be compared with the results of experimental values [18]. For proton transfer the binding energy should be corrected for the coulomb potential and 'α' can be expressed in terms of the effective binding energies for the transferred particles in the projectile(B_p) and target (B_t) as [8]

$$2\alpha = [\alpha_p\sqrt{1-E_x/2B_p} + \alpha_t\sqrt{1-E_x/2B_t}] \qquad (3.24)$$

Here E_x is the mean excitation energy for the proton transfer channel, α_p and α_t are the average slope parameters for the projectile and target nuclei. The partition factor is fixed as 0.5 because it has very little influence on the result. For proton transfer the binding energy E_B of the transferred proton should be corrected [19] for the coulomb field of the approaching collision partner ΔV and for the coulomb barrier V_b. Using the average transfer distance of closest approach d = 1.555 fermi, the approximate value of ΔV and using the radius parameter R_c = 1.2 fermi, the value of V_b can be calculated.

System	$^{32}S+^{60}Ni$ [V_{CB}=90.99MeV]				$^{32}S+^{64}Ni$ [V_{CB}=89.91MeV]			
Exit Channel	Q-value	V_{CB} MeV	ΔB MeV	Q_{eff} MeV	Q-value	V_{CB} MeV	ΔB MeV	Q_{eff} MeV
+1p	-7.25	93.09	-2.09	-9.34	-10.26	91.97	-2.05	-12.31
-1p	-4.06	88.50	2.49	-1.57	-1.41	87.46	2.45	1.04
+1n	-2.74	90.86	0.13	-2.61	-1.01	89.77	0.14	-0.87
-1n	-7.22	91.15	-0.16	-7.38	-8.94	90.07	-0.16	-9.10
+2p	-9.95	94.78	-3.79	-13.74	-15.87	93.63	-3.72	-19.59
-2p	-4.88	85.57	5.42	0.53	0.21	84.61	5.30	5.51
+2n	-0.33	90.73	0.26	-0.07	3.56	89.63	0.28	3.84
-2n	-9.67	91.31	-0.32	-9.99	-13.03	90.25	-0.34	-13.37
+n+p	-6.20	92.95	-1.96	-8.16	-7.24	91.83	-1.92	-9.16
-n-p	-7.48	88.66	2.33	-5.15	-6.65	87.63	-2.28	-4.37
+n-p	-7.83	88.35	2.64	-5.19	-3.38	87.31	2.60	-0.78
-n+p	-15.51	93.23	-2.24	-17.74	-19.99	92.12	-2.21	-22.20

Table 3.2 : List of the barrier shift and effective Q-values for the different transfer channels for the $^{32}S+^{60,64}Ni$ systems.

The Q-window of transfer probability is centered at Q = 0. For proton transfer, the quantity Q of Q-window is replaced by a factor $\omega = Q-Q_{opt}$ in the following relation for transfer probability [17].

$$P_{tr} = [1/\hbar \int_{-\infty}^{+\infty} F(r(t)) \exp(i\omega t)dt\ ]^2 \qquad (3.25)$$

In another approach the Q-value is replaced by the effective Q-value as $Q_{eff} = Q + V_b^{(i)} - V_b^{(f)} = Q + \Delta B$ where V_bs denote the barrier heights before and after the transfer process. Table 3.2 shows the effective Q-values for the $^{32}S+^{60,64}Ni$ systems. The effective Q-value acts as a driving force for the additional absorption in the evolution of transfer in to more complex and deeper reaction channels such as fusion.

3.4.1 Optimum Q-value

The Q-value of the reaction will change for proton transfer due to the rearrangement of nuclear charge. If Z^fs represent the nuclear charge of the projectile and target after proton transfer, Z^i s represent the nuclear charge before proton transfer and E_{cm} is the incident beam energy in the centre-of-mass, the optimum Q-value can be defined as [20]

$$Q_{opt} = [\ (Z_p{}^f Z_t{}^f / Z_p{}^i Z_t{}^i) - 1]\ E_{cm} \qquad (3.26)$$

For neutron transfer there is no change in Z values and hence Q_{opt} becomes equal to zero. Different trajectories exist for the entrance and exit channels because of the change in mass, charge and energy (Q-value). For transfer channels the outgoing trajectories will be smeared because of the spread in Q-value. The distance of closest approach for the exit channel will have an additional spread due to the variation in the product Z_pZ_t due to charged particle transfer. According to the orbit matching condition proposed by Buttle and Goldfarb [21], the transfer is most probable when the incident and outgoing orbits at the distance of closest approach are matched. The Q_{opt} calculated on the basis of this condition can describe its charge dependence, but not able to describe the mass dependence of charge. In some other treatments [22] the relative velocity at the distance of closest approach is the same immediately before and after transfer. This velocity matching condition leads to an effective optimum Q-value which is proportional to the total number of nucleons transferred in the reaction.

Alhassid et al.,[23] included the frictional force proportional to the relative velocity at the distance of closest approach, where the duration of transfer process is proportional to the number of transferred nucleons. An expression as follows was obtained by considering the kinetic energy loss due to both momentum transfer and tangential friction.

$$Q_{opt\text{-}eff} = Q_{opt} + \Delta B = E_f - E_i = -[1-(1-x/\mu_i)\exp(-\alpha x/\mu_i)]E_i \qquad (3.27)$$

where x is the total number of nucleons transferred, μ_i is the reduced mass of the entrance channel, α is a single adjustable parameter related to the frictional constant, E_i is the initial

kinetic energy and E_f is the final kinetic energy. The value of 'α' is fixed for all exit channels and depends only on the entrance channel and is zero for no friction. ΔB is the shift in the coulomb barrier for each exit channels. The optimum excitation energy will be the centroid of the experimental distribution.

3.4.2 Form factor and Transfer probability

The global form factor F(r) at any distance 'r' is an exponential function smoothly matched to the quadratic function Φ(r) which limits F(r) at small distances at d_0 = 1.44 fermi where the absorption ≈1 [12].

$$F(r,Q) = F(r_0,Q)\{\exp[-\alpha(r-D_0)]\} = F_0\Phi(r)\{\exp[-\alpha(r-D_0)]\}/r \qquad (3.28)$$

where F_0 is a normalization constant fixed to reproduce the Q-integrated transfer angular distributions at forward angles and F(r) include all final states of each channel. In the first order perturbation approximation the Broglia and Winther semi-classical expression[2,3] for the amplitude of the colliding system for a transition to a channel β after the reaction with t = ∞ is given as

$$A_\beta = 1/i\hbar \int_{-\infty}^{+\infty} F_\beta(r,Q_\beta) \exp[i(Q_\beta - Q_{opt})t/\hbar]\, dt \qquad (3.29)$$

The term $F_\beta(r,Q_\beta)$ represents the form factor describing the transition from the entrance channel to an exit channel β, Q_β is the corresponding Q-value of the channel β. The above integral can be evaluated by considering the Rutherford trajectory around the distance of closest approach as

$$D(t) = D_0 + \frac{d^2D_0}{dt^2}t^2$$

where the second term is the acceleration at the turning point D_0. The distance of closest approach can be calculated for the entrance and exit channels by assuming the coulomb trajectory using the Rutherford classical expression given in equation (3.13) which should be modified for d_0 when including the nuclear potential. Using the above equation for trajectory the integral for the reaction amplitude can be evaluated [8] in a closed form by considering the radial dependence of F(r,Q) given by equation (3.28). The Q-integrated transfer probability to a given excited state β with a Q-value Q_β becomes

$$P_{tr}(D_0,Q_\beta) = |A_\beta(\infty)|^2 = \frac{\pi}{\sigma^2} |F_\beta(D_0,Q_\beta)|^2 \exp[-(Q_\beta - Q_{opt})/2\sigma^2] \quad (3.30)$$

From the above transfer probability for each channel, the effective coupling strength F_0 can be evaluated as the average form factor at the coulomb barrier radius $R_C = D_0$. This can be compared with the experimentally measured Q-integrated transfer probability given by the relation

$$P_{tr}(D_0,Q_\beta) = \sigma_{tr}/(\sigma_{el} + \sigma_{QE}) \quad (3.31)$$

The width of the Q-value distribution σ in equation (3.30) is given as

$$\sigma = \hbar\sqrt{(\alpha d^2D/dt^2)/2} = (\hbar E_{cm}\alpha^{1/2})/\sqrt{2Z_pZ_te^2\mu} \quad (3.32)$$

where 'α' is the slope parameter which is correlated to the binding energy E_B and can be derived from the average of binding energies of the nucleons in the initial and final reaction channels by correcting both for average excitation energy as given in the following equation (3.33). Here p is the partition factor such that $0.15 < p < 0.85$

$$\alpha(E_x) = 1/2[\alpha_i\sqrt{1-pE_x/E_B^i} + \alpha_f\sqrt{1-pE_x/E_B^f}] \quad (3.33)$$

Due to the resolution problems extraction of form factor F(r,Q) from experimental data is difficult for nucleon transfer to closely spaced states and hence the measured form factor is considered as the average strength $F_0^2\Delta N$ where ΔN is the number of states within the interval Q to $Q+\Delta Q$, where $\Delta Q = Q-Q_{opt}$. The average form factor per state F_0 is considered as a constant over the range of interest. The total transfer probability over the whole range of Q is obtained [12] by the summation for all single particle states as

$$P_{tr}(D_0) = \frac{\pi}{\sigma^2} \sum_{Q=-\infty}^{Q_{eff}} F_0^2 \Delta N \exp[-(Q + \frac{\Delta Q}{2} - Q_{opt})^2/2\sigma^2] \quad (3.34)$$

If the energy gap between ground state and excited state is large, the total transfer strength will be the sum of the ground state strength and the strength due to the excited state.

$$P_{tr}(D_0) = \pi/\sigma^2\{ F_0^2 \exp[-(Q-Q_{opt})^2/2\sigma^2] \} + \{\pi/\sigma^2 \sum_{-\infty}^{Q_L} F_0^2 \Delta N \exp[-(Q-Q_{opt})^2/2\sigma^2]\} \quad (3.35)$$

where Q_L is the Q-value for the lowest excited state. If the interval ΔQ is small the above summation can be replaced by an integral. In some cases especially 2-nucleon transfer etc.,

the semi-classical theory is not successful in explaining the nucleon transfer reaction. In semi-classical theory the angular distribution can be transformed into P_{tr}-d_0 plots which shows the anomalous behaviour of slope that results in the inapplicability of semi-classical theory mentioned above. This inapplicability of semi-classical theory forced the investigators to look for a more efficient theoretical approximation of diffractive quantum mechanical effects of the well known coupled channel approach.

3.5 Quantum Mechanical Model

At energies well below the barrier semi-classical theories are not successful in describing the transfer process. In such situation approximations based on quantum mechanical theories such as Distorted Wave Born approximation (DWBA), WKB approximation or Coupled Channel Approximation (CCA) are used for interpreting the experimental observations. Switkowski et al.,[24] reported that in DWBA, the cross section for a reaction a + A $\rightarrow$ b + B + Q is proportional to the square of the matrix element M between the regular coulomb wave functions F_ℓ in the entrance channel α and exit channel β.

$$M = \int_0^\infty F_{\ell\beta}(k_\beta r)\exp(-kr)F_{\ell\alpha}(k_\alpha r)dr \qquad (3.36)$$

At the low energy region the tail of the form factor is important and proportional to the exponential function e^{-kr} where k is related to the charge and binding energy of the transferred particle. The maximum value of 'r' at which the product $e^{-kr}F_{\ell\alpha}(k_\alpha r)$ is maximum, can be obtained from the WKB approximation for $F_{\ell\alpha}(k_\alpha r)$ as

$$r_{max} = (1/q)(\eta_\alpha/k_\alpha)\{1+[1+q/\eta_\alpha^2(\ell_\alpha+1/2)^2]^{1/2}\} \qquad (3.37)$$

where the Sommerfield coulomb parameter $\eta_\alpha = Z_pZ_te^2/\hbar v_\alpha$ and $q = 1+k^2/k_\alpha^2$. At low energies the wave number k_α becomes small and r_{max} reaches a constant value. At the classical turning point

$$r_{0\beta} = (\eta_\beta/K_\beta)\{1+[1+((\ell_\beta+1/2)/\eta_\beta)^2]^{1/2}\} \qquad (3.38)$$

when the two trajectories of exit and entrance channels coincides, the Q-value will have the optimum value Q_{opt} at $r_{max} = r_{0\beta}$. Since only low angular momentum contribute $\ell_\alpha \approx \ell_\beta < \eta_\alpha k_\alpha/k$[24] and hence

$$(1/q)\,(\eta_\alpha/k_\alpha) = \eta_\beta/k_\beta = Z_bZ_Be^2/2(E_\alpha + Q_{opt}) \tag{3.39}$$

$$Q_{opt} = [(Z_bZ_B/Z_aZ_A)-1]\,E_\alpha + (Z_bZ_B/Z_aZ_A)\,\hbar^2k^2/2\mu_\alpha \tag{3.40}$$

where μ_α is the reduced mass in the entrance channel and E_α is the centre-of-mass energy. So in quantum mechanical model an additional term $(Z_bZ_B/Z_aZ_A)\,\hbar^2k^2/2\mu_\alpha$ has to be included with the corresponding semi-classical expression to get Q_{opt} at low incident energies E_α. Switkowski et al.,[24] evaluated the above mentioned integral for the matrix element M using WKB approximation and deduced an expression for the total reaction cross section at the above Q_{opt} for the reaction $\alpha \rightarrow \beta$ as

$$\sigma_{\alpha\rightarrow\beta} = (1/E_\alpha)\exp[-4\eta_\alpha \arctan k/k_\alpha] \tag{3.41}$$

From the above total cross section the spectroscopic factor can be obtained using a first order expansion for the arctangent function for very low energies E_α.

$$S_{\alpha\rightarrow\beta} = \sigma_{\alpha\rightarrow\beta}\,E_\alpha \exp(2\pi\eta_\alpha) \approx \exp[4Z_aZ_Ae^2m_\alpha/\hbar^2k] \tag{3.42}$$

For heavy ion reactions the exponent in (3.41) is a large number. The cross section for an optimum Q-value transfer reaction exceeds the cross section for compound nuclear reactions at very low energies. The transfer cross section using the computer code PTOLEMY for the DWBA calculation can be obtained as [20]

$$\sigma = \sum_{p,t} S_pS_t\,\sigma_{pt} \tag{3.43}$$

where S_p, S_t are the spectroscopic factors obtained from light ion reactions and σ_{pt} is the calculated cross section of the corresponding states. The optical potential parameters can be obtained from elastic scattering analysis. The scattering amplitude at a given angle θ depends on all partial waves and the corresponding phase shifts δ_ℓ [14]

$$A(\theta) = 1/2ik\sum_{\ell=0}^{\infty}(2\ell+1)P_\ell(\cos\theta)\exp(2i\delta_\ell) \tag{3.44}$$

The asymptotic form of P_ℓ for larger ℓ-values is that

$$P_\ell \sim \frac{i\{\exp[i(\ell+1/2)\theta+i\pi/4] - \exp[-i(\ell+1/2)\theta-i\pi/4]\}}{\sqrt{(2\pi\ell\sin\theta)}} \qquad (3.45)$$

The scattering amplitude is maximum for the extremum values of $\theta(\ell) = \pm 2d\delta_\ell/d\ell$. In partial wave expansion the transfer cross section [16] can be written as

$$d\sigma/d\Omega = |(1/2ik)\Sigma_\ell (2\ell+1)F_\ell \exp(2i\sigma_\ell)P_\ell(\cos\theta)|^2 \qquad (3.46)$$

where σ_ℓ is the coulomb phase shift, F_ℓ is the parametrized form factor and $P_\ell(\cos\theta)$ is the Legendre polynomial of order ℓ. The width of partial wave distribution $\Delta\ell$ is associated with the width of the form factor F_ℓ. The critical width is given as the $\Delta\ell_c = \sqrt{\eta}/(\sin(\theta_m/2))$ where η is the Sommerfield parameter and θ_m is the maximum angle of angular distribution. For $\Delta\ell > \Delta\ell_c$ semi-classical model is used for explaining the transfer process. But for $\Delta\ell < \Delta\ell_c$ the reaction is very localized in ℓ-space, the process becomes a quantal diffraction and quantum mechanical models should be used. For 2-nucleon transfer, the ℓ-distribution and form factor are narrower than 1-nucleon transfer. For multistep transfer process form factor and ℓ-distribution are much more localized and use of classical trajectories can not be justified.

3.6 Slope Anomaly and Transfer Reactions

The nuclear absorption is negligible at large inter nuclear reaction distances and the transfer probability falls exponentially as the inter nuclear distance increases. The slope of this exponential fall off for 2N transfer with the angle dependent distance of closest approach is expected to be approximately twice that for 1-nucleon transfer. Several studies shows good agreement between theory and experiment. But some experimental measurement shows no agreement with the above expectation. The slope of 2N transfer is less than the predicted value, or similar to 1N transfer. This experimentally observed anomalous behaviour of the P_{tr}-d_0 variation is called slope anomaly. 2N transfer has been systematically investigated by Rehm et al.[16]. The slope anomaly is observed to disappear as the energy approaches the barrier from above. 2N transfer has more localized form factor and hence slope anomaly at higher energies can be attributed to the influence of diffractive

scattering. The narrow form factor and ℓ-distribution of 2-nucleon transfer process causes localization in ℓ-space which may results in the slope anomaly leading to diffractive scattering. The slope parameter is given in section 3.4. The slope anomaly is expected to be caused by the distortion of coulomb orbits by the tail of the attractive nuclear potential. The tail causes the probability to rise faster by pulling or refracting the coulomb orbit inward forcing the actual apsidal distance to be smaller than the corresponding distance of closest approach. A systematic study of slope anomaly in neutron transfer reactions is reported by Marta et al.[25]. They have proposed [26] a model to analyze one- and two-proton transfer probabilities. Here the relative motion of the colliding heavy ions is governed by the real part of the total coulomb plus nuclear optical potential. The slopes determined from experiment are often smaller than those calculated by equation (3.22) in the case of transfer measurements above coulomb barrier. This slope anomaly can not be explained by transfer from excited states. Below the coulomb barrier the transfer cross section behave normally and obeys the theoretical predictions as per equation (3.22). But above the barrier multinucleon transfer and at very high energies single nucleon transfer probabilities have slopes differing by the above prediction. Energy dependence of slope anomalies were well studied by Saha et al.[8]. A simple and satisfactory explanation for the slope anomaly is given by Baba et al.[27]. For energies above coulomb barrier the deflection function is not single valued because of the dramatic change of the path of the particles for small impact parameters due to strong nuclear forces [28]. Also for same angle of deflection there will be more impact parameters. Since transfer probability depends exponentially on d_0, contributions from small impact parameters can be quite large. The main contribution in understanding slope anomalies arises from nuclear branch of the impact parameter.

$$d\sigma/d\Omega\,|_{nucl} = P(r_0,nucl)\,(b_{nucl}/\sin\theta)\,|\,db_{nucl}/d\theta\,| \qquad (3.47)$$

The two important features of slope anomaly are the following :

i)The slope anomaly occur only with energies higher than coulomb barrier. This is because only at these energies projectile and target nuclei can approach each other closely enough to feel the attractive nuclear force between them.

ii)The slope anomaly is more dominant in multinucleon transfer compared to one nucleon transfer because of the larger value of exponential slope α in the former case.

3.7 Coupled Channel Approach

In this approach the various reaction channels such as elastic, inelastic, transfer etc. are treated as not independent of each other. The effect of other channels have to be considered in order to obtain information about a particular channel. A thorough understanding of the process helps in the extraction of the form factor which together with the energy state will enable CC calculations. Dasso et al.,[1,4] proposed that coupling of non-fusion channels such as inelastic, transfer etc. to the incident channel can modify the barrier and lead to sub-barrier fusion enhancement. The fusion cross section can be calculated by estimating the transmission through the modified barriers. The coupling lowers some of the barriers which enables the enhancement of sub-barrier fusion cross section. The inelastic states normally coupled in CC calculations are 2^+, 3^- states of the projectile and target. The inelastic coupling strength [12] is usually calculated as [28]

$$F_{inel} = \beta_\lambda/\sqrt{4\pi}\{-R\, dV_n(r)/dr + [3Z_pZ_te^2/(2\lambda+1)][R^\lambda/R_b{}^{\lambda+1}\} \qquad (3.48)$$

where β_λ is the deformation parameter with multi polarity λ of the transition, the radius of the excited nucleus $R=1.2A^{1/3}$, R_b is the position of the barrier and V_n is the nuclear potential. The deformation can be evaluated from the electromagnetic transition probabilities. Under the constant coupling approximation [1,4], the set of coupled equations in (3.49) are decoupled to get the equations in (3.50) by neglecting the channel dependence of nuclear and centrifugal potential.

$$[-(\hbar^2/2\mu)d^2/dr^2 + V_t(r) - E]\psi_\alpha(r) = -\Sigma_\beta \langle\alpha \mid H_0 + V_{cpl}(r, \xi) \mid \beta\rangle \psi_\beta(r) \qquad (3.49)$$

$$[-(\hbar^2/2\mu)d^2/dr^2 + V_t(r) + \lambda_\alpha(R_b) - E]\, \Sigma_\beta U_{\alpha\beta}\psi_\beta(r) = 0 \qquad (3.50)$$

Here $U_{\alpha\beta}$ is a unitary matrix which diagonalises the coupling matrix $M_{\alpha\beta}$ to give a set of eigen values λ_α. The coupling matrix $M_{\alpha\beta}$ is given as

$$M_{\alpha\beta} = \langle\alpha \mid H_0 + V_{cpl}(r, \xi) \mid \beta\rangle = \delta_{\alpha\beta}\varepsilon_\beta = F(x) \langle\alpha \mid G(\xi) \mid \beta\rangle \qquad (3.51)$$

The coupling replaces a single barrier by a set of barriers. The transfer amplitude is given as [29]

$$i\hbar a_\beta(t) = \Sigma_\alpha F_{\beta,\alpha}(r,t) \exp[i(Q_{\beta\alpha} - Q_{opt})t/\hbar\,]a_\alpha(t) \qquad (3.52)$$

where a_0 represents the elastic channel, $a_\beta(-\infty) = \delta_{\beta,0}$ is the initial condition, Q-value $Q_{\beta\alpha}$ = E_β-E_α and form factor $F(r(t)) = F_0 \exp(-\alpha[r(t) - R_b]$. Here r(t) is the distance between two colliding partners. The form factor can be normalized at the position of the coulomb barrier R_b. The exponential slope 'α' of the form factor can be calculated using equation (3.22). The absorption and nuclear potential can be neglected for simplifying the CC calculations. The constant coupling approximation is under the assumption that the coupling strength in the vicinity of uncoupled potential barrier $V_\alpha(R_b)$ is more important. The eigen values λ_α can be obtained by diagonalising the $\varepsilon_\beta\delta_{\alpha\beta} + V_{\alpha\beta}$ at the barrier with a unitary matrix $U_{\alpha\beta}$

$$\lambda_\alpha(r) = \Sigma_{\alpha\beta} U_{\alpha\beta}^{*}(r) [\varepsilon_\beta\delta_{\alpha\beta} + V_{\alpha\beta}] U_{\alpha\beta} \qquad (3.53)$$

The set of eigen channel barrier obtained as $B = V(R_b)+\lambda_\alpha(R_b)$. The transmission coefficients for each eigen channel barrier weighted by a factor $|U_{0\alpha}|^2$ is summed to get the total transmission T as shown in previous chapter (section 2.7.2). The index '0' in $U_{0\alpha}$ denotes the ground state channel.

3.8 Experimental Methods for Transfer Studies

The overlap of the wave functions of the initial and final states can be measured experimentally using direct nucleon transfer reactions. By resolving the individual final states populated experimentally, the interpretation of the data becomes simple using the following two methods. In the first method the beam is allowed to react with thin targets and the final states are resolved using a high resolution detection system such as magnetic spectrometers to identify the residual nuclei. The second method involves the high resolution studies of the de excitation γ-rays in coincidence with the reaction products for identifying the residual nuclei and deducing the final state population distribution. The experimental measurement of transfer reaction is more complicated as the mass of the probing nuclei is increased. The excitation of the projectile-like and target-like nuclei makes the problem of resolving the final states quite cumbersome. At energies well above the coulomb barrier, the process such as strong inelastic excitation, deep inelastic excitation (non quasi-elastic) and fusion makes the transfer reaction mechanism more complicated. The above complication can be avoided by performing heavy ion transfer reactions below and around the coulomb barrier, where the quasi-elastic channels dominate. If the target

contains isotopic impurities which give residual nucleus of interest, the measurement at below barrier energies become more complicated. This difficulty can be overcome by the kinematics coincidence method discussed in section 3.8.1. The energy spread of the incident beam and energy straggling in target and detector materials reduces the resolution for heavy ion reactions.

3.8.1 Kinematic Coincidence Method

The kinematic coincidence measurement is the simultaneous detection of the reaction fragments - the low energy back scattered projectile-like ion and the complimentary forward scattered target-like ion carrying large fraction of the incident beam energy - by two detectors placed at kinematically correlated angles. This technique is widely used in binary elastic, quasi-elastic and deep inelastic reactions. A few cases are reported on the use of this technique for nucleon transfer measurements. Corradi et al.,[30] carried out low energy binary heavy ion reaction study using the so called kinematics coincidence method. They have measured the TOF for one of the two ions which allowed the determination of the masses with a linear dependence on TOF with optimum resolution. They have carried out the measurement of the elastic and quasi-elastic cross sections for medium mass systems such as $^{58}Ni+^{64}Ni$ and $^{58}Ni+^{91}Zr$ at energies near the coulomb barrier. They have detected the beam-like particles using a position sensitive silicon detector (PSSD) placed inside the scattering chamber. A detector telescope including 2 micro channel plates(MCP) and an ionization chamber for detecting the target-like recoils for the coincidence TOF measurement and for the ΔE and E measurement. The ^{58}Ni beam energies were E_{lab} = 183.3, 190.7 and 204.1 MeV with a current 5 to 15 pnA from LNL - XTU Tandem accelerator and the target was ^{64}Ni of thickness 18 to 35 $\mu g/cm^2$ enriched to 96.5% evaporated on carbon backing of 20 $\mu g/cm^2$. If E_1 and θ_1 are the energy and scattering angle of the target-like particles and E_2 and θ_2 are that of the beam-like particles, P_0 is the beam linear momentum and S_1 is the flight path, A_{tot} is the sum of the beam and target masses then the mass spectra and the Q-value spectra becomes

$$A_2 = A_{tot} - A_1 = \frac{TOF\ P_0\ Sin(\theta_2)}{S_1\ Sin(\theta_1+\theta_2)} \qquad (3.54)$$

$$Q = [A_0E_0/Sin^2(\theta_1+\theta_2)]\{Sin^2\theta_2/A_1 + Sin^2\theta_1/A_2\} \quad (3.55)$$

where A_0 is the mass of the beam and E_0 is the beam energy. Earlier on Pass et al.,[31] have used kinematics coincidence technique at Daresbury recoil mass separator to measure the excitation function for one neutron pick up at $\theta_{cm}=180^o$ (head on collision) for the systems $^{58}Ni+^{116,124}Sn$ and $^{58}Ni+^{144,154}Sm$. The energy range was from near barrier to well below (40 MeV) the barrier. They found that the transfer probabilities generally increases with target mass and a cross section ~ 1 mb/sr have been measured at lowest energies. The slopes of the excitation functions for the heavier Sm isotopes are significantly smaller than the simple theoretical predictions. A similar measurement of 180^o sub-barrier transfer reactions have been reported by Herman et al., for the $^{32}S+^{92,98}Mo$ system.

A systematic study of the quasi-elastic and transfer measurement on $^{32}S+^{64}Ni$ systems is reported by Napoli et al., using the kinematics coincidence technique.[9] They were able to resolve 1N transfer channels, but failed to get 2N transfer products due to m/q ambiguity – the unresolvability due to the focusing of particles of same m/q value to the same focal plane position. This problem was resolved in our measurement by using TOF information obtained by taking the START signal from the back SBD (sulphur) and stop from the anode of the focal plane MWPC detector of the RMS-HIRA.

3.8.2 Inverse Kinematics Method

The measurement of small transfer cross section is experimentally difficult. The energy of the back scattered projectile-like ions is low and it impose limitations on mass and charge resolution. These difficulties can be overcome by performing an inverse kinematics reaction. In this method light targets are bombarded with heavier projectiles. The target-like reaction products from close collisions are then emitted at forward angles with high energies. This simplifies the particle identification procedure. An inverse kinematics study by bombarding ^{58}Ni targets with ^{100}Mo beam was reported by Rehm et al., [32] to study the effects of multi nucleon transfer reactions.

3.8.3 Particle –γ coincidence Method

Here the mass number of the ions are identified by detecting the characteristic γ-rays in coincidence with the heavy ions. The γ-rays emitted by the target like ions can be detected using high resolution HPGe detectors or high efficiency NaI(Tl) detectors. The advantage of this method is that one can resolve the population of low lying levels in both inelastic and transfer channels. The observed particle energy spectra for a given nucleus can be corrected for contributions from other nuclei with the same atomic number. The particles in coincidence can be detected by position sensitive avalanche counters or so. Saha et al.,[8] also have reported about this method. The coincident γ spectra gated by Z bands shows the various transfer products corresponding to different channels. The disadvantage of this method are the following.

i) The cross section measurement require a detailed knowledge of the decay scheme of the final nucleus of interest.
ii) The transition to the ground state and low lying excited states which decay mainly via internal conversion can not be detected.

3.8.4 Radio Chemical Methods

The residual nuclei are stopped in a catcher foil and it is subjected to chemical separation process after irradiation. The specific elements or elemental groups are fractionated and the α and γ activity of the various fractionations are analyzed to get good mass and charge determination. Very small cross sections can be measured due to low back ground in offline counting. This method is highly sensitive due to the larger area of catcher foil and is very useful for reactions with very heavy nuclei. But this method is not so favorable for the detection of stable isotopes and isotopes with short half-lives.

3.9 Algorithms of Particle Identification

The identification of the many elements and isotopes produced in nuclear reactions above the coulomb barrier is a cumbersome problem in nuclear physics. This problem can be solved to some extend by using magnetic spectrographs in conjunction with focal plane detectors. The various parameters which can be measured using the above instrumentation are the following :

1) The product of the magnetic field and radius of curvature of the particle in the field($B\rho$)
2) Energy loss(ΔE)
3) Rate of energy loss of the ions through the medium(dE/dx)
4) Total energy of the ion(E)
5) Time-of-flight (TOF) within the spectrograph

There are two methods for particle identification in nuclear physics. They are energy loss method and velocity measurement method. The relation of atomic mass (A), atomic number (Z) and ionic charge (q) to the above parameters is made use of in these two methods. Measurement of TOF together with $B\rho$, ΔE and E specifies the particle parameters such as A, Z and q.

3.9.1 Energy Loss Method

For non relativistic particles $v^2 = 2E/A$ and $dE/dx \propto AZ^2/E$. The setup should consists of a thin ΔE detector followed by a second E detector in which particle stops. The sum of the detector signals gives total energy E and ΔE signal gives a measure of dE/dx at the begning of the particles track. The product $E(dE/dx)$ provides a measure of AZ^2. Hence Z identification is possible. Also $B\rho \propto \sqrt{(AE)/q}$. This relation separate particles with different A/q^2 for a particular choice of Z. Multiple scattering, energy loss fluctuation and variations in angle of incidence of different particle trajectories do not affect the total energy measurement. The range energy relation between particle range (R) and energy (E) is $R = aE^b$ where 'a' is a constant proportional to $1/Aq$ and 'b' is variable below 1.73 depends on E.

3.9.2 Velocity/TOF Measurement Method

The second useful parameter for the particle identification from detector signals is the TOF (t) which is proportional to $\sqrt{(A/E)}$. Therefore velocity $v \propto \sqrt{(E/A)} = K\sqrt{(E/A)}$, where K is a proportionality constant and equal to 1.4.

$$v = d/t = 1.4\sqrt{(E/A)} \tag{3.56}$$

Thus the mass of the particle to be identified can be determined as

$$A=2Et^2/d^2 \tag{3.57}$$

The fractional error in mass determination caused by a timing error δt for a flight path 'd' is given as

$$\delta A/A = 2.8[\sqrt{(E/A)}](\delta t/d) \tag{3.58}$$

3.10 Literature Review-Experimental transfer measurements

A detailed review of the transfer measurements on various systems is discussed in the following sections 3.10.1 to 3.10.15. Up to section 3.10.5, the reaction with sulphur beam on various targets is reviewed. In section 3.10.6 to 3.10.8 the reactions of silicon beam on Zn, Ni and Nb targets is given. A review of Ti+Ni transfer reactions is given in section 3.10.9. Sections 3.10.10 to 3.10.13 gives the reaction of Ni beam on different targets. In the last two sections the reaction of carbon and oxygen beams on different targets are given.

3.10.1 Sulphur - Molybdenum and Sulphur - Niobium systems

An extensive measurement of nucleon transfer cross section as a function of energy and angular distribution for nucleon transfer have been carried out for the $^{32}S+^{92,98,100}Mo$ system and $^{32}S+^{93}Nb$ system by Liang et al., [20] slightly above and well below the barrier. The data were used for a qualitative comparison of fusion and transfer. The transfer measurement was carried out at incident beam energies 109, 116 and 125 MeV on self supporting targets. The projectile-like particles were detected by 6 Si SBDs

and 4 ΔE-E telescopes mounted on two movable tables at 10° interval. The ΔE-E gas telescopes filled with P10 gas were used at forward angles for charge identification of the transfer products which deposit 0.25 to 0.5 part of their energy in the gas medium. Measurement of TOF for a flight path of 90 cm with the scattering chamber and energy was used for mass identification. START pulse from the detectors and STOP from the LINAC RF signals were fed to the TAC for obtaining TOF information. 100 $\mu g/cm^2$ gold foil was used for determining the timing width of the beam where the FWHM during the experiment was between 150 to 200 ps. The E-ΔE and E-TOF histograms (2D) were gated to get the mass spectrum by projecting on TOF axis which showed the 3N pickup and 4N stripping. The mass spectrum from the charge gating of E-ΔE is used for the identification of pickup of neutron and stripping dominated by proton. The major channels identified are +2n, +1n, -1p, -2p, -2p1n and -2p2n. The results of angular distributions were compared with the DWBA predictions using the code PTOLEMY. Energy and angle integrated transfer cross sections were determined from various channels which shows that the multinucleon transfer cross sections are about 30 to 40% of the total transfer cross section for all targets. The total transfer cross sections were about 30 to 40% of the total reaction cross section.

3.10.2 Sulphur - Zirconium Systems

An extensive measurements of the differential transfer cross section had been carried out by Corradi et al., [11,17] for the $^{33}S+^{90,91,92}Zr$ systems. The measurements were done at beam energies 110.6,118.7 MeV for the $^{90,91}Zr$ targets and 110.8,118.9 MeV for the ^{92}Zr target. The TOF information was obtained from two micro channel plates (MCP) and energy E and charge Z informations from focal plane ionization chamber. They were able to identify different transfer channels with probable errors. The errors were mainly due to the monitor positions, sliding seal chamber angular positions, telescope and beam alignment etc. They have obtained the Q-distributions of the transfer products at various angles of the detection and found that there was no difference in Q-distributions for different observation angles within the relatively large statistical uncertainities. The angle-integrated transfer cross sections (σ_{tot}) have been found from differential transfer cross

sections. The Q-integrated transfer probabilities and angular distributions were obtained from experimental Q-distributions. The slope parameters and Q-averaged form factors were determined to perform CC calculations. The results of the calculations were compared with the experimentally measured fusion cross sections. They have also measured the asymptotic barrier shifts and plotted ΔB versus $\Delta\sigma_t$ and $\Delta\sigma_f$ versus $\Delta\sigma_t$. Here $\Delta\sigma_t$ and $\Delta\sigma_f$ are the missing transfer and fusion cross sections in angular distribution measurements. They were compared these results with semi- classical model.

3.10.3 Sulphur - Nickel Systems

Napoli et al., [9] measured the 1p stripping and 1n pickup transfer cross sections for $^{32}S+^{64}Ni$ system by the interesting technique of kinematic coincidence between the low energy back scattered projectile-like ions and the corresponding forward going recoils carrying large fraction of the incident energy. The experiment was carried out at LNL - XTU Tandem accelerator and the forward recoiling target particles were detected by the RMS. Angular distribution at E_{cm} = 54.2 MeV for θ_{lab} ranging from 5° to 30° for Ni-like particles and θ_{cm} ranging from 170° to 120° for S-like particles has been measured. Excitation function at θ_{cm} = 170° has also been measured for energies E_{cm} = 45.5 to 61.6 MeV. The ^{64}Ni target thickness was 330 $\mu g/cm^2$ and abundance of 93.4% which was bombarded with ^{32}S beam of current about 10 pnA in a sliding seal scattering chamber. The RMS was set for target-like particles which disperse them proportional to m/q ratio across the focal plane. The acceptance of RMS is maximum solid angle = 10 msr, maximum energy ≈ ±20%, maximum mass ≈ ±7% and angular rotation +5° to –50°. A position sensitive PPAC and a Bragg chamber was used as the focal plane detectors. The Ni-like recoils were detected at the above θ_{lab} because of the poor beam rejection. The position-energy 2D spectrum was used to determine m/q ratio from the X-position and the recoil energy for each channel from the E projection. For the maximum probable charge state ($q=17^+$), they tried to overcome the m/q ambiguity due to the degeneracy $(m-4)/(q-1) \approx m/q \approx (m+4)/(q+1)$, by different offline corrections to the measured yields for target impurities. The absolute normalization of the cross section was obtained by assuming the Rutherford cross section as the total quasi-elastic and transfer yields. The angular

distribution measurement shows that the transfer cross section for -1p channel is about 25% lower than +1n channel and both are about 0.3 to 1.5% of Rutherford cross section. Excitation function measurement illustrated that the minimum cross section corresponds to a probability of 0.25% and maximum cross sections correspond to 3.5%. The experimental data is compared with complex WKB (CWKB) theory for one particle transfer and with semi-classical theory based on coulomb trajectory. For +1n channel this comparison shows well matching between theory and experimental data, but for the charged particle (–1p) channel the theory underestimates the data by a factor of 2, which points out the inability of DWBA to fit heavy ion charged particle transfer reaction. The comparison has been done by considering the first order perturbation theory, proper experimental nuclear structure information and all transitions around the fermi energy. This experimental investigation was not successful in resolving the m/q ambiguity and identifying 2-nucleon and multinucleon transfer.

Saha et al.,[7,8] have studied 1p and 2p transfer reactions around coulomb barrier for the $^{32}S+^{64}Ni$ system. They have used the BARC-TIFR 14UD pelletron accelerator facility at Bombay for the measurement. The beam energies were 100 and 110 MeV. A 1D position sensitive parallel grid avalanche counter (PSPGAC) followed by a large area Bragg curve spectroscopy (BCS) detector with an angular acceptance of 30° was used for the E and Z determination of the beam-like particles. The Z identification was done with the BCS detector and A identification by detecting the γ-rays in coincidence with the heavy ions by resolving the population for low lying levels for both inelastic and transfer channels. The transfer probabilities were obtained as a function of distance parameter at various bombarding energies. The slope parameter for 1p and 2p stripping were determined. The effective coupling strengths for these channels were obtained from measured transfer probabilities using semi-classical theory which were used in CCFUS for calculating fusion cross sections around barrier. They have concluded that not only the proton stripping but the neutron pick up channels also contribute to the sub- barrier fusion enhancement.

The coupled channel effects in the elastic scattering of $^{32,36}S+^{58,64}Ni$ had been well studied by Stefanini et al.,[33] by measuring the angular distributions at several energies around coulomb barrier. They have analyzed the data using optical model potential. At the strong absorption radii remarkable energy dependence of the potentials had been observed. The largest effects had been observed for $^{32}S+^{64}Ni$. They have performed CC calculations for fusion and elastic scattering by inducing the elastic excitation of projectile and target and quasi-elastic transfer. A comparison of the reaction cross section extracted from elastic scattering with their previous fusion and transfer measurement was also done.

3.10.4 Sulphur - Ruthenium Systems

A study of the correlations discussed in section 3.10.2 was carried out for the $^{32}S+^{100,101}Ru$ systems by Corradi et al.[11]. The fusion studies of these systems were carried out by Munich group. The systems were characterized by large +ve Q-values for the +2n and –2p transfer channels. The role of these channels in sub-barrier fusion enhancement and the lack of multinucleon transfer data for these systems in sub-barrier region motivated the Corradi group. They have used LNL - XTU Tandem accelerator to produce ^{32}S beam with intensities 10 to 20 pnA. The thickness of the $^{100,101}Ru$ targets were 140 and 170 $\mu g/cm^2$ and the beam energies were 118 and 127 MeV. They have used two MCPs for the TOF measurement and a ΔE-E ionization chamber for the nuclear charge and energy determination. An independent array of 8 silicon SBDs was positioned at ≈ 15 cm from the target for obtaining more experimental points for the elastic + inelastic scattering at forward angles. This was to extract the absorption probability with good accuracy to be used in semi-classical formalism. The monitor detectors were mounted at ≈ 18cm from the target at $\theta_{lab} = 20^\circ$ w.r.to the beam line. They have measured the Q-value integrated differential cross section for the most relevant transfer channels. They have also measured the angular distributions for different transfer channels and compared with theoretical calculations. The transfer cross sections have been analyzed with a semi-classical formalism to study the correlation between fusion and transfer. They found that the proton stripping channel (-2p) plays a major role in the sub-barrier fusion enhancement for the

two targets. They have used the code CCFUS for CC calculations. Coupling to the lowest inelastic excitations explains sub-barrier fusion enhancement partially. By invoking coupling to transfer channels, they were able to reproduce the asymptotic barrier shifts reasonably well.

The transfer reactions at the energies 106,110,116 and 130 MeV were studied by Schindler et al.,[28] for the $^{32}S+^{102,104}Ru$ systems. They have measured the differential cross sections for the strong transfer channels with an experimental set up yielding good mass number, nuclear charge and energy resolution. The measured transfer cross sections were analyzed to extract the transfer form factors within the frame work of semi-classical description. Slope anomalies had been observed at energies slightly above the coulomb barrier. By considering the higher order effects in perturbation theory and slope anomalies, good agreement was found between theoretically predicted and experimentally measured cross sections. They have concluded that instead of multi channel, each transfer channel contributed to the sub-barrier fusion enhancement according to its form factor and Q-value.

3.10.5 Sulphur - Samarium and Sulphur - Erbium Systems

An investigation on the deformation effects in the one-neutron pick up reactions around coulomb barrier was carried out by Thomasi et al.,[18] using sulphur beam on ^{144}Sm (spherical) and ^{166}Er (quadrapole deformed) targets. The one-neutron transfer channel was chosen for this study because there was no need to consider sequential process and coulomb effects. The 20 MV Tandem accelerator facility at TANDAR laboratory was utilized for obtaining ^{32}S beam at energies ranging from 123.5 to 152.5 MeV for the experiment. The relevant transfer cross sections have been determined as a function of the bombarding energy by measuring the activity of delayed X-rays emitted by the reaction products such as ^{143}Sm ($T_{1/2}$ = 8.83 min) and ^{165}Er ($T_{1/2}$ = 10.36 hours). For this X-ray yield method the target-like transfer products were collected using gold catcher foils placed behind the targets. For the ^{144}Sm target the irradiation time was 2 hours and for the ^{166}Er target it was 6 hours. The monitor detectors were placed at $\pm 30^{\circ}$ w.r.to an auxiliary gold target. They have obtained the transfer cross sections by fitting the delayed X-ray

activities via a minimization procedure. From the known half-lives and absolute number of photons produced per decay of each isotope in each mass chain, the time dependence of the K X-ray yields for both parent and daughter activities were calculated. The transfer cross sections were deduced by minimizing the χ^2 function constructed from the experimental X-ray activities and theoretical calculations. The identification of mass and charge was done using the characteristic X-rays. Transfer probabilities were analyzed by considering barrier penetration mechanisms as a classical tunneling process between donor and acceptor core. A comparison of the enhancement factor obtained from a simple semi-classical model with that of the deformed S+Er system w.r.to the spherical S+Sm system was done which showed consistency between theory and experiment.

3.10.6 Silicon - Zinc systems

A measurement of the one- and two-nucleon transfer reaction cross sections for the system $^{28}Si+^{68}Zn$ was carried out by Kataria et al.,[34] using the RMS-HIRA-at NSC. The TOF of the recoils were measured using the buncher RF and arrival time of recoils at the focal plane. They have corrected the transfer yields at higher energies by considering the impurity contamination in the target from neighbouring isotopes. The TOF information was used to determine the energy of the recoils. From the recoil energy the Q-value spectra was obtained. They have obtained the transfer probabilities as a function of distance of closest approach. The slope parameters and the form factors were extracted from the transfer probability for +1n, +2n, -1p, -2p channels. They have performed CC calculations using the code CCNSC. The coupling of inelastic and transfer channels to 1DBPM showed good agreement with experimental measurement of fusion excitation function of Dasgupta et al.[35].

One- and two-nucleon transfer reactions for the $^{28}Si+^{68}Zn$ system had been studied by Saha et al.,[7,8] using scattered ion-gamma coincidence method. The experiments were carried out with ^{28}Si beam from BARC-TIFR pelletron accelerator in the energy range 80 to 120 MeV. The cross sections for the +1n and +2n channels corresponding to a few selected γ-transitions of the product nuclei belonging to those transfer channels were measured from the γ-gated charged particle spectra. The spectroscopic strengths from light

ion transfer reaction data were used to estimate the missing probabilities due to transfer leading to ground state. A semi-classical approach was used to estimate the transfer form factors and coupled channel calculations were performed using inelastic+ transfer coupling. Good agreement was observed between this study and existing data.

3.10.7 Silicon - Nickel and Silicon - Neodimium Systems

A measurement of sub-barrier transfer reaction for the systems $^{28}Si+^{64}Ni$ and $^{28}Si+^{144}Nd$ has been reported by Sinha et al.[10]. They have used kinematic coincidence method by detecting the back scattered beam-like particle in coincidence with the forward recoiling target-like particle using the RMS-HIRA-at NSC. They were able to resolve the m/q ambiguity and obtained clear separation of the 1N and 2N transfer channels with TOF measurements. In the case of the first system a silicon surface barrier detector (SBD) was used for detecting the back scattered projectile-like ions. Where as in the case of later system a ΔE (gas) - E (SBD) detector telescope was used. From the TOF-position spectra the transfer probabilities, slope parameters and form factors were extracted and used in CC calculations. The various combinations of coupling such as low lying excited states (2^+,3^-), 2N transfer and 2 phonon coupling had been attempted which showed good agreement between theory and experiment for the Si+Ni system. In the case of Si+Nd system coupling of the above 3 channels over predicted the experimental results.

3.10.8 Silicon - Niobium System

A measurement of the one- and two-nucleon transfer probabilities and fusion excitation function for the $^{28}Si+^{93}Nb$ system was reported by Lagy Baby et al.[12]. The ^{28}Si beam was obtained from NSC pelletron and target-like particles were selected by HIRA. The energy range was 84 to 98 MeV and the target impurity was checked at 70 MeV. A better beam rejection was obtained by keeping HIRA at 7^o from the beam direction. The beam-like particles had been separated from the target-like recoils using TOF technique by taking the START from the MWPC anode and STOP from the RF signal. The form factors had been extracted from the 1N and 2N transfer yields and CC calculations have been

performed. 1DBPM predictions showed severe disagreement with the experimental measurement of fusion cross sections. But coupling of transfer + higher order phonon and transfer + linear coupling showed good agreement between experimental results and CC calculations.

3.10.9 Titanium - Nickel Systems

As an extension to the fusion measurements on Ti+Ni systems Varier et al.,[6] carried out the transfer measurements for the systems $^{46,48}Ti+^{64}Ni$ at NSC using the pelletron accelerator and HIRA facility. They have used the kinematic coincidence technique for resolving the m/q ambiguity at the focal plane of HIRA. The beam energy range was 120 to 142 MeV. The target-like recoils scattered through HIRA to its focal plane were detected with the position sensitive MWPC in coincidence with the back scattered projectile-like ions using Si SBD. From the TOF vs position spectra the transfer probabilities for 1N and 2N transfer channels were determined. From this the slope parameter and form factors have been extracted and used in CC calculations. The coupling showed considerable agreement with the experimental measurement of fusion cross section reported earlier[5,36].

3.10.10 Nickel - Nickel Systems

Using the XTU Tandem accelerator facility at LNL, the measurement of quasi-elastic process for the $^{58}Ni+^{64}Ni$ had been carried out by Corradi et al.[17]. They have used the kinematic coincidence technique for the TOF measurement, consisting of a position sensitive Si (PSSD) and a counter telescope with MCP detectors. The START signal was taken from the MCP_2 detector and the STOP from the PSSD. A mass resolution of 1/20 and Q-value resolution of ~ 1 MeV was achieved which was most suitable for quasi-elastic studies. These resolutions depends on TOF and scattering angle θ_2(of the projectile-like ions) which could be improved at the cost of solid angle. The calculated resolutions were found to be in good agreement with experimentally measured resolutions. The contribution of the TOF error is large for small θ_1(of target-like ions) and comparable with the error of θ_2 for large θ_1.

3.10.11 Nickel - Molybdenum System

The multinucleon transfer reaction studies are complicated due to the uncertainities in the analysis and due to small cross sections at incident energies around the barrier. For understanding and eliminating these experimental difficulties Rehm et al.,[32] performed one- to multinucleon transfer measurement for the $^{58}Ni+^{100}Mo$ system. They have used inverse kinematics method by bombarding ^{58}Ni targets with ^{100}Mo beam. The Ni-like recoils emitted in the forward angles with sufficient energies were detected in the mass region ^{59}Ni to ^{64}Ni. They have measured the angular distributions for ^{58}Ni and for the above mentioned Ni isotopes corresponding to one to six neutron transfer channels. The Q-value spectra and energy and angle integrated cross sections for these channels have been measured. The angular distributions showed a smooth angle dependence without any symptoms of oscillations predicted by theories. The upper limit of the two-, four- and six-neutron transfer cross sections obtained are about one order of magnitude smaller (by a factor of 10) than the calculations for similar systems within the pairing model. The experiment was performed at Argonne super conducting LINAC-ATLAS with ^{100}Mo beam of energy 380.4 MeV. The CC calculations were performed by using the code PTOLEMY. Analysis of the forward scattered particles was done according to their magnetic rigidity using a split-pole spectrograph. Hybrid focal plane detectors were used for measuring the position, energy, range and TOF. From these parameters the mass,Z,q of the recoils and Q-value of the reaction were determined. The normalization was done using two monitor detectors on either side of the beam. The most forward elastic yields were normalized to the corresponding Rutherford cross sections to get the absolute cross sections.

3.10.12 Nickel - Tin System

Using the ATLAS facility at Argonne National lab, an inverse kinematic reaction [37] was performed with ^{124}Sn beam on ^{58}Ni target. The beam energies selected with super conducting LINAC was 480.3 to 512 MeV. The reaction products are momentum analyzed using an Enge split-pole spectrograph and detected in a hybrid focal plane detector. The parameters measured was position(x), TOF(t), nuclear charge(Z), total energy(E) and range(R) in the counter gas. They have measured the angular distributions of Ni-like

particles. The angular distributions were normalized using monitor detectors. From the angular distributions the transfer probabilities were extracted as the ratio between transfer and Rutherford cross sections. The experimentally observed slope parameter showed good agreement with the predictions of semi-classical theory in the case of one-nucleon transfer. But in the case of two-nucleon transfer slope parameter agrees with the predictions of semi-classical model only at below barrier energies. For multinucleon transfer decay constant α shows saturation due to small cross sections. Using the computer code GRAZING they have calculated the angle and energy integrated neutron pickup cross sections and compared with the experimental results. It showed an exponential fall off with increasing number of transferred neutrons. They also extracted the average reduction in cross section per each transferred neutron. At the highest centre-of-mass energies this average reduction agrees well with the prediction of Winthers's code GRAZING.

3.10.13 Nickel - Uranium System

A study of the multinucleon transfer with neutron rich ^{64}Ni beam on neutron rich stable ^{238}U target was reported by Corradi et al.[38]. They have chosen this system due to the expected large transfer cross sections. This system had been studied earlier also, but it was with the a poor mass resolution and without a determination of the charge of the fragments. Corradi et al., used the LNL accelerator facility for the study of ^{64}Ni+^{238}U system. The TOF information was obtained using two MCPs and nuclear charge and energy information from a multi parametric ΔE-E ionization chamber. Using a sliding seal scattering chamber the angular distributions had been measured in laboratory angles 50° to 105° at E_{lab} = 390 MeV, they have observed a transfer of 6 nucleons and more with the high efficiency spectrometers. A comparison of the Q-value integrated angular distributions of the main transfer products with theoretical calculations was done. As expected in grazing collisions they found that the reactions are dominated by proton stripping. They have used the code GRAZING for theoretical calculations. The theoretical and experimental differential and total cross sections for the quasi-elastic channels was compared. A clear separation between grazing regime (quasi-elastic and deep inelastic) and quasi-fission reactions had been observed. They also found that neutron evaporation from the primary fragments strongly affects the final yields.

3.10.14 Carbon - Strontium, Carbon - Thorium and Carbon - Indium Systems

A study of the single and multinucleon transfer reactions for the systems $^{12}C+^{88}Sr$ had been reported by Roy et al.[15]. The energy of the incident beam was 87.5 MeV from BARC-TIFR pelletron. The one- , two- and three-nucleon transfer cross sections were measured and corresponding transfer probabilities had been determined. The magnitude of the enhancement was found as depending on the strength of interactions. A measurement of the angular distributions of the quasi-elastic scattering normalized with Rutherford cross section data was carried out by Biswas et al.,[19] for the $^{12}C+^{232}Th$ system. Differential cross sections for the dominant transfer channel had been determined for the above system, which showed low enhancement for fusion. That is this system showed a remarkable tendency for fusion-fission. Transfer probability, cross section for transfer yield and the ratio of $\sigma_{tr}/\sigma_{tr}+\sigma_{ff}$ had been measured for this system. Slope parameter, classical deflection function and classical cross section were determined from the experimental data and compared with semi-classical calculations. Multinucleon transfer measurement for the system $^{12}C+^{115}In$ was reported by Roy et al. [39]. The beam energy was 84 MeV. They have measured the absolute cross sections. The energy spectra showed an optimum in the cross section at a certain excitation energy corresponding to a Q_{opt} in that particular channel. In this constrained phase space approach the optimum Q-value forms the constraint.

3.10.15 Oxygen - Nickel and Oxygen - Thorium Systems

In order to understand the large fusion enhancement of $^{18}O+^{58}Ni$ system compared to the $^{16}O+^{60}Ni$ system a study of the pair transfer reaction was carried out by Broges et al.[13]. They found that two-neutron transfer channel contribute markedly to the sub-barrier fusion of $^{18}O+^{58}Ni$. A comparison of the experimental results with a simple theoretical model based on the effects of zero point pairing fluctuations showed good agreement between theory and experiment. Biswas et al.,[19] reported about the single and multinucleon transfer in the $^{16}O+^{232}Th$ system around coulomb barrier. This system showed

large transfer cross section relative to the total reaction cross section at sub-barrier energies. A measurement of angular distribution was carried out and analyzed to get transfer probabilities and slope parameter(α) for the stripping of 1p and 2p. The classical deflection function and classical cross section had been measured. Angle and energy integrated cross sections of the dominant transfer reaction channels had been measured as a function of $E_{lab,}$ and were compared with fusion cross section obtained by Wong's theoretical calculations. They also compared with the total fusion-fission cross section. A comparison of the ratio of the transfer cross section to the total reaction cross section (transfer + fusion-fission) as a function of bombarding energy is also done for the above system with similar systems such as $^{19}F+^{232}Th$. The transfer probabilities obtained from cross sections showed an exponential decrease with increasing distance of closest approach. The energy spectra were centered at energies corresponding to the optimum Q-values. The characteristic behaviour of the direct transfer reactions were obtained from measured angular distributions.

References

[1] C.H. Dasso, S. Landowne and A. Winther, Nucl. Phys.**A407**(1983)221.

[2] R.A. Broglia, C.H. Dasso, S. Landowne and G. Pollarolo, Phys. Lett. **B133**(1983)34.

[3] R.A. Broglia, C.H. Dasso, S. Landowne and A. winther, Phys.Rev.**C27** (1983)2433.

[4] C.H.Dasso, S.Landowne and A.Winther, Nucl. Phys. **A405**(1983)381.

[5] N.V.S.V. Prasad, A.M. Vinod Kumar, A.K. Sinha, K.M. Varier, D.L. Sastry, N. Madhavan, P. Sugathan, D.O.Kataria and J.J. Das, Nucl. Phys. **A603**(1996)176.

[6] K.M.Varier, A.M. Vinod Kumar, N.V.S.V. Prasad, P.V. Madhusudhana Rao, D.L. Sastry, Lagy. T. Baby, M.C. Radhakrishna, N.G. Puttaswamy, J.J. Das, P. Sugathan, N. Madhavan, A.K. Sinha and D.O. Kataria, Pramana **53**(1999)529.

[7] S.Saha and Y.K.Agarwal, Nucl. Phys.**A601**(1996)251.

[8] S.Saha, Y.K.Agarwal and C.V.K.Baba, Phys. Rev.**C49**(1994)2578.

[9] D.R.Napoli, A.M. Stefanini, H. Moreno Gonazalev, B. Million, G. Prete, P. Spolaore, M. Narayanasamy, Zi Chang Li, Nucl. Phys. **A559**(1993)443.

[10] A.K.Sinha, L.T.Baby, N. Badiger, J.J. Das, S.K. Hui, D.O. Kataria, R.G. Kulkarni, N. Madhavan, P.V. Madhusudhana Rao, I. Majumdar, M.C. Radhakrishna, N.V.S.V. Prasad, N.G. Puttaswamy, P.P. Shakkeeb, R. Singh, D.L. Sastry, P. Sugathan, V.Tripathi, K.M. Varier and A.M. Vinod Kumar, Journ. Phys. G. Nucl. Part. Phys. **23**(1997)1331.

[11] L.Corradi, S.J. Skorka, T. Winkelmann, K. Balog, P. Janker, H. Leitz, U. Lenz, K.E.G. Löbner, K. Rudolph, M. Steinmayer, H.G. Thies, B. Million, D.R. Napoli, A.M. Stefanini, S.Beghini, G. Montagnoli, F. Scarlassara, C. Signorini, F. Soramel, Z. Phys. **A346**(1993)217.

[12] Lagy.T.Baby, Vandana Tripathi, D.O. Kataria, J.J. Das, P. Sugathan, N. Madhavan, A.K. Sinha, M.C. Radhakrishna, N.M. Badiger, N.G. Puttaswamy, A.M. Vinod Kumar, N.V.S.V. prasad, Phys. Rev.**C56**(1997)1936.

[13] A.M.Broges, C.P. da Silva, D. Pereira, L.C. Chamon, E.S. Rossi Jr, C.E. Aguair, Phys. Rev.**C46**(1992)2360.

[14] Robert.J.Ascuitto and Earnest.A.Seglie, "Treatise on heavy ion science", **Vol.1**, (1984) 463, Plenum, Newyork.

[15] B.J. Roy, B. Srinivasan, E. Shallom, M.G. Betigeri, H.C. Jain and M.L. Jhingan, Nucl. Phys. **A588**(1995)706.

[16] K.E. Rehm, B.G. Glagola, W. Kutschera, F.L.H. Wolfs and A.H. Wuosmaa, Phys. Rev.**C47**(1993)2731.

[17] L.Corradi, S.J. Skorka, U. Lenz, K.E.G. Löbner, P.R. Pascheloti, U. Quade, K. Rudolph, W. Schomburg, M. Steinmayer, H.G. Thies, G. Montagnoli, D.R. Napoli, A.M. Stefanini, A. Tiveli, S. Beghini, F. Scarlassara, C. Signorini and F. Soramel, Z. Phys. A. Atomic Nuclei, **Vol.334**(1990)55.

[18] D.Thomasi, J.O. Fernandez Niello, A.O. machiavelli, A.J. Pacheco, J.E. Testoni, D. Abriola, O.A. Capurro, D.E. Di Greegorio, M. di Tada, C.P. Massolo and F. Penayo, Phys. Rev.**C48**(1993)2840.

[19] D.C.Biswas, R.K. Choudhary, B.K. Nayak, D.M. Nadkarni and V.S. Ramamurthy, Phys. Rev. **C56**(1997)1926.

[20] J.F.Liang, L.L. Lee,Jr., J.C. Mahon and R.J. Vojtech, Phys. Rev. **C50**(1994)1550

[21] P.J. Buttle and J.L.B.Goldfarb, Nucl. Phys. **A176**(1971)299.

[22] P.J. Siemens, J.P. Bondrof, D.B.E. Gross and F. Dickmann, Phys. Lett.**B36**(1971)24.

[23] Y.Alhassid, R.D. Levine, J.S. Karp and S.G. Steadman, Phys. Rev. **C20** (1979)1789.

[24] N.E. Switkowski, R.M. Wieland and A.Winther, Phys. Rev. Lett.**33**(1974)840.

[25] H.D. Marta, R. Donangelo, D. Thomasi, J.O. Fernandez Niello and A.J. Pacheco, Phys. Rev.**C58**(1998)601.

[26] H.D. Marta, R. Donangelo, D. Thomasi, J.O. Fernandez Niello and A.J. Pacheco, Phys. Rev. **C54**(1996)3156.

[27] C.V.K.Baba, V.M. Datar, K.E.G. Löbner, A. Navin and F.J. Schindler, Phys. Lett. **B338**(1994)3156.

[28] F.J. Schindler, C.V.K. Baba, T. Beha, S. Issmer, Th. Kerscher, H. Leitz, K.E.G. Löbner, M. Moralles, K. Rudolph, H.G. Thies and C. Zotti, Nucl. Phys. **A603** (1996)77.

[29] C.H. Dasso and S. Landowne, Comput. Phys. Comm. **46**(1987)187.

[30] L.Corradi, G. Montagnoli, D.R. Napoli, P. Spolaore, A.M. Stefanini, Xu Jincheng, S. Beghini, F. Scarlassara, G.F. Segato, F. Soramel and C. Signorini, Nucl. Instr. and Meth.**A297**(1990)461.

[31] C.N. Pass, P.M. Evans, A.E. Smith, L. Stuttge, R.R. Betts, J.S. Lilley, D.W. Banes, K.A. Connell, J. Simpson, J.R. Smith, A.N. James and B.R. Fulton, Nucl. Phys. **A. 499** (1989)173.

[32] K.E.Rehm, C.L. Jiang, J. Gehring, B. Glagola, W. Kutschera, M.D. Rhein and A.H. Wuosmaa, Nucl. Phys. **A 583**(1995)421.

[33] A.M.Stefanini, A. Tivelli, G. Montagnoli, D.R. Napoli, D. Bonamini, S. Beghini, F. Scarlassara, F. Soramel, C. Signorini, A. De Rosa, G. Inglima, M. Sandoli, G.Cardella, M. Papa and F. Rizzo, Phys. Rev.**C41**(1990)1018.

[34] D.O.Kataria, A.K. Sinha, J.J. Das, N. Madhavan, P. Sugathan, Lagy.T.Baby, I. Mazumdar, R. Singh, C.V.K. Baba, Y.K. Agarwal, A.M. Vinod Kumar and K.M. Varier, Phys. Rev. **C56**(1997)1902.

[35] M.Dasgupta, A. Navin, Y.K. Agarwal, C.V.K. Baba, H.C. Jein, M.L. Jhingan and A. Roy, Nucl. Phys. **A539**(1992)351.

[36] A.M.Vinod Kumar, K.M. Varier, N.V.S.V. Prasad, D.L. Sastry, A.K. Sinha, N. Madhavan, P. Sugathan, D.O. Kataria, J.J. Das, Phys. Rev.**C53**(1996)803.

[37] C.J.Jiang, K.E. Rehm, H. Esbensen, B. Glagola, J.P. Schiffer and A.H. Wuosmaa, Phys. Rev.**C57**(1998)2393.

[38] L.Corradi, A.M. Stefanini, C.J. Lin, S. Beghini, G. Montagnoli, F. Scarlassara, G. Pollarolo and A. Winther, Phys. Rev.**C59**(1999)261.

[39] B.J.Roy, B. Srinivasan, M.G. Betigeri, H.C. Jain and M.L. Jhingan, Nucl. Phys. **A597**(1996)151.

Chapter 4

Theoretical Aspects and Review of Gas Detectors

Nuclear radiation deposits energy in the medium through which it traverses via interaction with the medium. Energetic charged particles interact with the electrons of the atoms and molecules of the medium through Coulomb force and lose energy by excitation and ionization of the atoms of the medium continuously through a series of binary collisions. Analyzing this energy deposition is the technique of Radiation detection. Gas detectors such as Proportional counters, GM counters, Avalanche counters etc. are developed on the basis of the internal gas amplification of free charge carriers by secondary ionization process in the fill gas by the application of high electric field. In gas ionization detectors charged particles produce electron-ion pairs which form the free charge carriers. Ionization concerns total ionization and specific ionization. If N is the total number of free charge pairs produced by an incident charged particle of energy E, the average energy W required to form a free charge pairs is W = E/N which is nearly a constant for all incident particle energies and is a characteristic of the gas used. This near constancy of W makes possible an accurate measurement of energy of the incident charged particle by measuring the total ionization produced in the detector medium. For light ions W is almost constant. For heavy ions and fission fragments W shows a significant mass dependant deviation as $E = WN + E_0$ where E_0 is the mass dependant ionization defect varying from 5.7 MeV to 6.7 MeV for fragment masses in the range 100 to 140. The energy loss process is statistical in nature and hence the number of ion pairs produced by a particle of energy E shows a statistical spread around average N. For measuring particle energy the pulse height of the signal from a detector must be proportional to the ionization produced. For measuring the time signal corresponding to the instant of particle detection, the charge collection should be fast and the jitter in the time signal deduced from the output pulse should be minimum. In gas filled detectors the radiation sensitive gas volume where ionization is produced is subjected to a high electrostatic field by applying suitable voltage between the two electrodes. Depending on the function of this electrostatic field gas detectors are broadly classified into three types : (i) Ionization chambers, (ii) Proportional counters and (iii) Geiger –Muller counters. In the case of Ionization chambers, the

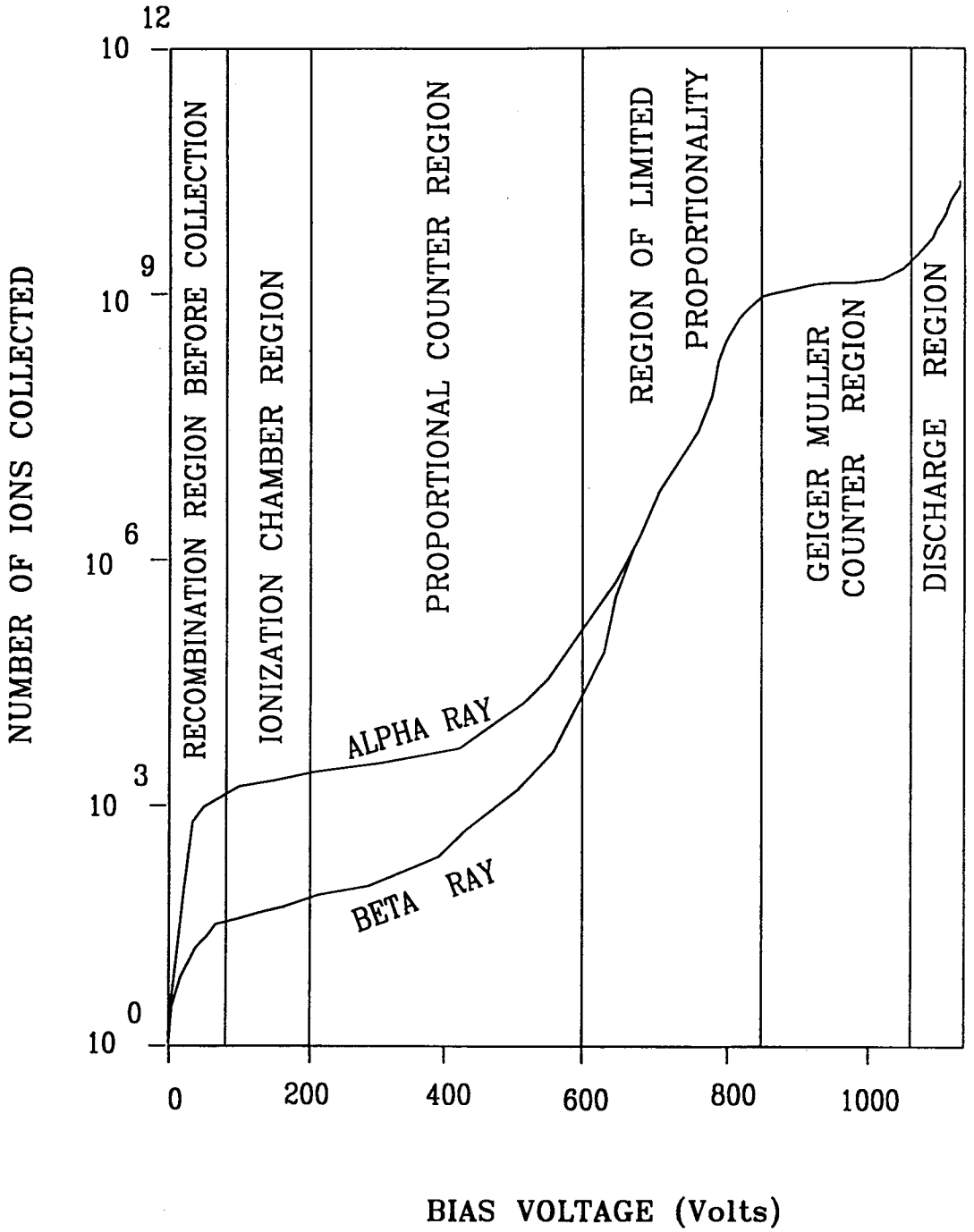

Figure : 4.1 Bias Voltage–Pulse Height (Gain) plot showing the various regions of operation of a Gas Detector

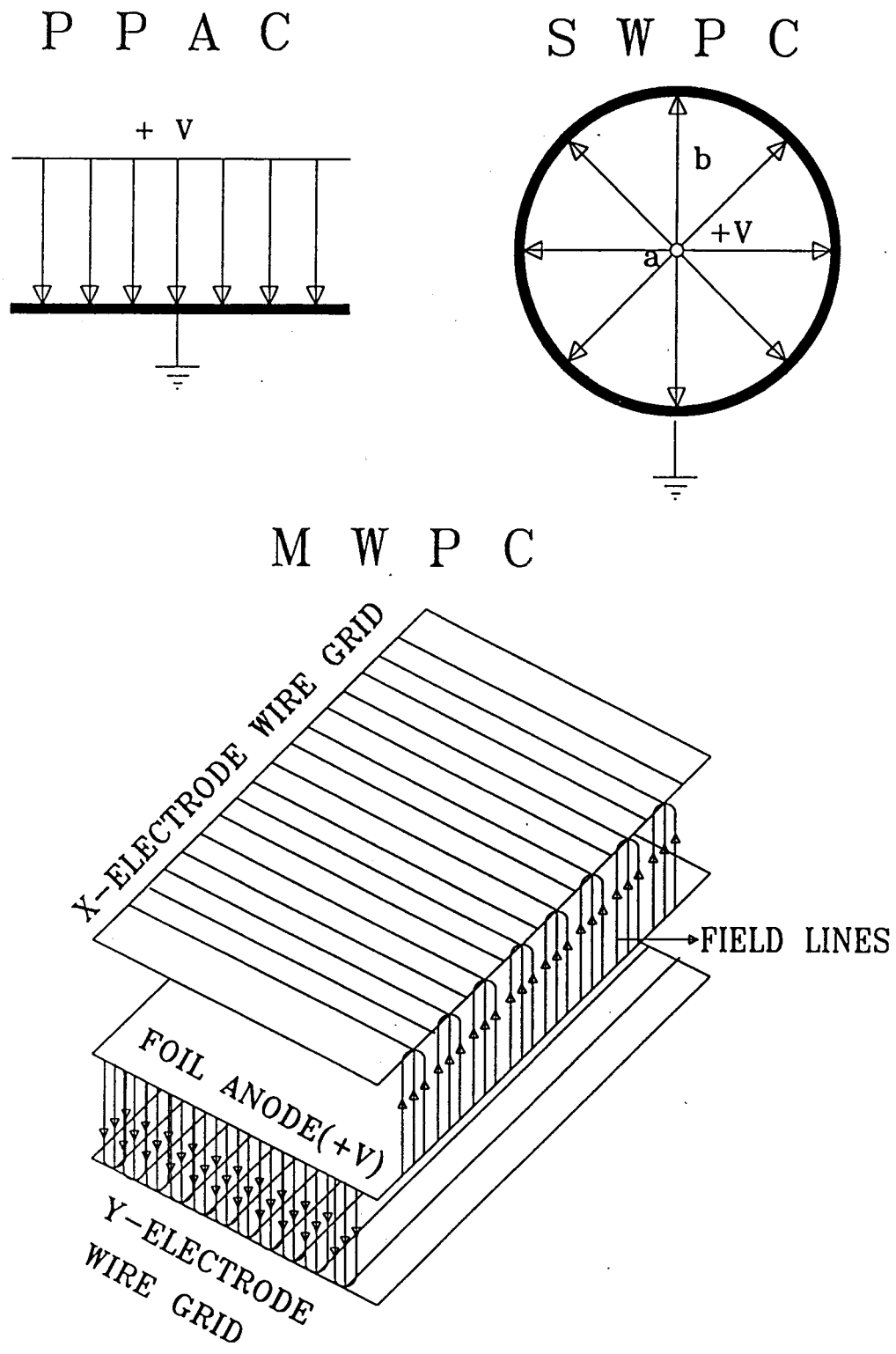

Figure : 4.2 Diagram showing the electric field of PPAC, SWPC and MWPC

function of the electrostatic field is only to collect the charges created in the process of interaction of the gas with the ionizing radiation. In Proportional counter, the applied field is high enough to produce internal multiplication of the initial ionization. Here the total number of free charge carriers generated during gas multiplication is proportional to the initial number of the free charge carriers directly created by ionizing radiation. In GM counter, the electrostatic field is higher than that in proportional counters and the number of free charges produced by internal multiplication is not proportional to the initial quantity of ionization. Thus the electrical signal of GM counter does not contain any information on the energy.

The various regions of operation of a gas detector are shown in figure 4.1. Region I is the recombination region, where the charges formed by ionization recombine due to the low electric field. Region II is the ionization region where the charges formed are collected by the electrodes and the recombination is negligibly small because of comparatively higher electric field. But this field is not sufficient to produce secondary ionization. Hence pulse height remains constant. In Region III the electric field is high and the energy gained by the electrons is large. They collide with neutral atoms and cause secondary ionization. The pulse height proportionately increases with the bias voltage and this region is called proportionality region. In Region IV the field is high and the proportionality is limited, called limited proportionality region. In region V the field is very high and the detector act as a mere counter for radiation. This region is called Geiger-Muller counter region. After GM counter region, the field is very very high (Region VI) and continuous electric discharge takes place. This region is called discharge region. Figure 4.2 show the electric field distribution for PPAC, SWPC and MWPC. The present work concerns the development of some gas detectors for detection of heavy ions. The proportionality region of the detector characteristics discussed above has been used. The major part of the work has been carried out under a research project funded by Department of Science and Technology.

4.1 Selection of Fill gases for detectors

Gas detectors can be filled with different gases. An ideal detector gas is one which can with stand high voltage at low pressure without sparking, easily ionizable, and having high electron drift velocity. Some gases which can be used in gas detectors and some of their properties are given in Table 4.1[1]

Gas and Symbol	Electron drift Velocity 'v_e' (cm/μs)	Work Function W (eV)	Electric field V/cm/torr
Neon (Ne)	---	36.2	---
Argon (Ar)	0.4	26.4	0.8
Krypton (Kr)	---	24.0	---
Xenon (Xe)	---	21.7	---
Methane (CH_4)	10	29.1	1.0
Ethylene (C_2H_4)	0.5	28.0	1.0
Isobutane (iso-C_4H_{10})	2.5	26.3	1.0
Isobutylene (iso-C_4H_8)	---	26.7	---
Heptane (C_7H_{16})	1.4	---	1.0
Carbondioxide (CO_2)	9.0	20.0	8.0
P10 (90% Ar+10% CH_4)	5.5	---	0.2

Table 4.1: Parameters of the fill gases for gas detectors

4.2 Drift Velocity and Mobility of Charge Carriers

The velocity attained by the charge carriers (ions and electrons) by the influence of the applied electric field is called drift velocity. If E is the field strength and **P** be the gas pressure, the drift velocity is given as[1]

$$V_i \propto (E/P)^n = \mu_i \times (E/P)^n \qquad (4.1)$$

where n = 0.5 to 0.8. The proportionality constant μ_i is called mobility of the ions which depends on the ion mass and nature of the gas. μ_i slightly increases with the ion mass and the molecular weight of the gas. It's value is of the order of 10^3 cm/s $(V/cm)^{-1}$.torr and charge collection time for ions is of the order of milliseconds. Electron mobility is of the order of 10^6 and collection time is of the order of microseconds. For E/P values up to 1 to 10 V/cm/torr, the electron drift velocity can be increased by adding hydrocarbons such as methane to the inert gases such as argon. A mixture of 90% argon and 10% methane is commonly used as fill gas in gas detectors which is called P10, which has high electron drift velocity for a limited E/P range.

4.3 Purity of the fill gas

Since the electron drift velocities are a few order highers than that of ions, gas detectors operate in the pulse mode by the collection of only electrons which result in fast pulses. To obtain quantitative information on the ionization produced from electron collection alone, electron loss via negative ion formation by electron attachment with neutral atom or molecule and the combination of the electrons with positive ions should be minimum. So the fill gas should be free from electronegative impurities with large cross section for electron capture to form negative ions. Examples for such impurities are O_2 , H_2O , Halogens, HCl, NH_3 etc. The presence of electronegative pollutants such as oxygen and water vapor reduces the detected pulse height because of electron capture. A 1% pollution of air in argon will remove about 33% of the migrating electrons per cm of drift due to electron capture. Since gas detectors worked on the basis of electron collection, the fill gas should have a high degree of purity. The acceleration of electrons through the counter gas results in the emission of ultra-violet(UV) photons due to atomic excitations and de-excitations. This UV rays produce photo ionization and photoelectric effect and lead to the loss of proportionality and affects the performance of the counters operating with large multiplication factor M >100. The photon induced events can be suppressed by adding photon absorbing poly atomic gas like methane. The use of gases like n-heptane , xenon, xenon + hydrogen, neon + hydrogen, argon and argon + hydrocarbon mixtures were reported by different groups [2-8]. Mixtures of noble gases with quenchers are mainly used in proportional and avalanche counters.

4.4 Proportional Counters

Proportional counters are gas filled ionization detectors operated in the proportionality region of applied voltage. In proportional counter, the number of electron-ion pairs formed during the primary ionization caused by the incident radiation is multiplied within the gas by applying high electric field. Internal amplification is of the order of 10^6. The energy threshold of proportional counter for detection of radiation above the electric noise is lower than that of semiconductor detectors. But energy resolution of proportional counters is poorer than that of semiconductor detectors. Proportional counters are widely used for detecting weakly ionizing low energy X-rays, β-rays, γ-rays, α-particles, heavy ions and for spectroscopy of neutrons.

Gaseous proportional counters are mainly of two types. Single Wire Proportional Counters (SWPC) and Multi Wire Proportional Counters (MWPC) which are used for a wide variety of applications in accelerator based research such as charged particle spectroscopy.

4.4.1 Review of Proportional Counters

The application of proportional counters in nuclear physics had been reviewed by Braid [9]. The advantages of proportional counters as focal plane detectors for nuclear spectroscopic measurements with recoil magnetic spectrographs was reviewed by Ford [10]. A detailed discussion of the theory of operation of proportional counters as well as readout techniques such as rise time method and charge division method had been reviewed. A comparative study of the position and energy resolution with the measured position and energy loss was carried out. Method of particle identification and the applications other than nuclear spectroscopy had been discussed. Kosuke and Kogeyama [11] reported about the characteristic of a single wire proportional counter with very thin rectangular cross section. They had developed a 40 x 160 x 3 mm^3 SWPC and tested with P10 gas. To avoid the effects of energy loss fluctuations and multiple scattering on position resolution due to slant (non normal) incidence of heavy ions, they have constructed this thin SWPC. They have used brass for making the SWPC and nichrome wire of 25 μm diameter as the anode. The counting rate of the detector for α-rays was 30 s^{-1} and pulses were recorded with multichannel pulse height analyzer. The detector was operated in ionization chamber region and proportionality region. The plateau characteristics and multiplication factor at different applied voltage have been measured with ^{241}Am-alpha source at 4.4 mm using P10 gas at atmospheric pressure. This gas gain was compared with that obtained by ^{55}Fe-Xray source. The pulse height spectra was measured with source at different distances from the anode wire at an applied voltage of 1000 V. This bias was chosen due to the enhancement of gas gain for α-source over X-ray source by a factor 10^3. The dependence of peak-height variation on shaping time, distance of incidence from anode wire had been studied. They also gave a simple expression for the electric field strength with distance and a formula of conformal mapping from which they have concluded that the practical limit of detector height is 5 times the thickness.

Sanada [12] investigated about the dependence of the gas multiplication factor M on the shape of the avalanche around the anode wire. They had used a collimated α-source to operate the detector from ionization region to proportionality region. From the saturated values of induced voltage on the anode wire in two regions the gas multiplication factor was determined as a ratio between induced voltages. Using polar plots and contour maps they have seen the shape of avalanche as a function of gas multiplication M. They found that between M = 10^3 and 10^4 the avalanche is heart shaped. When the growth of avalanche around the anode wire was indicated by M as a parameter, they have seen that there exists a proportionality law of discharge. In GM region the center of the avalanche distribution was found deviating to the side of α-source. Sanada et al.,[13] also made a needle counter and carried out a comparative study between their performance. Sanada [14] also studied about the growth of avalanche along the anode wire in a gas counter in the pre-Geiger region. Kataria [15] reported about the proportional counters developed at NSC. The active area of the detector was 14 x 85 mm^2 and depth 14 mm. A 10 μm anode wire was connected across the SHV connectors. Window foil is 6 μm thick mylar foil. They have tested this detector with charged particle as well as X-rays. They have used P10 gas at 101 torr pressure and tested at an anode voltage of 650 V. The energy resolution obtained for SWPC was 8%. They have obtained a position resolution of 0.8 mm using a mask with two 1 mm wide slits spaced 10 mm apart. The SWPC was tested with a ^{55}Fe X- ray source at a bias voltage 1250 V at a pressure slightly above 1 atm. The energy resolution of the detector for 5.9 keV X-ray is ~18% .

4.4.2 Theory of Proportional Counters

A physical understanding of the theory of operation of proportional counter as a position sensitive device is available in the review article by Ford [10]. He had treated the position sensitive proportional counter as a distributed RC line. If the inductance of this line is negligible a telegraph equation can be used for expressing the voltage distribution along the line as

$$d^2U/d^2x - R_0C_0dU/dt = 0 \qquad (4.2)$$

where R_0 is the resistance per unit length of the wire and C_0 is the capacitance per unit length of the detector. If L is the total length of the detector, the total resistance $R = R_0L$ and total capacitance $C = C_0L$. The above equation is identical to that of heat

diffusion along a thin rod. The solution of this equation gives the voltage as a function of space and time in response to a charge Q_0 at time t = 0 and position P.

$$U(x,p,T) = (2Q_0/C)\sum_{n=1}^{\infty} \mathrm{Sin}(n\pi x)\mathrm{Sin}(n\pi p)\exp(-n^2T) \qquad (4.3)$$

where x = X/L, p = P/L and $T = t/\pi^2RC$. The ends of the wire are held at zero potential by connecting charge sensitive preamplifiers at each end of the wire with load capacitors $C_L >> C$. The charge distribution along the wire becomes symmetric about the mid point and the charge delivered to each end of the wire is

$$Q_1(p,T) = 2Q_0/\pi \sum_{n=1}^{\infty} \{\mathrm{Sin}(n\pi p)/n\}[1- \exp(-n^2T)] \qquad (4.4)$$

$$Q_2(p,T) = -2Q_0/\pi \sum_{n=1}^{\infty} \{\mathrm{Sin}(n\pi p)\mathrm{Cos}(n\pi p)/n\}[1- \exp(-n^2T)] \qquad (4.5)$$

The position information about the point of incidence can be obtained from the above two equations for Q_1 and Q_2 . If $T \rightarrow \infty$, $Q_1 = (1 - p)Q_0$ and $Q_2 = pQ_0$. The ratio $[Q_2/Q_1+Q_2] = p/L$ is related to the initial position of incidence of the detected particle.

4.4.3 Single Wire Proportional Counter(SWPC)

The SWPC is a gas filled coaxial cylindrical cathode with a central anode wire. With reasonable applied voltages this geometry provides high electric field near the anode wire to cause gas multiplication of primary ionization. If r_a is the radius of the anode wire, r_c is the radius of the outer cylindrical cathode maintained at ground potential, V is the positive potential applied to the anode through a load resistance R (input resistance of preamplifier), E is the electric field and **P** is the pressure of the gas or gas mixture, then reduced electric field strength at radial distance r from the anode wire is given as

$$S(r) = \frac{E(r)}{P} = \frac{V}{P\, r \ln(r_c/r_a)} \qquad (4.6)$$

The electrons produced inside the sensitive volume of counter move towards the central wire colliding with the gas molecules and pickup energy from the field in between collisions. Up to radial distance r_c from the axis of the cylinder the field is sufficiently large enough to produce secondary ionization and Townsend avalanche

starts. Neglecting the effects of space charge, electron-ion recombination, electron attachment and photo electric effect at the counter wall, the average gas gain multiplication factor is defined as

$$M = \exp \int_{r_c'}^{r_a} \alpha(r)\ dr \qquad (4.7)$$

where α is the first Townsend coefficient defined as the mean number of secondary electrons produced per centimeter of its path by a free electron, $r_{c'}$ is the critical radius at which gas amplification starts and r_a is the anode radius which is the terminal point of gas amplification. Therefore

$$\ln M = \int_{r_c'}^{r_a} \alpha(r)\ dr \qquad (4.8)$$

From the above equations (4.7) and (4.8)

$$\ln M/Pr_aS_a = \int_{S_c}^{S_a} \frac{\alpha(r)}{P}\ dr \qquad (4.9)$$

where S_a and S_c are the electrical field strength per unit pressure at the surface of the anode wire and cathode respectively. α, S and **P** are related to each other in various ways according to different formulae. In equations (4.8) and (4.9), $M = n/n_0$ where n is the number of electrons or ions reaching the anode or cathode and n_0 is the number of electrons or ions produced in primary ionization. Using proper assumptions about energy distribution of electrons and about the losses of electron energy in collision with gas molecules and neglecting secondary effects accompanying the electron multiplication process, one can obtain expressions for α/P and for gas gain as $\ln M/Pr_aS_a$ after the integration of the expression(4.9)

4.4.4 Avalanche Formation

In coaxial geometry the electric field increases rapidly close to the wire. If the wire diameter is a few microns the field at vicinity will be very very high. At far distances from the anode wire electrons simply drift towards the anode and positive ions towards the cathode as shown in figure 4.3. As the electrons move closer to the anode secondary ionization starts and most of the charges produced will accumulate a few

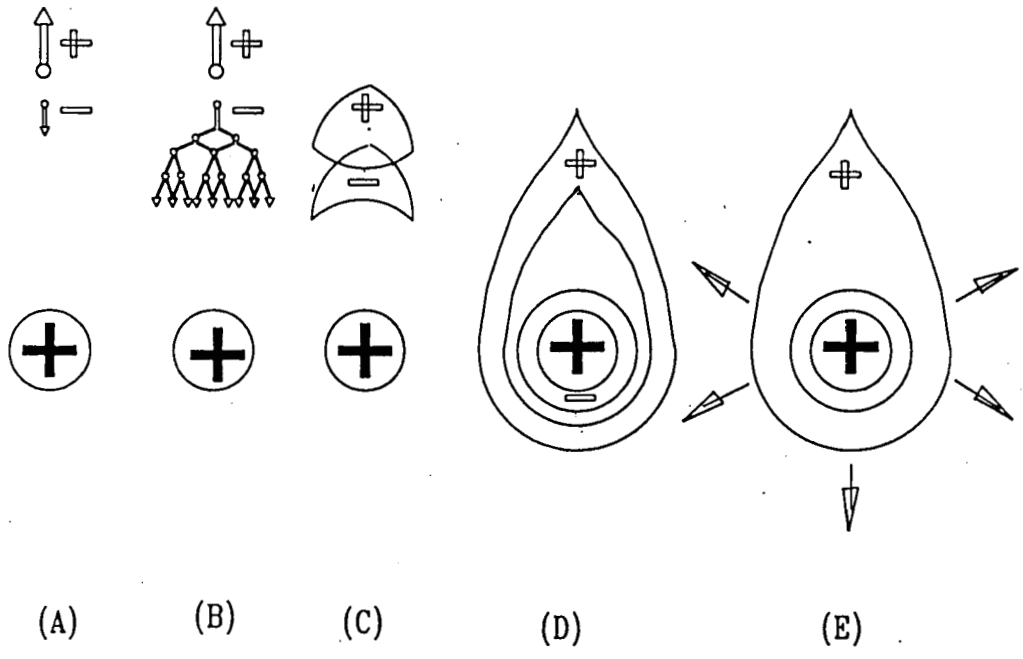

Figure : 4.3 Diagram showing the various stages of avalanche formation in the case of a Proportional Counter

microns away from the anode. The electrons are collected very quickly and contribute only about 1% to the signal. The sudden drift of the positive ions away from the anode produces the useful signal. Since the field is very high, close to the anode wire and charge multiplication takes place within a few diameters from the anode, the geometry of the detector has no considerable role in the performance. So we have constructed proportional counters with rectangular and cylindrical geometry such that any geometry can be reliable. Formation and growth of avalanche around the anode wire in gas proportional counters has been well studied by Sanada [12,14] and Sanada and Matsuda [16]. They investigated the shape of avalanche around the anode wire as a function of gas multiplication factor M. They reported that between M = 10^3 to 10^4 the avalanche is heart shaped and there exist a proportionality law of discharge. A very similar investigations were reported by Charpak et al.[17,18].

4.4.5 Time Development of Signal Pulse

The electrons produced in the primary ionization process initially drift towards the anode and later multiply on entering the avalanche region of the electric field. The contribution to the output pulse by primary ionization is negligibly small compared to the contribution MN_0 by the electron-ion pair produced in the corresponding avalanche. Since the multiplication takes place very close to the anode electrons travel only very short distance before collection and therefore their contribution to the pulse is very small. Thus voltage pulse is formed due to motion of positive ions which form a thin layer around the central anode. Assuming that the positive ion sheath does not alter the field, the voltage pulse caused by the motion of positive ions is given as

$$v^{+}(t) = - \frac{eMN_0}{C} \frac{\ln(r/a)}{\ln(b/a)} \qquad (4.10)$$

where M is the gas multiplication factor, N_0 is the number of primary ions, C is the detector capacitance, 'r' is the distance at which the pair production occurred, 'b' is the cathode radius and 'a' is the anode radius. The voltage pulse will rise to its full value at time T [1] given by the following relation where V_B is the positive potential applied to the wire **P** is the gas pressure and μ_i is the mobility of the ions.

$$T= \frac{(b^2-a^2)P\ln(b/a)}{2\mu_i V_B} = \frac{\pi\varepsilon_0 P(b^2-a^2)}{\mu_i C V_B} \qquad (4.11)$$

The electron contribution and +ve ion contribution to the signal are given as

$$v^- = [-Q/2\pi\varepsilon_0 L] \ln(a + r)/a \qquad (4.12)$$

$$v^+ = [-Q/2\pi\varepsilon_0 L] \ln b/(a + r) \qquad (4.13)$$

Here L is the length of the counter. The total maximum signal induced on the anode $v = v^+ + v^- = -Q/LC$. The ratio of the two contributions will be

$$v^-/v^+ = \frac{\ln(a+r) - \ln a}{\ln b - \ln(a + r)} \qquad (4.14)$$

The time development of the signal is given by Sauli [19] as

$$v(t) = [-Q/4\pi\varepsilon_0 L] \ln(1+ t/t_0) \qquad (4.15)$$

where Q is the total charge produced, L is the length of the counter, ε_0 is the permittivity of free space, 't' is time taken for the development of pulse. The total drift time of the ions is given as above equation (4.11). The three important factors [13] which are related to the time dependence of the voltage induced on the anode of the proportional counters with gaseous multiplication is given below :

(i) The time taken by the primary radiation to travel through the effective volume in counter.

(ii) The time required by the electrons produced by primary radiation to reach the anode.

(iii) The time for the ions produced in the avalanche to move away from the anode.

The first factor is neglected when the velocity of the primary radiation is large (i.e $>10^9$ cm/s). The second factor determine the rise time of the pulses. The third factor has been treated by Wilkinson [20] in detail for zero track length. The number of electrons per unit length along the track of the primary ionization is constant. Only a quarter of the total number of electrons produced near the anode is effective in avalanche. The remaining electrons produced near the cathode being ineffective because of the weakened electric field due to positive ion sheath around the anode.

4.4.6 Position and Energy Measurement

A proportional counter is equivalent to a distributed RC line where R is the distributed resistance of the anode wire and C is the distributed capacitance between the anode and cathode. The radiation entering the detector injects a charge impulse at the point of incidence. The amplitude and rise time of the current pulse formed at both ends of the proportional counter depend on the above position of incidence. The amplitude of the signal formed at each end depends on the current flowing to that end of the anode wire from the point of incidence. This current or the charge accumulated at each end is inversely proportional to the resistance between the point of incidence of the detected particle and the end of the wire. The ratio of these signals at both ends can be used for determining the position of incidence of radiation. This is the so called charge division method. The rise time of the current pulse formed at each end of the detector depends on the distance between the detector end and the position of incidence. When this distance increases rise time of the pulse also increases. The position information can be obtained by comparing the pulse shape or rise times of the signals from both ends of the proportional counter. This technique is called rise time method. The charge division method was first applied to proportional counters as a position measuring device by Kuhlmann et al.[21]. Earlier reports have seen about the applicability of this technique in the case of semiconductor detectors. Rise time method was first reported in the case of proportional counters by Borkowski and Kopp[22].

Gas detectors are used for measuring the position and energy of incident radiation. Position sensing detectors are called position sensitive detectors. The heavy charged particles analyzed by magnetic spectrometers (RMS) can be detected using position sensitive proportional counters (PSPC) in which a resistive wire is used as the central anode. There are two methods for position measurement. They are charge division method and rise time method. In charge division method [10,23] the signals Q_1 and Q_2 from the two ends of the resistive anode wire are fed to charge sensitive preamplifiers and the position X of the point of origin of the signal along length L of the wire is determined from the relation :

$$X = Q_2.L/(Q_1+Q_2) = (Q_2/Q_0)L \qquad (4.16)$$

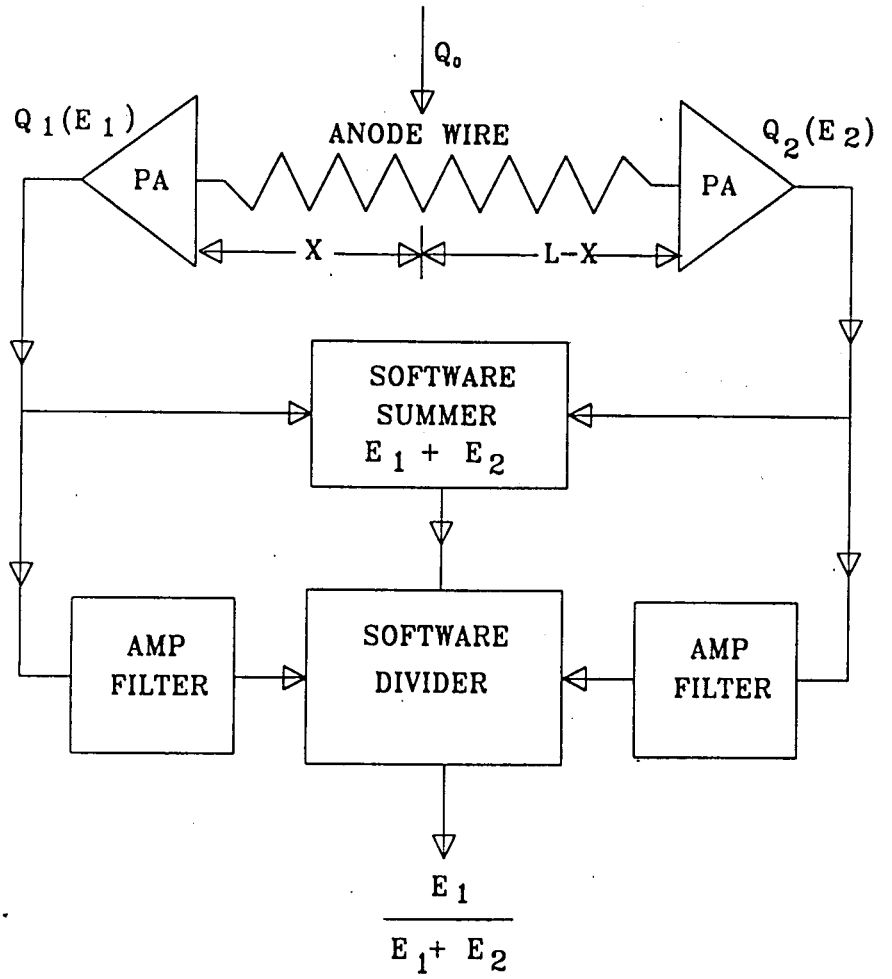

Figure : 4.4 Schematic diagram of the extraction of position information about the incident particles using proportional counter

Position can be determined manually or by using hardware or software adders and dividers. Figure 4.4 shows the method of extraction of the incident radiation energy using proportional counter. The sum $Q_0 = Q_1 + Q_2$ is proportional to the total energy loss E of the particle in the gas and can be obtained from the sum of the outputs of the two charge sensitive preamplifiers connected at the two ends of the anode wire. The signal induced at the cathode foil in the case of proportional counter with foil cathode can also serve the same purpose as reported by Ford [10] and Ford et al.,[23]. In rise time method [22,24], the difference in rise times of the pulses appearing at the two ends of the anode wire is determined by forming a bipolar pulse and the zero crossing time of the polar pulse is used to measure the rise times. The sensitivity of this method is given by the product RC_T where R is the wire resistance per unit length and C_T is the total system capacitance. Rise time readout scheme is described in [22,23,25]. The two readout methods are compared in [26,27]. Position sensitivity and accuracy in measurement using the above two methods is well studied by various groups [2-4, 28].The various techniques for making a proportional counter position sensitive is described in reference [10]. The charge induced in the wire will undergo resistive division as in figure 4.4. For a charge Q_0 produced at a distance X from one end of the wire of length L, the signal obtained at two ends is given as

$$Q_1 \propto E_1 = (Q_0/C)[(L-X)/L] \tag{4.17}$$

$$Q_2 \propto E_2 = (Q_0/C)X/L \tag{4.18}$$

where C is the detector capacitance. The total energy of the incident particle is

$$E = E_1 + E_2 = Q/C \tag{4.19}$$

and position of the incident radiation is

$$P = E_1/(E_1 + E_2) = (L-X)/L \tag{4.20}$$

The dependence on C can be eliminated using charge sensitive preamplifiers to extract the signal.

4.4.7 Position Resolution

Position resolution is the most important characteristic of detectors used in conjunction with recoil mass spectrographs. Various effects which contribute to the finite resolution are (i) thermal noise (ii) multiple scattering and (iii) energy loss fluctuations. By choosing the amplifier parameters and RC line the preamplifier noise can be reduced. The pick up and ground loop problems due to the large separation between spectrograph and counting room cause large thermal noise besides the noise due to detector itself. Such noise and pickup problems can be eliminated by proper grounding of the detector using shunt capacitance. The relative spatial uncertainty due to thermal noise is given as

$$\Delta L/L \approx 2.34\,(C_{GT}/Q)\,(kT/C)^{1/2} \qquad (4.21)$$

where $C_{GT} = C + 2C_L$, $C = C_0L$, Q is the total charge generated in the avalanche, k is the Boltzmann's constant and T is the absolute temperature. Multiple scattering in the entrance foil of the counter leads to a spread in the position resolution. For particles normally incident to the detector

$$\Delta X_{\perp}|_{MS} = d \tan \theta_{MS} \qquad (4.22)$$

where d is the detector depth and θ_{MS} is the angle due to multiple scattering. If the angle of incidence is δ

$$\Delta X|_{MS} = d \tan \theta_{MS}/\sin^2\delta \qquad (4.23)$$

The energy loss fluctuations can seriously affect the position resolution for normal incidence of the particle on detector. The energy loss fluctuations for heavy ions can be represented by a Gaussian distribution. The position is determined by the centroid of the charge distribution of ionization produced as the incident particle losses energy within the counter. If ΔE is the energy loss and δE is the energy straggling, line broadening is given as

$$\Delta X|_{EL} = (d/\sqrt{12})\,\delta E \cot\delta / \Delta E \qquad (4.24)$$

4.4.8 Energy Resolution

If H_0 is the peak centroid of the energy spectrum, then the energy resolution is defined as $R = FWHM/H_0$. If N is the total number of charge carriers developed then $H_0 = KN$ and $FWHM = 2.35\sigma = 2.35K\sqrt{N}$ where σ is the standard deviation of the peak in pulse height spectrum. The variance is given as

$$\sigma^2 = \sum_{j=1}^{n} 1/n[\,(Y_j - \bar{Y}_j)^2] \qquad (4.25)$$

where Y_j is the measured value of $\ln M/Pr_aS_a$ and $\bar{Y}_j$ is the calculated value using L and $G = \ln[(1-m)V_i]$ with $V_i = L/K$. Thermal noise, fluctuations in the number of primary ions produced, energy loss in nuclear collision which leading to ionization etc. are not contributing to energy loss (ΔE) resolution. But straggling in the energy loss of the particle, multiple scattering and the resulting variations in the path length in the detector gas causes charge state fluctuations and hence affect energy resolution.

4.4.9 Advantages of SWPC

SWPC is easy to construct and to make position sensitive and require only simple electronics for testing. Choosing suitable gas pressure and bias voltage SWPC can be used for the detection of light and heavy charged particles, X-rays, γ-rays, etc. SWPC can be used in combination with other detectors as detector telescopes which can be used for TOF measurements over long flight paths, for example within recoil mass spectrometers etc. The important advantages of SWPC [10] over the old conventional detectors such as nuclear emulsion plates are the following :

1) Good back ground suppression allowing the observation of very weak interaction process

2) Simultaneous accumulation of adequate statistics for both weak and strong particle groups. But plates require two different exposures.

3) Feasibility of measuring the particle trajectories at the focal plane in order to utilize the full solid angle of the spectrograph, while applying kinematic corrections for different particle groups.

4) Feasibility of coincidence experiments

5) Feasibility of particle identification

6) On line monitoring and modification of the experiment is possible.

7) Immediate access to the data (Emulsions require weeks to read)

8) Sufficient length to cover almost all of the focal plane permits the measurement of a large interval in excitation energy.

4.5 Multi Wire Proportional Counter(MWPC)

Multi Wire Proportional Counter is used for the position localization of ionizing particles in high energy (particle) physics and recently in heavy ion physics. MWPC was first developed by Charpak[17]. MWPC normally developed in the geometry of Foil-Grid-Foil or Grid-Foil-Grid. The central electrode will act as the anode. Wires used are made of Gold Plated Tungston (GPT) or Molybdenum of diameter 10 to 20 μm. The wire spacing will be 1 to 2 mm and inter electrode spacing is of a few mm. The electrons of primary ionization drift towards the closest wire and get multiplied in the vicinity, and induce a signal in that wire. From the signals from X-Y wire electrodes the position of the incident radiation can be extracted. MWPC is well studied in literature [17,18,24,27,29,30]. In heavy ion physics MWPC is operated at low pressure of a few torrs [19,31-38], so as to reduce the window thickness and therefore the energy loss and straggling of the heavy ions in the entrance foil. But in high energy physics MWPC is widely used which operates normally at atmospheric gas pressure. The important features of MWPC such as very good time resolution, good position accuracy, self triggered operation and fast response made it highly useful in high energy studies as well as in X-ray and heavy ion astronomy, nuclear medicine and protein crystallography.

In MWPC operation each wire acts as an independent counter and negative signal spreading on wires due to large capacitive coupling can be compensated by the positive ion induced signal in all electrodes. This merit was recognized by Charpak and collaborators. When the ionizing radiation passes through the MWPC +ve ions and –ve electrons are produced. The electrons drift along the field lines and reaches the high field region very close to the +ve electrode where the avalanche multiplication occurs. The signal then appears only on one wire. The event can be automatically localized in the dimension perpendicular to the wires. Using X-Y electrodes a two-dimensional localization can be possible. The wires of X-Y planes near the event carry large induced charge which give signals corresponding to the position of incidence.

4.5.1 Theory of MWPC

The expression for the capacitance per unit length of MWPC is [19]

$$C = 2\pi\varepsilon_0/ [\pi d/s - \ln(2\pi a/s)] \quad (4.26)$$

where 'a' is the electrode wire radius, 's' is the gap between adjacent wires and 'd' is the gap between foil electrode and wire plane. The electric field of the MWPC at a point (x,y) is given as

$$E(x,y) = (CV_0/2\varepsilon_0 s)[1+t_g^2\pi x/s + t_g h^2\pi y/s]^{1/2}[t_g^2\pi x/s + t_g h^2\pi y/s] \quad (4.27)$$

Along the symmetry lines x = 0, y = 0 and the electric field becomes

$$E_y = E(0,y) = (CV_0/2\varepsilon_0 s) \coth(\pi y/s) \quad (4.28)$$

$$E_x = E(x,0) = (CV_0/2\varepsilon_0 s) \coth(\pi x/s) \quad (4.29)$$

The gain M depends exponentially on the charge per unit length of the wire $Q = CV_0$

$$M = K\exp(CV_0) = K\exp Q \quad (4.30)$$

Differentiating this expression

$$\Delta M/M = \ln M(\Delta Q/Q) \quad (4.31)$$

That is the gain variation depends on the charge variation on wires. Here

$$\Delta Q/Q = (C/2\varepsilon_0)(\Delta a/a) = (C/2\varepsilon_0 s)(\Delta\ell/\ell) \quad (4.32)$$

The electrostatic force between two wires of equal linear charges CV_0 at a distance 'r' per unit length is

$$F(r) = (CV_0)^2/2\pi\varepsilon_0 r \quad (4.33)$$

By equating the electrostatic deflecting force and the restoring force due to tension on the wire and by applying boundary conditions on the solution of this equation the required tension on the wires can be obtained as $T = (CV_0 L)^2/4\pi\varepsilon_0 s^2$. The field at the foil electrode (cathode)

$$E_s = E_y/2 = CV_0/4\pi\varepsilon_0 s \quad (4.34)$$

For a given maximum tension T_M corresponding to the elastic modulus of the material of the wire, the critical stability length is given as $L_C = S\sqrt{(4\pi\varepsilon_0 T_M)}/CV_0$. The electrostatic pressure on the foil electrode $P = C^2V_0^2/8\varepsilon_0 S^2$. The maximum inward deflection of the above foil electrode of area A^2 stretched with a linear tension T at a gas pressure **P** is given as $\Delta y = PA^2/8T$. When an avalanche occurs in a MWPC, the motion of the +ve ions away from an active wire causes a negative signal to appear on that wire and causes a +ve signal to appear on the neighbouring wires. It is easy to identify the signal from an active single wire. In a digital readout scheme the anodes are connected to separate amplifiers and trigger circuits which generate the logic signals for fast (< 1 μs) readout of addresses via diode matrices. Analog read out were used with anode wires or cathode strips by connecting taps of a resistor chain or delay line in the case of slant incidence applications. This improves resolution and offers simplicity.

4.5.2 Review of MWPC Works

The application of MWPC for nuclear physics studies was introduced by Charpak [17]. Later Charpak and Sauli [35] carried out a lot of works and modifications on the design and development of MWPC. A 40 mm x 40 mm MWPC was developed by Breskin [36] which gave a time resolution of 0.8 ns FWHM when tested with 5.5 MeV alpha source and ethylene gas at 5 torr. A review article on MWPC was reported by Ball [37]. In that report MWPCs developed at Munich and Chalk River had been reviewed. Munich MWPC was developed by Glässel , which is having a length 2 m, wire spacing 0.5 mm and wire diameter 20 μm. The conditioning of this detector was done at 2400 V after assembling and using CO_2 as fill gas. Under normal operation they have used a mixture of 75% isobutane and 25% argon. The effect of sparking at maximum voltage was reduced by applying 1% xenon. For heavy ions the ΔE signal was taken by connecting a charge sensitive preamplifier to the back cathode and Glässel found that ΔE resolution tends to a constant value of 16% FWHM, which was sufficient for Z identification of heavy ions. This detector was used for Q-value measurements. They had modified this MWPC with same geometry but using 8 μm anode wires.

The Chalk River MWPC consists of two MWPCs – one 2 mm thick front detector and a 1.6 cm thick back detector at a 6 cm maximum separation. The wire spacing for front detector was 0.56 mm and back detector was 2.3 mm. These detectors were designed to operate at 10 kPa for heavy ions and at 1 atm for light ions. They have used a winding machine for the fabrication of the wire electrodes with an error of 1%. The gas used was 10% CO_2 + 90% argon mixture. Lynen et al., [32] reported about a MWPC in which the anode wires were spanned in a diagonal direction. The cathode wire planes were mounted at 15 mm distance on both sides of the anode. Two readout planes were used at 5 mm from the anode plane on both sides. They have used Cu-Be wires of diameter 50 μm, at a spacing 2 mm. The active area of the detector was 88 x 88 cm^2 and operated with isobutylene gas at 10 torr. Becker et al.,[39] obtained a resolution of 0.5 to 1.5 mm for MWPC using a resistor chain connected to the anode wires and using a charge division readout . The wire spacing in this case was 2.5 mm. Beardsworth et al., [40] obtained a position resolution of 0.2 mm with ^{16}O beam at 48 MeV for their MWPC. This was a cathode strip MWPC with lumped-constant delay line readout in a Q3D magnet. Kataria et al.,[38] developed a MWPC which was using at the focal plane of HIRA. It consists of an anode sand witched between two wire plane cathodes consists of 25 μm GPT wires at 1 mm separation. The active area of this detector is 190 mm x 60 mm. The entrance window was made by 1.5 μm thick aluminised mylar foil glued on a 6 mm thick G10 frame. The window foil was supported by 70 μm tungsten wires spaced 10 mm apart vertically and horizontally. The exit window of dimension 135 mm x 35 mm was open to the ionization chamber following the MWPC. They have used this detector combination for several experimental studies of sub-barrier fusion and transfer. We have used this detector for our transfer measurements of S+Ni systems. Our aim was to develop a similar detector to be used in conjunction with the above MWPC for TOF measurements.

4.5.3 Read out systems for MWPC

The readout systems used for MWPC includes both digital and analog types. In digital readout systems, current sensitive preamplifiers are used for each anode wire and the resulting logic signals are processed in a digital manner. The main advantage of digital readout systems are the following:

1) Good position resolution which is independent of the length of the counter.

2) Good timing and high count rate capability.

3) Effective neutron and gamma suppression resulting from the coincidence requirement between adjacent wires for inclined tracks.

4) Good integral linearity and absolute position calibration-both are limited only by mechanical tolerances.

The analog read out methods are simple and low cost. The main analog methods are the following. (a)Charge division method(b)Rise-time method and (c)Delay line method. Analog read out -delay line- methods are also used for the read out from cathode strip or wires. The strip electrodes will minimize the energy loss fluctuations affecting the position resolution. Charge division method and rise time method were discussed earlier. Delay line method is discussed in the following section.

4.5.4 Delay line read out method

Position information can be obtained from MWPC by using electromagnetic delay line. Lumped constant and continuous distributed lines are both suitable. In lumped constant case the junctions between the segments of the line are connected to antenna electrodes. The time delay between the signals reaching the two ends of the line is the basis of position determination. The total delay should not be much less than 1 μs, due to the rise time of the counter being of the order of 10^{-7} s. In continuous distributed line case, a single wire is wound in the form of a helix. The length delay time (1 μs) times the velocity of light would be of the order of 300 m if there is no magnetic or dielectric substance is present nearby the length of the delay line. The turn spacing can be 0.5 mm. since the helix lines are bulky, flattened helices are used for geometrical convenience. The delay line signals are usually processed through amplifiers, constant fraction timing discriminators and time to amplitude converters (TAC). Pulse transformers can be used to match the delay line to output cables connected to remote amplifiers. Since the position of the event is given directly by the

output of a single TAC, only one ADC is required per line and a minimum computer time is required to process the event. Kataria et al., [38] reported about using delay line read out for MWPC. They have used chips from Peizoelectric -model PE21173, having nine taps and 40 ns delay per chip, for taking the position information. Each wire of the X-electrode was connected to the tap of delay line. A double sided PCB with plated through the holes had been used to accommodate the high density of lines. This was essential for minimizing differential non linearity and to achieve better than 1 mm position resolution. Since Y-resolution was not so important, they have interconnected three wires together and then connected to delay line tap. Signals could be taken from the two ends of the delay line chains. 100 Ω resistances were connected between the ground and two ends of the chain for impedance matching.

4.5.5 Applications of MWPC

It is used in astrophysics for detecting the air showers produced by cosmic ray high energy photons in the upper atmosphere. It is also used in medicine and biology. The regional up take of sugars in the heart under different stimulation conditions can be studied by recording the β-activity distribution using MWPC. It is used for clinical measurement of bone mineral content in peripheral skeleton by taking the single photon absorption (SPA) transmission images using radioactive X-ray sources such as ^{125}I(27.4 keV) and ^{153}Gd(42 keV). In nuclear physics it is used for detecting the transfer, fusion and fusion-fission products. MWPC is used for detecting the radiation sensitive areas of human body and in solid state physics for X-ray diffraction studies.

4.6 Avalanche Counters

The operational principle of an avalanche counter is based up on the primary ionization and the rapid amplification of charge carriers in the detector gas under the action of more or less homogeneous but strong electric field. The avalanche counter is operated with a high field near the break down and neglecting the secondary process.

4.6.1 General Features of avalanche counters

i) No serious problem of radiation damage when used for detecting heavy charged particles, unlike semiconductor detectors.

ii) Geometrical dimensions can vary within broad limits

iii) Convenient tool in heavy ion physics for detecting high intensities of efficient radiation from heavy ion accelerators.

iv) Works quickly

4.6.2 Parallel Plate Avalanche Counters (PPAC)

The traditional gaseous PPAC detectors are reliable, relatively cheap and easy to construct and operate. The readout of this detectors is well developed. PPAC is single gap gaseous detector with parallel plane electrodes possessing the following basic features. The gap between the electrodes is narrow and the uniform electric field is large enough to give rise to the Townsend avalanche multiplication of primary ionization at any point of the gas volume. A moderate gas gain of 10^3 to 10^4 may be obtained without considerable spark discharges. The detected signals in a PPAC depends on the distance of primary ionization from the anode. There is a finite probability for a minimum ionizing particle to pass through the chamber gap without any interaction in the gas medium. If the ion pairs are created near the collecting electrode the avalanche length is small and the charge collected at the anode may be below the level of detection. The gas used should not be transparent to UV light to avoid the photo absorption at the cathode resulting in secondary avalanche. Pure isobutane has high absorptive power for light, large dE/dx and high efficiency for relativistic particles. The following are the basic features :

i) Counting rate capability up to $10^7/cm^2/sec$.

ii) Very fast response for timing measurement applications.

iii) Excellent time resolution of a few nanoseconds.

iv) Good position, energy and mass resolution.

v) Very inexpensive (low cost per surface unit).

vi) Radiation resistance 100 times higher than the conventional detectors and radiation damage is negligible compared to solid state detectors.

vii) Large solid angle.

viii) High efficiency.

ix) Easy to handle.

x) Negligible background sensitivity.

4.6.3 Various Aspects of PPAC

A PPAC operates in the proportionality region and serves as an excellent timing detector for heavy ionizing particles. It consists of two parallel electrodes separated by an insulating material of 1 to 2 mm thickness. If two electrodes are made of metallised foils (eg:alumnised mylar), it is called transmission type. Another type-stop type- in which only one electrode is made of metallised foil and other electrode is thick enough to stop the radiation. The anode foil is given a high voltage while cathode is grounded through a resistance in the amplifying circuit. The counter can be filled with a hydrocarbon gas like isobutane or P10 at a reduced pressure of 5 to 30 torr. At moderate applied voltage, large E/**P** values can be achieved. The primary electrons generated by the ionizing particle drift towards the anode and gas multiplication takes place along the path. A multiplication factor of 5000 can be obtained at E/**P** value of 500 V/cm/torr. For a primary electron the final number of secondary electrons produced in a distance 'x' is given by $\exp(\alpha x)$. Thus bulk of electrons are generated in a distance $1/\alpha$ in front of the anode. The rise time 't_e' of the electronic component of the signal can therefore be approximately written as

$$t_e = (1/\alpha)/v_e \qquad (4.35)$$

where v_e is the drift velocity. For v_e=5 cm/μs and α =100 cm^{-1} the value of t_e = 2 ns. So very fast timing measurement can be carried out using the fast electronic component of the pulse height. The component of the signal due to the motion of the ions will be slow but larger in magnitude by αd than the electronic component. This is because the electrons travel only a distance $1/\alpha$ while the ions move nearly the total gap distance 'd' before collision. The fast component of the output signal from PPAC are typically a few mV and are amplified with a fast amplifier for further processing by CFD. PPAC for various dimensions for heavy ion timing purpose have been constructed and operated by various authors [41-45,60-62]. Stelzer [44] had constructed and operated PPACs of active area up to 550 cm^2. He found that for a counter of 50 cm^2 area and 1 mm inter

electrode gap, a time resolution of 160 ps was obtained with ^{16}O ions at 10 torr isobutane gas. The electrode foils were 2.5 mil hostaphan evaporated with conductive gold layer of thickness 30 μgm/cm ^{2} and resistance 1 Ω/cm ^{2}. The foils were glued with epoxy on to the frames of plexy glass. Pure hydrocarbons, butane, pentane etc. were found as best suited fill gases. P10 gas is not so suited for using in PPAC. Even though a detailed discussion on the review of PPAC as a separate section is not given, Table 4.2 shows the review of the development and testing of PPACs by various groups. Here 'A' is the active area of the detector, 'd'is the inter electrode spacing 'V' is the bias voltage and **P** is the gas pressure.

Authors	Area(A)	Electrode Spacing(d)	Bias Voltage (Vvolts)	Gas Pressure **P** torr	Source used for testing	Reference
Stelzer	2 x 26 cm^2 24x23 cm^2	1mm,2 mm 4 mm	300 to 600	8 to15	^{241}Am, ^{16}O ^{40}Ar, ^{132}Xe	[44]
Harrach et al.	24 x 26 cm^2 1x1 m^2	1 mm	upto 650	3 to 20	α, ^{16}O ^{208}Pb	[45]
Breskin et al.	15 cm^2 40 x 40 mm^2		upto1500	10 to 60	p,α, ^{16}O	[42]
Gaukler et al.		1 mm	450	5	^{20}Ne	[46]
Jan Sernicki	354 x 22 mm^2 80cm^2	1 to 4 mm	400 to 1300	5 to 30	^{241}Am	[60-62]

Table 4.2 : Review of PPAC studies

4.6.4 Position Measurement

A PPAC can be used for position sensitivity by placing a wire grid between the anode and cathode foil, by applying half the cathode potential to the grid. This assembly will work as a normal PPAC and charge induced on the grid wire which is in the avalanche region can be read by charge division method or delay line technique [45] for extracting the position information. Fast signals are induced on the foil electrodes and

nearest sense wires by the avalanche from primary ionization, which can be used for timing measurements. The position information can be obtained from the arrival time of the signal at either end with respect to this fast trigger signal from the foil electrode. By keeping the signal rise times larger than discrete delay between sense wires the position information can be derived. Harrach and Specht [45] reported about the development of a 2D X-Y position sensitive PPAC which was used for heavy ion reaction studies. In a normal PPAC the electrodes uniformly spaced apart and the electric field is uniform. The pulse height of the output signal which depends on the reduced electric field strength S=V/**P**d is therefore constant and is independent on the position of incidence of heavy ions. The usual method to derive the position information is by using a wire plane as one of the electrode to obtain position by resistive charge division method or delay line readout method.

4.6.5 Principle of PPAC

A PPAC operates on the basis of the principle of non self sustaining discharge through the fill gas. In this operation the external factors or internal mechanisms fail to keep up in the generation of new electrons needed for the regeneration of +ve ions and electrons. In a uniform high electric field the multiplication process of charge carriers occur in the gap due to the primary electrons created by external factors according to the following relation

$$n = n_0 \exp\left[\int_0^x \alpha(x)\, dx\right] = n_0 \exp(\alpha x) \qquad (4.36)$$

where n is the number of secondary electrons, n_0 is the number of primary electrons, x is the migration path and α is the first Townsend Coefficient. If **P** is the gas pressure, E is the applied electric field between the anode and cathode, A and B are the specific constants of the fill gas

$$\alpha/\mathbf{P} = A \exp(-B\mathbf{P}/E) \qquad (4.37)$$

The discharge can be self sustained (maintained) if the ions generated in the gap are given a chance to expel at least one electron from the cathode. The condition for self sustained discharge under uniform electric field is

$$\gamma[\exp(\alpha d) - 1] \geq 1 \qquad (4.38)$$

where γ is the second Townsend Coefficient and d is the spacing between electrodes. For a given gas α and γ are functions of reduced electric field S = E/**P**. Cathode material and surface structure affects the value of γ. For a uniform field the above condition in equation (4.38) can be modified as

$$\gamma \left[\exp\left(\int_0^d \alpha(x)dx\right) - 1 \right] \geq 1 \qquad (4.39)$$

A modified Townsend theory is used for the explanation of self sustained avalanche discharge. According to this theory the ionic charge built up in successive avalanches dynamically deforms the initial distribution of the electrical field in the gap leading to a large cathode fall and apparent contraction of the gap size. The self sustaining discharge occurs at an inter electrode voltage U_B given by the following expression for the over all electrical strength of the arrangement.

$$U_B = BPd/[\ln(APd) - \ln \ln\beta] \qquad (4.40)$$

where $\beta = 1+1/\gamma$, $\gamma = F(S)$, S = E/**P** and E = V/d. U_B is affected by the following factors.

1) Mechanical imperfections of the electrodes.

2) Deformation of electrode geometry due to electrostatic forces.

3) Effect of electrode material on the gas discharge growth.

4) Effect of local space charge on the electron multiplication in primary avalanche.

5) Dependence of ionic space charge on the counting rate.

4.6.6 Signal Formation

The development of PPAC signal and pulse shape is determined by the motion of both electrons and ions. After the passing of a highly ionizing charged particle, avalanche multiplication occurs for a few nanoseconds and the electrons drift towards the anode and positive ions towards the cathode. The electronic component of the signal is very fast because of the high electron drift velocity in the strong electric field and narrow gap. Fast potential change at the anode causes the production of the signal.

4.6.7 Time Resolution

Time resolution of PPAC is well known and similar to that of a spark chamber. Time resolution (Δt) can be measured by observing the delay between pulses from two counters by means of a time-to-amplitude converter (TAC). PPAC with time resolution greater than 500 ps can be used with multi parameter systems to detect charged particles, heavy ions and fission fragments, for precise timing measurements in heavy ion physics.

4.6.8 Applications of PPAC

PPAC with elongated electrodes can be used for analyzing nuclear reaction products separated by magnetic spectrographs. Large improvement in pulse height (energy) resolution may be helpful for particle identification. PPAC can be used for TOF measurements of fission fragments for analyzing photo-fission and electro fission cross sections and also in α-particle spectroscopy.

4.7 Gas Amplification

The mechanism of gas amplification in proportional counter has been studied theoretically by several authors using different formulae which can fit with experimental data [47-55]. Zastawny [52]proposed that there are five distinct regions in each of which α/P has a different dependence on E/P. Various authors have derived different expressions for the dependence of gas amplification factor as a function of the applied potential (V), fill gas pressure (P) and the geometrical parameters of the detector. The earliest expressions of Rose-Korff [48] and Khristov [53] was modified by Curran-Craggs [5]. To minimize the effect of space charge resulting from positive ions created in the initial ionization track one has to use the correct analytical expression for M. In theoretical studies of the physical phenomena involved in proportional counter it is necessary to know the expressions for α/P and for gas gain as a function the reduced field strength S_a and of the nature of the fill gas. These gas gain formulae were derived independently by various authors assuming the forms for α/P as a function of $S = E/P$ and there is no relation between the formulae.

4.7.1 Townsend Avalanche

If E/P is sufficiently large electrons will attain enough kinetic energy from the electric field, between successive collisions and cause secondary ionization of the gas molecules by collision. This results in the production of a large number of electron-ion pairs and hence the name gas amplification. The gas multiplication can be characterised by the quantity α which is the reciprocal of the mean free path for secondary ionization. This quantity α is called the First Townsend Coefficient which represents the average number of electron-ion pairs formed per unit path length due to motion of an electron along the direction of the electric field. The gas multiplication factor M of primary ionization caused by the motion of electrons in the electric field from r_1 to r_2 can be given by an equation similar to equation (4.7) where α, the ionization number per unit path length is an important parameter determining the overall performance of the gas detectors operated under gas amplification. Gas multiplication is made use of in proportional and GM counters. The field strength required for causing secondary ionization has a typical value of about 10^6 V/m. The primary electrons and secondary electrons drift towards the anode and are accelerated by the electric field between consecutive collisions with neutral gas molecules. This causes additional ionization and in this way secondary multiplication process takes the form of a cascade known as "Townsend Avalanche".

4.7. 2 Relation between Pulse height and Gas multiplication

The output pulse height 'h' from a gas detector is related to gas amplification M by the relation : $\ln M = \ln(h/fP)$ (4.41)

where 'f ' is the overall gain factor.

$f = (ge/C)(K/W)$

g = the net gain of the electronics used for detector pulse processing

e = electronic charge

C = detector capacitance

K = a factor such that KP gives the energy deposited by the incident ion within the active volume of the detector

W = work function or average energy required for the production of one electron-ion pair in the gas used

P = the gas pressure

Authors	α/P	Reference
Rose and Korff	$(C_1/2)\, S^{1/2}$	[48]
Khristov	C_2	[53]
Diethorn	$D\, S$	[51]
Williams and Sara (Townsend)	$A \exp(-B/S)$	[8]
Ward and Charles	$C_3 \exp(-C_4 / S^{1/2})$	[54,55]
Kowalski	$C_5\, S^d$	[49,50]
Aoyama	$K\, S^m \exp(-L\, S^{m-1})$ $(0 \leq m \leq 1)$; $L/K = V_i$	[56]
Zastawny	$D'(S - S_0)$	[6,7]

Table 4. 3 : Formulae for First Townsend Coefficient

Authors	SWPC	PPAC
Rose and Korff	$-C_1/S_a^{-1/2} + K_1$	$C_1 S^{-1/2}$
Khristov	$-C_2/S_a + K_2$	C_2/S
Diethorn	$D(\ln S_a - \ln S_c)$	D
Williams and Sara (Townsend)	$(A/B)\exp(-B/S_a) + K_3$	$A\exp(-B/S)/S$
Ward and Charles	$(2C_3/C_4^2)(C_4 S_a^{-1/2}+1)\exp(-C_4 S_a^{-1/2})+K_4$	$C_3\exp(-C_4 S^{-1/2})/S$
Kowalski	$C_5/(d-1)S_a^{d-1} + K_5$	$C_5 S^{d-1}$
Aoyama	$\exp(-LS^{m-1})/[(1-m)V_i] + K_6$ $(0 \leq m \leq 1)$; $L/K = V_i$	$K\, S^{m-1}\exp(-LS^{m-1})$
Zastawny	$D'[\ln(S_a/S_o) - \ln(S_o/S_a) - 1] + K_7$	$D'(1-S_o/S)$

Table 4.4 : Expressions for $\ln M/Pr_a S_a$ for SWPC and $\ln M/PdS$ for PPAC ($M = h/fP$)

Measuring the pulse height 'h', the gas gain M at a pressure **P** can be determined if 'f' is known. Various formulae are available in the literature for the First Townsend Coefficient as a function of reduced electric field strength S = E/**P** . Each formulae is characterized by a set of parameters. The range of values of S over which these formulae are valid vary from one formula to another. Overlapping ranges of applicability also exist for some of these formulae. Some formulae are purely empirical but some are derived from models on the behaviour of electrons in an electric field using appropriate initial assumptions [50,56]. Various formulae for First Townsend Coefficient α/**P** as a function of reduced electric field S proposed by various authors and corresponding gas gain as $\ln M/\mathbf{P}r_aS_a$ for SWPC and $\ln M/\mathbf{P}dS$ for PPAC is given in table 4. 3 and table 4.4. Here **P** is the gas pressure, S_a is the reduced field at anode, r_a is the anode radius, d is the inter electrode spacing and S is reduced electric field in the case of PPAC. C_1, C_2 etc. are specific constants which are functions of the microscopic parameters of the fill gases. These constants have to be determined from the measurement of gas amplification factor M by the least square analysis of the data which can be fitted by straight lines according to various expressions for gas gain. The gas gain formula proposed by Aoyama [56] is a generallised one. The other formulae can be derived as a special case of Aoyama formula such as m = 0 gives Williams and Sara's formula [8], m = 1 gives Diethorn's formula [51] and m = ½ gives a product of forms proposed by Rose and Korff [48] and by Charles [55]. The Zastawny [52] form is derivable as another special case. With L = 0 Kowalski[49] form and with L = 0, m = 0 Khristov's [53] form can be obtained. In the Aoyama expression the ratio L/K = V_i has the significance of an effective ionization potential.

4.7.3 Controversy about the applicability of various gas gain formulae

Extensive measurements of gas gain (amplification) factor have been carried out by several groups of researchers using various counters with variety of gases and gas mixtures at different pressures. The predictions of the various theoretical expressions of M given in table 4.4 have been compared with experimental results[1]. Depending on the values of S and **P** some of these expressions would be found fitting the experimental

data. There is some controversy about the applicability of different gas gain formulae. Experimental verification of these formulae are usually made at large values of M (10^2 to 10^5) and over small ranges of S using argon based mixtures or pure gases. Kowalski [49] found that the two parameter formula for gas gain can not be used over the whole range of gas gain and S_a over which measurements were made. But the formula proposed by Kowalski [57] can be used for majority of gases in proportional counters, which is best suited for the two parameter dependence on gas gain. Different authors make various assumptions about the energy distribution of the electrons and about the electron energy losses in knocking collisions with gas molecules. All the above mentioned formulae were derived under the assumption of neglecting the space-charge effects, recombination of electron-ion pairs and the photoelectric effect at the cathode and in the gas.

Kocharov and Korolev [58] found that the Diethorn, Curran-Craggs and Khristov formula for gas gain are satisfactory. But Zastawny [6,7,52] claimed that Diethorn, Khristov and Rose-Korff formulae are unsuccessful. Kiser [59] suggested that Diethorn formula is not suited for all gas mixtures. There is a general agreement that Williams-Sara formula in unsuitable, but Zastawny formula is most suitable. Kowalski [57] found that best agreement between theory and experiment exist for the Zastawny and Diethorn formulae. The various gas gain formulae have been derived independently by each author assuming the forms for $\alpha/\mathbf{P}$ as a function of S = E/P and there is no inter connecting relation between these formulae. The formulae of Rose-Korff [48], Williams-Sara [8] and Zastawny [52] were derived from the models on the behaviour of electrons in an electric field. But Diethorn [51] and Charles [55] formulae were derived only by assuming analytical forms for $\alpha/\mathbf{P}$, without any theoretical consideration. There fore these relations for gas gain can not be considered as universally valid.

4.7.4 Review of experimental verification of gas gain

The detectors such as PPAC, SWPC and MWPC are the main detectors used for gas amplification because their operating voltages and gas pressure correspond to proportional gas amplification region where the net number of ion pairs produced is proportional to the energy deposited in the gas volume by the incident ion. Not many works have been reported in the experimental area to verify various gas gain formula

and to determine the relevant parameters. Early measurements refer to relatively low values of S. Jan sernicki [60-62] and Brunner [63] extended these works for S values ranging from 173.5 to 940 V/cm/torr for n-heptane gas. Later investigations attempted to test the validity of various gas gain formulae and to determine the parameters used in this formula. Charles [55] reported that errors were caused during the measurement of pulse heights for the determination of gas gain. These errors were in the resultant gas gain values and were caused by the difference in rise times between pulses from the counter and pulse generator if calibration for the pulse heights was not taken in to account. He also pointed out that the experimental gas gain values which had been measured by Rose-Korff [48], Diethorn [51], and Williams-Sara [8] had poor reliability. It is necessary for the determination of gas gain that the pulse heights should be linear for different energies of incident radiation. The gain should not be saturated for larger pulses. Aoyama [56] proposed and experimentally verified the gas gain data obtained by Charles [55] and Hendricks [64] for the gases P10 and a mixture of Xe + 5% CO_2.

4.8 First Townsend Coefficient

The gas multiplication or amplification M responsible for the pulse formation in a gas counter operating in the avalanche region can be represented by the expression

$$M = n/n_0 = \exp \int_{r_1}^{r_2} \alpha \, dr \qquad (4.42)$$

or

$$\ln M = \int_{r_1}^{r_2} \alpha \, dr \qquad (4.43)$$

where 'n' is the number of secondary electrons produced by 'n_0' number of primary ions or electrons. For parallel plate avalanche counters M can be expressed as M = exp(αd). Here 'd' is the path length in the field direction and 'α' is the ionization number per unit path length called the first Townsend Coefficient. The essential features of avalanche counters such as pulse heights, their sensitivities to pressure and field variations are characterized by 'α' as a function of the reduced field strength (S = E/**P**). Even though there are various functions used in literature for representing the variation of 'α' with reduced field S, the relation proposed by Townsend is more popular, which is expressed as

$$\alpha/\mathbf{P} = A \exp[-B/(E/\mathbf{P})] \quad (4.44)$$

where A and B are two constant parameters related to the pressure, voltage and dimensions of the avalanche counters. For PPAC the electric field is uniform as shown in figure 4.2 and there fore the integration in equation (4.42) is simple and straight forward. Brunner reported that this technique has been used for determining A and B and hence the coefficient 'α' using PPAC geometry. This was done by measuring the current produced in the PPAC at various E/**P** values using a sensitive picoammeter. If i_0 is the current with n_0 primary electrons without amplification in the uniform electric field and 'i' is the current due to 'n' secondary electrons at distance L under avalanche conditions, the gas multiplication factor M is given as $n/n_0 = i/i_0 = \exp(\alpha L)$. Brunner used the following relation for αL in PPAC method.

$$\alpha L = (\partial n/\partial \mathbf{P})\, \mathbf{P}/n + (\partial n/\partial U)U/n \quad (4.45)$$

where 'n' is the total number of charge carriers collected at the counter anode for a single incident radiation and U is the PPAC supply voltage such that U = EL. The average distance traveled by an electron between ionizing collisions is called the mean free path. Inverse of this mean free path is the number of ionizing collisions per unit length is called the first Townsend coefficient 'α'. It depends up on many parameters such as nature of the fill gas, electric field and gas pressure. The field is a useful parameter to be varied for best chamber performance. The first Townsend coefficient 'α' smoothly increases with the field E depending on pressure **P.**

Much effort has gone for the determination of 'α' and a lot of data exist for a wide variety of pure gases and at low values of electric field [60,63]. Mixtures of noble gases with quenchers are also used in proportional and avalanche counters with high gain fields of 10^4 to 10^5 volts/cm. But most of the data exist in 10^2 to 10^3 volts/cm field region. At high fields the data is limited because of the experimental limitation of handling high voltages. Performance of a detector can be optimized by playing with a number of important factors such as gas mixture, geometry, read out electronics materials etc. It is not desirable to use too low gas gain and too high gas gain (due to spark), for getting a detectable signal in a small gas volume. There should be an optimum condition for the better performance of a detector. This optimization requires the knowledge about the distortions due to space charge effects which can be estimated by modeling the avalanche in a gas. For this purpose the Townsend coefficient as a

function of field must be measured. Sharma and Sauli [65] reported the measurement of 'α' for various widely used gas mixtures using drift chambers. This measurement was done to understand the operating characteristics of drift chambers. Investigations of Sernicki [60] had gone beyond the Brunner's [62] PPAC method. He determined the avalanche counter amplification over a substantial portion of applicable operating conditions. Sernicki's Townsend coefficients are slightly higher than those reported by Brunner. The amplitude of the pulse formed due to the collection of ion pairs at the respective electrodes is given by ne/C where C is the detector capacitance. Then the subsequent output pulse height becomes

$$h = gne/C = gen_0M/C = geEM/CW \tag{4.46}$$

But $n_0 = E/W$, where E is the energy loss of the particle inside the gas volume between r_1 and r_2. If dE/dx is the average stopping power in MeV/mg/cm^2 , ρ is the gas density at operating pressure **P** and A is the atomic mass

$$E = (r_2 - r_1)\rho \quad dE/dx \tag{4.47}$$

But $$\rho = (A/22400)\,\mathbf{P}/760 \tag{4.48}$$

$$E = (r_2 - r_1)\,(A/22400)(\mathbf{P}/760)\,dE/dx = K\mathbf{P} \tag{4.49}$$

K is a constant for a given detector and incident ion. Thus

$$h = ge\,KPM/CW = f\,PM \quad \text{or} \quad M = h/f\,P \tag{4.50}$$

$$\text{therefore } \ln M = \ln (h/f\,P) \tag{4.51}$$

For a proportional counter with cylindrical geometry inner anode wire radius r_a and critical radius at which gas amplification starts r_c, then $r_1 = r_c$ and $r_2 = r_a$. Then equation (4.43) becomes

$$\ln M = \int_{r_c}^{r_a} \alpha\, dr \tag{4.52}$$

and $$S = E/P = V/Pr\ln(r_c/r_a) \tag{4.53}$$

hence $$dr = [-r_a/S_aS^2]dS \tag{4.54}$$

$$\ln M/Pr_aS_a = \int_{S_c}^{S_a} [\alpha\,(S)/PS^2]\,dS \tag{4.55}$$

For parallel plate geometry r2 – r1 = d, the electrode spacing and the electric field is uniform, given by the relation $E = \varepsilon V/d$. Here ε is the dielectric constant of the gas and nearly equal to 1. So $S = \varepsilon V/Pd$ and hence

$$\ln M/PdS = \alpha d/\varepsilon V = (\alpha/P)(Pd/\varepsilon V) \quad (4.56)$$

The above formula for $\ln M/Pr_aS_a$ proposed by Aoyama is a generalized one from which others can be derived as special cases. For m = 1/2, α/P is a product of forms proposed by Rose and Korff [48] and Charles [54].

$$\alpha/P = KS^{1/2} \exp[-L/S^{1/2}] \quad (4.57)$$

That is the forms used by these authors can not exist separately but occurs in combined form. The rapid advances in the technology and use of PPAC necessitated the knowledge of 'α' for larger values of S. Brunner [63] demonstrated that PPAC itself can be used for measurements for the range 190 to 290 V/cm.torr. In the case of SWPC the electric field E is quite non uniform as in figure 4.2. The field varies as proportional to 1/r and the integration in equation (4.42) becomes much complex. A method of analysis has been developed for determining 'α' using SWPC assuming [66-70] that the expression (4.44) satisfies for non uniform field case by assuming average values for A and B. In this method, final observed pulse height can be expressed as

$$h = f' n = f' n_0 \exp(\int \alpha dr) \quad (4.58)$$

where f′ is the over all gain, $n_0 = KP$, K is a constant such that $f = Kf'$. Therefore

$$h = f P \exp(\int \alpha dr)$$

$$h/f P = \exp(\int \alpha dr)$$

$$\ln(h/f P) = \int \alpha dr$$

$$\ln(h/P) - \ln f = \int \alpha dr \quad (4.59)$$

Here 'h' is the pulse height which is equivalent to the channel number. For coaxial cylindrical symmetry of SWPC applied potential V_0 and the electric field is expressed as follows

$$V_0 = \lambda/2\pi\varepsilon_0 \ln(r_0/a) \quad (4.60)$$

$$E = [\lambda/2\pi r\varepsilon_0] = V_0/r\ln(r_0/a) \quad (4.61)$$

$$E/\mathbf{P} = Z/r\ln(r_0/a) \quad (4.62)$$

where $Z = V_0/\mathbf{P}$ and V_0 is the anode voltage. Therefore equation (4.44) becomes

$$\alpha/\mathbf{P} = A \exp [-Br\ln(r_0/a)/Z]$$

$$\int \alpha dr = \mathbf{P}A \int \exp [-Br\ln(r_0/a)/Z]dr \quad (4.63)$$

By applying the limits for the integral $r = \infty$ to $r = r_0$, the above integral in equation (4.59) becomes

$$\ln (h/\mathbf{P}) - \ln f = [AV_0/B\ln(r_0/a)\ ] \exp[-B\ln(r_0/a).r_0/Z] \quad (4.64)$$

Taking logarithm on both sides of equation (4.64)

$$\ln[\ln (h/\mathbf{P}) - \ln f] = \ln[A/B\ln(r_0/a)\ ] + \ln V_0 - B\ln(r_0/a).r_0/Z \quad (4.65)$$

This expression can be summerised as

$$\ln[\ln (h/\mathbf{P}) - \ln f] = C - K(1/Z) \quad (4.66)$$

The above equation (4.66) represents a straight line with slope = $Br_0\ln(r_0/a)$ and intercept = $\ln V_0 + \ln[A/(B\ln(r_0/a)]$. The constants C and K depends on A and B respectively. Sernicki [60-62] observed a dependence of the coefficients A and B on the electrode spacing. Hendricks [64] carried out measurements on commonly available xenon filled SWPCs and found that Diethorn and Zastawny equations obeyed equally well. Kowalski [49,50,57] established that his experimental results as well as those of Jelen [71], Zastawny et al.,[6] could be well described by the equation proposed by him for krypton+ethanol, Xe+H_2, Ar, Ar+isopentane. Othman et al., [72,73] measured the gas amplification using a mixture of Ne+H_2 and showed that the Zastawny and a modified Rose-Korff formula satisfactorily described the data. All the above referred works had been carried out with the fill gases at near or sub atmospheric pressure ranges typically ~ 1 atm and below for SWPCs and 5 to 30 torr for PPACs. More recently tests have been carried out at pressures up to about 30 atm by Ye et al.,[74] with argon or xenon. Such high pressure counters are useful for high energy cosmic ray experiments. They have shown that the data at low pressures can not be extrapolated to higher pressures because of the changing mobility of positive ions. Kowalski [49,50,57] had made measurements for krypton at pressures up to 7.6 atm and Miyahara et al.,[75] for argon at pressures up to 10 atm.

References

[1] S.S. Kapoor and V.S. Ramamurty, "Nuclear Radiation Detectors", Wiley Eastern Ltd.

[2] H.W. Fulbright, R.G. Markham and W.A. Lanford, Nucl. Instr. and Meth. **108**(1973)125.

[3] R.G. Markham and R.G.H. Rpberson, Nucl. Instr. and Meth.**129**(1975)131.

[4] P. Moller and H.V. Klapdor, Nucl. Instr. and Meth.**142**(1977)447.

[5] S.C. Curran and J.D. Craggs, "Counting Tubes", Academic Press, London(1949).

[6] A. Zastawny and J. Mizeraczyk, Nukleonika **11**(1966)685.

[7] A. Zastawny, J. Sci.Instr.**44**(1967)395.

[8] A. Williams and R.J. Sara, Intern. J.Appl, Iso.,**13**(1962)229.

[9] T.H. Braid, Proc. Roy. Soc. Edinburgh(1972)9.

[10] J.L.C. Ford, Nucl. Instr. and Meth.**162**(1979)277.

[11] Kosuke Kageyama, Shogo Hayashibe, Masaaki Kanazawa, Hiroshi Watanabe and Manabu Fujioka, Nucl. Instr. and Meth.**A342**(1994)509.

[12] J. Sanada, Nucl. Instr. and Meth.**196**(1982)23.

[13] J. Sanada and Y. Fujita, Nucl. Instr. and Meth.**131**(1975)469.

[14] J. Sanada, Nucl. Instr. and Meth.212(1983)291.

[15] D.O. Kataria, Phys. Edn(1995)356.

[16] J. Sanada and K. Matsuda, Nucl. Instr. and Meth.**203**(1982)605

[17] G. Charpak, Ann. Rev. Nucl. Sci.**20**(1970)195.

[18] G. Charpak, H.G. Fischer, C.R. Gruhn, A. Minten, F. Sauli, G. Plch and G. Flugge, Nucl. Instr. and Meth.**99**(1972)279.

[19] F.Sauli, CERN Academic Training Programme Lecture notes, Geneva(1977).

[20] D.H.Wilkinson, "Ionization chamber and counters", Univesity Press, Cambridge(1950).

[21] W.R.Kuhlmann, K.H. Lauterjung, B. Schimmer and K. Sistemich Nucl. Instr. and Meth.**40**(1966)118.

[22] C.J.Borkowski and M.K.Kopp, Rev. Sci. Instr.**39**(1968)1515.

[23] J.L.C.Ford, P.H.Stelson and R.L.Robinson, Nucl. Instr. and Meth.**98**(1972)199.

[24] C.J.Borkowski and M.K.Kopp, IEEE Trans. Nucl. Sci.,**NS17,No.3**(1970)340.

[25] B.G.Harrey, J. Mahoney, F.G. Puhlhofer, F.S. Goulding, D.A. Landis, J.C.aivre, D.G. Kovar, M.S. Zisman, J.R. Meriwether, S.W. Cosper and D.L. Hindrie, Nucl. Instr. and Meth.**104**(1972)21.

[26] V.Radeka, IEEE Trans. Nucl. Sci.,**NS21,No.1**(1974)51.

[27] J.Alberi and V.Radeka, IEEE Trans. Nucl. Sci.,**NS23,No.1**(1976)251.

[28] G.L.Miller, N. Williams, A. Senator, R. Stensgard and J. Fischer, Nucl. Instr. and Meth. **91**(1971)389.

[29] K.M.Urbanczyk and M.P.Waligorski, Nucl. Instr. and Meth. **124**(1975)413.

[30] S. Parker, R. Jones, J. Kadyk, M.L. Stevenson, T. Katsura, V.S. Peterson and D. Yount, Nucl. Instr. and Meth. **97**(1971)181.

[31] F.Binon, V.B. Bobyr, P. Duteil, M. Gounnere, L. Huygon, M. Spiinghel and J.P Stroot, Nucl. Instr. and Meth. **94**(1971)27.

[32] U.Lynen, H. Stelzer, A. Gobbi, H. Sann and A. Olmi, Nucl. Instr. and Meth. **162**(1979)657.

[33] A.Breskin, R.Chechik and N.Zwang, Nucl. Instr. and Meth.**165**(1979)125.

[34] G.Charpak, Nucl. Instr. and Meth. **196**(1982).

[35] G.Charpak and F.Sauli, Nucl. Instr. and Meth. **162**(1979)405.

[36] A.Breskin, Nucl. Instr. and Meth. **141**(1977)505.

[37] G.C.Ball, Nucl. Instr. and Meth. **162**(1979)263.

[38] D.O.Kataria, J.J. Das, N. Madhavan, P. Sugathan, A.K. Sinha, G.D. Dhayanand, M.C. Radhakrishna, A.M. Vinod Kumar, K.M. Varier, Mahendrajit Singh and N.V.S.V. Prasad, Nucl. Instr. and Meth. **A372**(1996)311.

[39] H.Becker, S. Kelbitzer, D. Rieck and C.A. Weidner, Nucl. Instr. and Meth.**95** (1971)525.

[40] E.Beardsworth, J. Fischer, S. Iwata, M.J. Levine, V. Radeka and C.E. Thorn, Nucl. Instr. and Meth. **127**(1975)29.

[41] G. Hempel, F.Hopkins and G.Schatz, Nucl. Instr. and Meth.**131**(1975)445.

[42] A.Breskin and N.Zwang, Nucl. Instr. and Meth. **144**(1977)609.

[43] J.Eyal and H.Stezler, Nucl. Instr. and Meth. **155**(1978)157.

[44] H.Stezler, Nucl. Instr. and Meth. **133**(1976)409.

[45] D.V.Harrach and H.J.Specht, Nucl. Instr. and Meth. **164**(1979)477.

[46] G. Gaukler, H. Schmidt-Bocking, R. Schuch, R. Schule, H.J. Specht and T. Tserruya, Nucl. Instr. and Meth. **141**(1977)115

[47] J.S.Townsend, "Electricity of gases", Clarendon, Oxford(1915).

[48] M.E.Rose and S.A.Korff, Phys. Rev. **95** (1941)850.

[49] T.Z.Kowalski, Nucl. Instr. and Meth.**A234**(1985)521.

[50] T.Z.Kowalski, Nucl. Instr. and Meth. **A243**(1986)501.

[51] W.Diethorn, USAEC Report NYO-**6628**(1956).

[52] A.Zastawny, J.Sci.Instr.**43**(1966)179.

[53] L.G.Khristov, Dolk. Bulg. Akad. Nauk.**10**(1947)453.

[54] A.L.Ward, Phys. Rev.**112**(1958)1852.

[55] M.W.Charles, J.Phys.**E5**(1972)95.

[56] T.Aoyama, Nucl. Instr. and Meth.[Netherlands],**A234**(1985)125.

[57] T.Z.Kowalski, Nucl. Instr. and Meth. **216**(1983)447.

[58] G.E.Kocharov and G.A.Korolev, Izvest. Akad. Nauk. SSSR. Ser. Fiz. **27** (1963)301.

[59] R.W.Kiser, Appl. Sci. Res. **B8**(1960)183.

[60] J.Sernicki, Nucl. Instr. and Meth. **A288**(1990)555.

[61] J.Sernicki, Nucl. Instr. and Meth. **A263**(1988)446.

[62] J.Sernicki, Nucl. Instr. and Meth. **A251**(1986)81.

[63] G.Brunner, Nucl. Instr. and Meth. **154**(1978)159.

[64] R.W.Hendricks, Nucl. Instr. and Meth. **102**(1972)309.

[65] A.Sharma and F.Sauli, Proc. 6^{th} Int. Wire chamber Conf., Vienna(1992).

[66] K.M.Varier, P.P. Shakkeeb, A.M. Vinod Kumar, Antony Joseph and B.R.S. Babu, Proc. DAE Symp. on Nucl. Phys.,Bombay **35B**(1992)430.

[67] P.P.Shakkeeb, Antony Joseph, A.M. Vinod Kumar, K.M. Varier and B.R.S. Babu, Proc. DAE Symp. on Nucl.Phys., Calicut **36B**(1993)450.

[68] P.P.Shakkeeb, Antony Joseph, A.M. Vinod kumar and K.M. Varier, Ind. Journ. of Pure and Appl. Phys.,**33**(1995)317.

[69] P.P.Shakkeeb, K.M. Varier, A.M. Vinod Kumar and Antony Joseph, Proc. DAE Symp. on Nucl. Phys., Bhubaneswar **37B**(1994)449.

[70] P.P.Shakkeeb, A. Joseph, A.M. Vinod Kumar, K.M. Varier and B.R.S. Babu Nucl. Instr. and Meth. **A366**(1995)320.

[71] K.Jelen, Sci. Bull. Stainslaw Staszic Univ. of mining and metallurgy Gracow, **No.786**(1980).

[72] A.Othman, Nucl. Instr. and Meth. **A216**(1983)447.

[73] A.Othman, M.A.Kenaway and A.Morrey, Ind. Journ. Pure and Appl. Phys. **29**(1991)396.

[74] Z.Ye, R.K. Sood, D.P. Sharma, R.K. Manchanda and K.B. Fenton, Nucl. Instr. and Meth. **A329**(1993)140.

[75] H. Miyahira, M. Watanabe and T. Watanabe, Nucl. Instr. and Meth. **A241** (1985)186.

Chapter 5

Development of Gas Detectors and Experimental Studies

Magnetic spectrographs have been widely used in nuclear research for analyzing the reaction products and for high resolution spectroscopy. At the early stages of research in this field, nuclear emulsions were used for particle identification at the focal plane of the spectrograph. Even though they can cover large distances along the focal plane with excellent position resolution, their particle identification capability is limited, reading the plates is a tedious time consuming job and the online monitoring and modification of the experiment is impossible. The attempts to overcome the above well known disadvantages of nuclear emulsions led to the design and development of gas counters for the on line detection of reaction products at the focal plane of magnetic separators [1]. Recently study of gas counters has found interesting applications in many fields of ionizing radiation detection. According to the experimental requirements gas detectors can be designed and developed by knowing the gas gain for the fill gases as a function of the gas pressure, applied voltage and counter geometry. The present work concerns the development of some gas detectors for detection of heavy ions. They work in the proportionality region of the gas detector characteristics discussed in previous chapter. The major part of the work has been carried out under a research project funded by DST. The various detectors developed under this project are PPAC, SWPC, MWPC, PPAC with tilted electrode and Capacitance manometer. The detectors were mainly used for heavy ion detection and for position measurement. They work on the basis of the internal gas amplification. In the following sections, the details of the fabrication of the various types of gas detectors, their testing and results are presented.

5.1 Alpha Sources

Most α-particle (^{4}He) energies are limited between 4 and 6 MeV. The energy of the α-particle and the half-life of the parent isotope are mutually related. If energy is above 6.5 MeV the half-life is very short and below 4 MeV the half-life is very large. This is due to the variation in barrier penetration probability. The intensity of long lived isotopes is normally very feeble compared to the short lived isotopes. The α-particle loses energy in materials and hence mono-energetic sources are prepared in very thin layers to preserve the original energy. The different α-particle sources used for testing our gas detectors is given in table 5.1. These sources have been procured from BARC, Mumbai.

Source	Symbol	Half-life	Energy
Polonium	^{210}Po	138 d	5.30 MeV
Amerecium	^{241}Am	433 d	5.48 MeV
Californium	^{252}Cf	85 y (Fission) 2.65 y (Alpha)	6.11 MeV

Table 5.1 : Different alpha sources used for testing the gas detectors

5.2 General Electronics set up

The general electronics set up used for testing the gas detectors include pre amplifiers (PA), high voltage (HV) bias supply, timing single channel analyzer (TSCA), gate and delay generator (GDG), analog-to-digital converter (ADC), multichannel analyzer (MCA). We have used mainly EG&G ORTEC electronic devices for processing the detector signals. A brief discussion of the electronic components used for the detector testing is given in the following sections.

5.2.1 Preamplifiers

EG&G ORTEC preamplifiers (model no.142A and 142IH) were used in the set up. A short connecting cable was used between the detector output and the preamplifier to minimize the noise. The 142A preamplifier is a charge sensitive unit designed to operate over a detector input capacitance range from 0 to 100 pF. This model has a low noise intercept and moderate slope. The energy range expected in typical applications is from 0 to 200 MeV. The 142A series has two outputs-one for energy (E) measurements and the other for timing (T) applications-both signals are isolated from each other. The T output can be terminated with a 50 Ω resistor when it is not in use. A bias circuit is included to accept the voltage by the detector. The bias input circuit in the preamplifier includes a 100 MΩ load resistor and any detector leakage current will have to pass through the high resistance. The 142IH preamplifier is a charge sensitive minimum cost general purpose unit which can be used in conjunction with detectors producing large noise level. The 142IH can be used for applications with bias up to ±3 kV. An input protection unit is built in to the preamplifiers to protect the input FET of the two models.

5.2.2 Amplifiers

EG&G ORTEC spectroscopy amplifiers (model 571 and 572) were used for shaping and amplifying the detector signal pulses. A shaping time of 1 μs was kept for all measurements. Model 571 is a single width NIM module with a versatile combination of switch-selectable pulse-shaping and output characteristics. Extreme low noise, wide gain range and excellent overload response for universal application makes it suitable for high resolution spectroscopy. It can accept input pulses of +ve and –ve polarity. The input impedance is 100 Ω, the rise time < 650 ns and fall time > 40 μs. The pole zero cancellation drastically reduces the under shoot after the first differentiator and greatly improves overload and count rate characteristics. Amplifiers model 571 and 572 can be operated with a gain parameter of ±1 to ±1500 and they can process semi-Gaussian, unipolar and bipolar pulses with shaping time constants 0.5, 1, 2, 3, 6 and 10 μs. The peak position stability and good energy resolution at high counting rates can be obtained by

removing the dc offset of the earliest stages of the amplifier by using a base line restorer. It is a gated, auto or manual noise discriminator. The pile up of the amplifier pulses corresponding to two events within the width of the spectroscopy amplifier gives amplitude distorted pulses which can be rejected by using a pileup rejecter. In the present measurements no pile up rejector was used as the count rates never exceeded 1 k/sec.This is an added advantage of models 571 and 572.

5.2.3 High Voltage(HV) Detector Bias Supply

A regulated power supply procured from EG&G ORTEC (model 428) provided the variable voltages in the range 0 to 1000 V. It is able to give bias voltages of both positive and negative polarities to two detectors and the current in each detector can be externally monitored through jacks on the front panel. The outputs are selected independently by 10 turn direct reading potentiometers. The unit can supply constant bias voltage by high grade circuits with < 0.0002% noise and ripple. This model 428 is with EG&G ORTEC preamplifiers. The temperature instability is $\leq \pm 0.02\%$ per degree Celsius for 0 to 50°. The output impedance is of the order of 1.3 MΩ, which is negligible compared to the detector load resistor in the preamplifier ranging from 22 to 2000 MΩ. The voltage at the output connector of the model 428 can be calculated by the following formula where V_{dial} is the voltage indicated by the 10 turn dial and I_D is the detector current.

$$V_O = V_{dial} - I_D \times 1.3 \times 10^6 \qquad (5.1)$$

A power supply unit of EG&G ORTEC (model 659) was used at NSC for testing the PPAC and SWPC. It can be operated in the range 0 to 5 kV or 0 to 500 V at a current rating of 0 to 100 μA. A 10 segment bar graph indicator is used for verifying the selected voltage. The MWPC was biased at NSC using the EG&G ORTEC (model 710) which is a QUAD 1 kV bias supply unit containing 4 HV power supplies with independently selectable output voltages and polarities. Each supply can deliver an output voltage that is continuously adjustable over the range 0 to ± 100 V or from 0 to ± 1 kV with a maximum output current of 20 μA. It can automatically shut down if the detector current exceeds 20

μA. The output current or voltage can be monitored using an LED display. The current can be measured with a 0.01 μA resolution. It is also have an alarm output for stopping the data collection if a detector or vacuum failure occurs. EG&G ORTEC high voltage unit (model 556) was used for biasing the silicon surface barrier detectors (SBD) in the experimental set up shown in chapter 6.

5.2.4 Timing Single Channel Analyzer (TSCA)

EG&G ORTEC TSCA (model 551) performs the dual functions of single channel pulse height analysis and timing signal derivation. The module was used for generating the strobe to the ADC -AD811- from the amplifier output. The model 551 can be operated in normal, integral and window modes. In the window mode the unit operates as a high resolution narrow window SCA. For wide window applications normal mode is used. In this mode the lower and upper level controls are independently variable from 0 to 10 V, and an output is generated for pulses analyzed between the levels. For leading edge timing applications it can be used in integral mode as a wide dynamic range discriminator. This unit has separate lower level and upper level discriminator outputs. The input is dc coupled which makes it possible to take full advantage of the base line restoration of the main amplifier for maximum performance at widely varying count rates. The continuously adjustable output delay (0.1 to 11 μs) makes it possible to align output signals which have actual time difference without a need for additional delay devices. The trailing edge constant fraction timing technique provides unexcelled timing on either unipolar or bipolar signals and shows better results than conventional leading edge discriminators. It can give both +ve square pulses and –ve differential outputs.

5.2.5 Gate and Delay Generators (GDG)

The EG&G ORTEC model 416A were used as gate and delay generators. It can accept either polarity of input logic pulse. It can give a delay for the input between 0.1 to 110 μs and furnishes an output logic pulse with selected amplitude (±2 to ±10 V), polarity and width (0.4 to 4 μs). This module is used for gating MCA and for the alignment

of coincidence timing between two channels using dissimilar pulse shaping modes. It can give excellent time stability and can be used in electronic setups requiring nanosecond time precision. It can also be used as a logical interface between EG&G ORTEC equipments and any other instruments.

5.2.6 Analog-to-Digital Converters (ADC)

The EG&G ORTEC ADC (model AD811) was used for converting the analog signals to the digital information. This model contains 8 peak measuring ADCs packaged in a single width CAMAC (see next section) module. This unit is capable of measuring positive unipolar or bipolar signals from nuclear shaping amplifiers in the range 0 to +2 V. The internal circuit is completely dc coupled. This module can be used for sampling dc or slowly varying voltages and hence can be used for wide range of applications. The resolution is 1 mV with a range of 11 bits and 2047 channels. The 12^{th} bit is included in the data registers for over flow detection. The input linear gates and peak detectors are normally in the closed condition and the unit must be triggered by an external strobe pulse to start a conversion. The total conversion time is 80 μs and is independent of the input signal amplitude in any channel. The readout is CAMAC based and a common strobe input is used for all ADCs. On receipt of the strobe input, an internal gate pulse is generated which opens all 8 linear gates and enable the peak detectors. All 8 inputs are processed parallely by Wilkinson conversion. A 0.5 μs fast clear pulse is used between consecutive strobes.

5.2.7 Computer Automated Measurement and Control (CAMAC) standard systems

The data acquisition electronic set up was controlled and monitored using a CAMAC standard system [2]. The CAMAC standard is based on a crate which is sub divided in to 25 individual module stations spaced 17.2 mm apart. Electrical connection between each module and the crate is made by a PCB edge connector with 86 contacts. PCBs were mounted with integrated circuits for each function. Within the crate each connector provides access to the data high way consisting of conductor buses for digital

data, control signals and power. The digital communication between plug-in modules within the crate occurs over this data way, which replaces the external inter connection of modules for many digital functions. The extreme right hand control station occupied by a crate controller plug-in module which provides the control functions necessary for the transfer of data between modules. It acts as an interface between crate and external equipments. The modules on the crate can communicate with each other only through the crate controller. AD811, borer ADC, buffers etc. can be mounted on CAMAC crate. Different CAMAC crates can be connected serially or parallely.

5.3 Multichannel Pulse height Analysis

The multichannel analyzers are essential part of most systems employed for analyzing event energies from alpha, beta, gamma and X-rays and for orderly storage of counter information which is used in nuclear, chemical and medical applications. There are two modes of operations. They are pulse height analysis (PHA) mode and multi channel scaling (MCS) mode. A multichannel pulse height analyzer (MCA) works on the principle [3] of converting an analog signal to its digital equivalent. This conversion is carried out by the key element analog-to-digital converter (ADC) [4]. The detector output signal is given to linear amplifier through preamplifier and then amplifier output is feeding to ADC. The ADC will convert the detector signal to a pulse height spectra which can be recorded and displayed using computer by providing an additional MCA plug-in card. The combination of ADC, MCA card, PC memory, display, input/output hard ware constitute the multichannel pulse height analyzer. The memory channels range from 512 to 8192 as a power of 2 and the maximum number of counts in a memory location ranges up to 2^{24}-1(1.68 x 10^6 counts). A 4K (4096 channels) ADC can divide the full pulse height range in to 4096 increments. Pulses of constant amplitude will be stored in a single channel. In normal cases the input voltage for an ADC span over 0 to 10 V and the minimum pulse width is of a few tenths of a micro second for the proper functioning of ADC. The resolution must be as good as possible in maximum gain. In multiparameter applications ADCs with multi inputs have been used. The memory requirements for two parameters are the square of the number of channels required for only one parameter. For more than two

parameters bulk storage devices such as magnetic disc or tape is required. A typical set up of the entire electronics for the testing the gas detectors is shown in figure 5.1. We have used the PC based Nucleonix MCA (1002) having the data reduction capability within the system for the data acquisition at our laboratory at Calicut University. In this system a special purpose software is used for performing the functions such as controlling the data acquisition, generation of display information, present condition etc. with the help of a hard wired 4K MCA buffer card. The PC-based 4K MCA is an efficient data accumulation and analysis system that is particularly useful in applications requiring programme control of the total analysis process. At the time MCA is not in use, PC can be used as a general purpose computer for any applications. MCA mode is used for accumulating a spectrum (histogram) of the frequency distributions of the heights from a sequence of random input pulses (events) with the capabilities for storage display and output functions associated with the analysis. The main constituents of a Nucleonix MCA system used at Calicut University are the following.

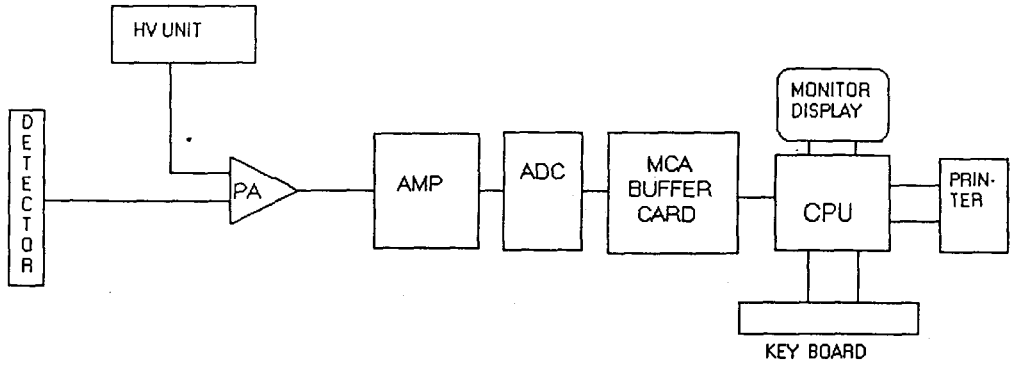

Figure 5.1 : A typical electronic setup of MCA system used for data acquisition using the gas detectors.

5.3.1 Nuclear ADC from Nucleonix (ADC 560)

The ADC accepts the analog signal and converts it into a binary address which is proportional to the peak amplitude of the input signal. In addition to this basic function of converting analog input in to binary address, the ADC performs several logic functions. At the end of conversion the address is transferred to a multichannel buffer card, suitably interfaced to a personal computer.

5.3.2 Multichannel buffer card

This card primarily functions as an acquisition interface to the computer and contains a memory sub system within it. In PHA mode the unit acquires data through ADC. The acquired data can be transferred by the buffer card to PC using proper commands.

5.3.3 Personal Computer and accessories

An IBM compatible PC is used as the central unit of MCA system, which executes the functions of control, data storage and processing with the help of Nucleonix MCA software. MCA system commands are given through key board for the above functions. The acquired data spectrum can be viewed in the display monitor for proper processing and the output was taken using a dot matrix printer.

5.4 Gas Handling System

A gas handling system was set up as in figure 5.2 using needle valves, brass tubes, spring valves, tygon tubing, laminated hose and rubber tubing. Two needle valves have been used one at each end of the detector facilitating easy handling of the fill gases to flow at controlled rate through the detectors. Two rotary pumps were used for the pumping. One rotary pump was used for pumping the chamber in which the detector is located for testing and the other for pumping the detector itself as well as for maintaining gas flow through the detector. These rotary pumps were of the model ED6 manufactured and supplied by Hind High Vac., Bangalore. The P10 gas has been supplied by M/s Indian Oxygen, Madras. The isobutane gas for the present measurements had been procured from M/s Alphagaz, France.

Figure 5.2 : Gas handling system and setup used for testing PPAC Overall view (top) and close up (bottom) showing PPAC inside the chamber

5.5 Vacuum testing of detectors

A vacuum system already developed earlier was used for initial vacuum testing of the detectors [5]. The detectors are assembled with suitable O-rings for better vacuum and tested for vacuum. The PPACs were tested inside the vacuum chamber as in figure 5.2. Rotary vacuum is required for off line testing of detectors, which can be checked using proper gauges such as pirani gauge, penning gauge and thermocouple gauge.

5.6 Foil Stretching Unit

A foil stretching unit as in figure 5.3 was developed for stretching thin poly propylene films and mylar foils to be used as the window foils and as electrodes for gas detectors [5]. It mainly consists an aluminium disc with smooth convex upper surface and plane lower side. The convex upper side is covered with a Teflon sheet where the foil is pressed for stretching. Bottom circumference of the disc is provided with a circular groove in which copper tubing is attached for cooling. A heating element is attached to the central part of the bottom surface. The temperature gradient produced due to central heating and peripheral cooling effects causes the fine stretching of the foil without wrinkles.

5.7 Constructional details of SWPC

We have developed two types of SWPCs. One is square type and the other is cylindrical type. The details of the construction of both are given in the following sections.

5.7.1 Square type SWPC

A proto type square SWPC was initially fabricated using Perspex casing. Gold plated tungsten wire of diameter 20 μm was used as the central anode. One side of the Perspex is replaced by aluminium sheet to provide the cathode. A 1 cm wide window is made on one side with mylar foil. This forms the entrance window through which ions can enter in to the detector volume.

Figure 5.3 : Thin foil stretching unit (in the foreground)

5.7.2 Cylindrical type SWPC

A cylindrical position sensitive SWPC was developed (figure 5.4 and 5.5) within an aluminium rod. The active region was of length 14 cm and inner diameter 2.5 cm. The central anode wire was made of isohm (alloy of nickel, chromium and tungston) material of diameter 20 μm. Resistivity of the isohm wire is about 16 kΩ per meter, so that the wire used in the cylindrical SWPC has a total resistance of 2.7 kΩ. The wire was properly stretched using light weights at both ends. A mylar foil of 8 μm thickness and active area 13 cm x 1 cm was used as the entrance window. Two ends of the cylindrical volume can be closed using circular aluminium flanges, which can be tight fitted using brass screws. O-ring grooves are provided at both end faces of the detector for putting O-rings to hold vacuum. Biasing of the detector and taking the signal output of the detector can be done using the SHV connectors provided at both ends as in figure. Gas inlet and outlets are provided by means of small steel pipes.

5.7.3 Testing of SWPC

The square type SWPC was tested with ^{210}Po alpha source, using P10 gas at pressures ranging from 250 to 500 torr and anode bias voltage ranging from 500 to 1000 V. The cylindrical SWPC has been tested using ^{241}Am alpha source. Both P10 and isobutane gases were used in the pressure range 25 to 500 torr. The bias voltage was ranged from 300 to 1000 V. Block diagram of the testing set up is shown in figure 5.6. The signals from the two ends of the SWPC are fed to charge sensitive preamplifiers and subsequently to shaping amplifiers. Shaping amplifier outputs were fed to Nucleonix ADC one by one and the data was acquired using a PC-AT based 4K MCA data acquisition system. Position sensitivity was tested by keeping the alpha source at various positions over the window of the detector. The position calibration is given in the figure 5.7. Cylindrical SWPC is calibrated for position and energy. From the two output spectra at varying bias voltage and pressure, energy and position of the incident radiation is determined. The SWPC was also tested at NSC with ^{241}Am alpha source using CAMAC based data acquisition system. Shaping amplifier output was fed to CAMAC ADC-AD811. The gate signal was

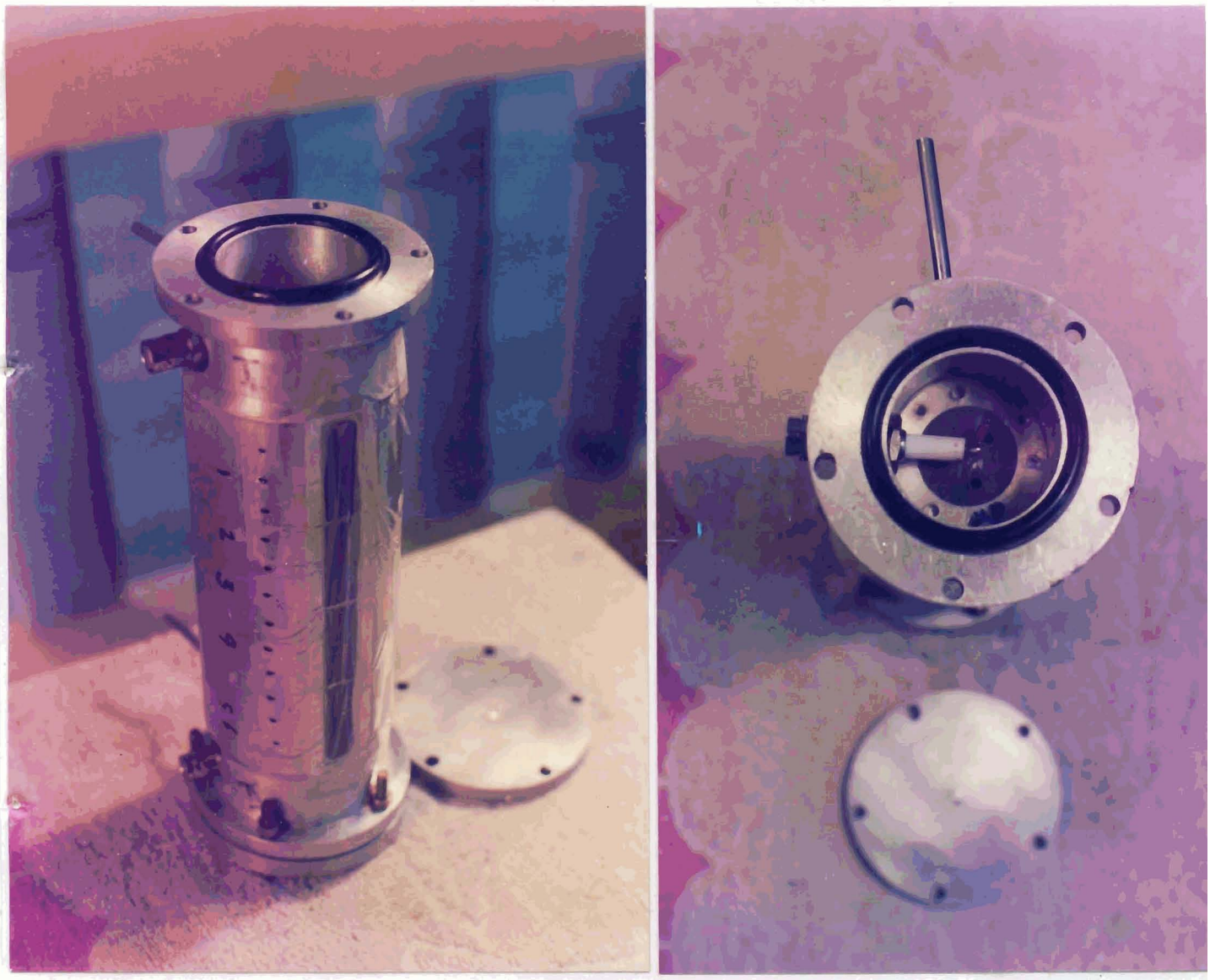

Figure 5.4 : Cylindrical Position Sensitive SWPC(left) and it's end view(right)

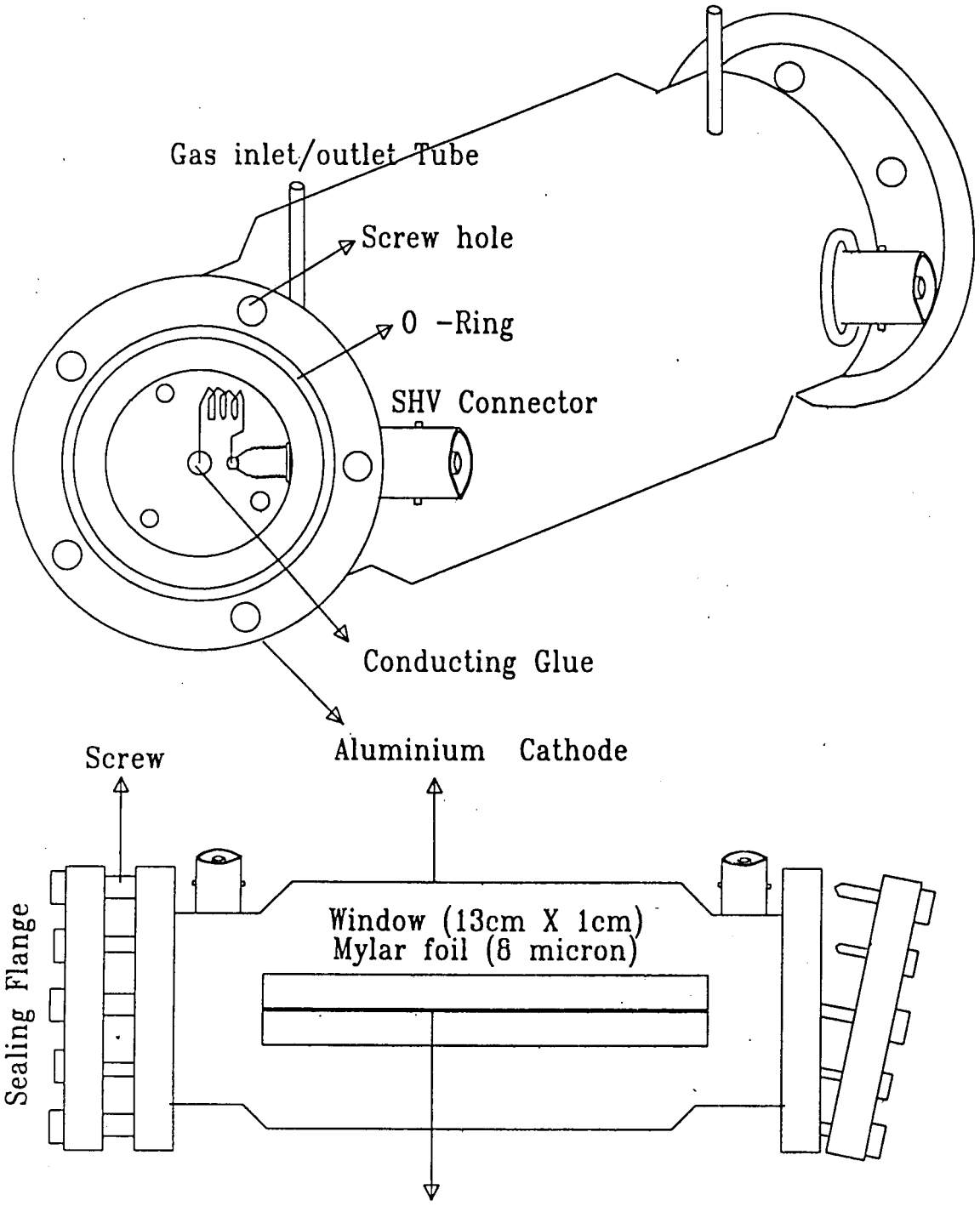

Figure : 5.5 Schematic digram showing the end view (top) and view from window-side (bottom) of the SWPC (Active Area 14cm X 2.5cm)

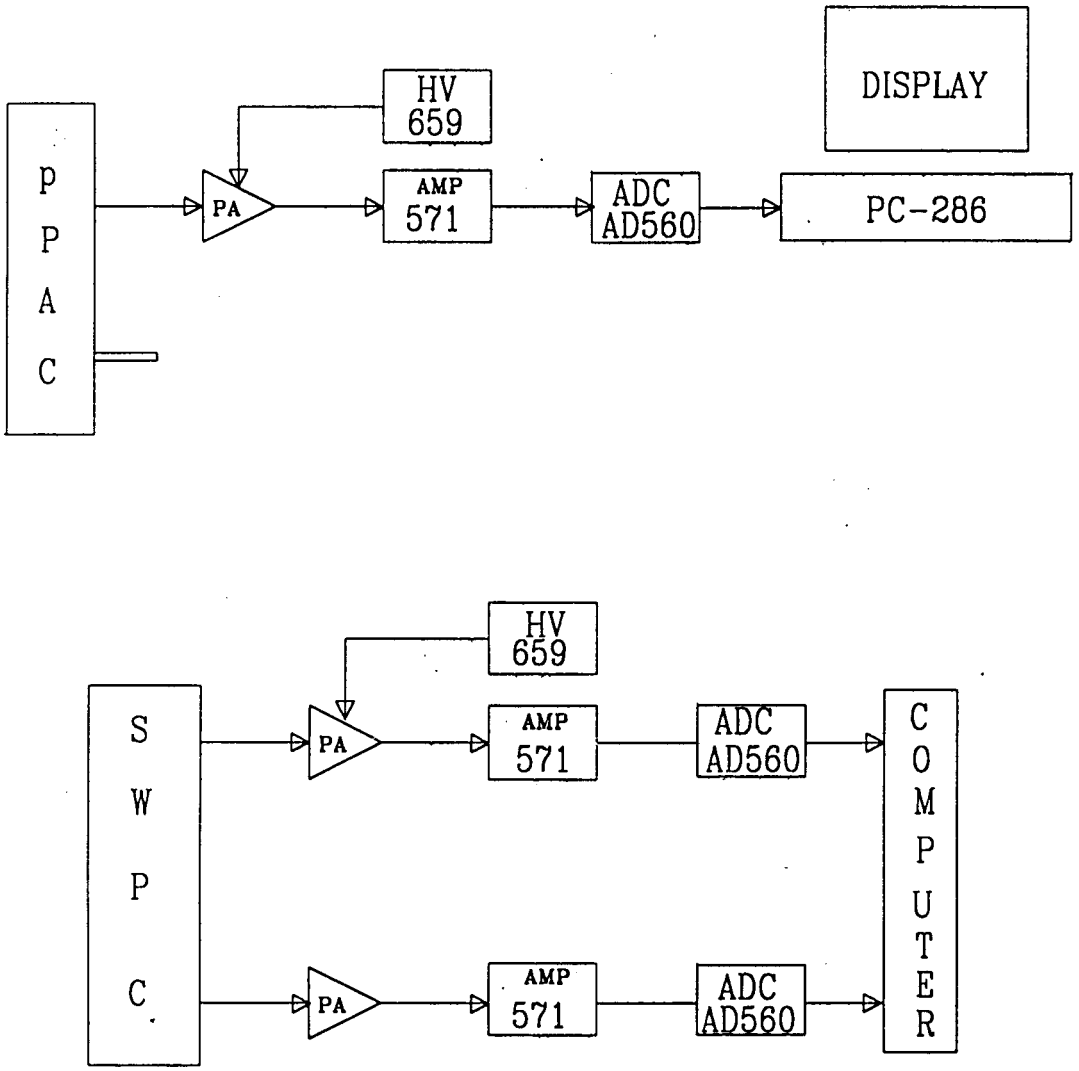

Figure: 5.6 Block diagram of the PC-based MCA and Electronic setup used for testing PPAC(top) and SWPC(bottom) at the University of Calicut. Modules are made of EG&G ORTEC and NUCLEONIX

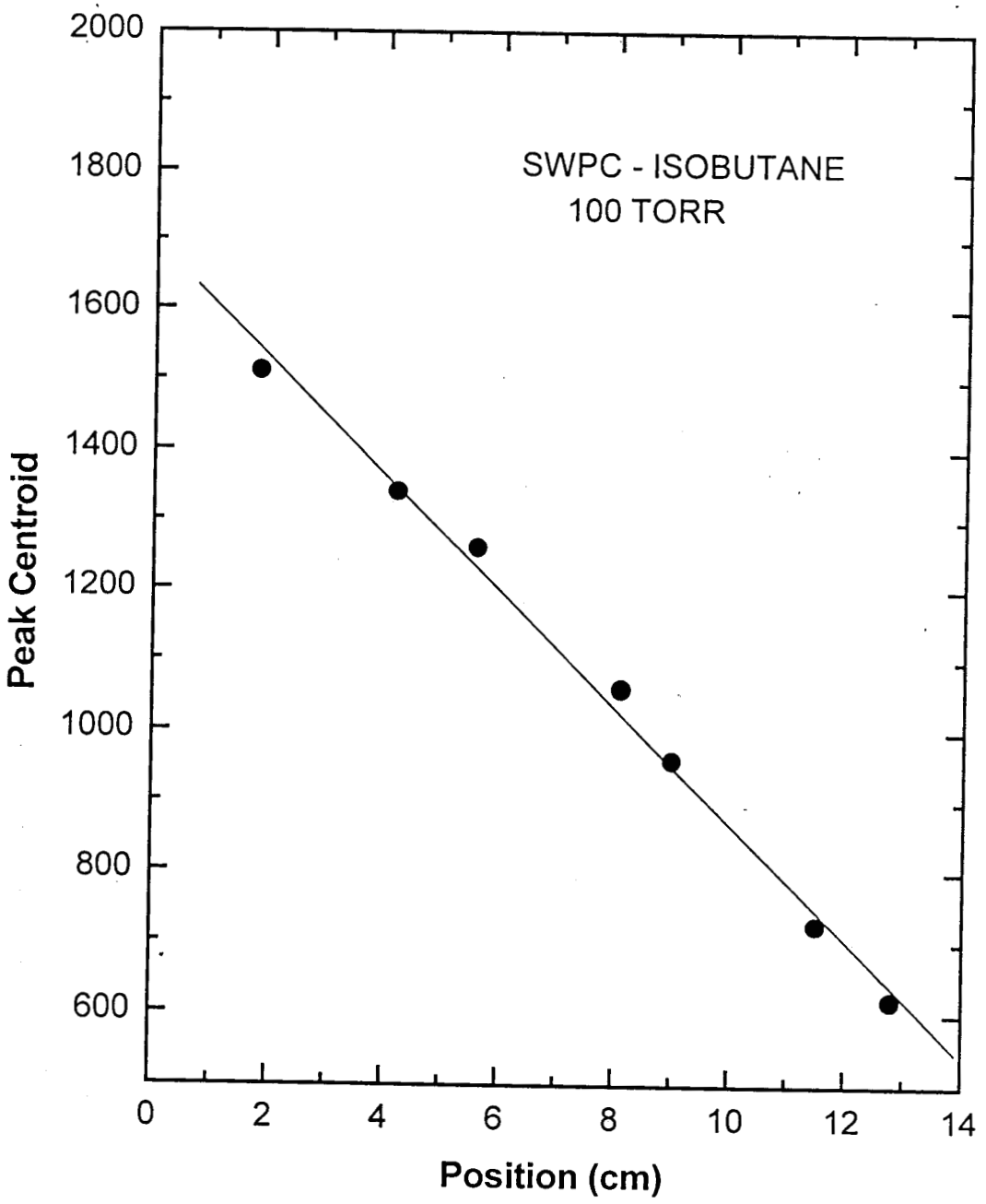

Figure 5.7 : Position calibration of cylindrical SWPC

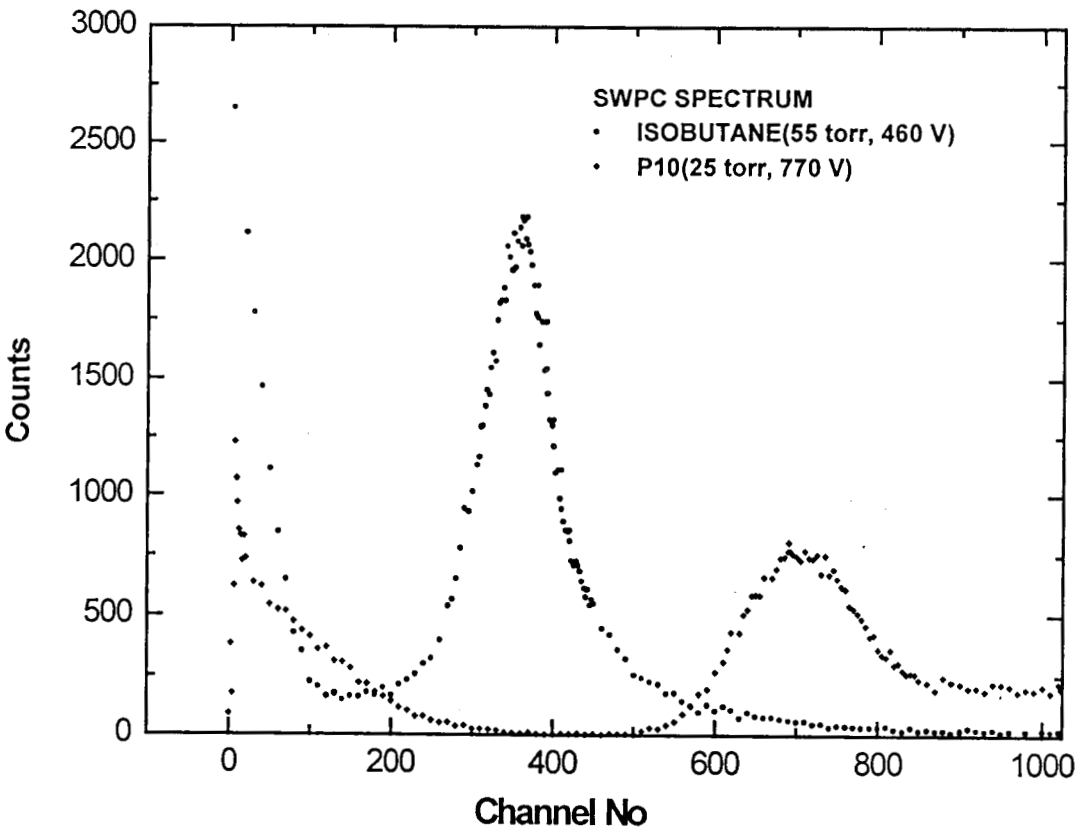

Figure 5.8 : SWPC spectrum taken during the testing at Calicut University using isobutane gas at 55 torr for a bias voltage 460 V and P10 gas at 25 torr for a bias voltage 770 V.

generated using TSCA from bipolar signal and used as the strobe for AD811. A PC-386 based data acquisition software NSCSPEC was used for acquiring the data. The addition and division of the detector outputs had been done using software to extract position and energy information as given in previous chapter (section 4.4.6). Figure 5.8 shows a typical spectrum obtained with SWPC for the ^{241}Am source.

5.8 Development of MWPC

The final aim of the present project was to develop [6] a focal plane MWPC with active sensitive area 14 cm x 14 cm for HIRA at NSC. The X-Y electrodes were made of 10 μm GPT wires on gold coated PCB of thickness 2.5 mm and anode by 2 μm aluminized mylar foil of single sided type on aluminium coated PCB of 1.5 mm pasted using rubber cement. The electrodes are mounted in the square slot of the housing made of aluminium plates of thickness 34 mm and 20 mm with dimensions 345 mm x 295 mm. The square slot is of dimension 205 x 205 mm^2 with depth 7 mm on the thicker aluminium plate and 3 mm on the thinner plate. O-rings of suitable dimensions-a square O-ring between the aluminium plates and a circular O-ring between the thinner aluminium plate and the G10 sealing plate which faces the focal plane of HIRA, were used. The window of the detector is circular of diameter 14.5 cm. Individual wires are separated by a resistance of 47 ohms. The X-electrode consists of about 140 wires and Y-electrode about 135 wires. The detector dimensions are compatible with the focal plane flange of HIRA at NSC, so that it can be easily mounted in position. Spacers of PCB pieces of thickness 1.6 mm were used in between the electrodes. Anode foil of wrinkleless effective area 140 x 70 mm^2 was used. Double sided alumnised mylar foil also tried as anode foil for X grid-Anode-Y grid geometry. A small portion of this foil was folded 3 way to get electrical continuity between the sides. KF10 connectors are provided for gas connections. 5 lemo connectors are used in this detector as shown in photograph - two for taking the signals from X-electrode, two for taking signals from the Y-electrode and one for the anode foil. Special square pits are made inside the slots for packing the projecting resistances. The depth of the pit is 16 mm on thick plate and 7 mm on the thin plate. These pits are lined with Teflon sheets for avoiding the shorting of the signals from the projecting resistance leads to the ground. The side facing HIRA is sealed with a thick G10 plate. Other side is covered with another relatively thin G10 plate with holes for source positions sealed by 6 μm transparent mylar window foil. Figure 5.9 shows the photograph of the final MWPC detector and figure 5.10 shows the inside views of the detector showing the assembly of the wire electrode and anode foil.

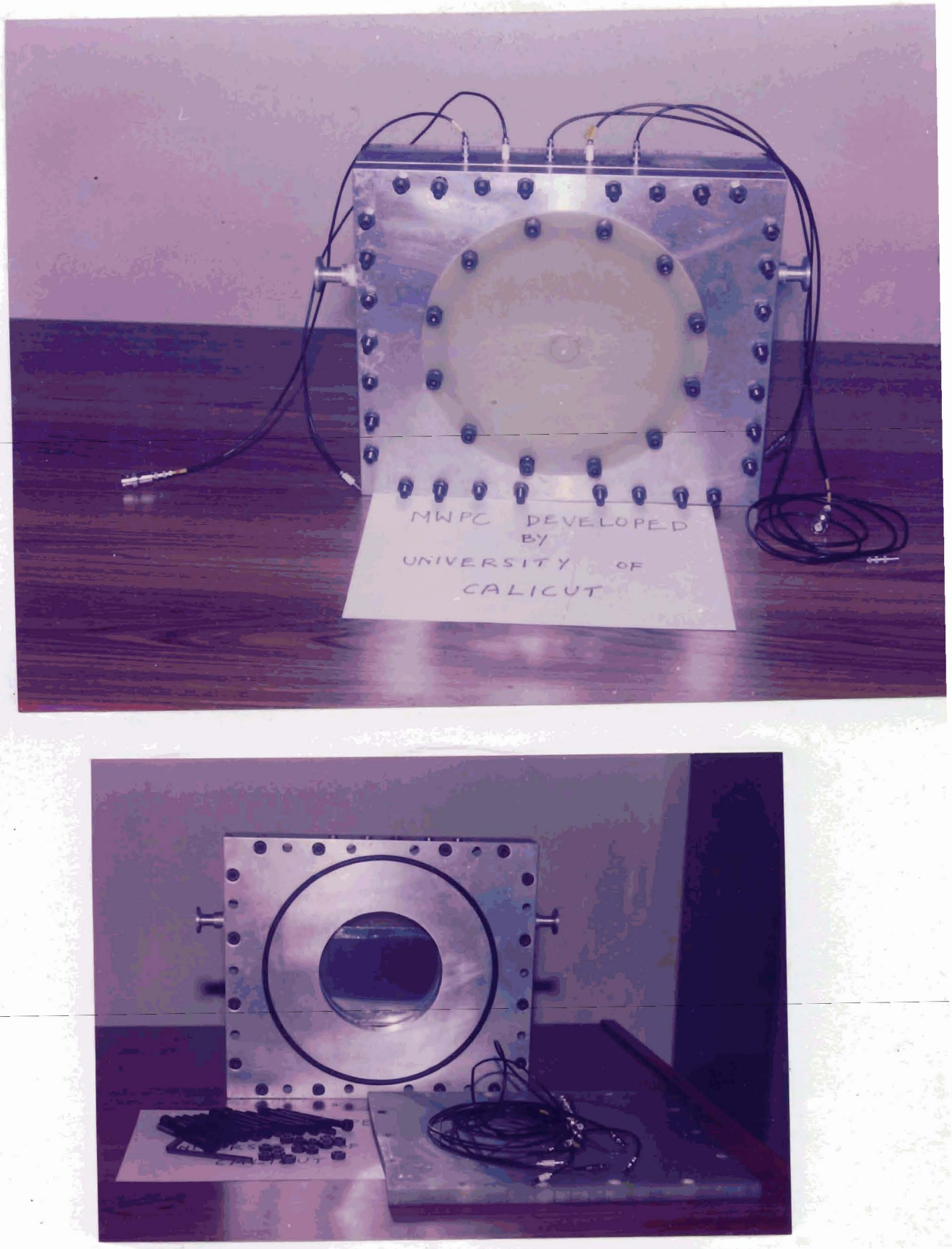

Figure 5.9 : Final Position Sensitive Multi wire Proportional Counter (top) and inside view from end facing Ionization Chamber (bottom)

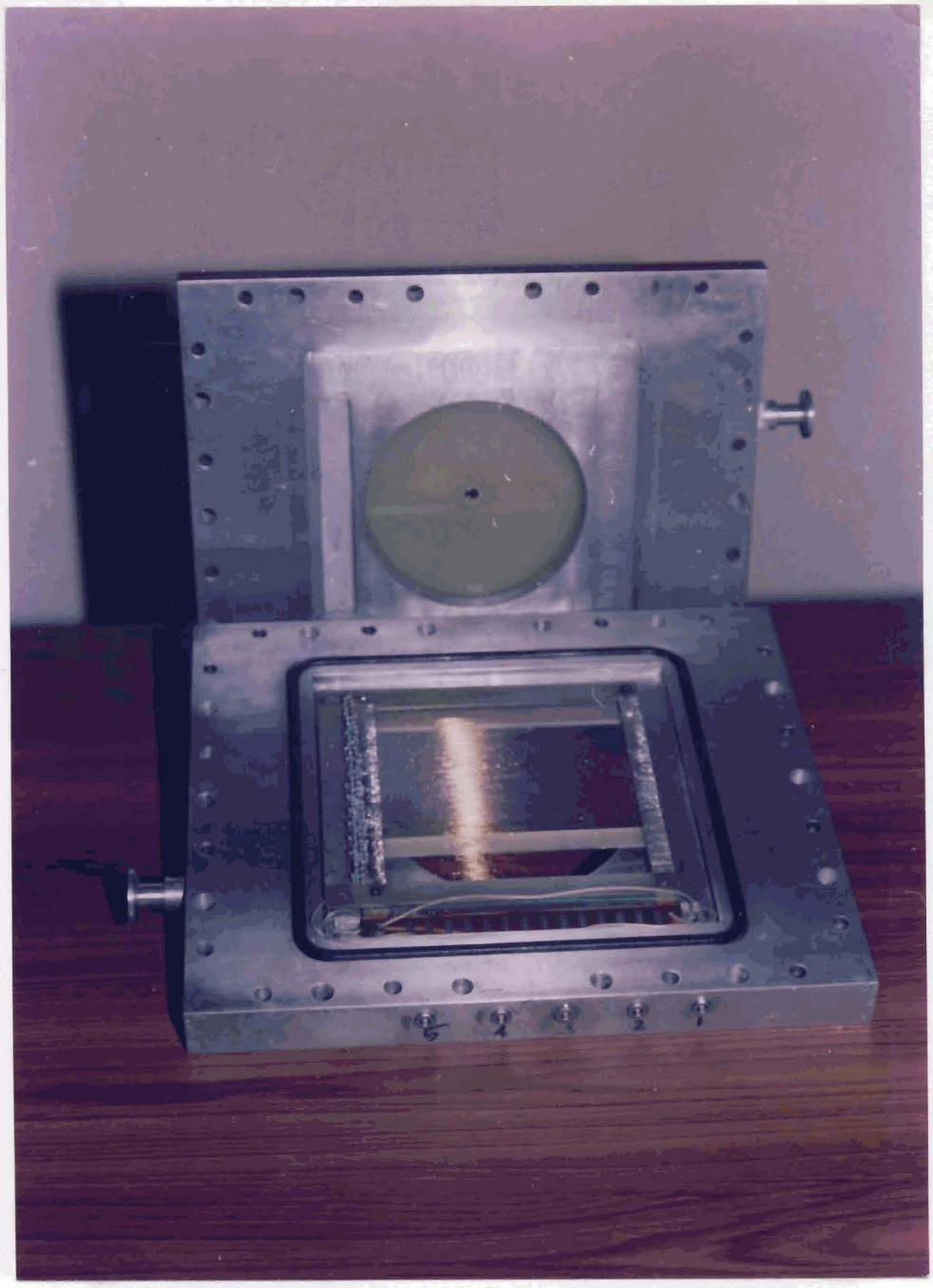

Figure 5.10 : Inside view of MWPC showing the electrodes

The electrodes are arranged in the order X grid-anode-Y grid pattern viewing from HIRA side as shown in figure 5.11. The total resistance of the X grid is 6.8 kΩ and Y grid is 5.4 kΩ. The source holes are of 1 cm diameter at the center and holes of 5mm on both sides of the central hole. The active area of wire electrodes was 140 mm x 140 mm on a frame of 185 x 170 mm^2. A one sided foil electrode of active area 142 x 142 mm^2 on a frame of 160 x 160 mm^2 were also used to test the MWPC in the geometry foil-X grid-Y grid with foil facing the source side.

5.8.1 Wire Stretching unit

This was made of 3 pieces of square aluminium rods and one aluminium square channel [7] as shown in figure 5.12. The active area was 22.5 x 20 cm^2. Two 15 cm steel scales were fixed on the outer side of the L channel and on the inner side of the parallel square rod. This was used for stretching GPT wires equally spaced. Using the pool rotating mechanical unit for providing tension developed at NSC, GPT wires are stretched with a pin and cellotape and parallely fixed using quick fix, crazy or loctite over the aluminium stretching unit at the mm marks for obtaining an equal spacing of 1 mm. After fixing a few wires, they are manually transferred to the wire electrodes (gold plated PCB frame) by soldering at both ends. This process was repeated for fixing about 130 to 150 wires on the X-Y electrodes which is sufficient to cover the position sensing requirements of ERs coming at HIRA focal plane. This method is little tedious and time consuming compared to the computer automated mechanism. Here we have to stretch the wire one by one and the setting time of the glue is so important. If the wire is cut out to do the next one before proper drying of the glue, they slightly loosened and loses proper tension. This time also depends on the type of glue used and varies from one another. The transferring of the wires to the electrode was done as a batch of nearly 10 wires at a time and the transferring of a large number of wires at a time is not a wise method due to tension and spacing problems. Thin coating of the glue on the aluminium frame some times causes tilting of the wire plane which affects interelectrode spacing. This problem can be solved by slightly pressing on the stretched wires with extreme care for not breaking while soldering to the electrode.

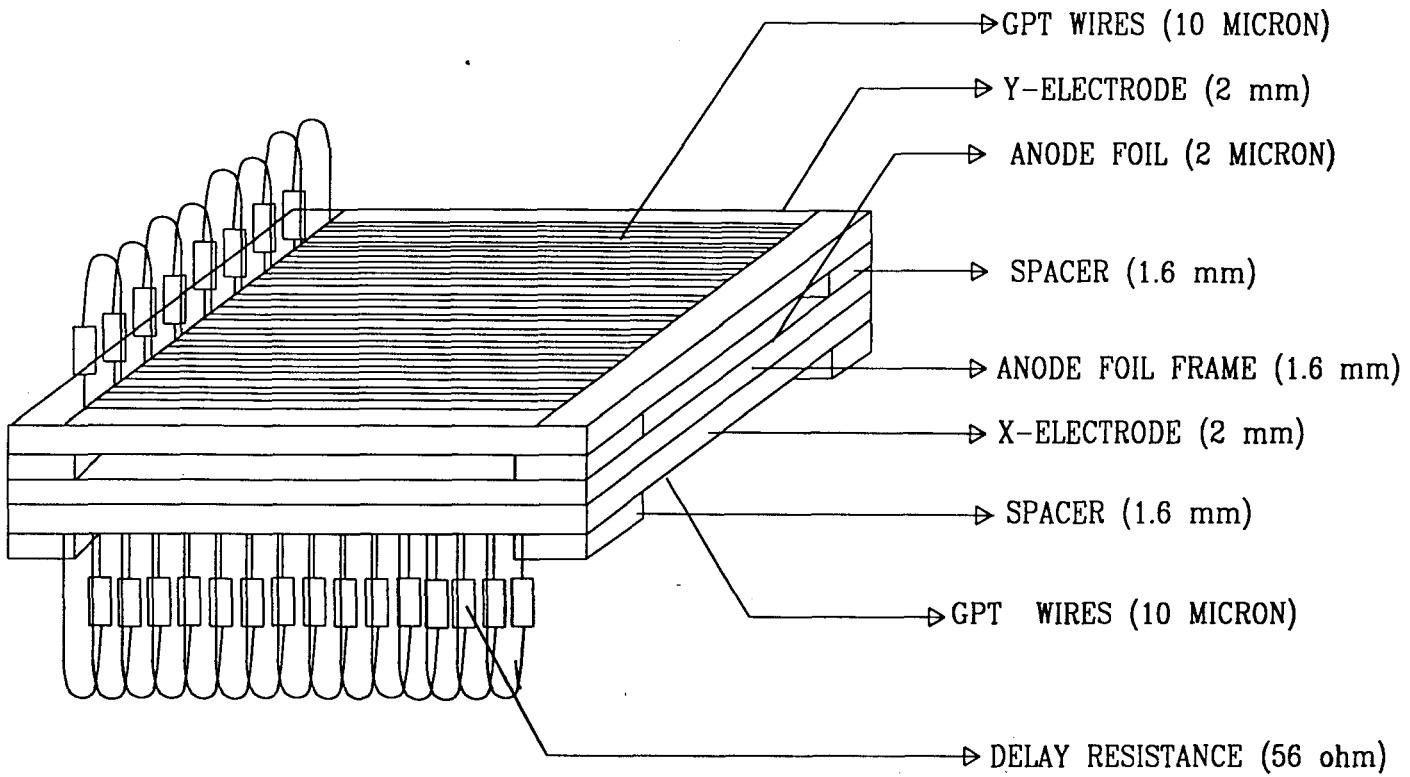

Figure : 5.11 The diagram showing the specifications and assembly of electrodes inside the MWPC

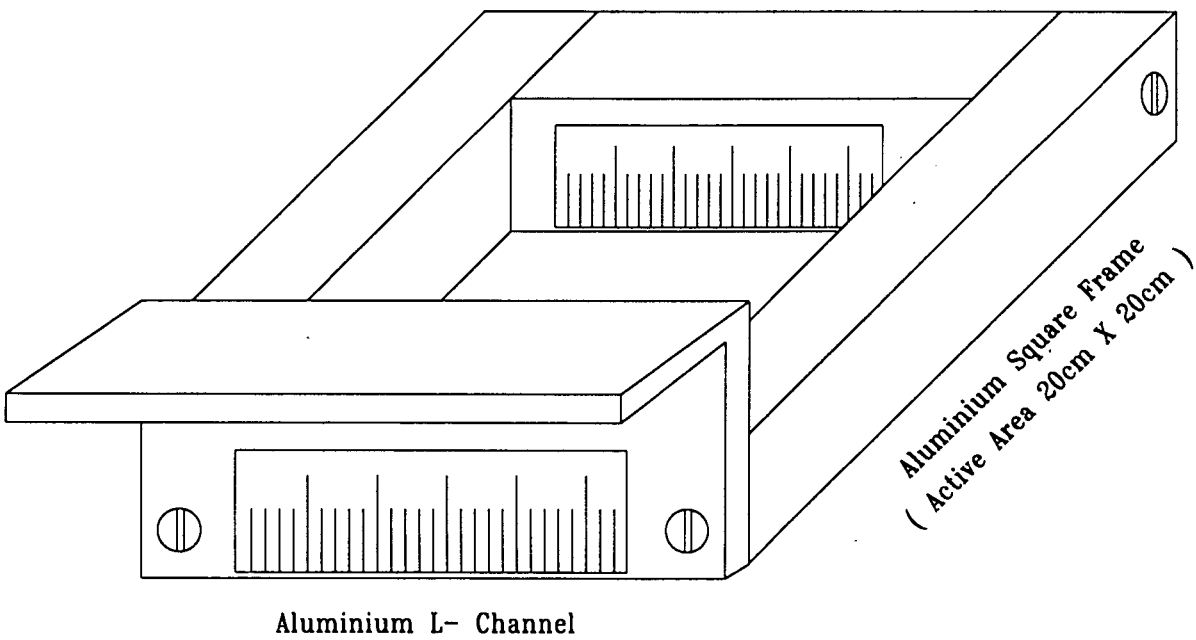

Figure : 5.12 Gold Plated Tungston wire stretching unit

5.8.2 Testing of MWPC

The MWPC was tested [8,9] firstly for vacuum and various sources of leak was analyzed with alcohol and improved to get a better rotary vacuum of 2.4×10^{-2} torr. The MWPC was tested for vacuum without putting the electrodes using mechanical pump and obtained a vacuum of 0.065 torr. After shutting off the pump a leake rate of 27 torr/hr was occurred. It is then tested with the electrode geometry and a better vacuum 0.024 torr was obtained with a leak rate of 0.46 torr/hr. It was then tested for position sensitivity with a 12.5 μCi ^{252}Cf alpha source using a metal mask with equidistant holes. Set up used for testing the detector is shown in figure 5.13 and the electronics used in figure 5.14. The peak heights h_1 and h_2 for the X and Y electrodes were noted for the two ends of the detector for various source positions. The pressure of the P10 gas was 12 torr. The anode voltage varied over 275 to 290 V. Figures 5.15 to 5.18 shows the various spectrum obtained using MWPC. Figure 5.19 shows the position calibration of MWPC. The MWPC was also tested for field variation with foil bias 263 V and mid grid bias 35 V. The non uniformity of the field causes the variation of peak height with position. The position information is derived from $X = h_1/(h_1+h_2)$. This is plotted in figure 5.20 as a function of the source position.

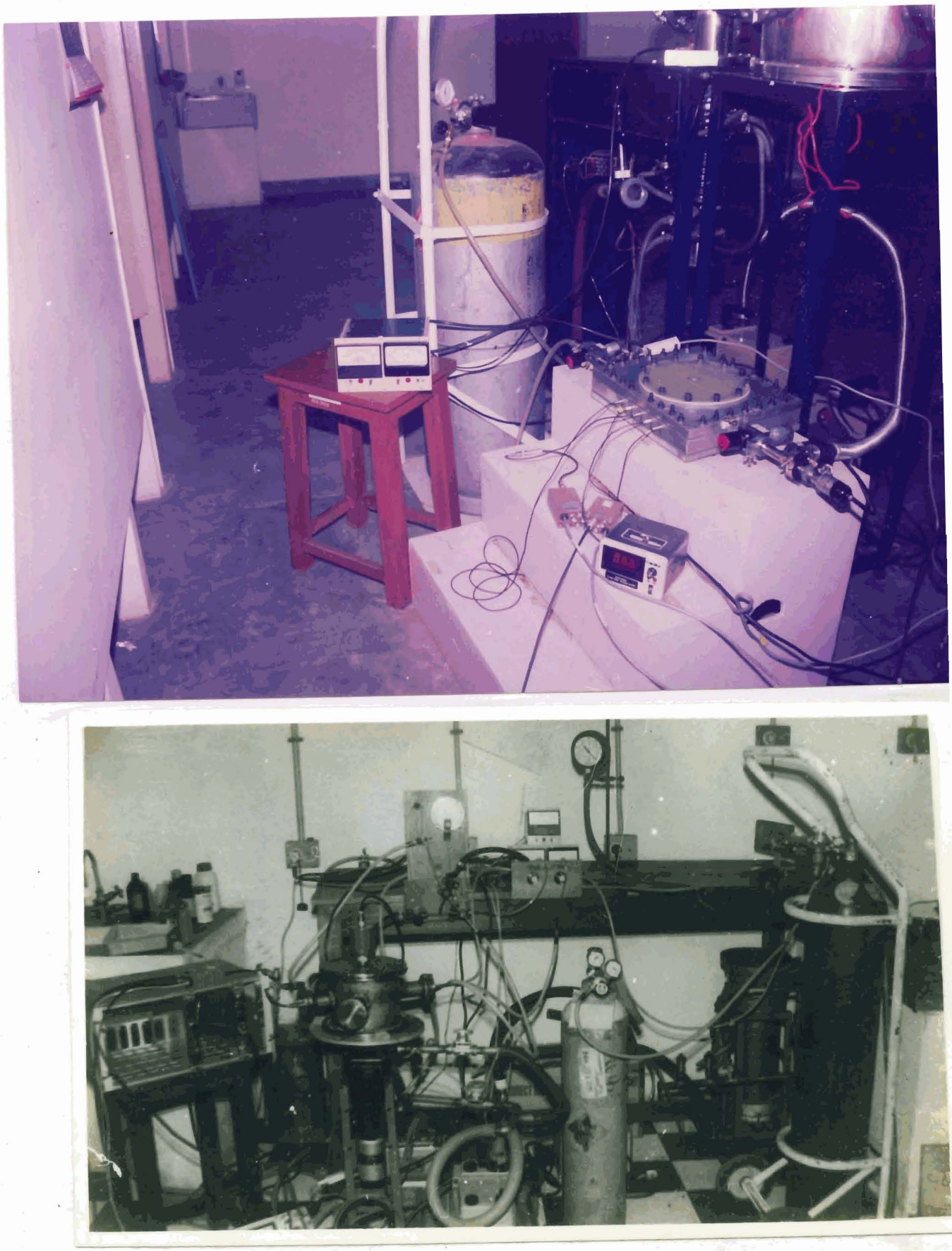

Figure 5.13 : Setup used for testing MWPC at NSC(top) and SWPC and PPAC at Calicut University (bottom)

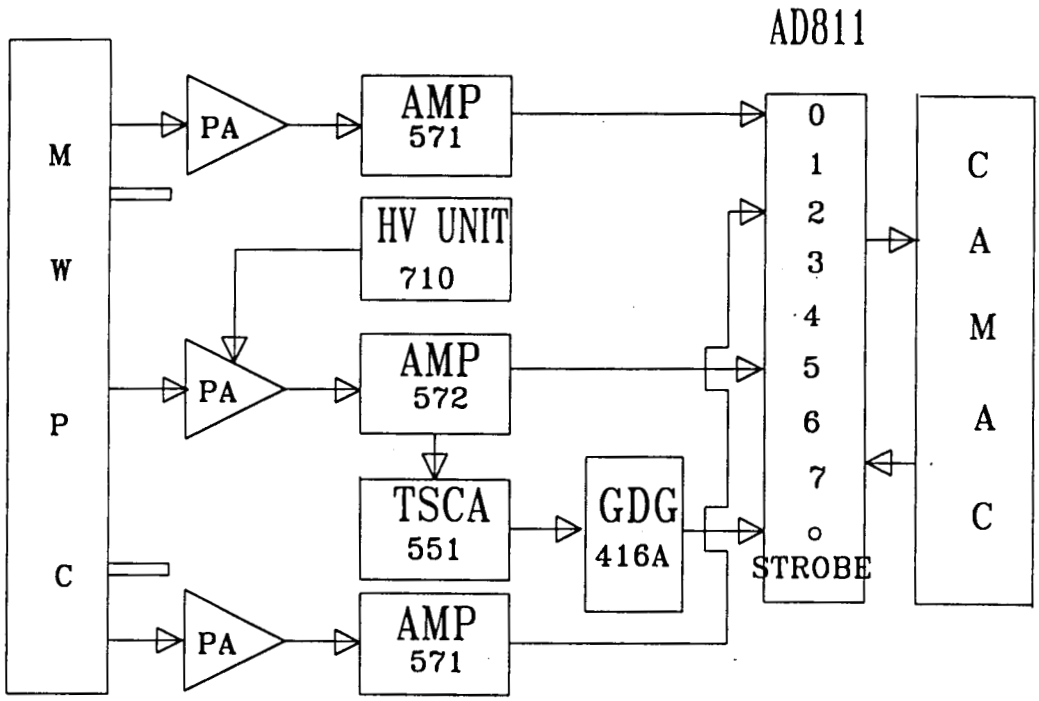

Figure: 5.14 Schematic diagram of the Electronic setup used at NSC for testing MWPC. Electronic modules used are mainly of EG&G ORTEC.

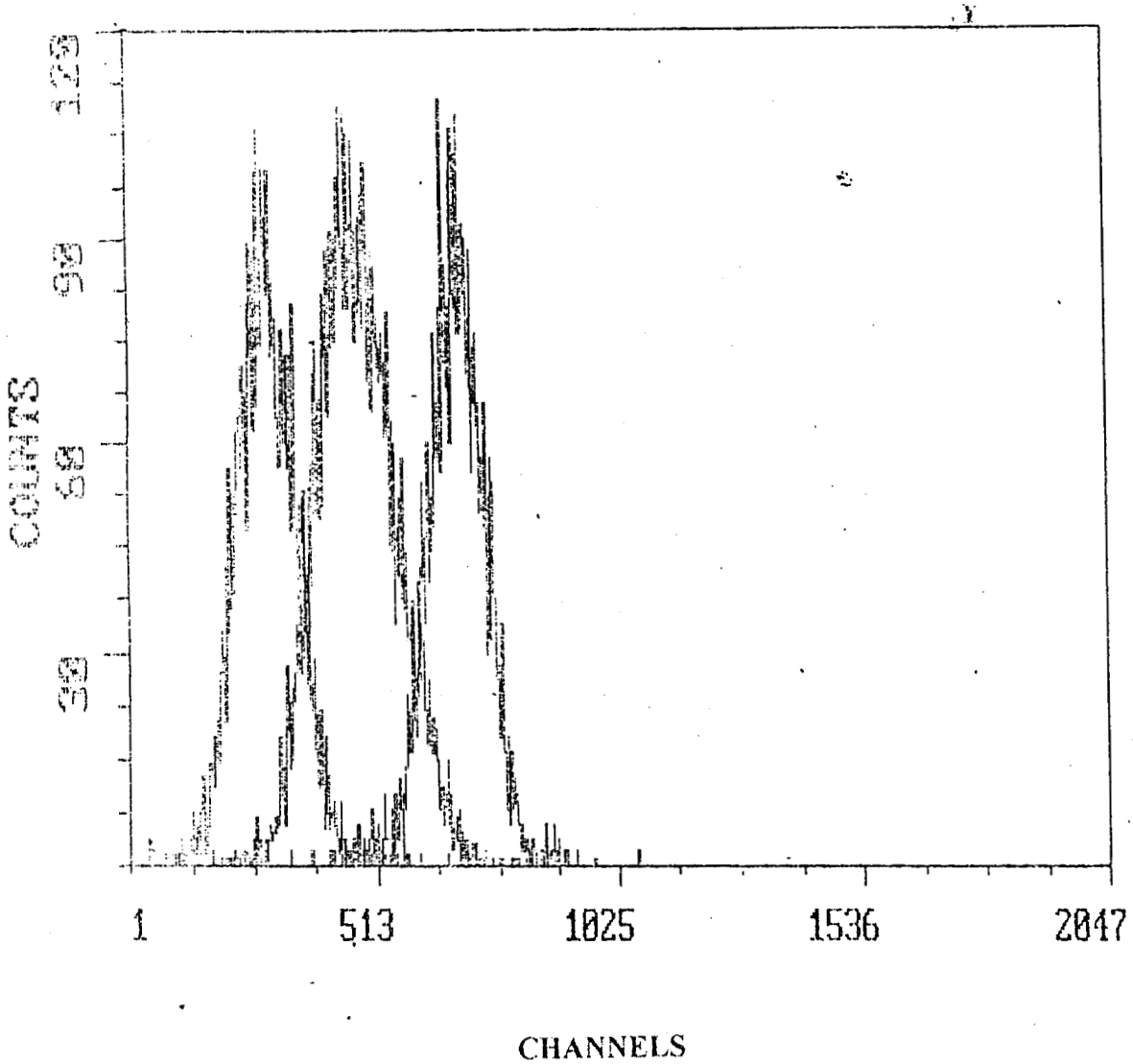

Figure 5.15 : A typical MWPC Spectrum with Alpha source at the two extremum ends and and central position on wndow side.

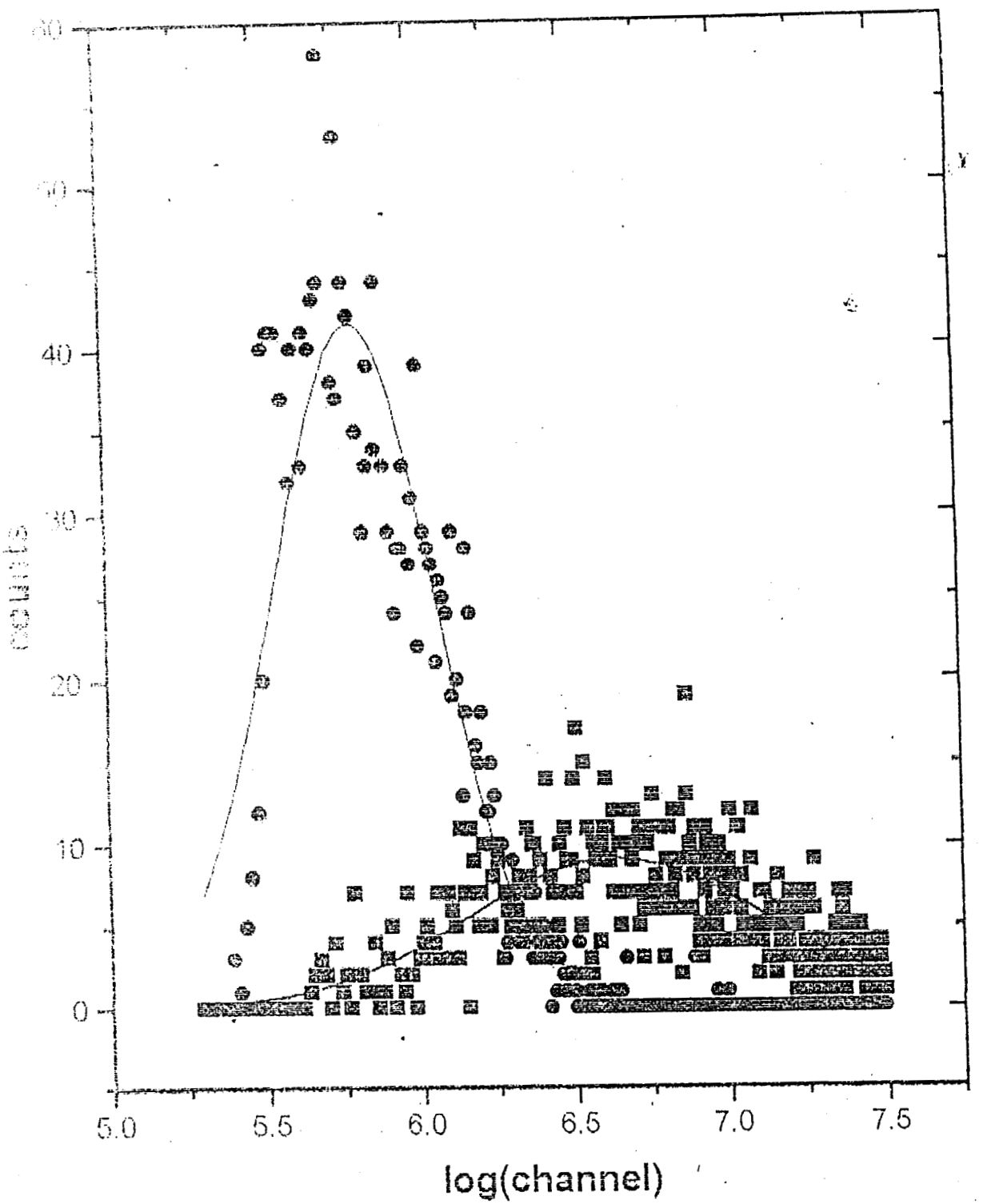

Figure 5.16 : The MWPC spectra taken from two ends of the detector with source at one end. Note the log scale on X-axis.

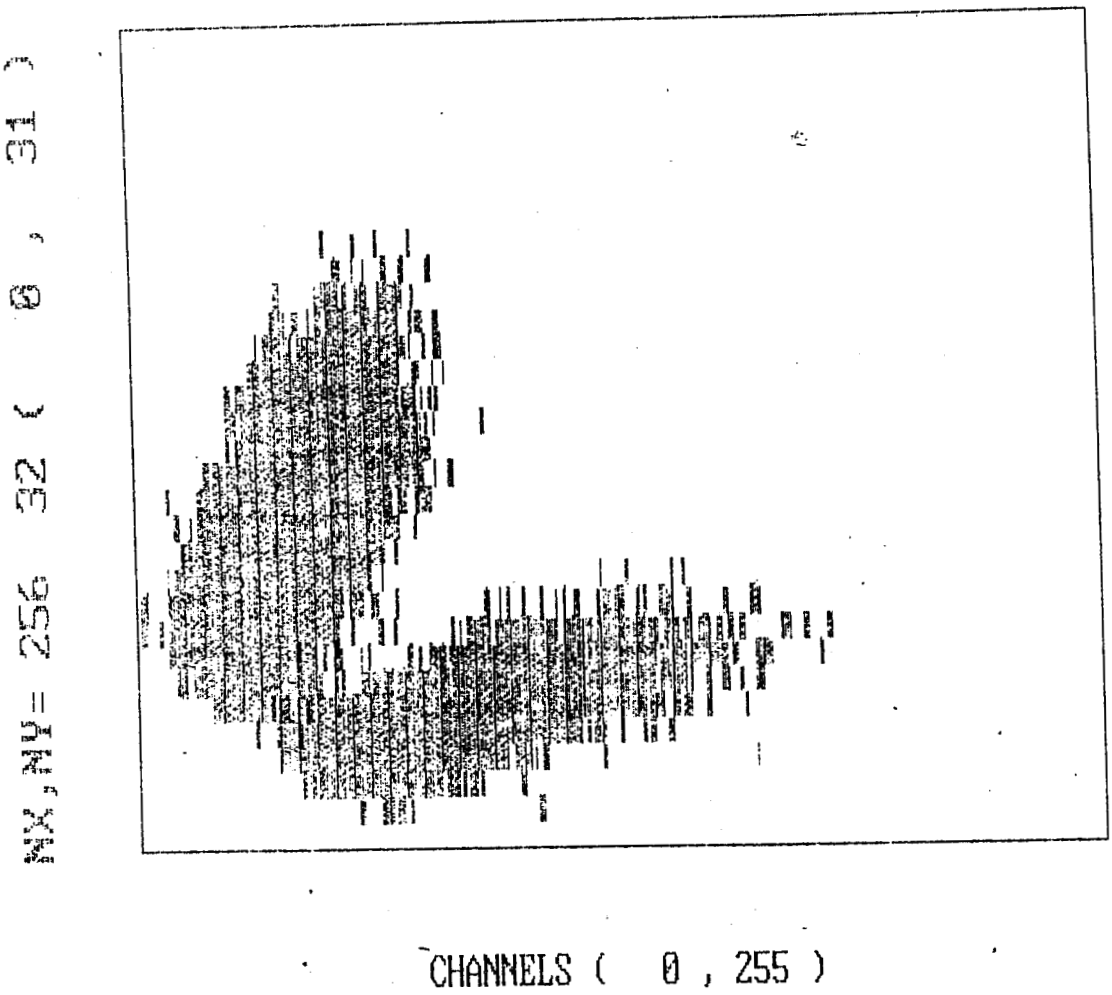

Figure 5.17 : 2D spectra of outputs from two ends of the MWPC detector taken using the data acquisition program NSCSORT.

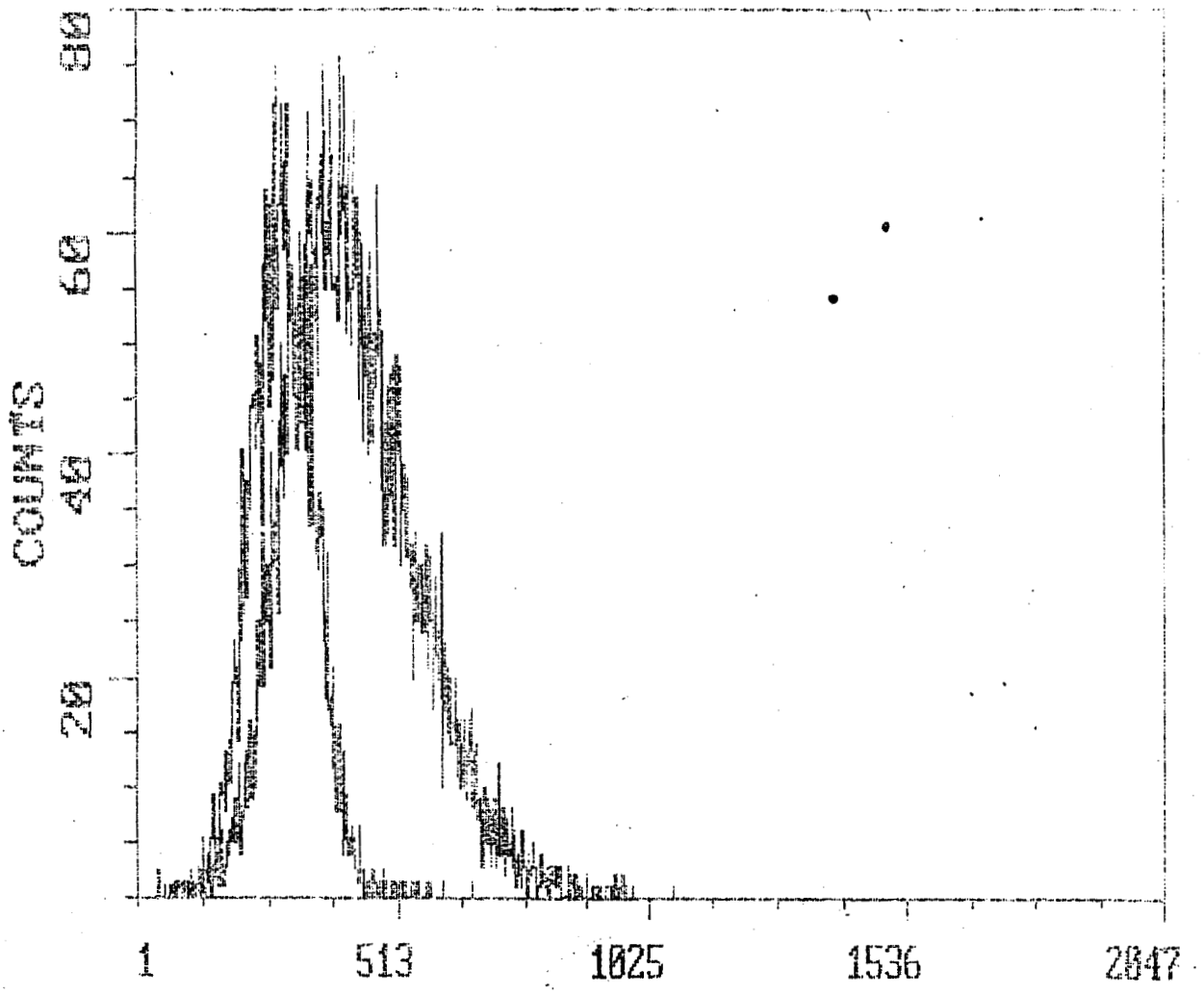

Figure 5.18 : Projection of the 2D spectrum 5.17 obtained using MWPC.

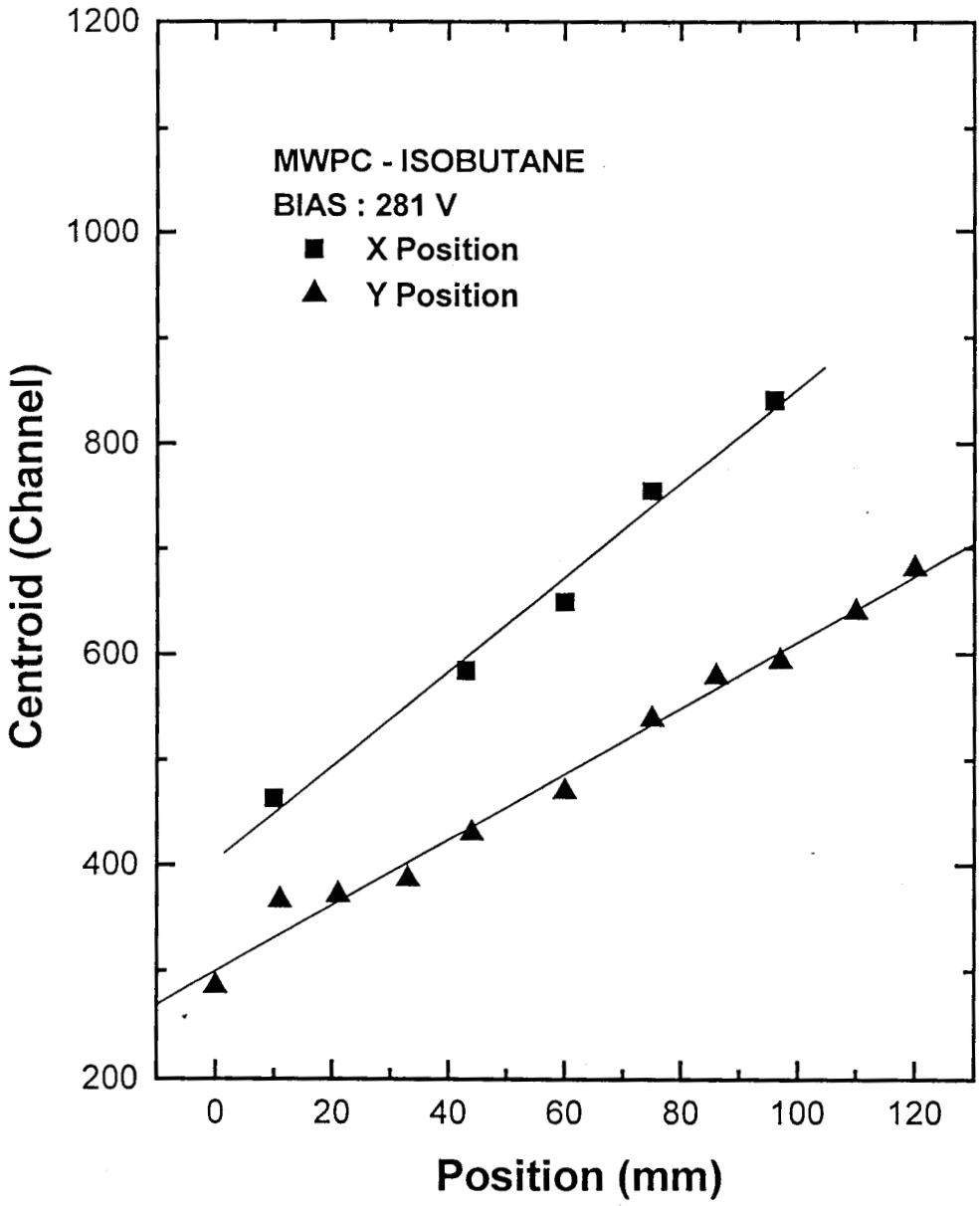

Figure 5.19 : X and Y position calibration for final MWPC. 15μCi californium-252 alpha source was used for testing X-position (at 4 torr) and Y-position (at 12 torr).

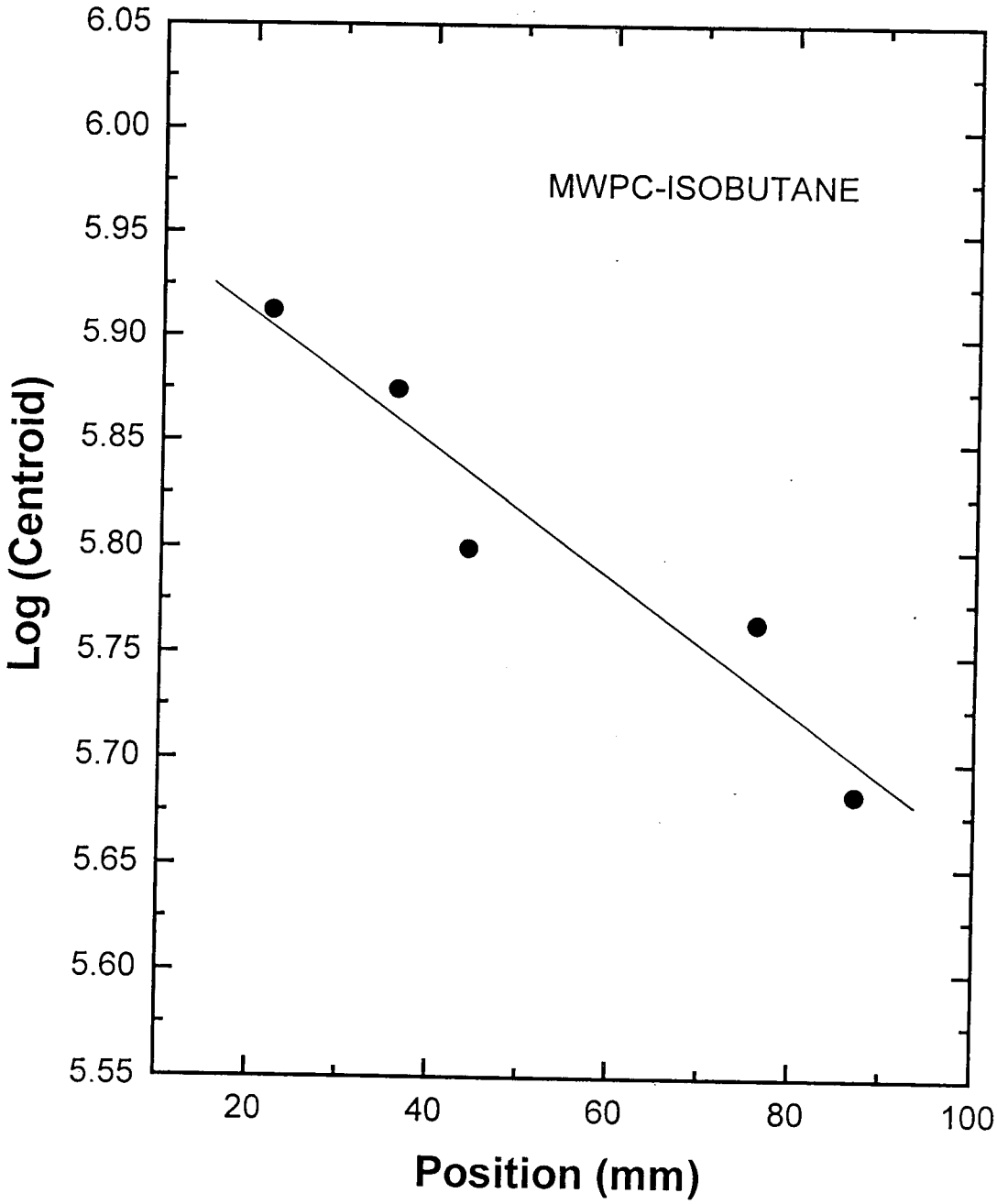

Figure 5.20 : Results of position sensitivity tests for MWPC with varying electrode bias

5.9 Development of PPAC

The first test PPAC developed [10] in our lab -figure 5.21- is mainly a stop type of active area 4 cm x 4 cm. The anode was 8 μm aluminized mylar foil. Cathode connection was taken from PCB insulated from anode foil by a rectangular PCB frame of thickness 0.14 cm. Anode is fixed in the aluminium housing. This housing can be used for testing both prototype PPACs of foil and wire electrodes. Two BNC connectors are used for providing biasing and for taking output signals. Two steel pipes are connected from the top side for the gas inlet and outlet. The detector is mounted on a base for holding vertically. A small stop type PPAC was developed using perspex and aluminium discs sandwitched with a PCB on which a window-cum-electrode foil has been stretched. The window diameter is 1 cm. Output was taken through a BNC connector. Figure 5.21 shows the diagram of inside geometry of PPAC and figure 5.22 shows the outside view from both sides.

5.9.1 Testing of PPAC

The small PPAC was tested with P10 and isobutane gases using ^{210}Po alpha source. Gas pressures ranging from 4 to 20 torr and bias voltage ranging from 260 to 300 V were used for these tests. The second PPAC shown in figure 5.22 was tested for parallel plate geometry, tilted electrode geometry and multi wire geometry [11,12]. For testing tilted electrode geometry, the source was mounted in front of the detector inside the vacuum chamber. The source can be kept at various positions without breaking the vacuum using sliding seal brass rod in horizontal direction. The electrode spacing also varies in this direction. Signals from the detectors were fed to an ORTEC 142IH preamplifier and then to a 571 amplifier. Pulse height spectra were stored on Nucleonix PC-based MCA. Anode voltage in the range 350 to 500 V was used corresponding to reduced field strength S values in the range 110 to 710 V/mbar.cm. A collimated 2.4 μCi ^{241}Am source supplied by BARC (Bombay) was used to get 5.48MeV alpha rays for the measurement.

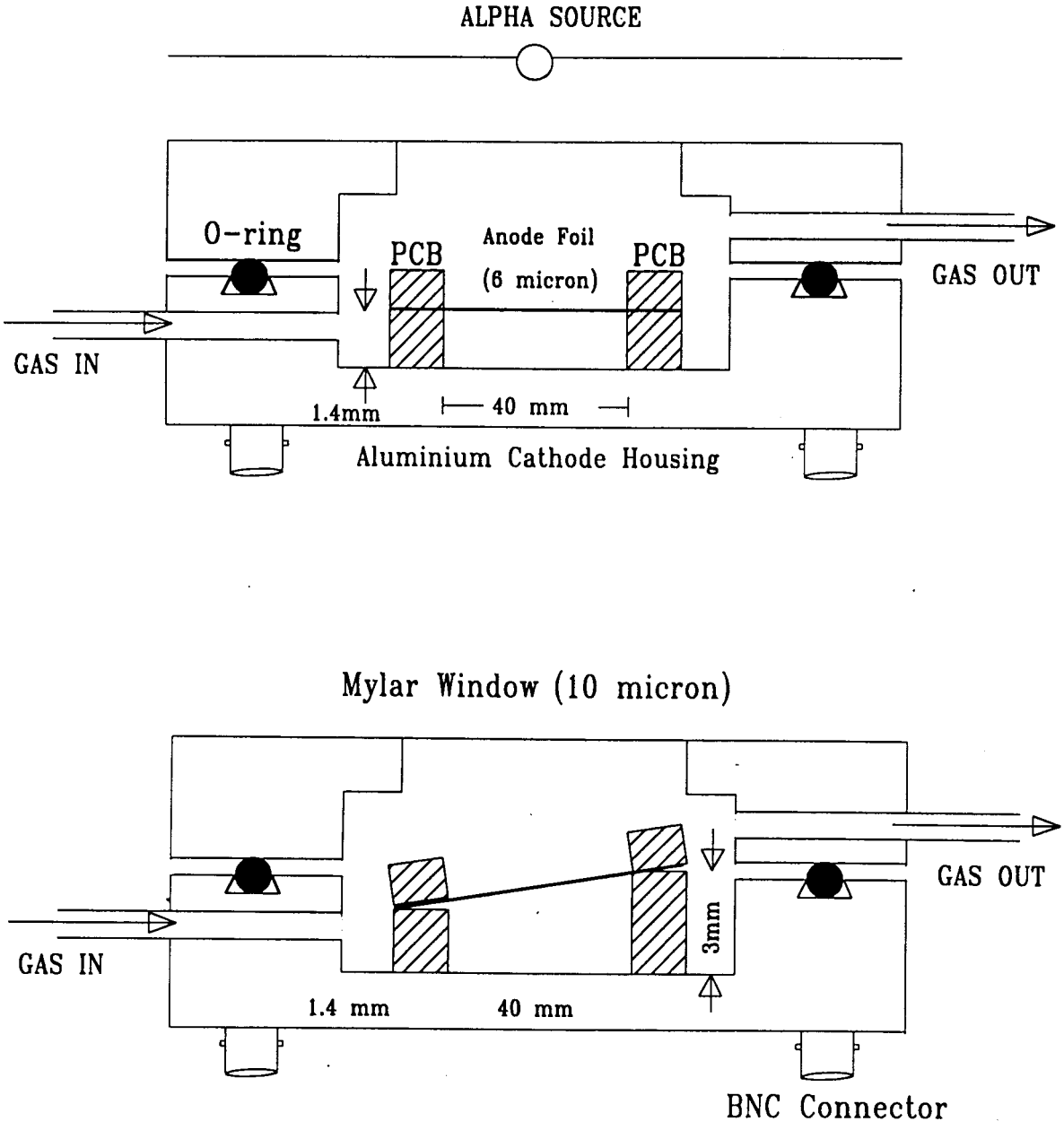

Figure : 5.21 Schematic diagram of the Parallel Plate Avalanche Counter-cum-resistive electrodegeometry-PPAC (top) and Tilted Electrode geometry(bottom).

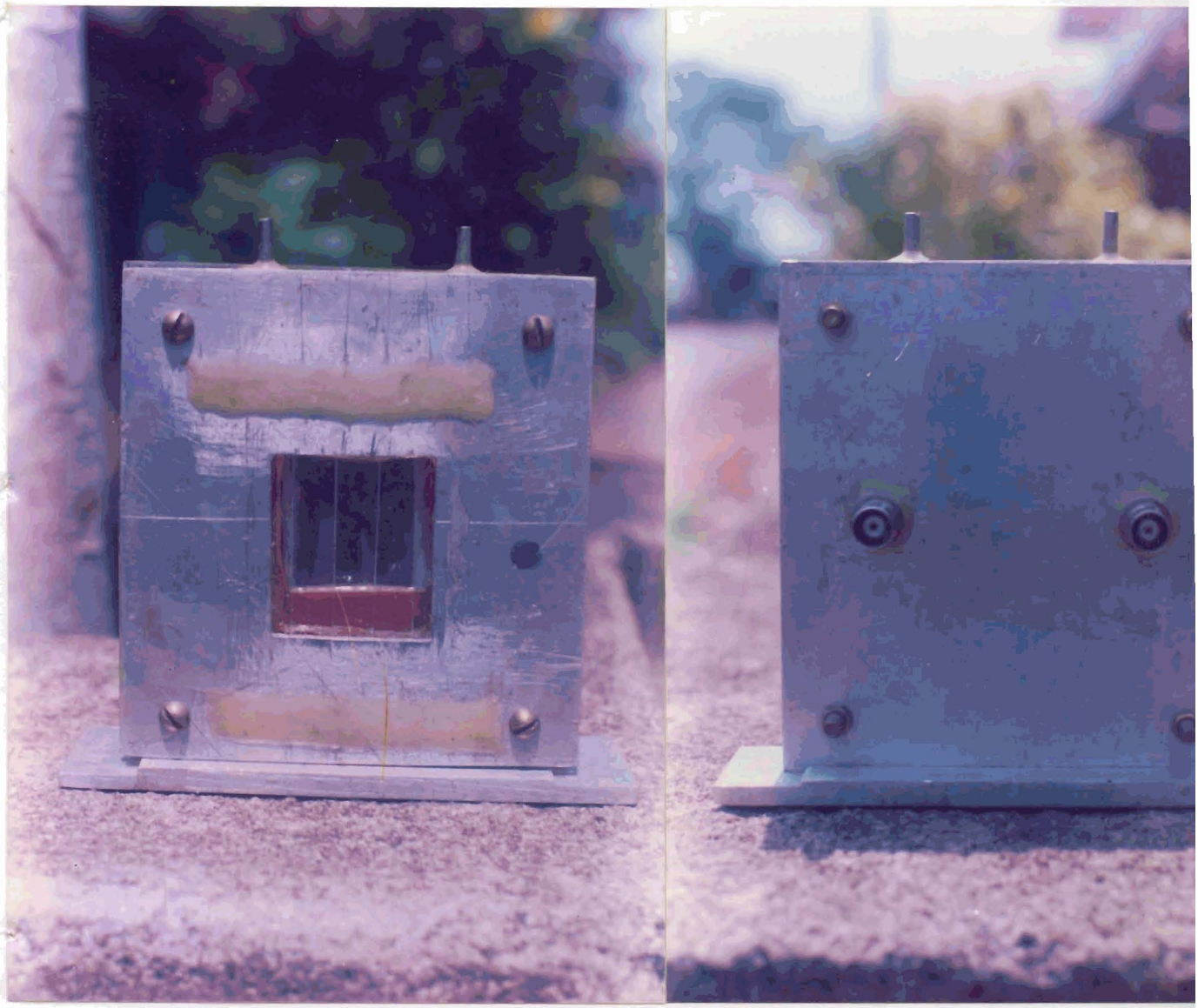

Figure 5.22 : Prototype PPAC used for PPAC, Tilted Electrode and Resistive Electrode geometry – View from window side (left) and connector side (right)

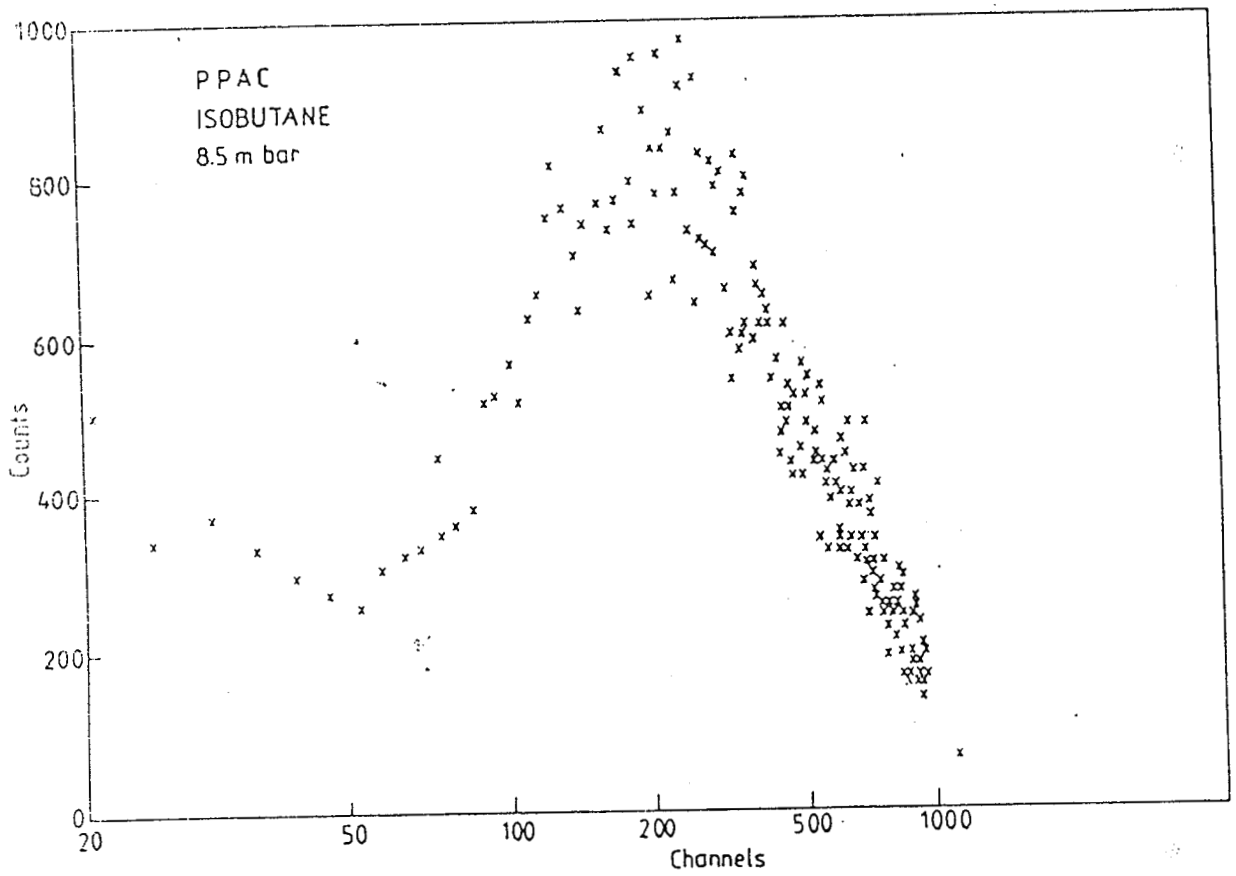

Figure 5.23 : A typical pulse height spectrum for ^{241}Am source taken with tilted electrode PPAC. Note the logarithmic scale on the X-axis

Figure 5.23 shows the typical pulse height spectrum obtained for one position of the source at **P** = 8.5 mbar of isobutane. The peak pulse heights are obtained from plots similar to that in figure 5.23. These are plotted against position X in figure 5.24 for two electrode configurations used. The excellent position linearity is evident from the figure 5.24. Similar results have been obtained for other gas pressures in the range 4 to 10 mbar. Measurements with P10 gas also gave similar results. The obvious problem in this method is the comparatively poor resolution. Figure 5.25 shows the variation of V with **P** for the two PPACs. Figure 5.26 shows the variation of peak pulse height with bias voltage for the two PPACs.

5.9.2 Resistive Electrode PPAC

If the reduced electric field S is allowed to vary with position, the pulse height becomes position dependent and this offers a possible method to derive position information. This can be achieved in practice by varying the electrode spacing 'd'. Another variation tried to get position sensitivity was to use a resistive electrode [5] across which a voltage was applied in addition to the cathode-to-anode voltage. This will produce a varying S across the plane of the PPAC just like the tilted electrode geometry. The resistive electrode used was silicon wafer of resistivity 20 kΩ.cm. A voltage of 60 V was applied across it.

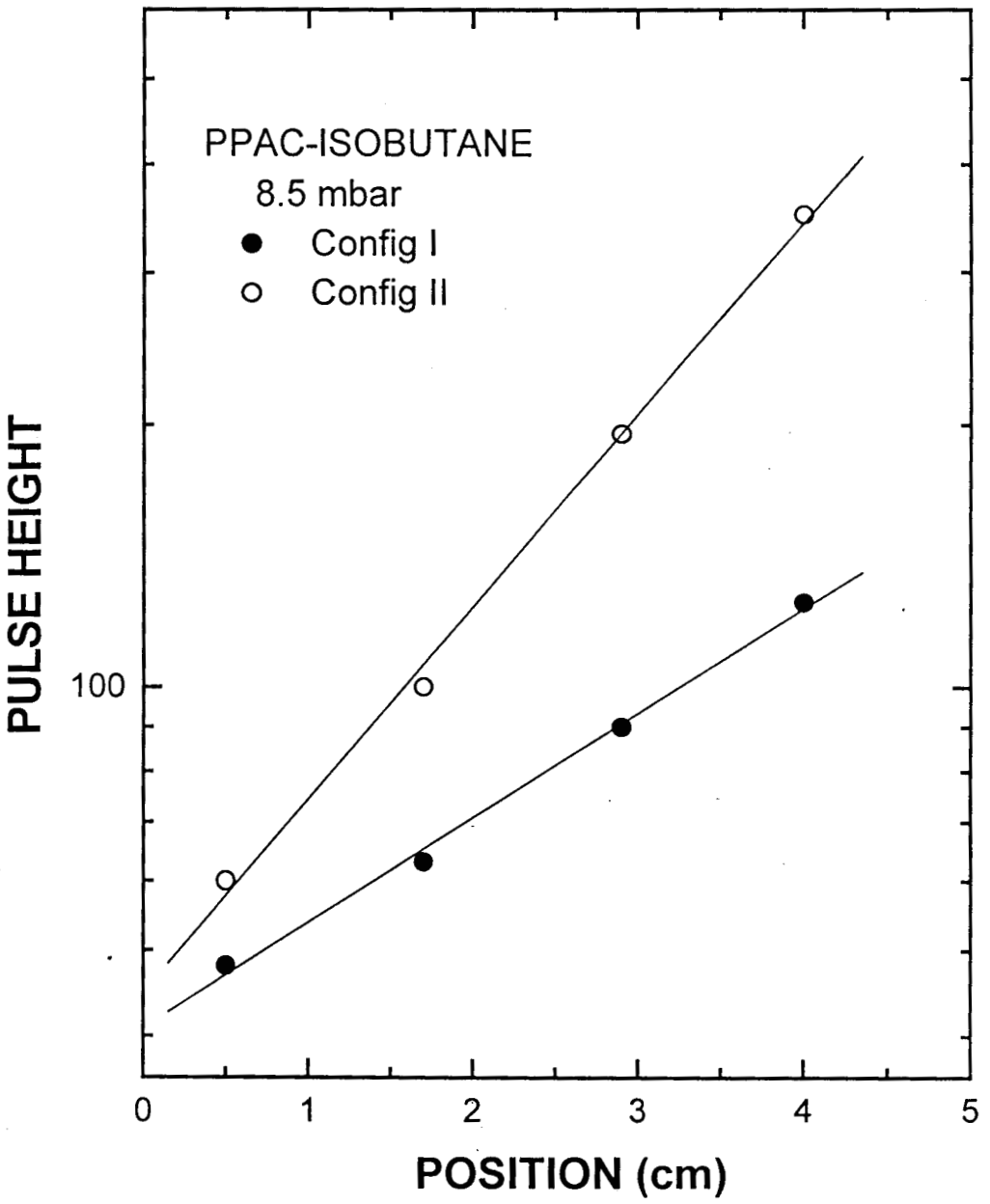

Figure 5.24 : Position calibration for tilted electrode geometry PPAC for two electrode configurations.

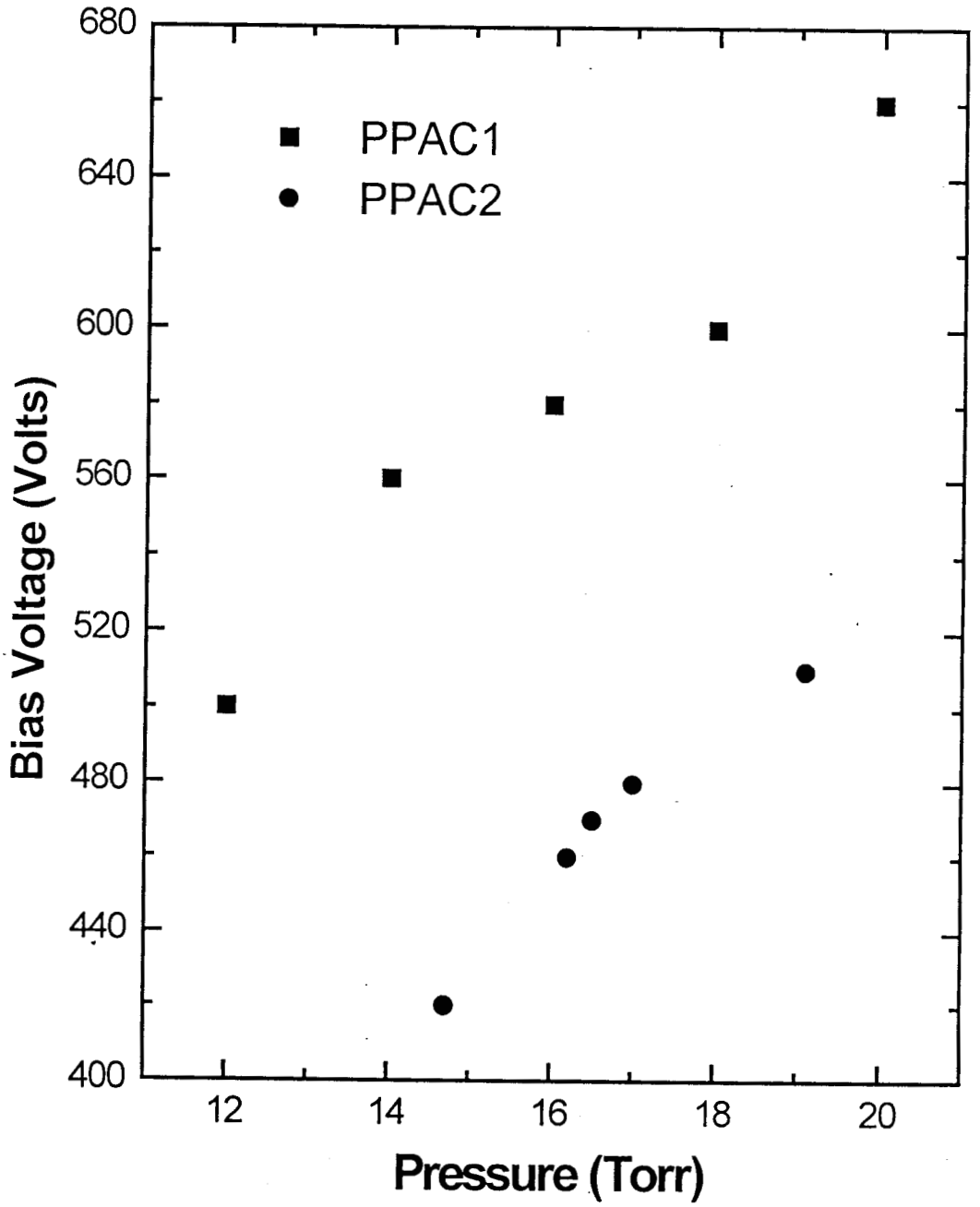

Figure 5.25 : Variation of the bias voltage with pressure for the two PPACs.

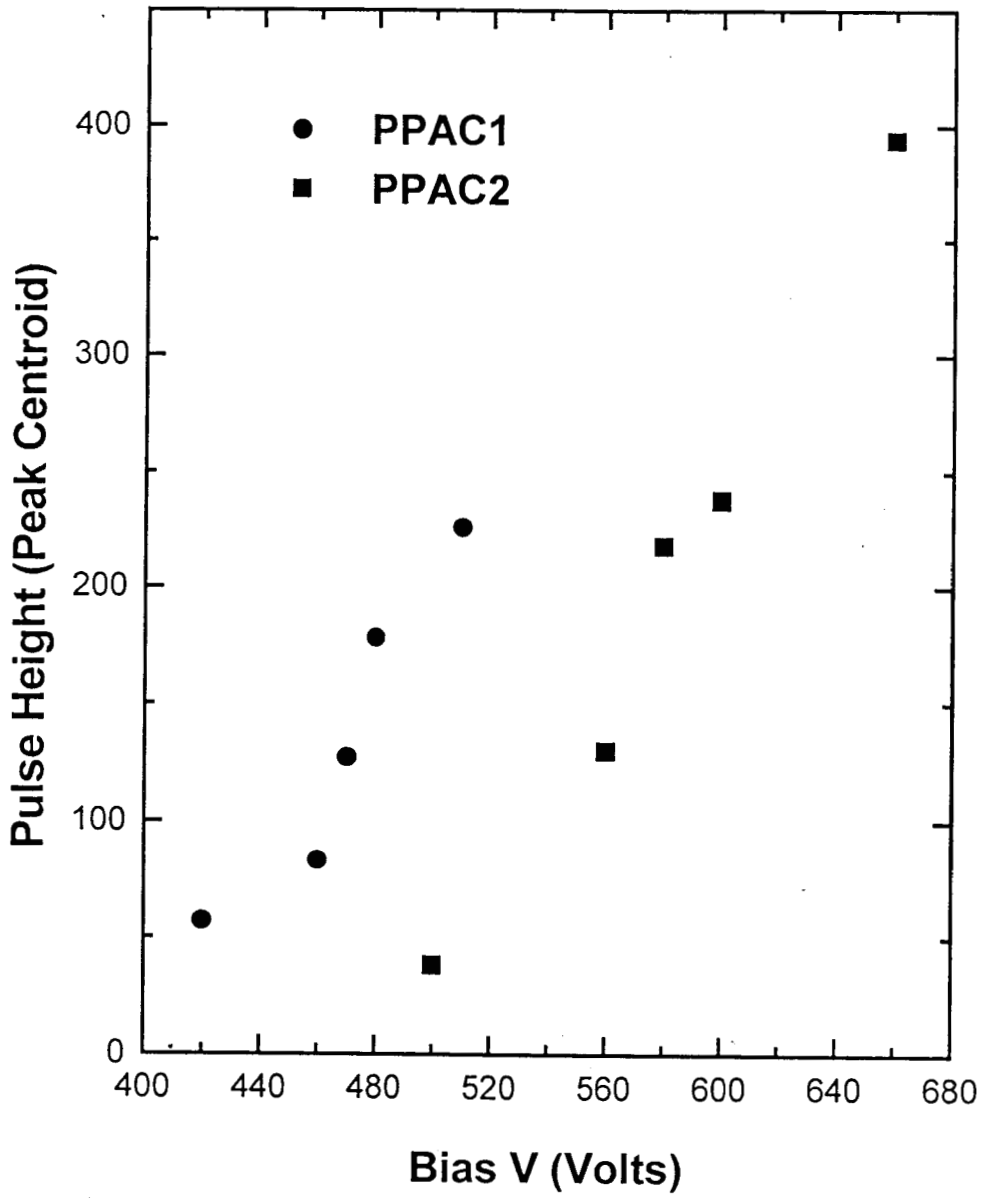

Figure 5.26 : Variation of the pulse height with the bias voltage for a particular source position.

5.9.3 Tilted electrode PPAC

In an effort to find out easier techniques to derive position information from simple PPAC configurations and using simple electronics we have explored the possibility of using tilted electrode geometry [11,12]. In most of the available formulae for gas gain the pulse height of the PPAC is seen to have a more or less exponential dependence on the reduced electric field and indirectly to the electrode spacing 'd'. If the spacing between the electrodes is made to vary across the plane of the PPAC, the reduced electric field varies and consequently the pulse height will also vary depending on the position of incidence of the heavy ion. The feasibility of this method has been tested for a PPAC with isobutane gas at pressure ranging up to 20 mbar. Figure 5.23 shows a typical PPAC spectrum. The position calibration of PPAC is shown in figure 5.24. In a normal PPAC, the electrodes are uniformly spaced apart and the electric field is uniform. The pulse height of the output signal which depends on the reduced electric field strength S = V/Pd. This S is there fore a constant and independent on the position of incidence of the heavy ions. The usual method to derive the position information is to use a wire plane as one of the electrodes and to obtain position by resistive charge division method or delay line readout method. The active area of the tilted electrode detector was 4 cm x 4 cm. Two electrode configurations were used where the electrode spacing 'd' was varied according to the relations

$$d(x) = 1.4 + 0.4x \text{ and } d(x) = 1.4 + 0.75x \qquad (5.2)$$

Here 'd' is in mm and 'x' in cm. The detector was of the stop type with an entrance window of mylar of thickness 10 microns. The electrode was one side aluminized poly propylene film with thickness 6 microns mounted on PCB frames. The window was supported by a nylon mesh. The configuration shown in figure 5.21 is called a tilted electrode PPAC. Isobutane supplied by M/s Alphagaz (France) and P10 supplied by IOL(Madras) were used as the fill gases. The standard gas handling system used for testing is shown in figure 5.13. This ensures uniform gas flow at specified pressures. The pressure control was made manually by using precision needle valves. Gas pressures were measured by a Leybold – Heraeus capsule vacuum gauge of range 4 to 10 mbar.

5.10 Signal-to-noise ratio

The undesired fluctuations super imposed with the detector signal is called noise, which can degrade the amplitude information carried by the detector pulse. At the beginning of the signal the noise ratio level will be dominating and comparable with the signal. Noise can be generally classified in to two types-series noise and parallel noise. The thermal noise in the FET of preamplifier belongs to series noise where as the noise due to the fluctuation in the detector leakage current and preamplifier input current constitute the parallel noise. By using pulse shaping linear amplifiers, the broad spectrum of noise can be removed by selective (low pass and high pass) filtering without considerable attenuation of the signal components using a combination of differentiating and integrating circuits. Signal is widely separated in time where as noise is broadly distributed in frequency. The signal-to-noise ratio becomes best if the signal pulses are in the form of an infinite cusp. But it is difficult to obtain cusp shaped signal due to the limitations of the practical shaping circuits. We have obtained Gaussian pulses for our detectors which is preferable than cusp shaped pulses due to the practical difficulties in processing cusp shaped signal. The signal-to-noise ratio for our detectors was obtained within the acceptable level.

5.11 Results and Discussions

The performance of the SWPC, MWPC and PPAC were investigated mainly using 2.4 μCi 5.48 MeV alpha source (^{241}Am). The signal collecting electrodes were connected to low noise, slow charge sensitive preamplifiers. Pure isobutane gas has been chosen as the working gas because of its high absorption power for light quanta. Large dE/dx and high efficiency are the other advantages of isobutane. From the reduced pulse height spectra, the peak pulse height in channels (h) were noted as a function of P and V - that is as a function of the reduced electric field strength S. The data has been analyzed by means of the generalized Aoyama formula[13,14] for m = 0, 1/2 and 1/3. Also the data were analyzed by means of Diethorn expression as a special case of Aoyama relation for m = 1.

The gas gain M is related to the pulse height h according to the relation ln M = ln(h/fP). In this relation 'f' is the over all gain (f = geK/CW) which in principle can be determined by measuring 'g' experimentally and by knowing other constants. However 'f' was treated as a free parameter along with the constants K and L of the Aoyama formula. A least square fitting was done for determining K and L for various 'f' values. The value of 'f' giving minimum χ^2 (chisquare) was chosen and the corresponding K and L were taken as the best fit. Figure 5.27 shows the Aoyama plot for m = 0 with SWPC using isobutane gas. The results [13] of measurement of Aoyama parameters is given in table 5.2 (using SWPC) and table 5.3 (using PPAC), Diethorn parameters using SWPC in table 5.4 and Zastawny parameters (using PPAC) in table 5.5.

Gas Used	m	L $[V.cm^{-1}.torr]^{1-m}$	V_i (V)
Isobutane	0	345	11.26
	1/2	48.4	10.90
	1/3	118	11.10
P10	0	513	12.70
	1/2	37.1	13.10
	1/3	84.3	13.60

Table 5.2 : Aoyama parameters using SWPC

Gas Used	m	L $[V.cm^{-1}.torr]^{1-m}$	V_i (V)
Isobutane	0	206	9.92
	1/2	12.9	9.99
	1/3	32.9	10.00
P10	0	307	13.83
	1/2	23.7	13.01
	1/3	52.8	13.39

Table 5.3 : Aoyama parameters using PPAC

Gas used	S_c $[V.cm^{-1}.torr^{-1}]$	D (V^{-1})
Isobutane	19.61	0.0216
P10	170.10	0.027

Table 5.4 : Diethorn parameters using SWPC

Gas used	S_c $[V.cm^{-1}.torr^{-1}]$	D' (V^{-1})
Isobutane	0.018	1.71
P10	0.025	1.67

Table 5.5 : Zastawny parameters using PPAC

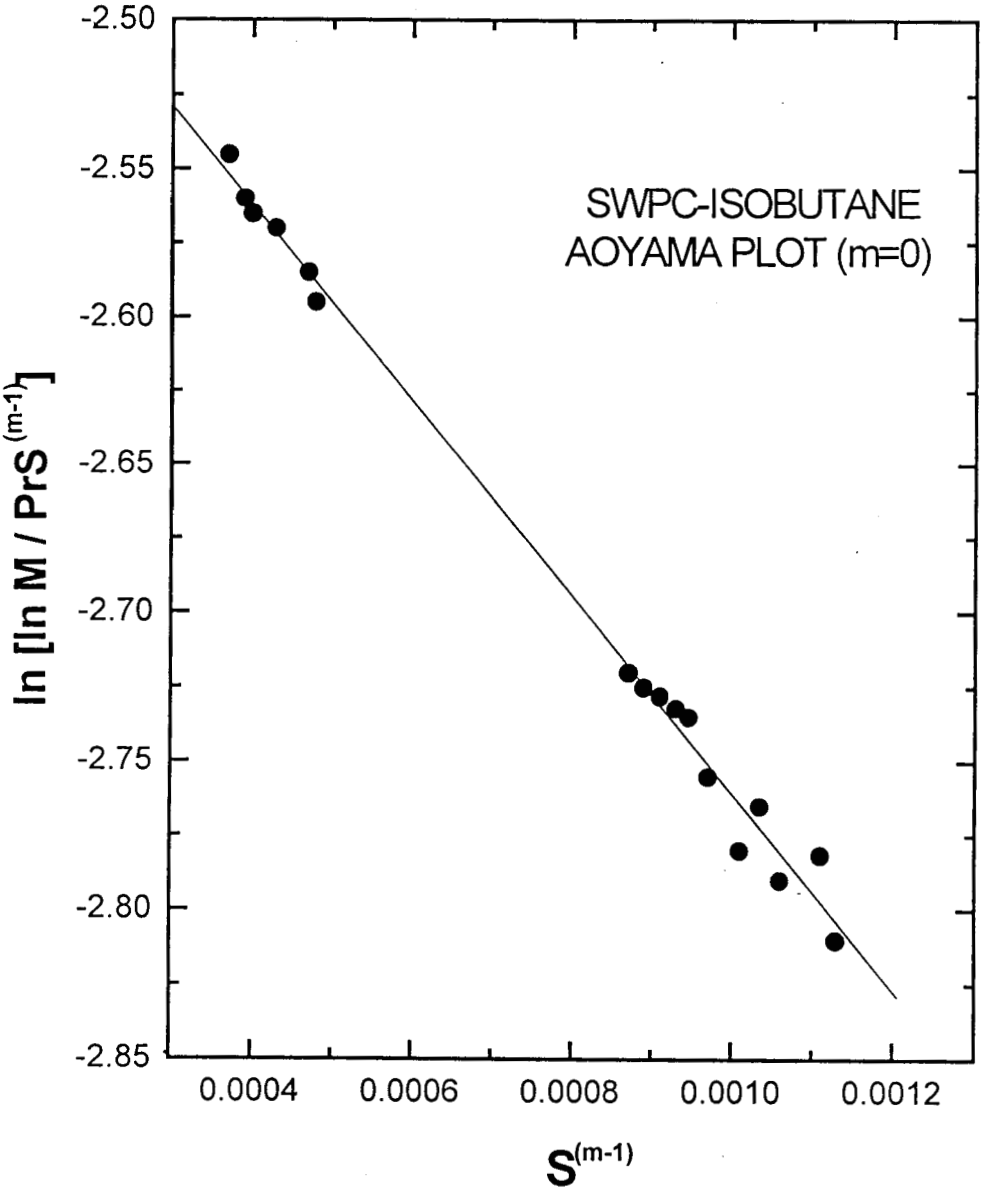

Figure 5.27 : A typical Aoyama plot obtained using SWPC with isobutane gas for m = 0.

5.11.1 Measurement of First Townsend Coefficient (α)

The constants C and K in equation (4.66) depends on the parameters A and B. The value of the over all gain f is unknown. It is treated as an apriori free parameter and least square fitting was done on ln[ln(h/**P**) – ln f] versus 1/Z with various ln f values to minimize chisquared [15,16]. A minimum chisquare of the order of 2.548×10^{-3} were obtained for ln f values 0.12 for P10 and -0.34 for isobutane. From the best fit values of C and K the slope and y-intercept of the plots were measured. From the y-intercept of the order of 3.03, the value of A and from the slope of the order of 6.59, the value of B were calculated. Using A and B the first Townsend Coefficient α was calculated as per the expression $\alpha/P = A \exp[-B/(E/P)]$. The same procedure was adopted for both P10 and isobutane gases for determining α. Figure 5.28 gives the result of the analysis done for P10 and isobutane based on equation (4.66). Figure 5.29 gives the variation of α/P as a function of E/P or $Z = V_0/P$ using SWPC. It was found that for a wide range of E and **P** the ratio α/P is a unique function of E/**P**.

5.11.2 Comparison of Townsend Coefficients measured using SWPC and PPAC

Using ^{241}Am source, the pulse heights of the SWPC and PPAC signals were noted for various values of the applied voltage V_0 and gas pressure **P** for P10 and isobutane gases. As explained in previous chapter a linearised relation between pulse height 'h' and the ratio $Z = V_0/P$ was obtained for SWPC. A similar linear expression can be obtained for PPAC by assuming $\alpha/P = A \exp(-BXd)$ as follows.

$$\ln [(1/P)\ln(h/P) - \ln f] = \ln(Ad) - BXd \qquad (5.3)$$

where X=P/V and 'd' is the inter electrode spacing. The constants A and B are determined from the observed values of slope and y-intercept of the resulting straight line graph.

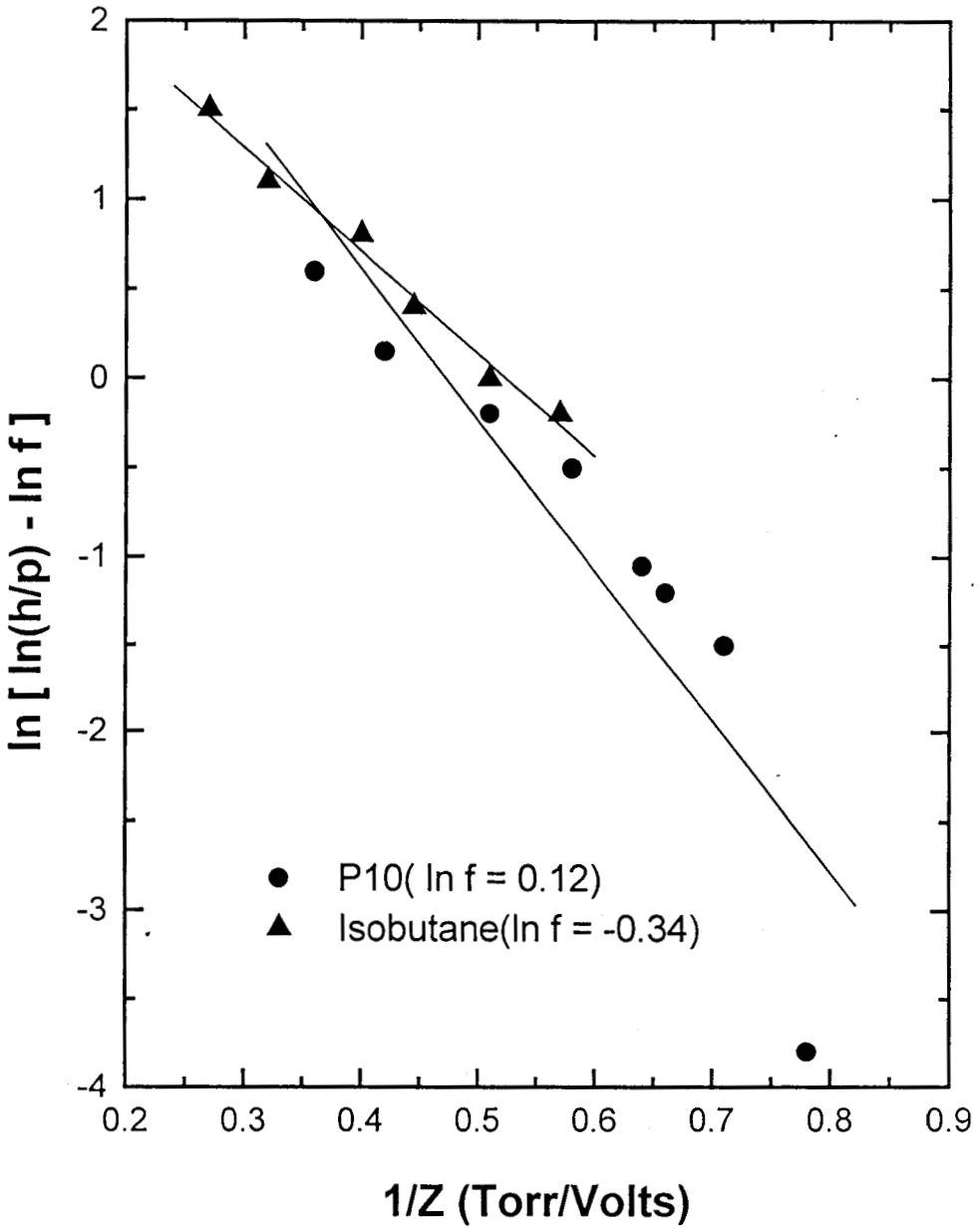

Figure 5.28 : Plots showing the dependence of ln[ln(h/P)-ln f] on the value of 1/Z=V/P for SWPC using P10 and isobutane.

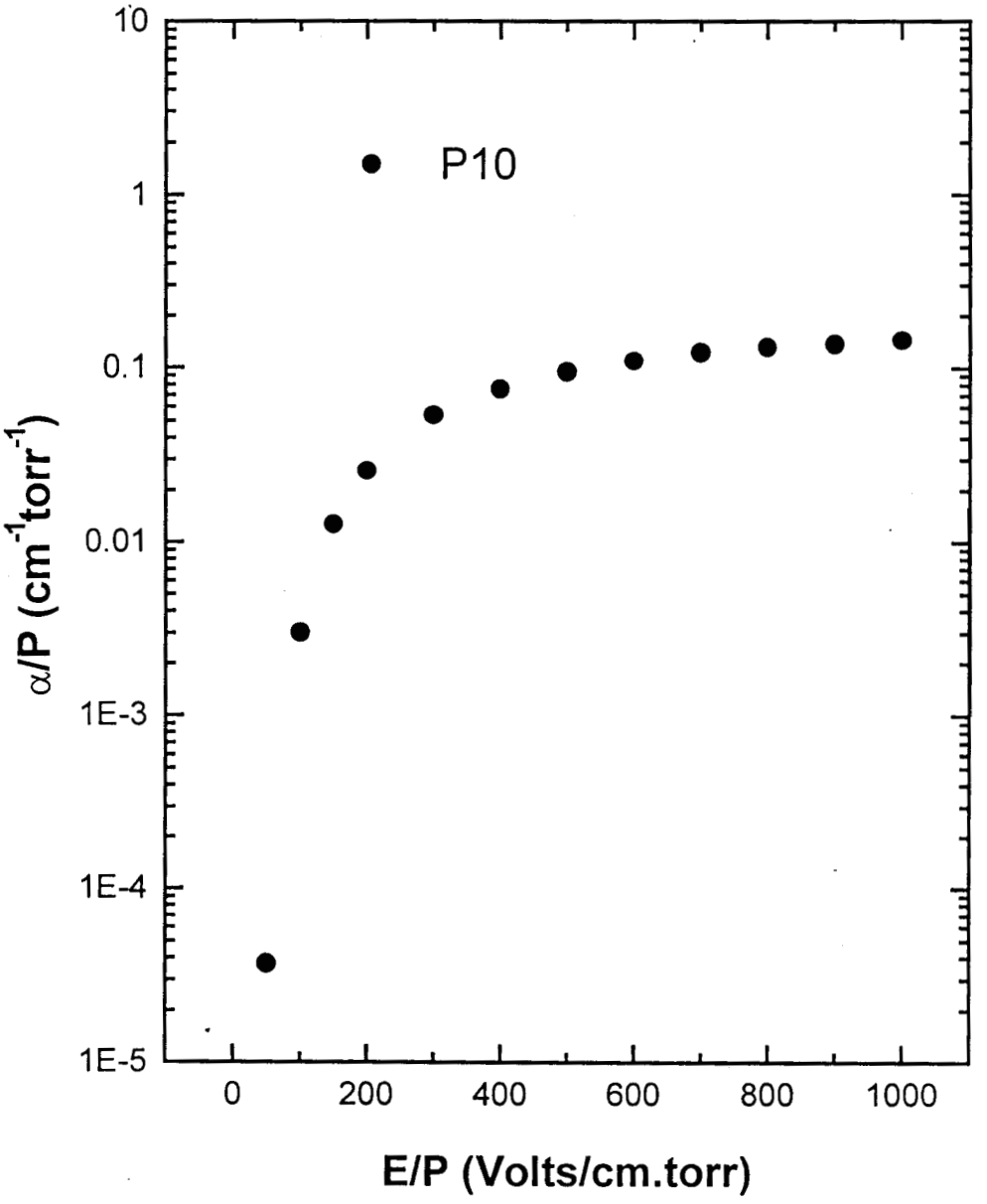

Figure 5.29 : Variation of α/P with reduced field.

The values of the coefficients obtained is given below [17]. It was observed that in the case of SWPC the coefficient values lie over a finite range depending on the number of points used in the calculation of A and B. But for PPAC such an effect is not observed. The range obtained with SWPC for isobutene is not so large and is close to and includes the values of the coefficients obtained with PPAC for isobutene. This verifies the basic assumption of the approximate constancy of A and B with reduced electric field assumed in the derivation of the linearised relation between pulse height 'h' and $Z = V_0/P$.

Gas used	DETECTOR	A(Torr.cm)	B[$V.cm^{-1}.Torr^{-1}$]
P10	SWPC	10 to 22	40 to 140
Isobutane	SWPC	18 to 35	220 to 510
Isobutane	PPAC	21.6	407.6

Table 5.6 : Values of A and B for P10 and isobutene

5.11.3 Measurement of Gas Amplification

The plots of the experimental value of ln ln(M/Pr_aS_a) are given in figure 5.30 and figure 5.31 for SWPC measurements for P10 and isobutane [13]. Here 'r_a' is the anode wire radius and S_a is the S value at the surface of the wire. Similar plots of ln(M/PdS) are given in figure 5.32 and figure 5.33 for the PPAC measurements for m = 0,1/2 and 1/3 where 'd' is the electrode spacing. Diethorn [18] plots (m=1) are given in figure 5.34 using SWPC. The PPAC data clearly do not satisfy Diethorn formula. Hence for these data the modified Diethorn formula viz that of Zastawny [19] has been used. The results are plotted in figure 5.35 for both gases used. It has been observed that the variance values are

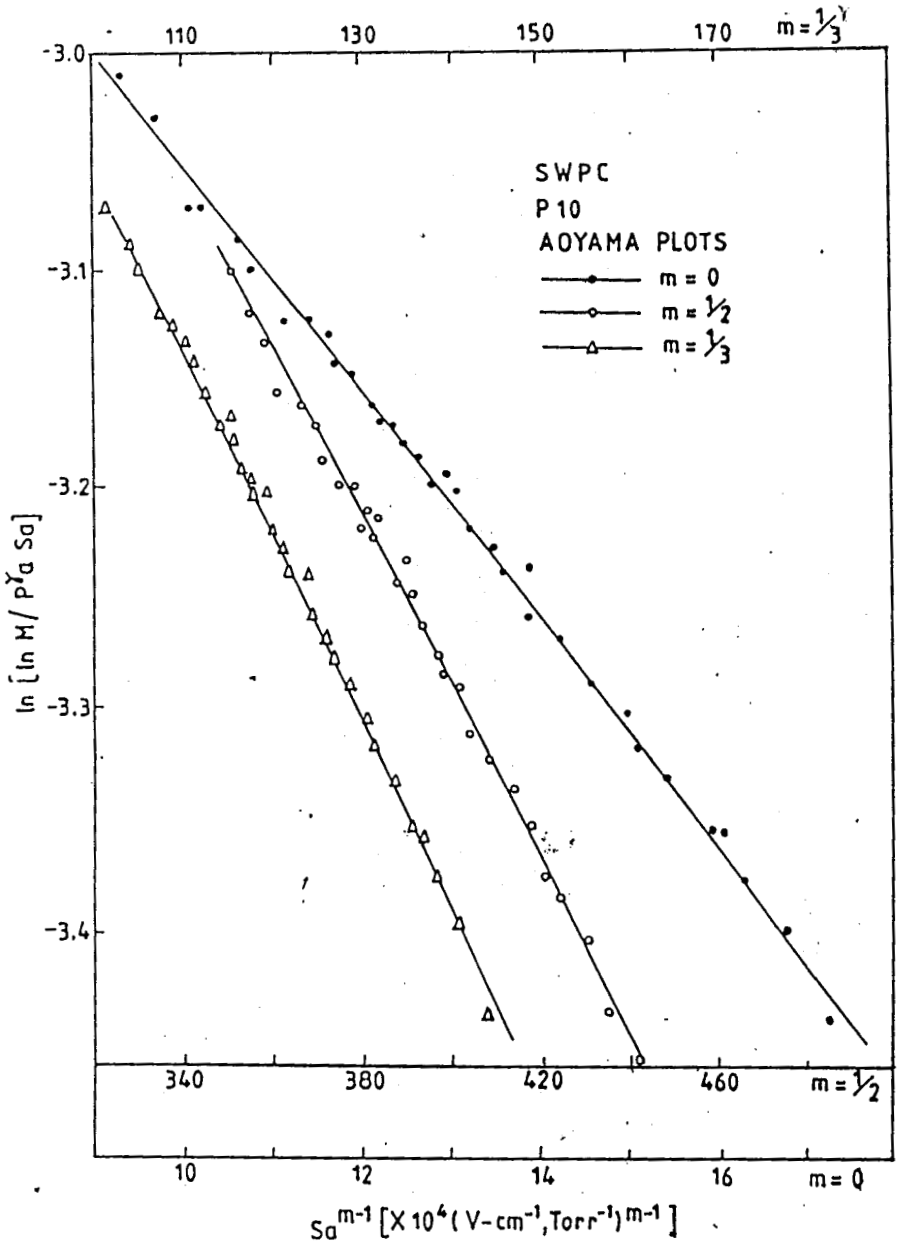

Figure 5.30 : Experimental plots of $\ln[\ln M/Pr_aS_a]$ vs S_a^{m-1} for SWPC using P10. The solid lines are the Aoyama fits for m = 0, 1/2 and 1/3.

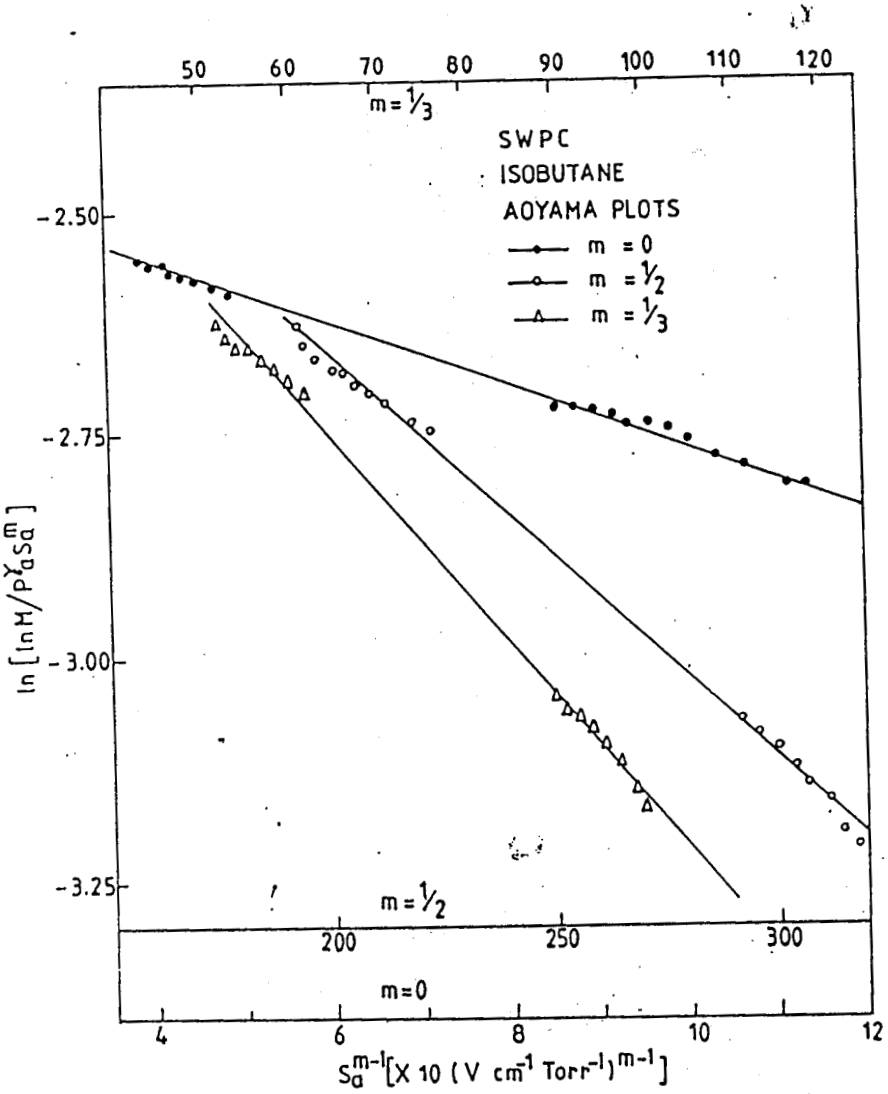

Figure 5.31 : Experimental plots of $\ln[\ln M/Pr_aS_a]$ vs S_a^{m-1} for SWPC using isobutane. The solid lines are the Aoyama fits for m = 0, 1/2 and 1/3.

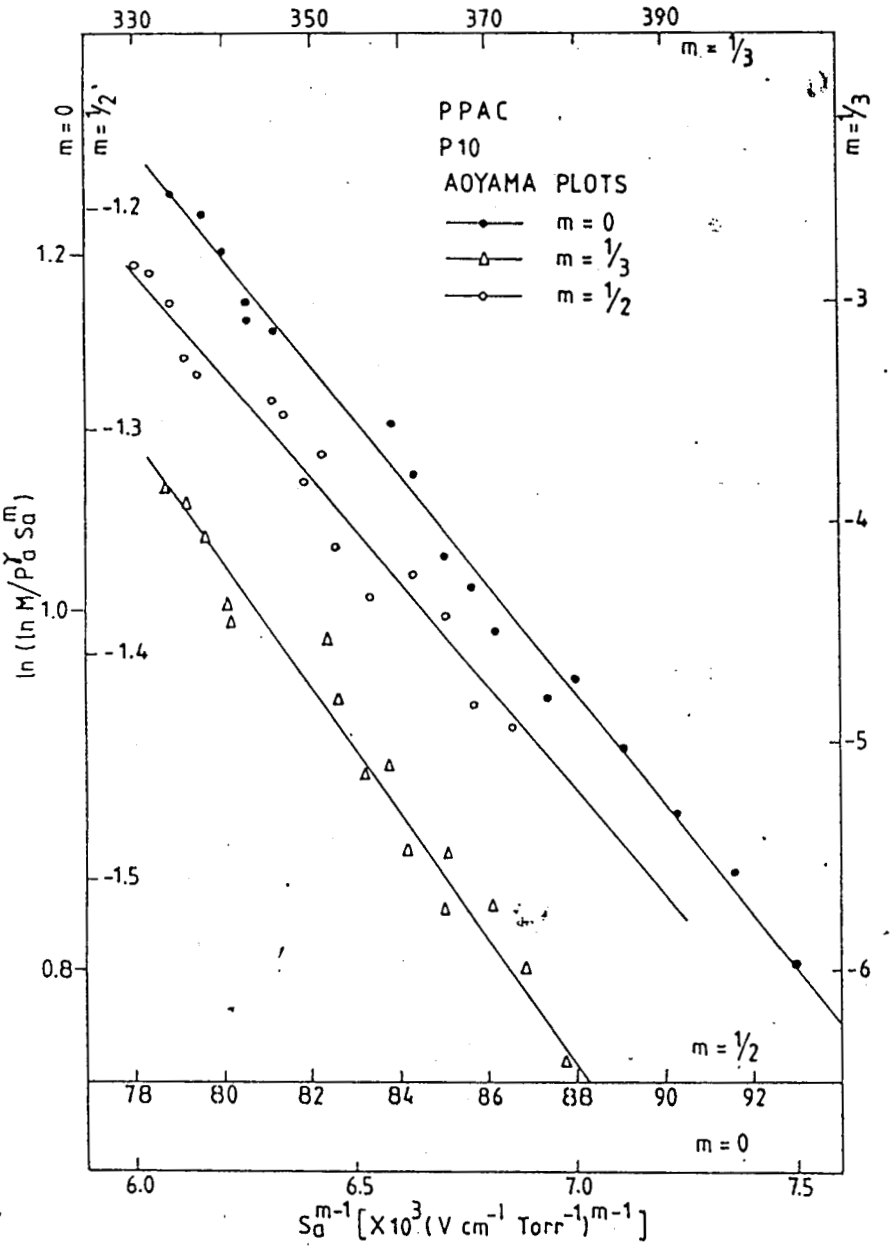

Figure 5.32 : Experimental plots of $\ln[\ln M/Pr_aS_a^m]$ vs S_a^{m-1} for PPAC using P10. The solid lines are the Aoyama fits for m = 0, 1/2 and 1/3.

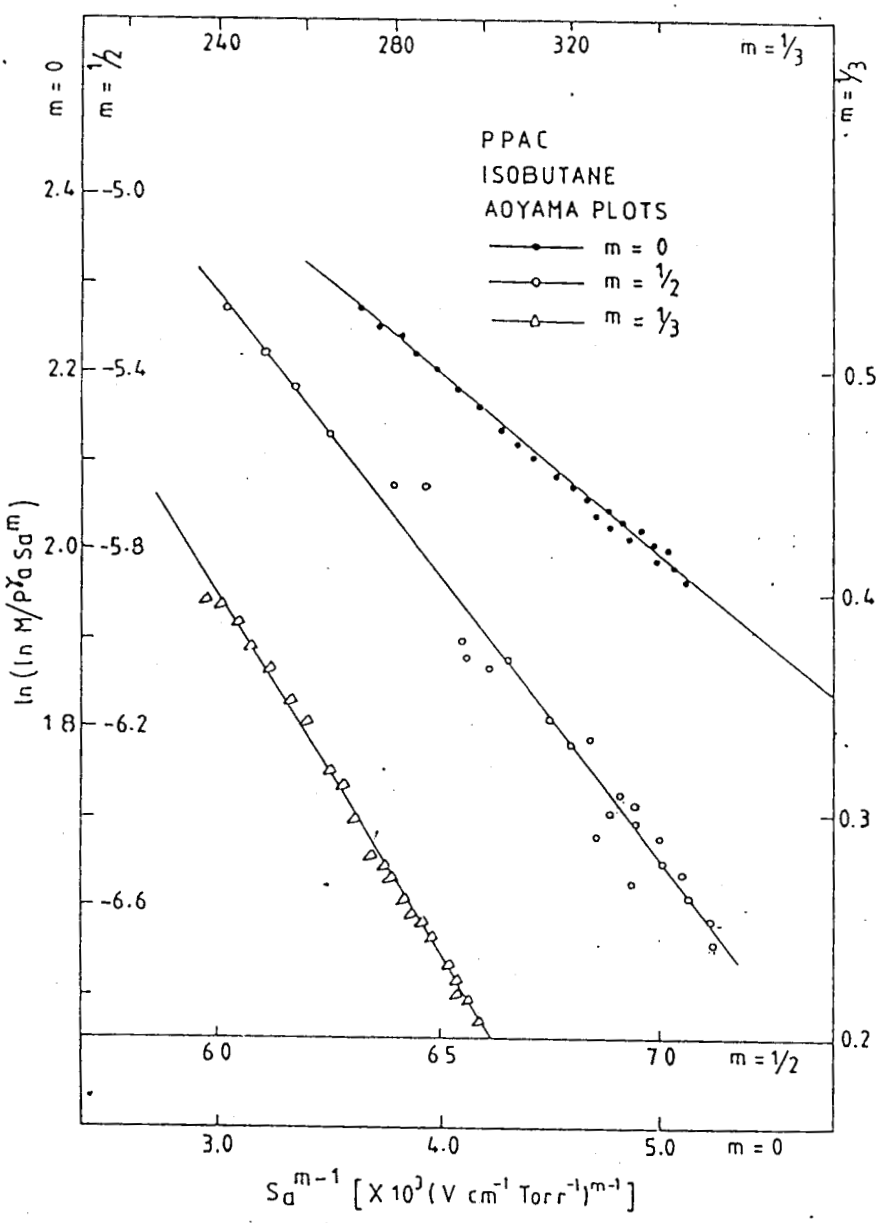

Figure 5.33 : Experimental plots of $\ln[\ln M/Pr_aS_a^m]$ vs S_a^{m-1} for PPAC using isobutane. The solid lines are the Aoyama fits for m = 0, 1/2 and 1/3.

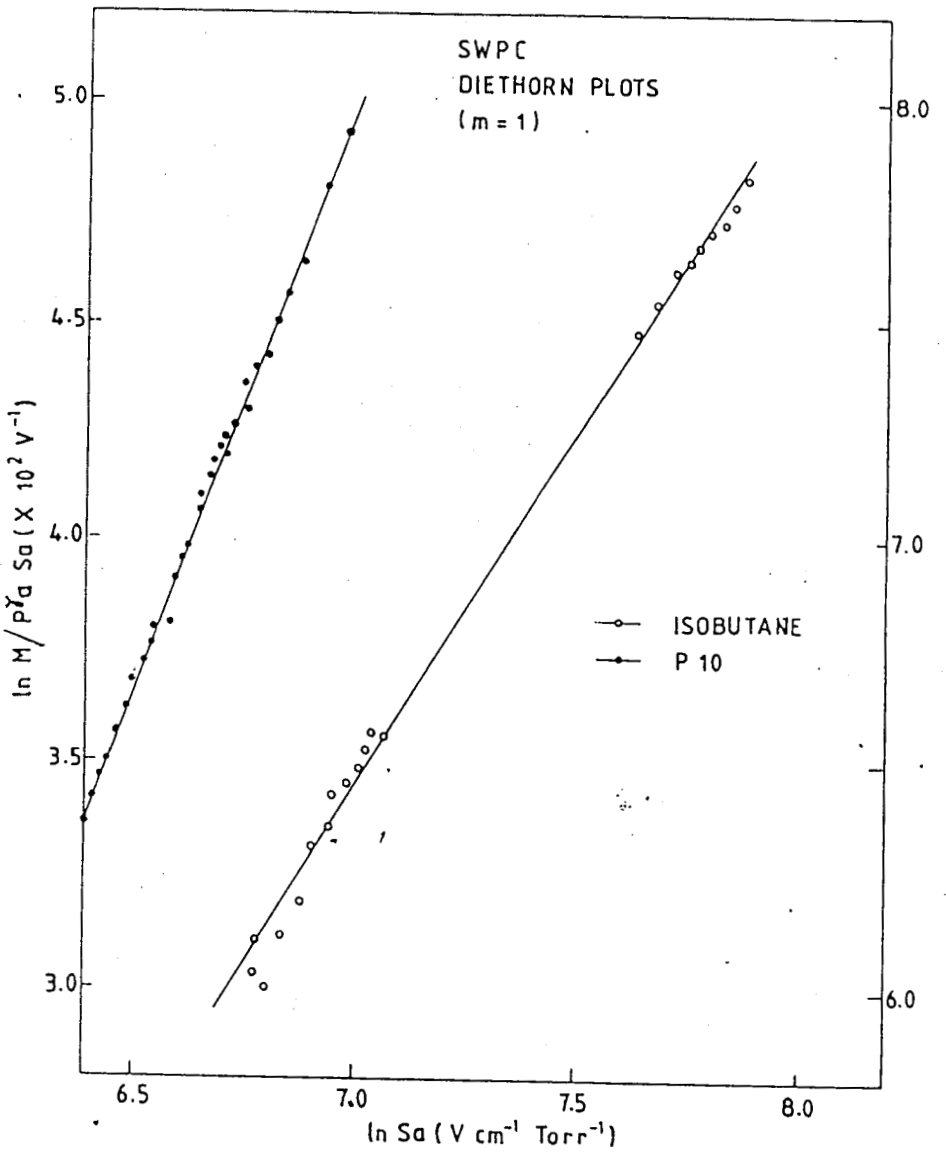

Figure 5.34 : Diethorn plots for SWPC for P10 and isobutane

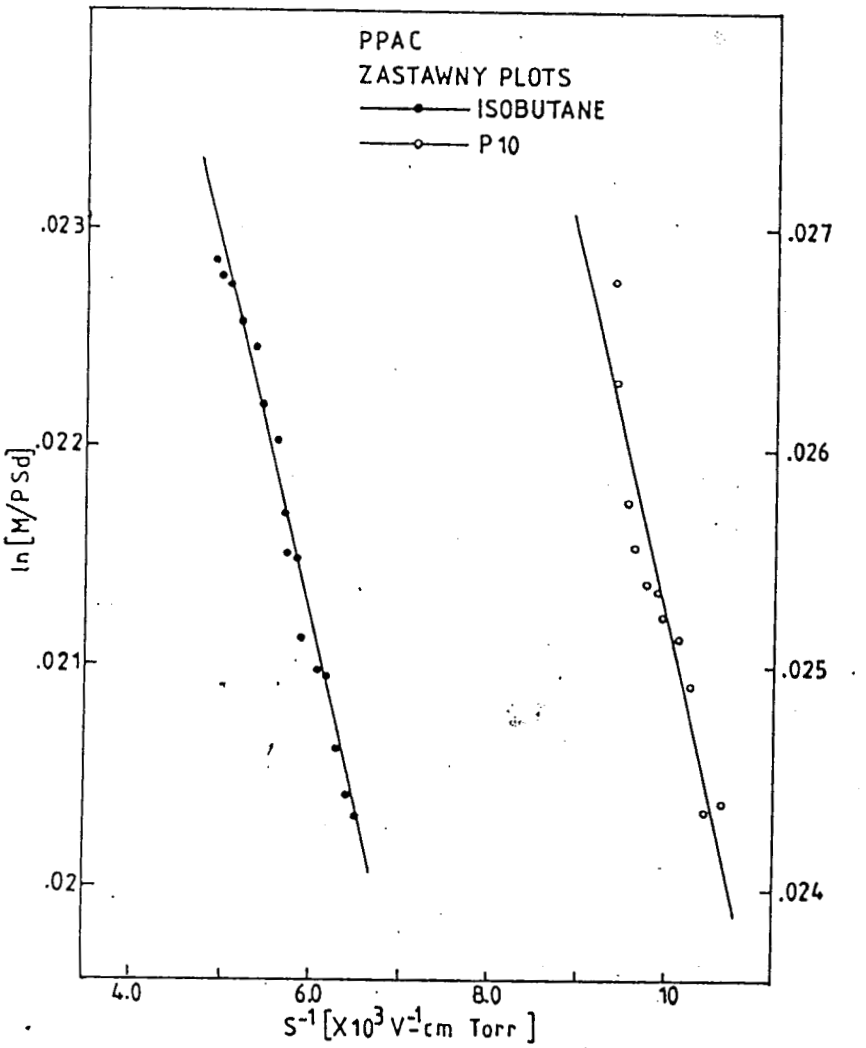

Figure 5.35 : Zastawny plots for PPAC for P10 and isobutane

minimum for m = 0 in the Aoyama expression [14] and for Diethorn expression as far as SWPC data are concerned. For the PPAC data, the variance were found to be minimum again for m=0 in the Aoyama expression and for the modified Diethorn expression (Zastawny formula). An over all error about 10% has been estimated for the values of Aoyama and Diethorn parameters. It is seen that the V_i values obtained from the SWPC data are agreeing well with those obtained from the PPAC data using P10. For isobutane the V_i values agree within the experimental error. However L values are seen to be different. This may be attributed to the fact that in the case of SWPC the reduced field strength S vary over a very wide range where as in the case of PPAC it is a constant. The observed variation in the value of L suggests a possible residual dependence of L on S so that in the case of the SWPC data what we are deriving from the fits is an average value only.

5.12 Summary and Conclusions

A good deal of experience has been gained in the fabrication and testing of various types of gas detectors for detecting heavy ions. Development of focal plane detectors progressed steadily and rapidly. Evolution from simple SWPC to sophisticated multiparameter systems capable of determining energy, energy loss, position, angle of incidence and time-of-flight of reaction products is quite fascinating. The position resolution of SWPC as a focal plane detector is not sufficient. This led to the development of MWPC having a better position resolution. A better energy resolution is also obtained. The final MWPC in the present form has reasonably good position sensitivity. It can be used as the end detector of HIRA focal plane ionization chamber for time-of-flight measurements. The performance of this detector is satisfactory. SWPC is simple to construct in a variety of forms, easy to operate and require simple electronics for testing. It is easy to make it position sensitive and by choosing suitable gas pressure and bias voltage, SWPC can be used for the detection of light and heavy charged particles, X-rays, gamma-rays, neutrons etc. SWPC can be used in combination with the other detectors

as detector telescopes and can be used for time-of-flight (TOF) measurements over the long flight path within the recoil mass spectrographs. The position resolution of the focal plane detectors is limited by target thickness effects and multiple scattering on the components of detector array. In such cases proportional counters can be used for position sensitivity. The position linearity of the SWPC has been verified. The position resolution obtained was about 5 mm, which can be hopefully improved by using higher resistivity anode wire. Both the tilted electrode geometry [11,12] PPAC and the PPAC with resistive anode [5] are simple and novel methods for deriving the position information using a PPAC detector. With more refinements and modifications, they can be adapted for the final PPAC detector for the HIRA at NSC. In this methods the reduced electric field varies across the plane of PPAC by using a resistive anode or by varying the spacing between the electrodes. The pulse height will also vary depending on the position of incidence of heavy ions. The feasibility of these methods are studied using PPAC with isobutane gas at pressures up to 10 mbar. The measurements of the Townsend coefficients [15] by measuring the parameters A and B constitute the first attempt in our knowledge which yielded new data useful in many applications of gas detectors. The basic formula for α/P proposed by Aoyama is applicable to various counters and gas conditions. Diethorn, Williams-Sara [20] and Zastawny formula can be derived as special cases of Aoyama's basic formula. The analytical form for α/P assumed by Rose-Korff [21] and Charles [22] could not exist separately, but exist in a combined form. Aoyama's generalized gas gain formula deriyed from basic α/P formula is found to fit for the experimental gas gain data measured by us for P10 and isobutane. Reasonable values for the Aoyama parameters – effective ionization potential (V_i) and L are obtained using SWPC and PPAC, by fitting of the gas gain formula. The generalized gas gain formula proposed by Aoyama is found applicable to many kinds of gases filled at a pressure of around 1 atm and to the counters other than SWPC such as PPAC. The measurements on gas amplification in P10 and isobutane constitute new data which will be quite useful in many applications of the gas detectors.

References

[1] J.L.C. Ford, Nucl. Instr. and Meth.**162**(1979)277.

[2] CAMAC Tutorial issue, IEEE Trans. Nucl. Sci. **NS-20, No.2**(1973).

[3] Glenn. F. Knoll,"Radiation detection and Measurement", John Wiley, Singapore (1989).

[4] Joby Antony, E.T.subrahmanyan and P.P.Shakkeeb, Proced. DAE Symp. on Nucl. Phys. 38B(1995).

[5] K.M. Varier, B.R.S. Babu, Antony Joseph and P.P. Shakkeeb, DST Project Completion Report, Calicut(1995).

[6] G.C.Ball, Nucl. Instr. and Meth. **162**(1979)263.

[7] R.Rock, G. Braun, H. Eber, K. Lubelsmayer, W. Karpinski, D. Pandoulas, D. Scmitz, R. Sielding, M. Wlochal, Nucl. Instr. and Meth. **A345**(1994)256.

[8] D.O.Kataria, J.J. Das, N. Madhavan, P. Sugathan, A.K. Sinha, G. Dayanand, M.C. Radhakrishna, A.M. Vinod Kumar, Mahendrajith Singh and N.V.S.V. Prasad, Nucl. Instr. and Meth. **A372**(1996)311.

[9] A.Guerrieri, G. Maron, G. Montagnoli, D.R. Napoli and G. Prete, Nucl. Instr. and Meth.**A299**(1990)133.

[10] H.Stelzer, Nucl. Instr. and Meth.**133**(1976)409.

[11] P.P.Shakkeeb, Antony Joseph, A.M. Vinod Kumar and K.M. Varier, Ind. Journ. Pure and Appl. Phys.**33**(1995)317.

[12] P.P.Shakkeeb, K.M. Varier, A.M. Vinod Kumar and Antony Joseph, Proced. DAE Symp. on Nucl.Phys.(Bhubaneswar)**37B**(1994)449.

[13] P.P.Shakkeb, A. Joseph, A.M. Vinod Kumar, K.M. Varier and B.R.S. Babu, Nucl. Instr. and Meth. **A366**(1995)320.

[14] T.Aoyama, Nucl. Instr. and Meth. **A234**(1985)125.

[15] K.M.Varier, P.P.Shakkeeb, A.M. Vinod Kumar, A. Joseph and B.R.S. Babu, Proced. DAE Symp. on Nucl. Phys.(Bombay)**35B**(1992)430.

[16] G.Brunner, Nucl. Instr. and Meth.**154**(1978)159.

[17] P.P.Shakkeeb, A. Joseph, A.M. Vinod Kumar, K.M. Varier and B.R.S. Babu, Proced. DAE Symp. on Nucl. Phys.(Calicut)**36B**(1993)450.

[18] W. Diethorn, USAEC Report., **NYO-6628**(1956).

[19] (a)A. Zastawny, J. Sci. Instr. **43**(1966)179 and

(b) A. Zastawny, J. Sci. Instr. **44**(1967)395.

[20] A. Williams and R.J. Sara, Intern. J. Appl, Iso., **13**(1962)229.

[21] M.E. Rose and S.A. Korff, Phys. Rev.**95**(1941)850.

[22] M.W.Charles, J. Phys. **E5**(1972)95.

Chapter 6

Experimental Techniques for $^{32}S+^{60,64}Ni$ Transfer Measurements

Considerable efforts have been put during the last 20 years or so on the experimental and theoretical investigations to understand the reaction mechanism of heavy ion collisions at energies around the coulomb barrier. Coupling of the collective modes of excitation of the interacting nuclei to the fusion channel has provided a good explanation of the observed sub-barrier fusion cross sections. Accurate calculations of coupling strengths of rotational and vibrational excitations are possible. But the coupling of transfer channel by measuring the transfer form factors is quite tedious for nuclei other than closed shells. Information about transfer coupling for various nuclear systems is still lacking. In the case of systems where projectile to target mass ratio is significant, the measurement of transfer yields at sub-barrier energies become difficult. This is due to the low yield of transfer products, and small energies of the backward peaking projectile like ions. The difficulty in the detection and identification of the low energy projectile-like products can be overcome by detecting and identifying the corresponding forward peaking high energy target-like recoils using the recoil mass spectrographs. The first report about such an investigation have came from Darsbury group [1]. Among the non-elastic channels usually coupled with 1DBPM to explain sub- barrier fusion enhancement the one- and two-nucleon transfer channels constitute the nuclear process with a longer range and play an important role in reaction mechanism. The present investigations have been carried out in order to understand the role of one- and two-nucleon transfer channels in the sub-barrier fusion enhancement for the $^{32}S+^{60,64}Ni$ systems. The experiments have been carried out at the inter University research facility of UGC at Nuclear Science Centre (NSC), New Delhi. This chapter gives the details of the experimental set up and the measurements. ^{32}S beams in the energy range 60 to 92 MeV were obtained from the pelletron accelerator at NSC. The transfer reaction products were separated from the elastically scattered beam by

the recoil mass spectrometer HIRA and identified by the focal plane detectors and the related data acquisition system. The identification of transfer products at sub-barrier energies for systems where the projectile has a significant fraction of the target mass is a difficult problem in experimental nuclear physics. The usual time-of-flight technique discussed in the following section for the measurement and identification of transfer products become invalid, due to the small transfer cross section and low energy of the back scattered projectile-like fragments. This problem can be well solved by adopting a relatively novel and effective technique called kinematic coincidence technique [2].

This technique is used for the mass identification of the out going heavy products and for the measurement of the reaction Q-value in the study of heavy ion reaction mechanism. This technique had been widely used in binary elastic, quasi-elastic and complex deep inelastic scattering reactions, but only a few reports exist about its applications in transfer studies. Kinematic coincidence offers optimum possibilities when the colliding ions have approximately the same mass and not too forward detection angles near the beam are required. Resolutions comparable with those of magnetic spectrometers can be obtained and almost all ion charge states can be measured at the same time. Kinematic coincidence method is a simultaneous detection technique of the reaction products by two detectors placed at kinematically correlated angles which allows a big freedom in the choice of parameters to be used in the analysis of the experiment.

6.1 Time- of-flight (TOF) technique

The fascinating interest in heavy ion physics over recent years led to considerable advances in the detection and identification technique for nuclear particles. One such technique is the measurement of particle velocities by time-of-flight (TOF), which together with a simultaneous energy or momentum measurement can be used to determine particle mass [3]. Determination of fragment charge by ΔE-E or similar techniques seems to be limited to a fractional resolution $\Delta Z/Z$ of the order of 2% where as the practical limit of mass resolution from TOF depends largely on the energy resolution available. The heavy ion experiments today require the measurement of both charge and mass which necessitates TOF measurements. The flight time (t) of the particle over flight path (ℓ) gives the velocity

$v = \ell/t$ which together with the particle energy (E) gives the mass (A) by a non relativistic equation as $A = 2E(t/\ell)^2$. The mass resolution obtainable is then

$$\Delta A/A = [(\Delta E/E)^2+(\Delta t/t)^2+(\Delta \ell/\ell)^2]^{1/2} \qquad (6.1)$$

where $\Delta E/E$, $\Delta t/t$ and $\Delta \ell/\ell$ are the fractional uncertainities in the measurement of energy, time and flight path. The contribution due to the uncertainity in the measurement of flight path to the over all mass resolution is usually negligibly small. But care must be taken in geometrical arrangement of timing and energy detectors especially when short flight paths are being used. The contribution due to time measurement is usually significant but can always be reduced by increasing the flight path at the cost of solid angle. Butler et al.,[4] reported about the limitation on mass resolution due to time resolution. An energy resolution of 1% and hence mass resolution of 1% can be obtained by TOF technique using ionization chambers. A better mass resolution can be obtained by energy measurement using magnetic analysis of the particles of interest which require the knowledge about particle charge. TOF measurement requires a flight path of fixed length which the particle of interest traverses before energy measurement. Constant fraction method gives timing signals independent of input pulse height.

6.2 15UD (16 MV) Pelletron Accelerator at NSC

The NSC pelletron is a 15UD vertical Tandem electrostatic Van-de-Graff accelerator [5,6]. Negative ions from the ion source are preaccelerated, mass analyzed and injected at energy of 250 keV to 350 keV into the accelerator. At the terminal the beam is stripped into various charge states using foil or gas strippers. Resulting positive ions are then repelled by the terminal to gain further energy. This beam is then energy analyzed by analyzer magnet of radius 1.8 m to give beams of the selected energy. Switching magnet is used to select the beam in desired directions along any one of the 7 beam lines. The 15° beam line leading to HIRA is used for the present experiments. A schematic diagram of the accelerator facility is shown in figure 6.1. The accelerator is installed [5,6] vertically in a steel tank of diameter 5.5 m and length 26.5 m. The tank is filled with highly insulating SF_6 gas of high dielectric constant at a high pressure of 6 to 7 atm, which can sustain higher voltages compared to air. The diameter of the HV terminal is about 1.52 m

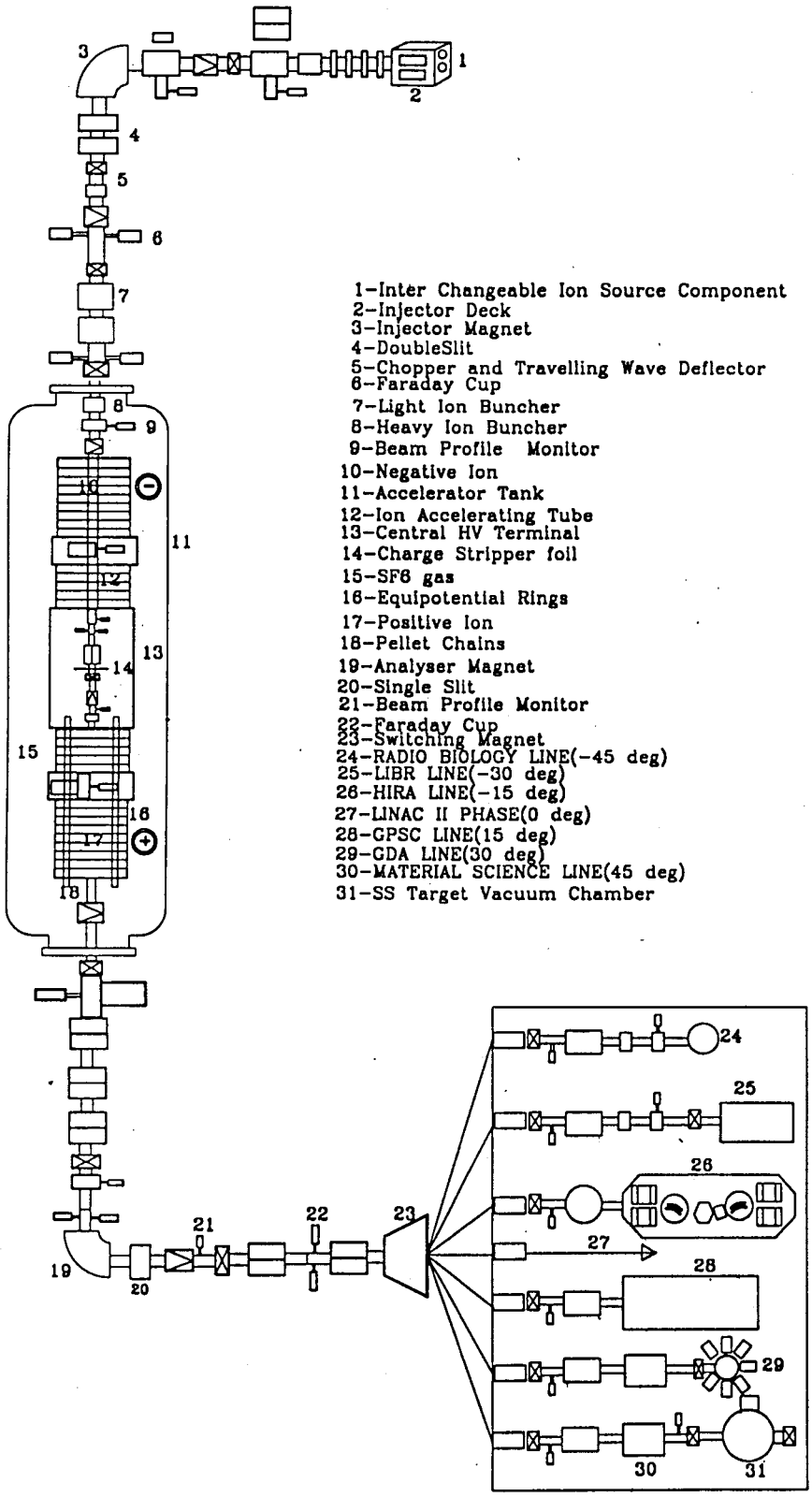

Figure : 6.1 A Schematic diagram of the Accelerator Research Fecility at Nuclear Science Centre, New Delhi which have been used for the Transfer Measurement for $^{32}S + ^{60,64}Ni$ System

and height 3.81 m. The terminal can be charged to high potential of 4 MV to 16 MV. The HV terminal is connected to the tank through ceramic-titanium accelerating tubes and a potential gradient is maintained through these tubes from HV to ground from top of the tank to the terminal as well as from the terminal to the bottom of the tank. The central terminal shell of the accelerator is maintained at a high voltage up to 16 MV. The negative ions traveling through the accelerating tubes from the top to the positive terminal get accelerated. The positive ions formed from the negative ions by stripping are repelled and again accelerated to the ground potential at the bottom of the accelerator. That is the same terminal potential is used twice for accelerating the ions. The energy gained by the ions emerging out of the accelerator is $E = E_{inj} + (1+q)V$ MeV, where V is the terminal potential in MV, q is the charge state of the ions after stripping and E_{inj} is the energy of the injected ions in MeV. The ions accelerated by the pelletron is bent through 90° by the analyzing magnet and by setting the field of this magnet for a particular mass, energy and charge state a required beam can be selected. The magnetic field of the analyzer magnet is related to the beam energy as

$$B_{analyser} = [(K\sqrt{AE_{beam}})/q](1+E_{beam}/3725.9A) \qquad (6.2)$$

Here the magnetic field B is in Gauss, mass number A in amu, E_{beam} in MeV and the q is the charge state of the beam. The magnetic calibration constant can be evaluated from the resonance field. The radius of curvature of analyzer magnet = 1.805 m. Madhavan et al.,[7] and Sarkar et al.,[8] reported about the beam energy measurements.

Parameter	Value
NMR	572.98 mT
Field of Injector Magnet	-4545 G
Field of Switching Magnet	2873 G
Terminal Voltage	9.88 MV

Table 6.1 : Typical values of some parameters of NSC pelletron during the S+Ni transfer experiment

Fifteen 1 MV units are connected on each side of the terminal inside the insulating column, the upper portion of which is called low energy section and the bottom portion is called high energy section. Two shorted units with no potential gradient, called low energy dead section (LEDS) and high energy dead section (HEDS), are provided for housing vacuum pumps and other beam handling equipments such as electron trap and sputter ion pump. Also LEDS is provided with an electrostatic quadrapole triplet lens and HEDS with a second foil stripper assembly. The equipments housed in the dead section and terminal are powered using four 400 cps generators. The typical values of some parameters of NSC pelletron during the S+Ni transfer experiment is given in table 6.1.

6.2.1 Injector system

The negative ions are produced in an ion source housed in a high voltage deck biased to a negative potential up to – 400 kV. An accelerator tube system having proper insulation and voltage gradient is connected to the high voltage deck which pre accelerates the ions to the ground potential. The required ion beam is then selected using injector magnet, focused, steered and injected to the pelletron using beam optical elements. The three inter changeable ion sources used in injector are: (i) Source of negative ion by Cesium sputtering (SNICS) which can give almost all beams (ii) Direct extraction duoplasmatron (DED) gives H^- ions (iii) RF charge exchange source (ALPHATROSS) gives He^- ions.

6.2.2 Control system

The entire pelletron accelerator, accessories and devices in each beam line can be remote controlled and operated from control room and data room by a PC-AT 386 computer with EGA graphics and running under MSDOS. Hardware is connected to PC through CAMAC crate controller supporting auxiliary controller bus (ACB). The software used was written entirely in C-language. The critical components such as magnets, vacuum level, valves etc. are driven by data base software through the output registers in the NSC made crate controller. The devices to be controlled at various locations of the accelerator are connected to the nearby CAMAC crates which in turn are connected to the computer and CAMAC system kept at the control room and data room through CAMAC serial

highway. The high voltage devices at the terminal dead sections and HV deck are connected to the CAMAC by using fiber optic cables. The voltage signals can be converted to frequency signals using voltage to frequency converters and vice versa and transmitted as optic pulses.

6.2.3 Charge Strippers

The negative ions are stripped to positive ions by the strippers mounted at the terminal and HEDS. For light ions thin carbon foil and for heavy ions nitrogen gas at low pressure are used as strippers. The charge state distribution of the emerging positive ions depends on the stripper foil thickness, gas pressure, the incident energy or the type of ions. The most probable charge state and the general distribution of other charge states after stripping can be calculated from the semi-empirical formula proposed by Sayer.[9]. High energy loss due to heavy ions in foil strippers causes its breaking and hence gas strippers are preferred for heavy ions. For light ions foil life time is several days where as for heavy ions it is a few minutes.

6.2.4 Selection of Charge, Mass and Energy

The required beam of desired charge state can be selected using charge selector at the terminal which consists of an off axis electrostatic quadrupole triplet followed by a matching axial quadrupole doublet. The selector can select any ion with an $E/q < 2.55$ where E is the beam energy at terminal and 'q' is the desired charge state. The field of analyzing magnet required to select a particular ion of mass M, energy E and charge state 'q' is given as $B = K(ME/q^2)$ where K is a constant.

6.2.5 High Voltage Charging System

The high voltage charging system at the terminal is an important aspect of the pelletron accelerator. A chain of small stainless steel cylindrical pellets connected to each other by nylon links are used for the production of high voltage and hence the name pelletron. The chain moving with high speed on two pulleys driven by motors and transfer a charge Q to the terminal induced on the chain. This charge will increase the terminal

potential to V = QC where C is the capacitance between the terminal and accelerator tank. The charge is induced on the pellets of the chain at the motor end by a cylindrical plate called inductor which is connected to a –50 kV power supply and this charge is carried to the terminal and transfer to it.

6.3 Heavy Ion Reaction Analyzer (HIRA)

The Heavy Ion Reaction Analyzer (HIRA) is a double focusing (energy and space) recoil mass spectrometer (RMS) designed for use with the beam from the pelletron heavy ion Tandem accelerator at NSC [7,10,11]. It is a large solid angle online device for the reaction products preserving the kinematic correlation and time correlation with the instant of reaction. It transports the ions within a short time (~ μs) and has the capability of zero degree operation. HIRA disperses the reaction products with good mass resolution at the focal plane with energy and space (X,Y) focusing. The electromagnetic configuration of HIRA is QQ-ED-M-MD-ED-QQ as shown in figure 6.2. The dispersive elements are the achromatic symmetric combination of two electrostatic dipoles (ED) and one magnetic dipole (MD), which first separate the nuclear reaction recoils from the primary beam and then disperse the reaction products according to their mass/charge (m/q) ratio. The first pair of quadrupole doublet (Q1&Q2) magnets at the entrance of the device HIRA enhance the solid angle acceptance and provide geometric point-to-parallel focusing of the recoils. The last quadrupoles (Q3&Q4) gives a m/q focus and disperse the reaction products at the focal plane. The focusing power of the magnetic quadrupole depends on the p/q value of incoming particles. The electric dipoles used for energy selection or filtering will bend only low energy recoils. But MD is used for momentum selection or filtering. The combination of ED and MD will act as the velocity filter. The Q1Q2 magnets enhance the solid angle acceptance of the device and hence retain long flight path capability. The quadrupole doublet near the focal plane can provide a mass dispersion over a broad range between zero to 20 mm per percentage of m/q. This doublet also minimizes the small dependent aberrations such as focal plane tilt, curvature etc., without affecting the energy dependent aberrations. Table 6.2 shows the various dimensions and capabilities of HIRA.

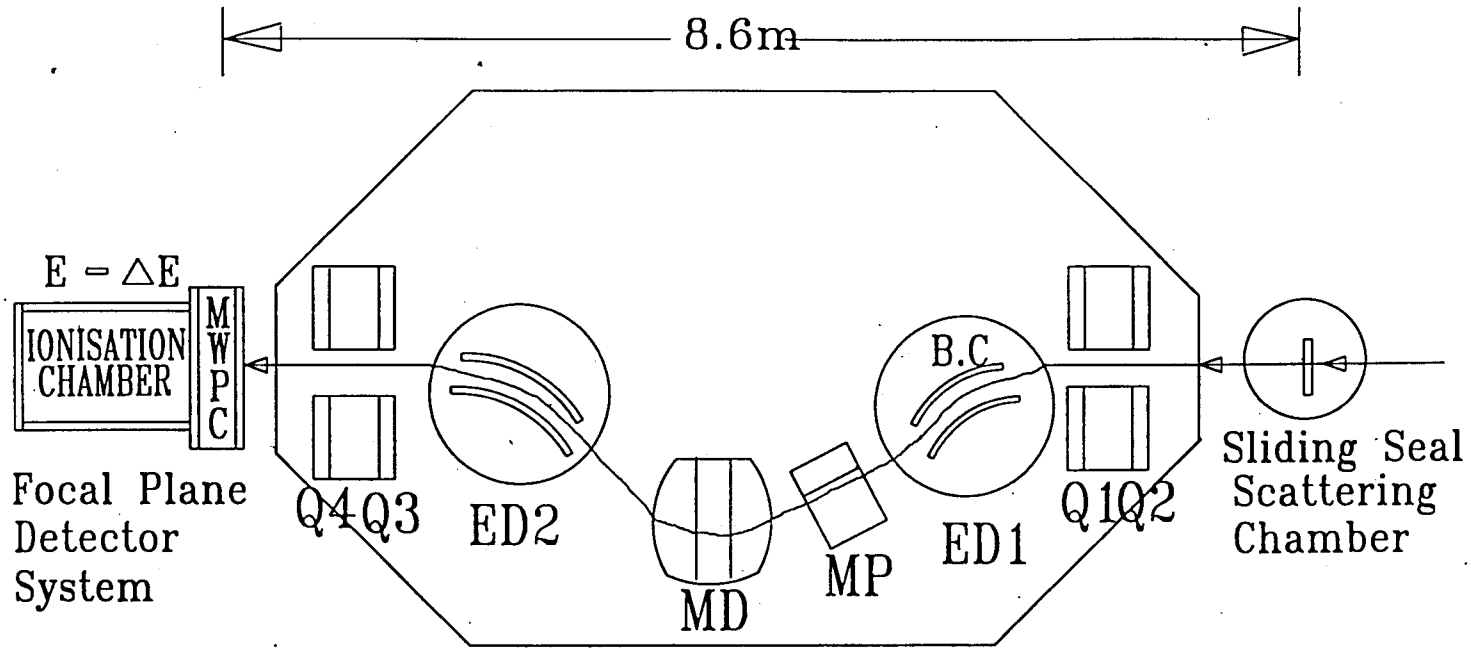

Figure : 6.2 Schematic Diagram of the Recoil Mass Separator – Heavy Ion Reaction Analyser (HIRA) at Nuclear Science Centre.

Angular rotation		-15° to 40°	
Mass Acceptance		± 20%	
Overall length		8.7 m	
m/q range		± 5%	
Energy range		± 20%	
Solid angle acceptance(Ω)		≅10 msr	
m/q resolution (at Ω=5 msr, ΔE= ± 10%)		1/350	
Dispersion		10 mm per %	
Dipoles	MD	ED1, ED2	
Deflection angle	36°	16°	
Radius of curvature	0.86 m	5 m	
EFB shim angles	7°	0°	
EFB radii	2.33 m	-	
Gap	8 cm	15 cm	
Maximum rigidity (central particle)	48.5 MeV.amu/q^2	15 MV/q	
Magnetic Lenses	Q1	Q2	Q3,Q4
Diameter (cm)	6	67.5	
Effective length (cm)	29	22	32,43
Maximum gradient (T/m)	10	10	6.5

Table 6.2 : dimensions and capabilities of HIRA

The first order performance of the dispersive elements is characterized by the following 6 parameters :

(i) Bending radii and angles of EDs (ρ_E,θ_E) and MD (ρ_M,θ_M)

(ii) The separation 'd' between the effective field boundaries (EFB) of ED and MD

(iii) The angles 'α' of the entrance and exit pole faces of MD

The horizontal slot in the anode plate of the first ED is a special feature of HIRA which is helpful in taking the beam out to a beam catcher placed behind, inside the vacuum chamber. This will enhance the beam rejection factor. The energy and angle related higher aberrations can be affected and re optimized by placing a multi pole (M) between ED1 and MD, which does not affect the mass dependent aberrations. The sextupole field of the

multipole is strong enough to nullify the position or angle related aberrations at the cost of energy dependent aberrations. The quadrupole field is used for the correction of residual energy dispersion and the octupole field for the correction of higher order aberrations. The electric rigidity of the device HIRA is given as $E\rho = 2T/q$ and magnetic rigidity is given as $B\rho = p/q$. Here E(=V/d) is the electric field of ED, ρ is radius of ED plate = 5 m, $T=K\varepsilon$, ε is the kinetic energy of the particle, p is the momentum of the particle, q is the charge state of the ion and B is the magnetic field strength. Both $E\rho$ and $B\rho$ coupled to give m/q dispersion at the focal plane. The voltage to be applied to ED for selecting a particle of energy ε and charge state 'q' is given as

$$V_{ED} = \varepsilon \times 30\ kV/q \qquad (6.3)$$

The mass m/q resolution of HIRA has been estimated as 1/300 at 1 msr and 1/240 at 5 msr. The beam rejection factor of HIRA is about 2×10^9 which can be obtained from the low energy loss signal peak of beam-like particles and high energy loss signal peak of ER-like particles. The width of the ER peak will give an idea about the energy acceptance of HIRA.

6.3.1 Beam Rejection

The ED1-MD-ED2 combination is a suitable device for excellent beam rejection because the electric rigidity (2T/q) and magnetic rigidity (p/q) of the beam and reaction products are different. Special consideration was given for the enhancement of beam rejection while designing HIRA [11]. The horizontal slot in the anode plate of ED1 is used to take the beam out to a beam catcher which will reduce the background events at the focal plane due to the beam scattering from the anode plate.

6.3.2 HIRA Control System

The various parameters related to HIRA such as currents, voltages, vacuum readings, temperature etc. are monitored and controlled remotely using an IBM PC based CAMAC system through RS232 serial crate controller. The various electromagnetic fields

required for a selected reaction products can be automatically or manually controlled and monitored by setting HIRA for a particular central particle of mass, energy and charge state using the user friendly menu driven control program written in Turbo-Pascal to communicate with different devices. Glassman HV power supplies are used for powering EDs. The safety interlock logic loaded into EPROM protects the system in the case of vacuum accident.

6.3.3 Focal Plane Detector System

A detailed discussion of focal plane detectors is given in chapter 4 and 5. The focal plane detector system of HIRA consists of a 2D position sensitive MWPC and a following gaseous ΔE-E ionization chamber [12]. MWPC has a configuration of X grid-Anode-Y grid with an entrance window of 200 mm x 60 mm. The wire planes are made by 25 μ isohm wire with a spacing 1 mm. The position information is derived by delay line read out method using PE21173 chips. A 180 mm deep split anode transverse ionization chamber (IC) of active area 120 mm x 30 mm is used as the ΔE-E detector which can also operate at the same gas pressure of MWPC. Isobutane at a pressure of 5 torr (MWPC) to 33 torr (IC) was used with a bias voltage of 490 V (MWPC) and ranging from 50 V (IC anode) to −175 V (IC cathode). EG&G ORTEC charge sensitive preamplifiers (model 142A) were used for taking the signals and for biasing. The information about the mass number A is obtained from focal plane detector MWPC and the Z identification is done from ionization chamber as $\Delta E \propto MZ^2/E$ using the ΔE-E spectrum. The typical values of the detector bias voltages and leakage currents of the focal plane detectors and monitor detectors used for the S+Ni experiment is given in the following table 6.3.

Detectors used	Bias Voltage (Volts)	Leakage Current (μA)
MWPC	490	0.00
IC (Anode)	52	0.01
IC (Cathode)	-175	1.56
Top SBD	156	1.91
Back SBD	65	0.61

Table 6.3 : Typical bias voltages and leakage currents of the detectors used during the S+Ni experiment.

6.4 Water Cooling System

The monitoring devices must be able to resist the full power output of several kilowatt for a few minutes. That is, the thermal stress to which the monitoring devices exposed is very high. So most of the monitoring devices must be cooled effectively with water. The cooling channels should not be too large and water should flow with high speeds for effective heat transfer. The boiling point of water will rise if the pressure is high. Beam profile monitors (BPM) take only a small amount of beam power and they have no need to cool by water. Only radiation cooling is sufficient for BPM. The MD, QDs and multipole are electromagnets and the coils of them are made by insulated copper tubes. Chilled water is allowed to flow through these tubes to measure the heat produced due to current flow.

6.5 Need of Vacuum System

An ultra high vacuum (UHV) of the order of 10^{-6} to 10^{-8} torr(1 torr=1 mm of Hg) is an essential requirement for the proper functioning of accelerators and for the accelerator based nuclear physics experiments. The system pressure can be reduced from 1 atm (760 torr) to 10^{-10} torr by using varieties of vacuum pumps. Since a single pump can not operate over the above range a combination of different pumps is used to attain ultra high vacuum, which is essential to reduce the collisions of accelerated ions or reaction products with the residual gas molecules. They have to travel a large distance through the accelerator to reach the target and then the products to reach the focal plane detectors through the various devices used in each beam line. Table 6.4 shows the typical vacuum and the pumps used at the various parts of HIRA during the S+Ni transfer experiment. The advantages of using UHV in accelerator are the following :

(i) The beam energy loss can be minimized (ii) Background noise can be reduced
(iii) Keeps SF_6 gas pure (iv) Improves dielectric constant to hold more voltage and
(v) Avoids stripping of negative ions in beam line.

Part of HIRA	Vacuum (torr)	Pump used
Sliding Seal Chamber	9×10^{-7}	Turbo molecular
ED1	9.4×10^{-8}	Cryo Pump
MD	6.5×10^{-8}	Ion Pump
ED2	8.1×10^{-8}	Cryo pump
Focal Plane	4.1×10^{-6}	Diffusion Pump
MWPC	5	Rotary Pump
Ionization Chamber	33	Rotary Pump

Table 6.4 : Typical vacuum at the various parts of HIRA during the S+Ni experiment.

6.6 Extraction of ^{32}S beam

The experiment was carried out using ^{32}S beam produced using SNICS[13]. Higher beam intensities and lower beam emittance are the advantages of SNICS. Isotopic abundance of ^{32}S is 95.02%. SNICS is used to produce ions from solid materials by the method of surface ionization and Cesium sputtering, which is a versatile source and has very good beam emittance [14-21]. The SNICS consists of a sputter cathode, ionizer and an extractor. The Cs in the Cs-canal is heated and Cs vapour strike the ionizer. The ring shaped ionizer having 6 turns made up of tantalum is heated by passing current, and act as the ionizing surface. Cs vapours hitting this ionizer leave the surface as Cs^+ ions and get accelerated towards the cathode maintained at a negative potential. Cathode contains material of which the ions have to be produced. The negative ions sputtered out by Cs^+ ions are extracted out of the source with extractor electrode maintained at positive potential. Freon gas is used for cooling the cathode which is getting heated by hitting Cs ions. Permanent magnets are used for suppressing the electrons produced in the sputtering process. Due to the low melting point ($\cong$113° C) and extremely higher vapour pressure elemental sulphur is not used as the sputter cathode and metallic sulphides with high melting point such as PbS (M.P=1114°C); Iron sulphide-FeS (M.P=1195°C) or Li_2S (M.P=900°C) is used as cathode.

The enriched sulphur purchased in elemental form is converted to iron sulphide by mixing, with iron powder and heated up to 300 °C under argon in a quartz test tube. The reaction is exothermic characterized by a distinct red glow. Iron sulphide mixed with 20% Ag powder can be well and easily packed with the cathode which can give rise a steady negative current in the range 100 to 250 μA. Cathode voltage is at –2.5 kV to 3.5 kV and extractor at +8 kV to 12 kV. The filament current is between 15 A to 32 A which is maintained at low (~10 V) voltage. The cathode can be changed by vacuum transfer. Focus supply is about 4 to 7 kV. The negative ion intensity can be controlled by varying the temperature of the Cesium reservoir. Cesium ions supplied for sputtering can be collected back by external circuitries. The field of the injector magnet is calculated for the mass ^{32}S and it is set to select ^{32}S beam to the accelerating column.

The negative ion beams are stripped at the terminal to form positive ions. The charge state of the positive ions can be selected using analyzer magnet. This selected beam can bring to the target chamber of HIRA using the switching magnet. A magnet can select a required mass and charge state according to m/q separation. The emittance or the number of particles emitted per second is given as beam current/charge state of beam. The isotopic abundance of sulphur is given in table 6.5

Isotope	Abundance	Properties
^{32}S	95.02%	Electron Affinity = 2.077 eV Ionization Potential = 10.36 eV Melting Point = 113°C
^{33}S	0.75%	
^{34}S	4.21%	
^{36}S	0.02%	

Table 6.5 : Isotopic abundance of sulphur

6.7 Targets for nuclear reaction

The main properties required for an ideal target are the following :

(i) It should be able to give a constant and adequate yield during the experiment. This may require isotopic enrichment in many cases.

(ii) The target should not break under beam irradiation through out the experiment.

(iii) Thickness should be uniform and acceptable.

(iv) Preparation methods should be easy.

(v) Chemically pure to avoid the background interference from unwanted elements.

(vi) Rare and expensive isotopic material should be conserved during the preparation of their target.

(vii) Target should remain stable under beam bombardment.

6.7.1 Measurement of Target thickness

The target thickness is expressed in $\rho \times t$ nuclei/cm^2 or μg/cm^2 where 'ρ' is the density of the target in gm/cm^3 and 't' is the thickness in cm. Only the area of the target is important and the depth of the target is no matter [22,23]. Target is almost empty because nuclear dimension is 10^{-14} cm and atomic size is 10^{-10} cm. So each projectile nuclei can interact with each target nuclei and so the reaction can take place any where in the target at any depth. Normally there is 10^{22} nuclei per cm^2. The thickness of the target foil can be measured as

$$t = \Delta E/(dE/dx) \qquad (6.4)$$

where $\Delta E = E_1 - E_2$ is the energy loss of α-particle in target, E_1 is the α-energy measured in vacuum, E_2 is the α-energy after passing through the target and dE/dx is the stopping power of the target film for α-particle. The energy per channel dE keV is determined from the peak position for the ^{241}Am alpha beam of energy 5.486 MeV. From the dE/dx for α energies 5 MeV and 6.4 MeV obtained from the TRIM program, the dE/dx for 1.4 MeV can be determined in MeV/mg/cm^2. This will give the dE/dx for 0.486 MeV and hence for 5.486 MeV alpha particle. If ΔC is the channel shift when α-particle is passed through the target, then $\Delta E = \Delta C \times dE$ in keV. From this value of ΔE, the target thickness can be

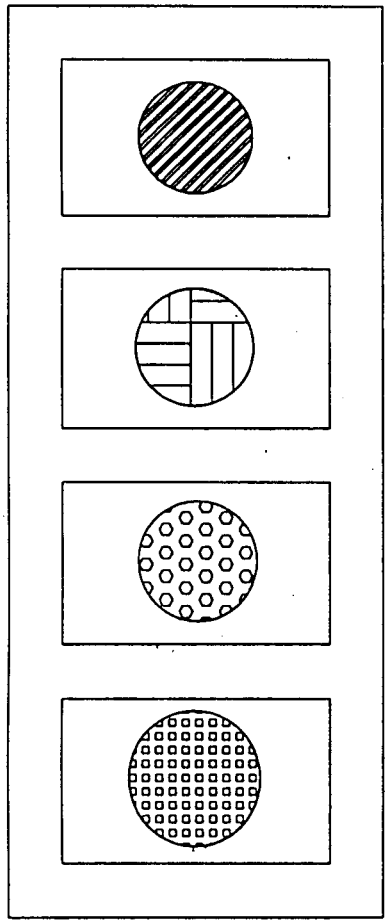

Figure : 6.3 Schematic Diagram of the Target Ladder used for the $^{32}S + ^{60,64}Ni$ transfer experiment at NSC

calculated using the equation (6.4). We have used enriched self supporting ^{60,64}Ni targets for our transfer experiment, which were brought from LNL, Italy and have been prepared by mechanical rolling. The details about the targets used in the present studies are given in table 6.6. Figure 6.3 shows the various targets used for the experiment.

Isotope	Natural Abundance	Isotopic Abundance (enriched)	Thickness ($\mu g/cm^2$)
^{58}Ni	68.3%	---	---
^{60}Ni	26.2%	99.83%	273
^{61}Ni	1.13%	---	---
^{62}Ni	3.59%	---	---
^{64}Ni	0.92%	98.00%	242

Table 6.6 : Details of the targets used for the present experiment

6.7.2 Impurity check of the targets

The enriched targets used for the experiment contains other isotopes in small contributions. The amount of this impurities such as ^{58,59,61,62,63,65,66}Ni have to be estimated for a correct measurement of transfer probability. The enriched ^{60,64}Ni targets contains few percentage of other isotopes according to suppliers specifications. The elastically scattered recoils from these impurities contribute to the yield of the transfer products. So experiment was carried out to get the data at 60 MeV, well below the barrier. At this energy the yield of the transfer products is negligibly small. The contribution of the other isotopes (especially ^{58}Ni) showed good agreement with suppliers specifications. The elastic scattering contributions of the impurity isotopes have to be considered for the necessary corrections of the transfer yield at higher energies around the coulomb barrier.

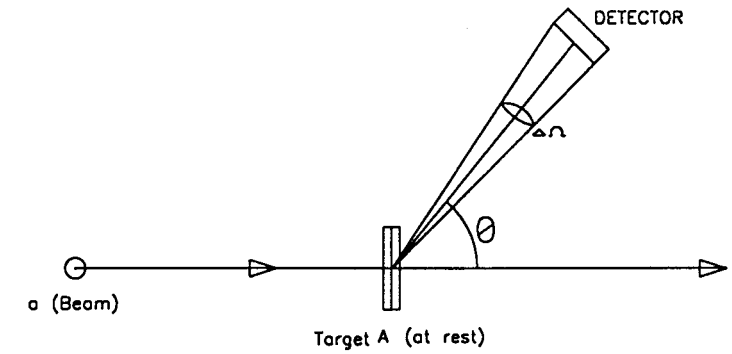

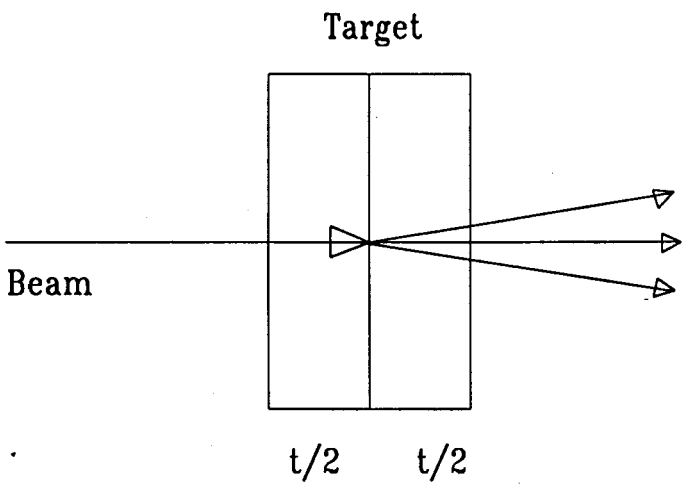

Figure : 6.4 Diagrams showing the differential scattering (top) and Half Thickness Energy Loss-HTEL (bottom)

6.7.3 Half thickness energy loss (HTEL)correction

Higher yield and minimum energy and angular straggling of the beam and recoils are the main features of an ideal target. Even though yield improves with the increase in target thickness, the above mentioned straggling also increases. So a correction is made in the E_{cm} by considering the half thickness energy loss (HTEL)[24] which can obtained from the stopping power dE/dx using the TRIM program for each beam energy for the given thickness of the target. The dE/dx is calculated as

$$dE/dx \propto mZ^2/E \qquad (6.5)$$

and the corrected E_{cm} is determined as

$$E_{cm}|_{corrected} = E_{cm} - HTEL \qquad (6.6)$$

Figure 6.4 shows the differential scattering and HTEL for a typical beam target combination.

6.8 Kinematic Coincidence Method for the Present Expt.

We have used this technique for our S+Ni transfer measurement [24,25]. The low energy back scattered projectile-like (sulphur) ions are detected in coincidence with the complimentary forward scattered target-like (nickel) fragments carrying a large fraction of the incident beam energy. Figure 6.5 shows the kinematic coincidence set up used for the experiment. A silicon back SBD (100mm^2) was placed at 146° for ^{64}Ni and 142° for ^{60}Ni w.r.to the beam direction to detect the back scattered sulphur-like ions. The corresponding forward scattered target-like ions were detected by focal plane MWPC. The targets used were mounted on the first ladder as mentioned in section 6.7.1. A second ladder was used to mount the Si monitor SBD of active area 50 mm^2 at an angle 45° with the horizontal beam direction as the top detector inside the sliding seal scattering chamber [26]. A 6 μm polypropylene film was also mounted at the bottom position of the second ladder for charge resetting and for determining the energy straggling. In front of the view port of the sliding seal scattering chamber a CCD-TV camera was set up to view the beam spot on the TV monitor placed at the control room. This was helpful to tune for obtaining good quality beam of uniform size (2 to3 mm) by viewing on quartz target. The monitor detector

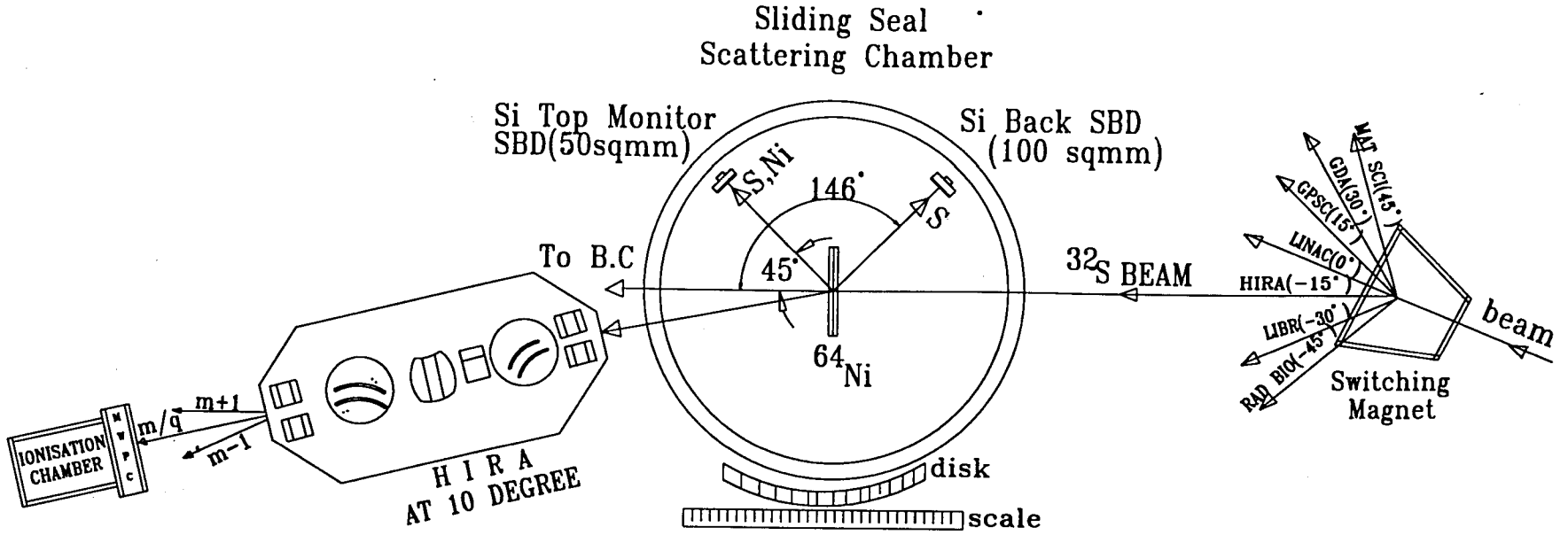

Figure : 6.5 Physical Layout of the setup used for the S+Ni Transfer Experiment using the Kinematic Coincidence Technique (TOF-TAC Start was taken from MWPPAC anode Timing and Stop from Back Sulphur Surface Barrier Detector (SBD) Timing Signals

counts was used for the normalization of the incident beam flux as well as to focus the beam on target by viewing for a better yield. The required recoil particle energy, back scattered projectile-like energy and the corresponding angles for recoil angles ranging from 10° to 30° were obtained using the computer program 'Kinematics'. This calculation has done for the beam energy range 60 to 92 MeV before the experiment, for different transfer reaction channels. Table 6.7 shows a typical kinematic calculation at E_{lab} = 89 MeV for the $^{32}S+^{60,64}Ni$ systems. The elastically scattered spectrum using gold (Au) target were observed at 0°, before starting the actual experiment. At 0° contribution from back ground is very high and difficult to see the transfer data. The actual experiment was performed by rotating HIRA through 10° w.r.to beam direction to eliminate the intense beam background. The remotely and manually controllable target ladder set up is assembled vertically at the sliding seal scattering chamber located in front of HIRA.

System : $^{32}S+^{60}Ni$ at E_{lab}(corrected) = 87.5 MeV										
Channel	M1	M2	M3	M4	Q	E_S(lab)	E_{Ni}(lab)	θ_S	θ_{Ni}	θ_{CM}
+2n	32	60	34	58	-0.33	9.22	77.95	138.7	10.01	160.42
+1n	32	60	33	59	-2.75	9.10	75.65	138.0	10.00	159.99
Elastic	32	60	32	60	0.00	10.50	77.00	139.9	10.00	159.99
System : $^{32}S+^{60}Ni$ at E_{lab}(corrected) = 87.68 MeV										
Channel	M1	M2	M3	M4	Q	E_S(lab)	E_{Ni}(lab)	θ_S	θ_{Ni}	θ_{CM}
+2n	32	64	34	62	3.563	11.96	79.29	142.9	9.99	160.76
-2p	32	64	30	66	0.216	13.51	74.39	142.8	10.00	159.52
+1n	32	64	33	63	-1.014	1 1.14	75.53	141.3	10.00	160.13
-1p	32	64	31	65	-1.412	12.27	74.00	141.8	10.01	159.60
Elastic	32	64	32	64	0.00	12.10	75.58	142.1	10.01	159.98

Table 6.7 : A typical kinematic calculation at E_{lab} = 89 MeV

6.9 Experimental Set up

The hardware set up used for our S+Ni transfer experiment is shown in figure 6.6. A solid angle defining aperture (SADA) was used for selecting the solid angle of the target-like particles entering the first quadrupole pair with provisions for 1 msr, 5 msr and 10 msr. SADA set for the long impurity check run at 60 MeV beam energy was 5 msr, and for the transfer experiment with ^{60,64}Ni it was 10 msr. The target- like particles scattered in the forward angle undergo m/q dispersion when they traverses through HIRA at a rate of 10 mm per percentage to the focal plane. The m/q acceptance of HIRA is ± 5%. There is no energy dispersion for the particles through HIRA and the energy acceptance is ± 20%. The HIRA fields were set so that mass 60 and 64 of the most probable charge state is brought to focus at the center of the focal plane. By varying the HIRA fields to sweep a particular mass across the focal plane and noting the change in normalized yield the mass efficiency of HIRA was determined. Similarly the charge state efficiency is also determined by setting HIRA fields for different charge states of the recoils to give charge state distribution. A detailed discussion of some of the electronic modules used for the experiment is given in chapter 5. A brief discussion of the other modules used for the experiment is given in the following sections.

6.9.1 Timing Filter Amplifier(TFA)

Model 474 modules were used for shaping the pulses and for optimizing the signal-to-noise ratio for timing measurements. This model is particularly suited for use with EG&G ORTEC constant fraction timing discriminator (CFD). It derives its input signal directly from preamplifier output. Fast rise time, high output drive and high gain capabilities, pole-zero cancellation network, dc coupling and time invariant base line restorer permit model 474 for using at ultra high count rate applications. The gain is continuously adjustable and it is having the provision for integration and differentiation of the pulse for exact time measurement.

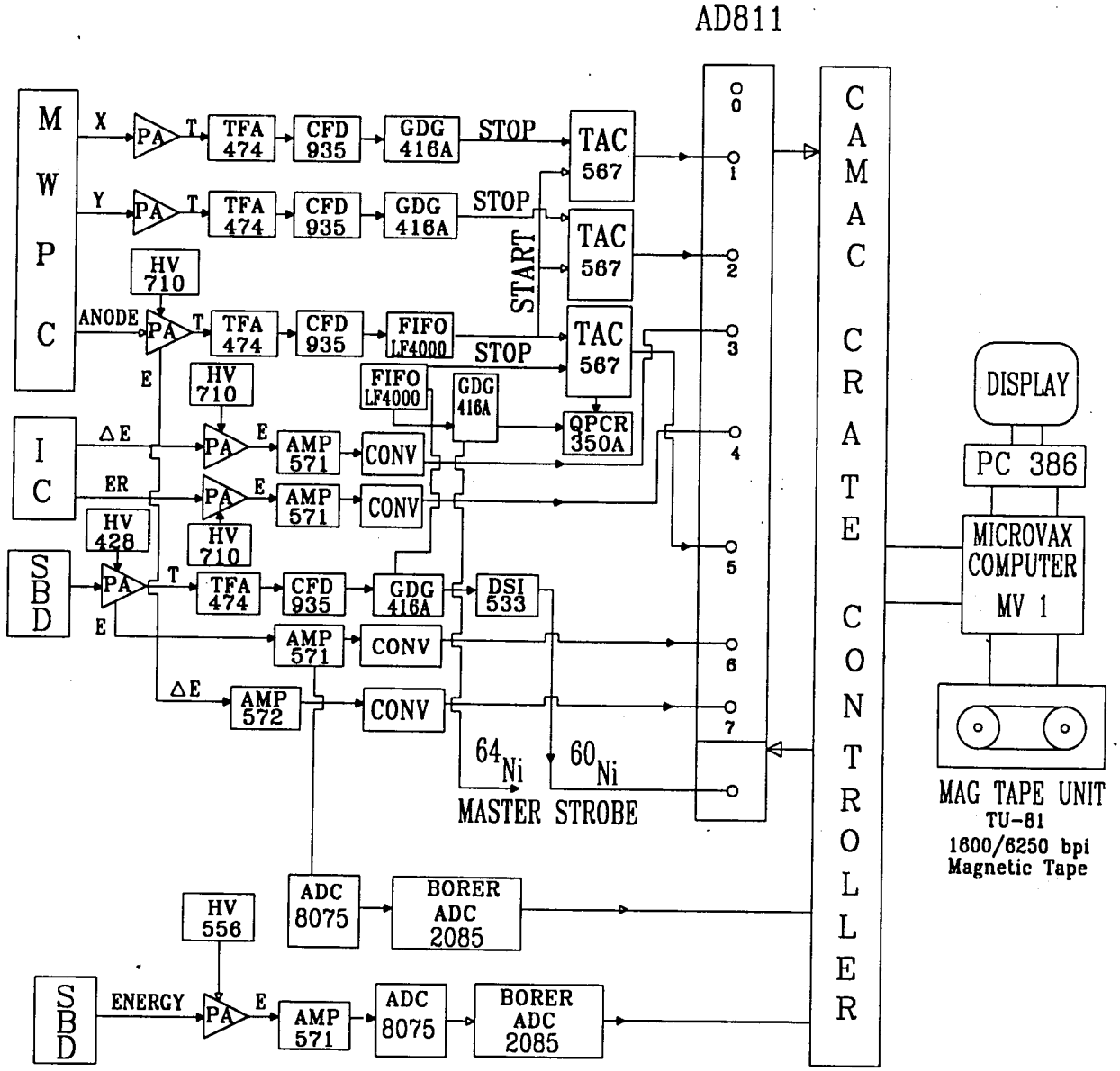

Figure : 6.6 Block diagram of the Electronic setup used for the S+Ni Transfer experiment at NSC Modules used are mainly of EG&G ORTEC.

6.9.2 Constant fraction discriminator (CFD)

The output of TFA 474 was fed to the input of EG&G ORTEC QUAD CFD (model 935). This CFD splits the input signal into two parts. One part is attenuated to a fraction (f = 20%) of the original amplitude and added to the delayed and inverted part. The delay is selected so that the optimum fraction of the delayed signal occurs at the peak amplitude of the attenuated signal. This causes the zero-crossing time of the constant fraction bipolar signal to occur at the optimum fraction. The main features of model 935 is given below :

(i) Constant fraction timing on signals as narrow as 1 ns.

(ii) The discriminator in the model 935 detects the zero-crossing point and generate the corresponding timing output pulse.

(iii) Walk is the systematic error in detecting the time for the 20% of the fraction as a function of the input pulse amplitude. This model 935 generates ultra low walk of $< \pm$ 50ps. Accurate walk adjustment is possible.

(iv) Pulse pair resolving time < 5 ns

(v) Model 935 has four identical and independent CFDs.

The output of the CFD is fed to the gate and delay generators (GDG) model 416A and function of which is discussed in chapter 5.

6.9.3 Quad logic Fan-in/Fan-out

The CFD output of the MWPC anode signal and the GDG output of the back SBD (sulphur) was fed to the Quad logic Fan-in/Fan-out module model LF4000. This module is used for interconnecting a large number of logic modules with minimum additional delay time when performing logic operations with fast NIM signals. It is having four sections and each section has 4 inputs and 6 outputs. Four outputs are non inverting and 2 outputs are inverting. It can be configured according to the requirement by OR gating.

6.9.4 Time-to-Amplitude Converter (TAC)

The anode timing signal of MWPC is used as the START signal and the gated and delayed output of GDGs were used as the STOP signal of the EG&G ORTEC time-to-amplitude converter/single channel analyzer (TAC/SCA-model 567). TAC measures the time interval between START and STOP input pulses and generates an analog output pulse proportional to the measured time. Model 567 provides a built-in single channel analysis of the analog signal. It is able to analyze random nuclear events occurring in the timing range of 10 ns to 20 ms. Separate gating (in anticoincidence or coincidence mode) of the START and STOP eliminates unwanted events from time spectra according to the externally imposed timing or energy restrictions. All inputs and outputs of model 567 are dc coupled so that the changing input count rates will not affect the normal operation of the module. The output width of TAC is selectable with variable delay and can be synchronized with STOP signal or an external strobe. Valid START and valid output are provided for each accepted START and STOP input respectively. In the TAC inhibit mode the model 567 gives a TAC output only if the output pulse falls within the window restrictions imposed by the SCA.

6.9.5 Dual Sum and Invert Amplifier (DSI)

The EG&G ORTEC DSI module model 533 was used for inverting the gated and delayed signal from the back surface barrier detector used for detecting sulphur-like ions. The inverted signal was used as the Master strobe of AD811 ADC for the $^{32}S+^{60}Ni$ experiment.

6.9.6 CAMAC Quad Preset Counting Register (QPCR)

QPCR Module 350 was used as a scalar having four separate preset counting registers. It is a binary counting device at a frequency rating of 75 MHz. The module can be set up to respond for TTL or negative 50 ohms NIM signals on the counting and individual inhibit inputs. Four registers can be used as separate modules with fully structured enable/disable LAM control together with carry, overflow and inhibit to be used separately on each register. LEDs on front panel show the counting in single strobe mode.

6.9.7 Canberra ADC and Borer ADC

The Canberra 8K ADC model 8075 is a single width NIM style ADC and accepts unipolar or bipolar pulse for pulse height analysis (PHA) operation. This module was used for digitizing the analog signals from the back SBD and monitor SBD. Borer ADC Model 2085 was used as an interface between Canberra ADC(8075) and CAMAC crate controller for processing the monitor and back SBD singles.

6.10 Data Acquisition System

A group of inter connected hardware instruments dedicated to the measurement and quantization of analog signals for digital analysis of processing is called a data acquisition system. A CAMAC based online data acquisition system with a MicrovaxIII (MVI) controlled from a PC-386 (having EGA graphics card and a RS232 link to Vax at 19200 baudrate) terminal was used for data collection, processing and display of large volume data [27]. The online data acquisition program is written in FORTRAN language called NSCSORT [28] which can display the histograms with the help of a graphics library using PC-386. The modules required for multiparameter data acquisition and the control equipments like scalars and buffered input output units were mounted on the CAMAC crate housed in the data room. Two Canberra ADCs 8075 were used to record the energy signals from the monitor SBD and back SBD(sulphur) after proper amplification of the preamplifier signals using EG&G ORTEC 571 amplifier.

The timing signals from the back sulphur SBD and MWPC anode were used as the STOP and START of the kinematic coincidence TAC. The master strobe of the data acquisition with ^{60,64}Ni targets was taken from back SBD timing signal after proper processing. The X and Y position signals, ΔE from MWPC, ΔE and E from ionization chamber, the energy signals from back SBD and the TAC between MWPC anode and back SBD timing signals were fed to a multi parameter ADC -AD811- and recorded in the event mode on magnetic tapes. A common logic trigger was used to gate the analog inputs to AD811 which determines whether an event is valid or not. The logic trigger is derived from the timing signal of the back surface barrier detector used for detecting sulphur-like

ions. The CAMAC hardware digitize the energy and timing signals fed to AD811 and sent to the list processor (HYTEC LP 1340) which reads all modules in succession and send the data to the buffer inside the crate. LP cleared and wait for the next START or LAM. The internal buffer memory size is 32 k(24 bit). This data from the buffer is then transferred to the memory of the computer. All these process of reading and buffering of data is controlled by the auxiliary CAMAC crate controller. The parallel bus crate controller (KSC3922) transfers the data of a full block up to 16 kB from CAMAC buffer to Microvax memory. High density magnetic tapes of 6250 BPI were used for saving the list mode data with the help of a 9 track TU plus magnetic tape drive of speed 75 kB/s connected to Microvax III computer. The various signals processed and the corresponding spectrum configuration at the time of experiment (online) is given in table 6.8. Acquired data is displayed as one dimensional (singles) spectra and 2 dimensional spectra formed from the event mode multiparameter data.

Spectrum	ADC	Specifications
1	ADC 8075	BSBD Singles
2	ADC 8075	Top Monitor
3	AD811-Channel 0 (ADC1)	NIL
4	Channel 1 (ADC2)	X-TAC
5	Channel 2 (ADC3)	Y-TAC
6	Channel 3 (ADC4)	IC(ΔE)
7	Channel 4 (ADC5)	IC(E_R)
8	Channel 5 (ADC6)	BSB-MWPC TAC
9	Channel 6 (ADC7)	BSB(E)
10	Channel 7 (ADC8)	MWPC-ΔE
11	ADC2 vs ADC8	X vs MWPC-ΔE(2D)
12	ADC2 vs ADC6	X vs TAC (2D)
13	ADC2 vs ADC7	X vs TAC gated BSB(E)
14	ADC4 vs ADC5	IC(ΔE) vs IC(E_R)
15		Buffer
16		Buffer
17		Spectrum#1+Spectrum#7
18		Spectrum#2+Spectrum#8
19		Projection Spectrum

Table 6.8 : Spectrum configuration at the time of experiment.

6.11 Data Analysis using NSCSORT

The offline program NSCSORT [29] developed at NSC was used for the sorting and analysis of the event wise data recorded on magnetic tapes by reading event by event. Hewlett Packard and Tata Elxsi computer running under UNIX operating system has been used for offline data analysis. Some of the algorithms used for data analysis are common for both online and offline programs. Two dimensional spectra and their X,Y or banana gated projections were viewed with or without specific conditions of linear or conditional gates. Arithmetic operations are also possible on the ADC signals and conditions. The option of banana gating of the program was used for separating the recoiled target-like evaporation residue particles from the beam-like particles reaching the focal plane. During the analysis one of the 2D spectra was the plot between X-position (m/q) against MWPC-BSB TAC (TOF). This spectrum was banana gated to obtain typical 2D plots as shown in figure 6.7 for $^{32}S+^{60,64}Ni$ at 89 MeV. A typical banana gating is shown in figure 6.8. The 2D spectrum contains only the target-like particles with different m/q values as shown in figure 6.7.

Spectrum	ADC	Specification
1	AD811-Channel 1(ADC2)	X-TAC
2	Channel 2(ADC3)	Y-TAC
3	Channel 5(ADC6)	BSB-MWPC TAC
4	Channel 6(ADC7)	BSB(E)
5	Channel 7(ADC8)	MWPC- ΔE
6	Not used	
7	,,	
8	,,	
9	,,	
10	,,	
11		X vs MWPC-ΔE(2D)
12		X vs TAC gated BSB(E)
13		TAC vs BSB
14		X vs TAC(2D)

Table 6.9 : Spectrum configuration at time of analysis.

$^{32}S + ^{60}Ni$ at E_{lab} = 89 MeV

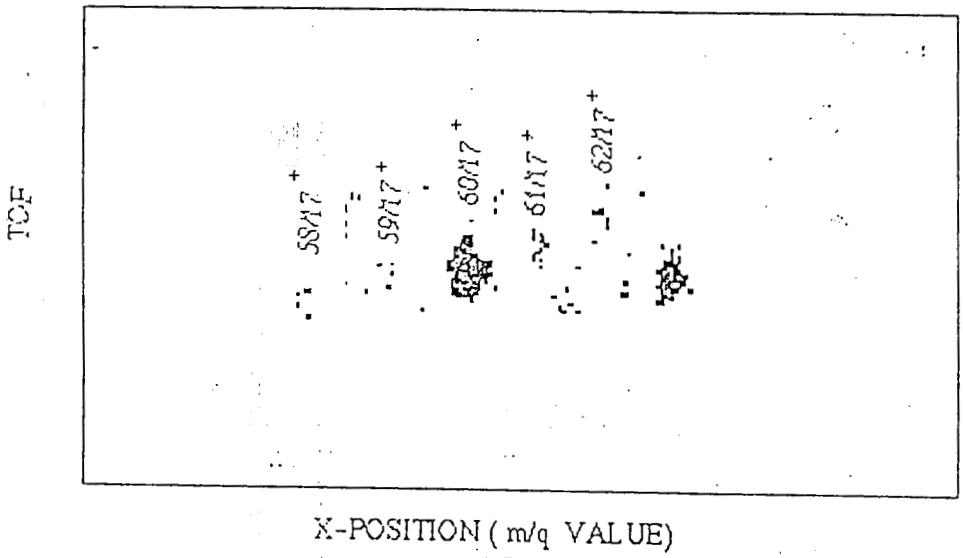

$^{32}S + ^{64}Ni$ at E_{lab} = 89 MeV

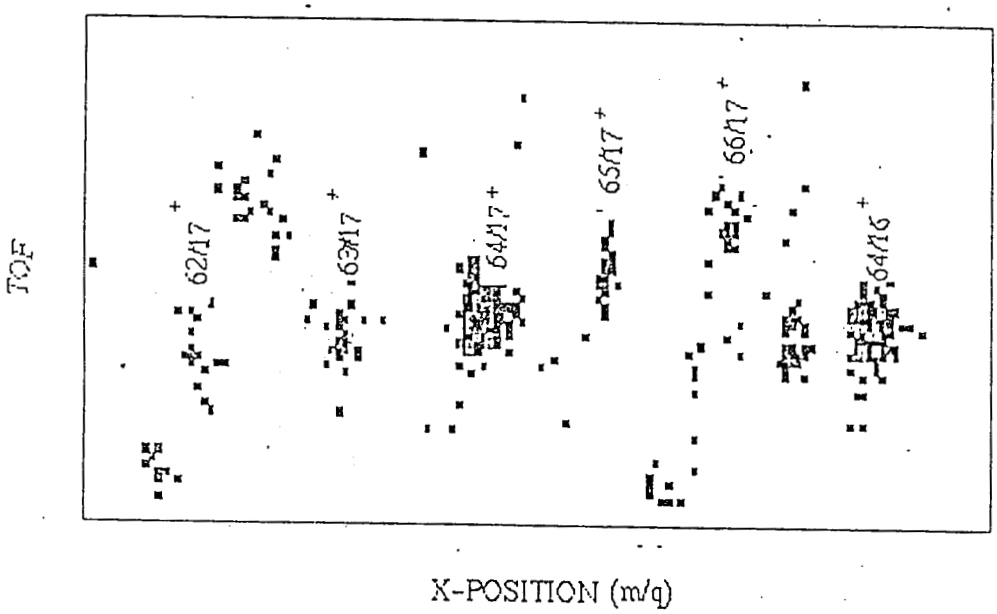

Figure 6.7 : TOF vs X-position (m/q) 2D spectrum for the $^{32}S+^{60,64}Ni$ system at E_{lab}= 89 MeV

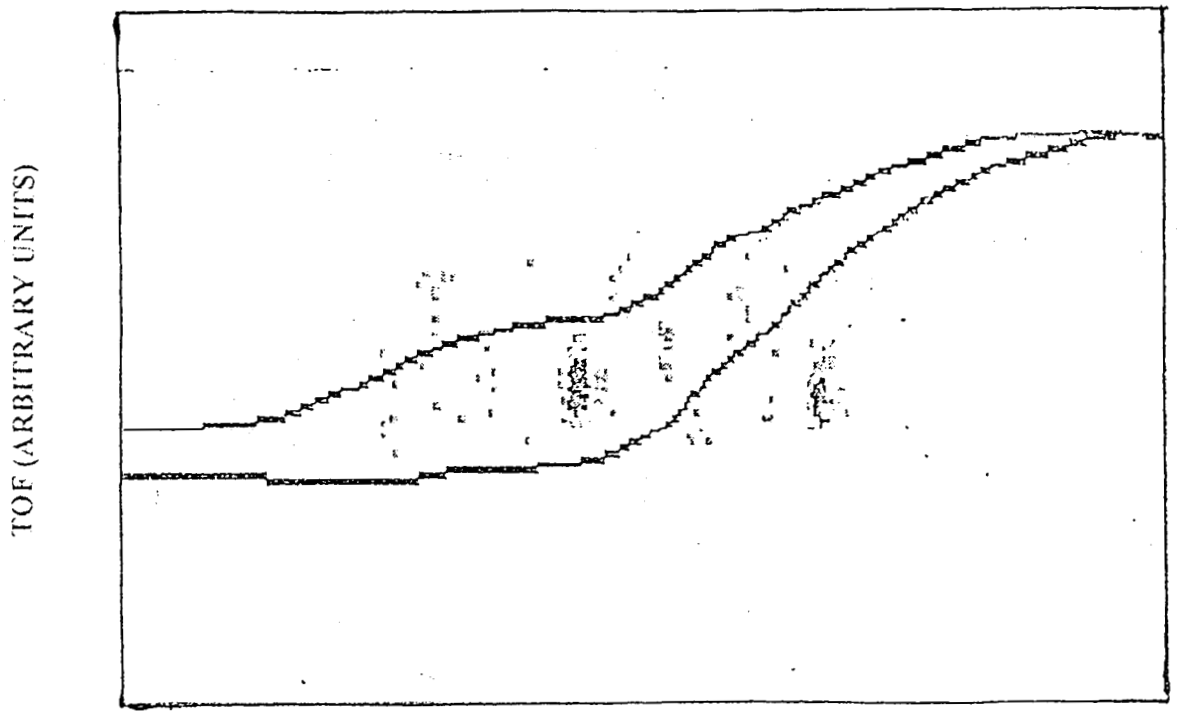

Figure 6.8 : A typical banana gating of the TOF vs X-position (m/q) 2D spectrum for the $^{32}S+^{64}Ni$ system.

The banana gated portion can be projected to the X-axis to obtain the m/q mass spectra. A typical mass spectra for the $^{32}S+^{60,64}Ni$ at 89 MeV is shown in figure 6.9, which contains elastic and transfer peaks. The peaks of the projected linearized mass spectrum of the recoiling target-like particles were fitted and identified. The fitted areas were normalized using monitor counts. Table 6.9 shows the spectrum configuration at the time of analysis. The 2D and the projected spectra contains two elastic peaks corresponding to $64/17^+$, $64/16^+$ and $60/17^+$,$60/16^+$ respectively. It is clear from the TOF-m/q 2D for ^{64}Ni that other m/q peaks such as 58/16, 62/17, 66/18, 63/17, 65/17, 58/15, 62/16, 66/17, 63/16 were also obtained along with the elastic peaks. The well defined peaks obtained for 1N,2N pickup and stripping channels for the $^{32}S+^{60,64}Ni$ systems are shown in the mass spectrum in figure 6.8. Even though HIRA has high efficiency for beam rejection, the focal plane position spectrum will be contaminated by a large number of beam-like particles. The recoils of interest were well separated from the beam-like scattered particles by setting a narrow energy and time window using TOF information. The TOF TAC was calibrated to 0.97 ns per channel and from the flight path length (ℓ=8.746 m) of HIRA, the TOF for the various mass peaks were calculated by considering the compression and Y-offset of the spectrum. The TOF was found to be ranging between 550 ns to 600 ns. From the TOF information the energy of the recoils were calculated with an energy of 1% as $E_R = m(\ell/t)^2$ which in turn gives the Q-value spectra. For a projectile energy E_P, the recoil energy is given theoretically as

$$E_R = [1-\{(A_p-A_t)/(A_p+A_t)\}^2]E_P \qquad (6.7)$$

The individual states are not well defined due to the kinematic broadening and energy spread in the target. The energy resolution obtained from the TOF was satisfactory. Figure 6.10 shows MWPC ΔE spectrum for the two systems where a clear separation between ERs and beam background was achieved with high energy recoils and low energy beam-like particles. The broadness of the recoil peak shows the high energy acceptance of HIRA. Another advantage of TOF TAC spectrum is the problem of m/q ambiguity can be well resolved. Actually the HIRA focuses particles of same m/q values to the same position. For example (a) 58/16≈62/17≈66/18 and (b) 58/15≈62/16≈66/17 and they focus almost to the same positions (a) and (b) respectively. But TOF varies according the

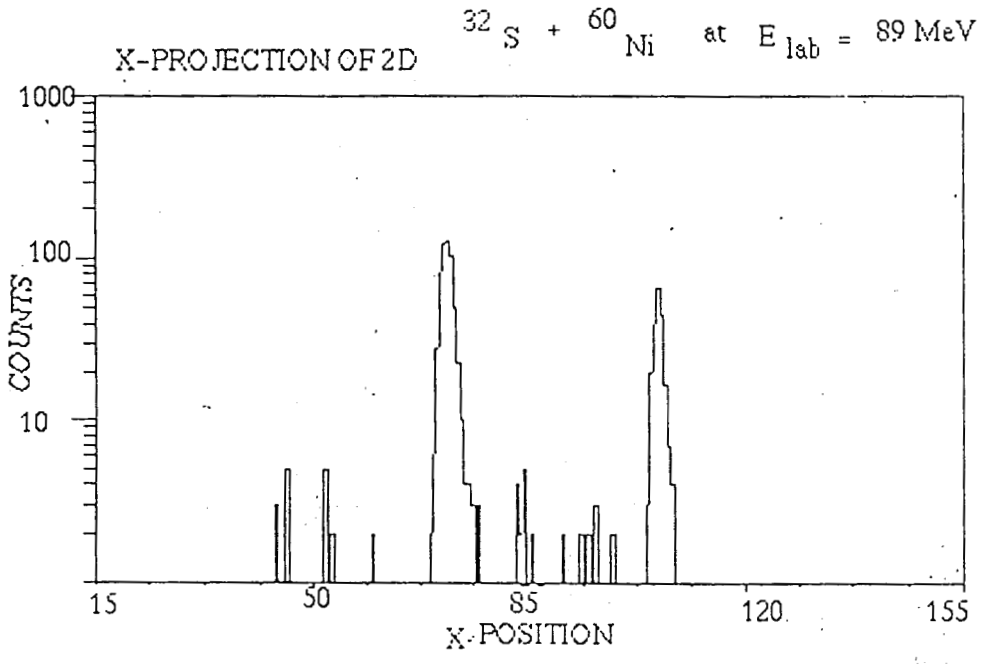

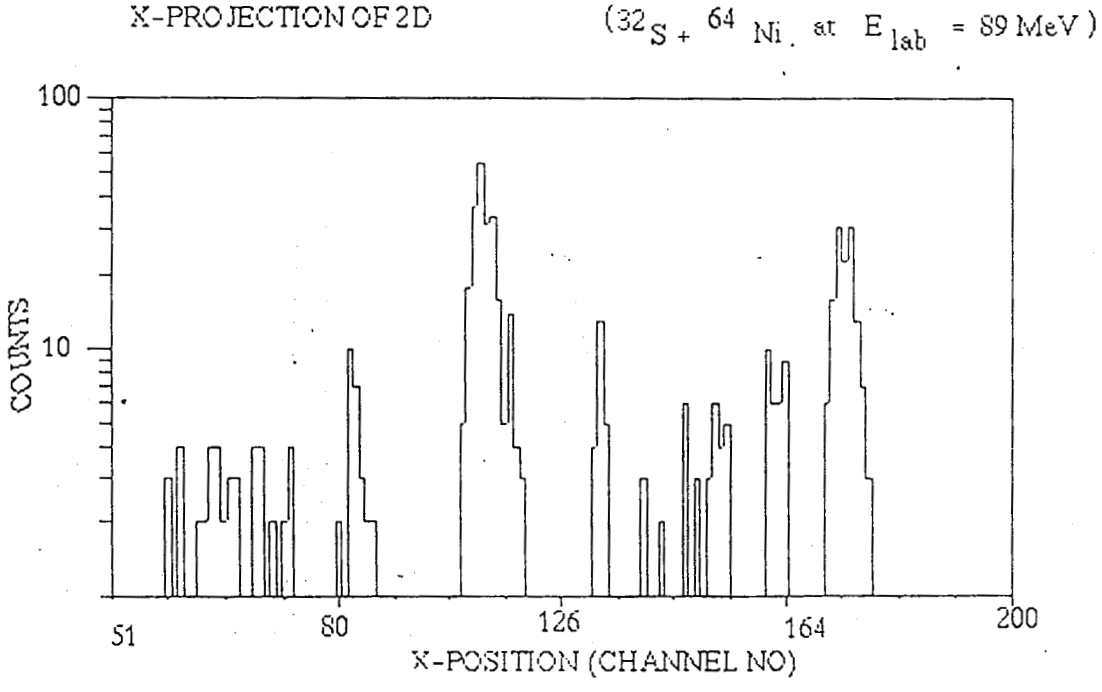

Figure 6.9: A typical mass spectra obtained by the banana gated projection of the TOF vs X-position (m/q) 2D spectrum for the $^{32}S + ^{60,64}Ni$ systems showing elastic and transfer peaks.

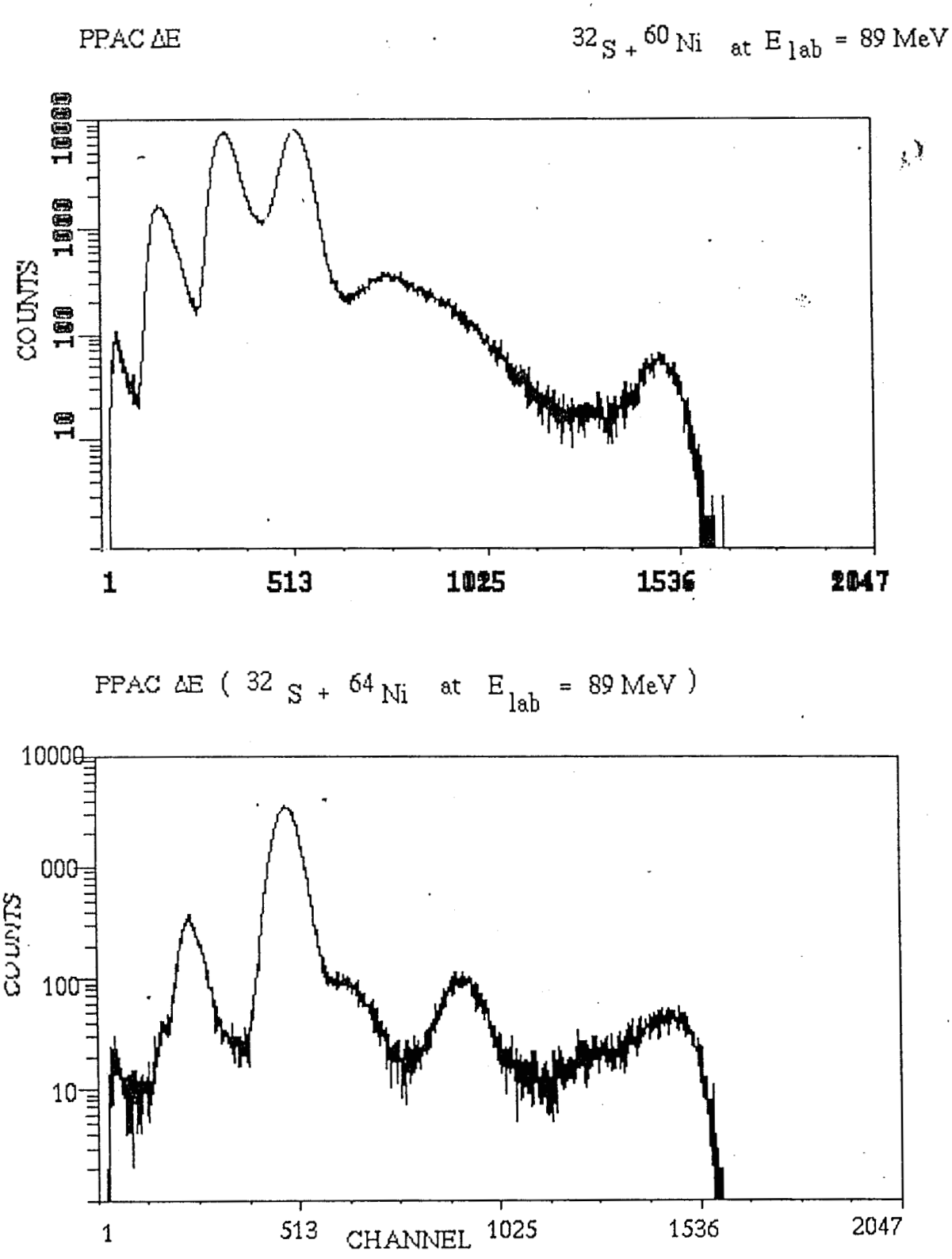

Figure 6.10 : MWPC ΔE spectrum obtained from the anode.

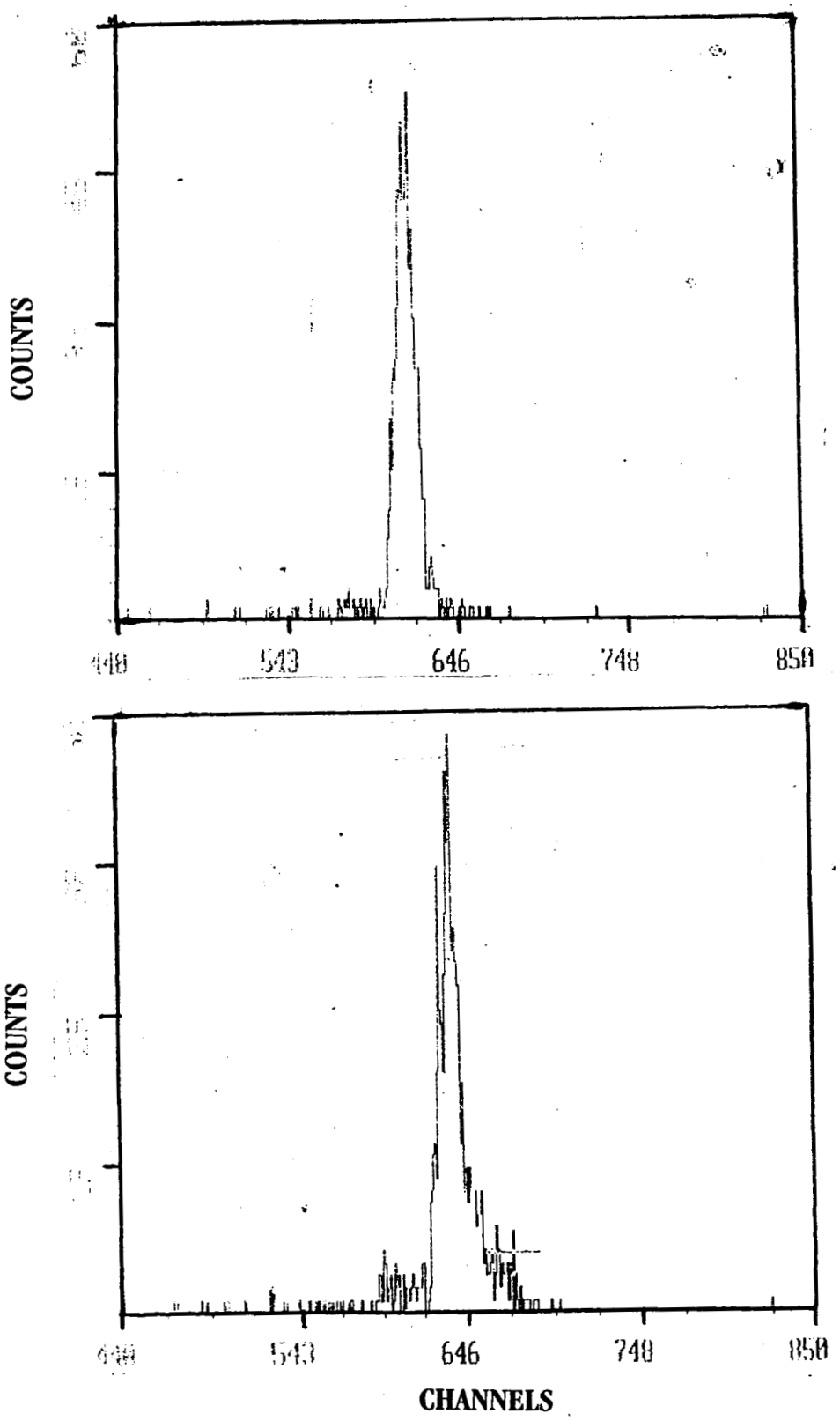

Figure 6.11 : TAC spectrum at 89 MeV for ^{60}Ni target (top) And ^{64}Ni target (bottom).

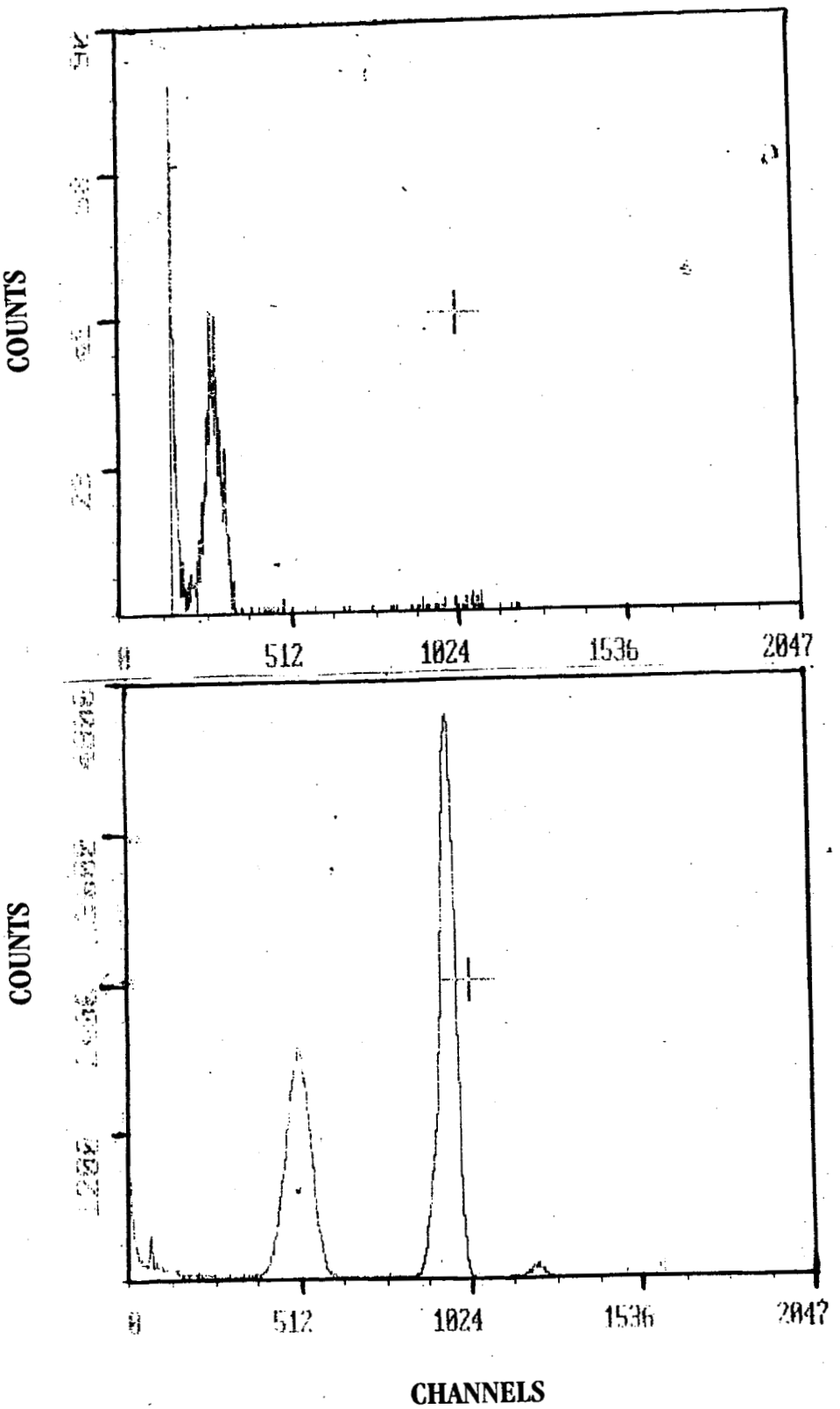

Figure 6.12 : Back SBD singles (top) and SBD monitor singles (bottom) for $^{32}S+^{60}Ni$ reaction at 89 MeV.

mass and it can well separate the different m/q combinations of the same value as shown in figure 6.7. The typical TAC spectra for the two targets is shown in figure 6.11 which gives the time spread for 60 and 64 amu at the focal plane of HIRA. The FWHM of TAC spectra gives the energy acceptance of HIRA. Back SBD singles at 86 and 89 MeV for the ^{60}Ni at 144° and the monitor singles for ^{32}S+^{60}Ni at 89 MeV is given in figure 6.12. If the recoil energy spread is large, the TOF spread become larger and the m/q ambiguity can not be resolved. The recoil energy with reasonable resolution can be obtained from ionization chamber energy spectrum and by putting energy gates on X position – TOF 2D spectra, the m/q ambiguity can be resolved.

6.11.1 Main advantages of NSCSORT

(i) Provision for X-Y compression and expansion.

(ii) Provision for selecting region of interest by drawing banana gates.

(iii) Provision for overlaying 1D spectra for comparison.

(iv) The capability for calculating dead time of the system from the ratio between the number of events actually processed (N_P) and the number of events recorded by the system(N_T).

(v) User can define virtual ADCs which can be used for particle identification.

(vi) Arithmetic operations such as addition, subtraction, multiplication and division are possible with ADCs with proper scaling by a factor.

(vii) The spectra can be projected with OR,AND or NOT gates.

(viii) Data from each ADC channel can be projected in to specific locations according to the requirements.

(ix) Non-linear least square fitting of single or multiple peaks is possible which gives centroid, FWHM and corresponding errors.

6.12 Charge State Distribution

A measurement of the charge state distribution to obtain the maximum probable charge state (optimal) having maximum yield was carried out as a part of the experiment for the $^{32}S+^{64}Ni$ system at 79 and 92 MeV. Figure 6.13 shows a typical charge state distribution at 92 MeV for the $^{32}S+^{64}Ni$ system. A Gaussian fit is given to guide the eye. Figure 6.14 shows the charge state distribution for the same system at 79 MeV. The measurement of the yield is done by setting up HIRA for different charge states and elastic counts are normalized by monitor counts to obtain the distribution. The optimal charge state selection decides the focal plane count rate, the observed separation between elastic scattered beam and evaporation residues and the amount of scattered particles in the mass spectra. HIRA can set for a particular recoil energy predicted by the computer code 'Kinematics' for any reacting nuclear system and the charge state distribution can be measured for a fixed incident energy. Using a carbon foil of thickness 5 $\mu g/cm^2$, the charge state can be resetted to study the effects of isomeric states.

At 79 MeV				
q +	Elastic Counts	Elastic Centroid	Monitor Counts	Normalised Counts
15^+	110	114	122890	0.0895
16^+	110	113	592287	0.0185
17^+	161	112	70672	0.2278
18^+	229	101	77072	0.2970
19^+	101	110	219784	0.0460
At 92 MeV				
q +	Elastic Counts	Elastic Centroid	Monitor Counts	Normalised Counts
15^+	337		49620	0.679
16^+	732		58526	1.250
17^+	1333	113	66233	2.013
18^+	1445		62119	2.326
19^+	672	113	69501	0.966

Table 6.10 : Charge state distributions of $^{32}S+^{64}Ni$ system at 79 MeV(top) and 92 MeV(bottom)

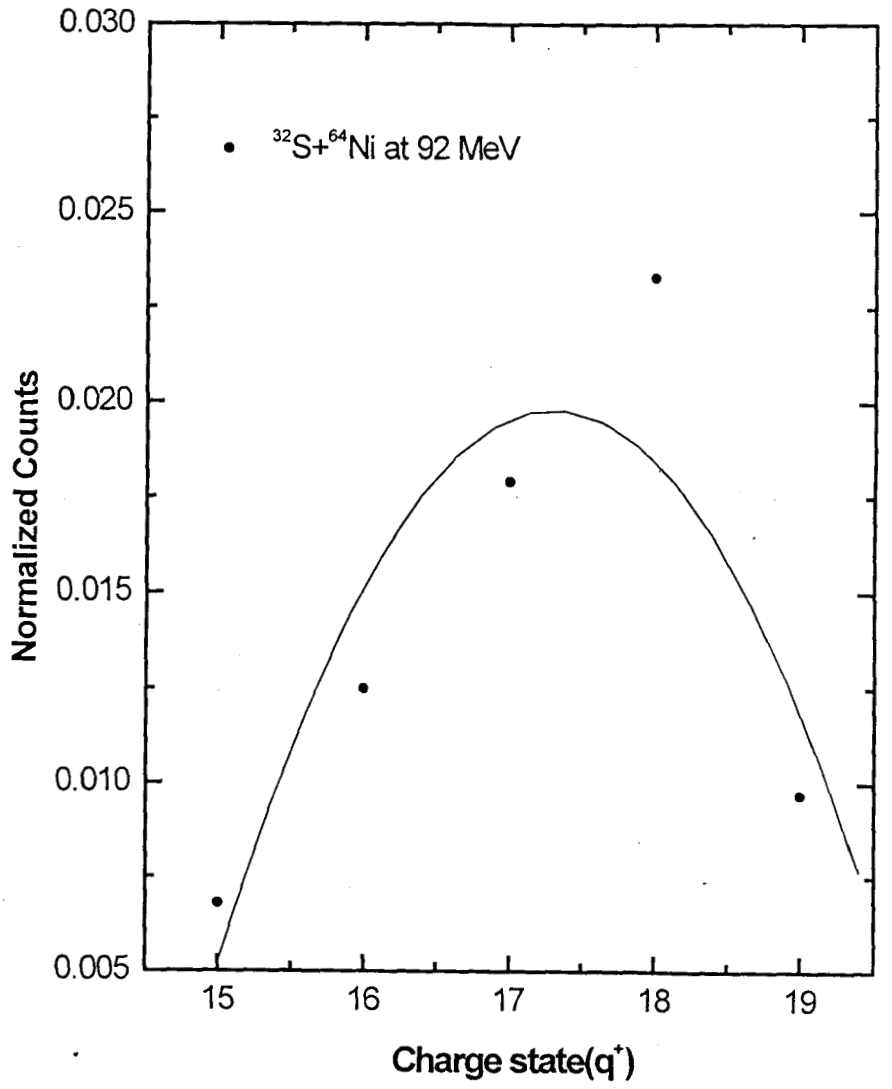

Figure 6.13 : Charge state distribution for $^{32}S+^{64}Ni$ at 92 MeV

An optimal charge state of 17^+ was obtained for $^{32}S+^{64}Ni$ system and 15^+ for $^{32}S+^{60}Ni$ system. So the experiment to measure the transfer products were carried out by setting HIRA for these charge states. Table 6.10 gives the results of the measurement of charge state distribution for the $^{32}S+^{64}Ni$ system at E_{lab} = 79 and 92 MeV. The peaking was observed near 17.5. But 17^+ was found to be better regarding beam back ground.

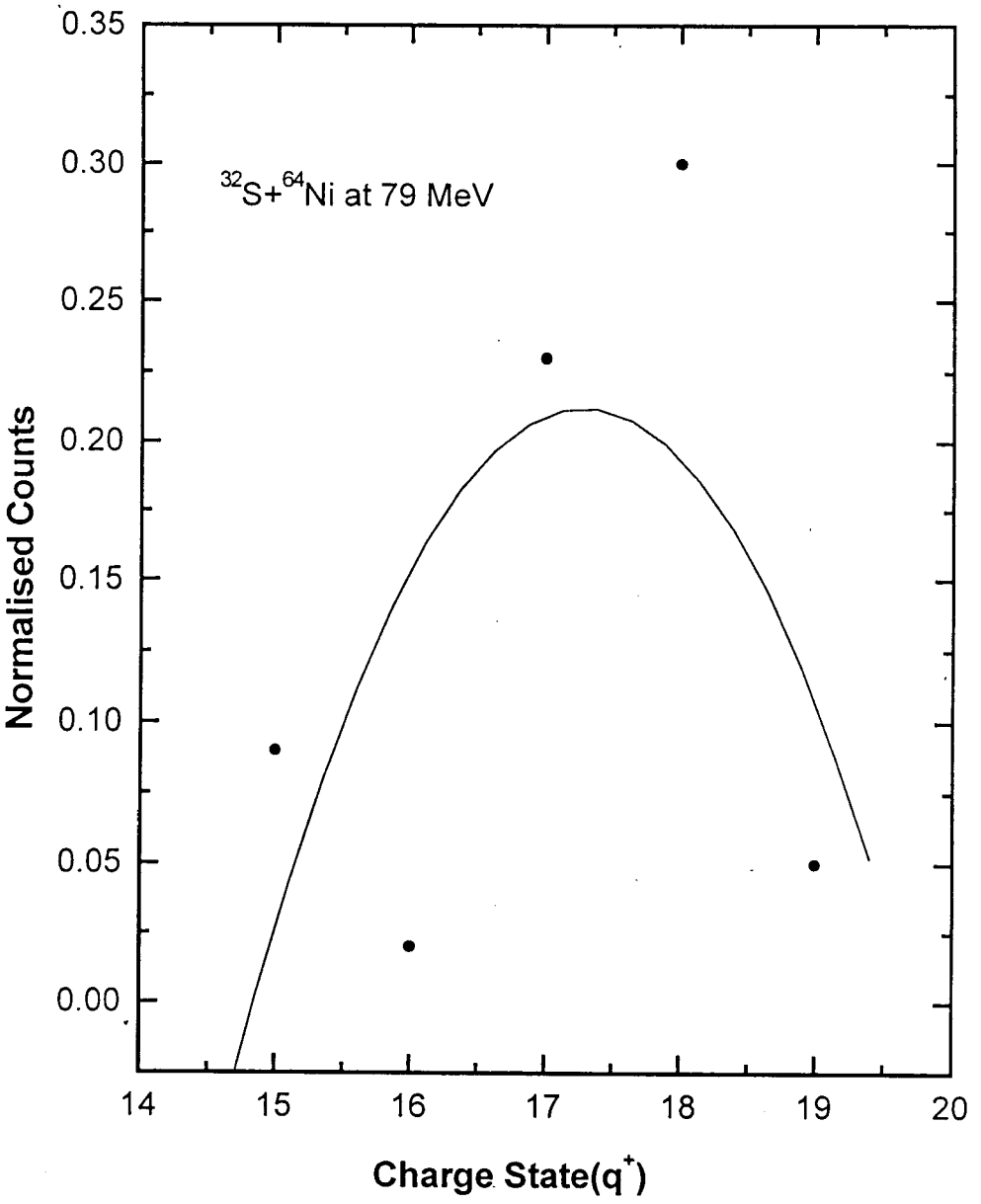

Figure 6.14 : Charge state distribution for $^{32}S+^{64}Ni$ at 79 MeV

6.13 Recoil Energy Scanning

HIRA was set for different recoil energies at a fixed charge state (17+) corresponding to the recoils of mass A = 64 amu. The recoil energy distribution were measured for the $^{32}S+^{64}Ni$ system at beam energies 79 MeV and 89 MeV. Details of the measurements is given in table 6.11. The expected recoil energy distribution can be obtained from the HIRA efficiency with a percentage variation ± 20%. If the observed recoil energy is peaking at some where on the broad efficiency distribution where the actual efficiency is a fraction of the expected efficiency, necessary corrections have to be incorporated to get the actual distribution. This was the aim of the recoil energy scanning using HIRA.

At 79 MeV				
E_R (MeV)	Elastic Centroid	Elastic counts	Monitor counts	Normalized counts
54.82	112	246	109423	0.00225
64.50	112	161	70672	0.00228
70.95	114	319	127919	0.00250
At 89 MeV				
E_R (MeV)	Elastic Centroid	Elastic counts	Monitor counts	Normalized counts
61.7	110.6	746	840705	0.0890
72.6	112.5	195	217527	0.0896
79.9	114.2	240	220703	0.1090

Table 6.11 : Results of the recoil energy scanning for the $^{32}S+^{64}Ni$ system

6.14 Mass Scanning

By varying the HIRA fields, a particular mass across the focal plane was selected. The corresponding yield was normalized by monitor counts. This gives the mass dependent efficiency of HIRA. This position dependent transfer efficiency is independent of the reaction and beam energy. The strong dependence of transport efficiency on focal plane shows that an efficiency correction is required for masses measured at different positions at the focal plane. If the peaking of different masses occur within the broad region of the maximum efficiency, there is no need of position dependent efficiency correction. But if the efficiency is a Gaussian distribution mass peaks shows a considerable variation from the

$^{32}S+^{64}Ni$ at 79 MeV					
m	m/q	Elastic centroid	Elastic Counts	Monitor Counts	Normalized Counts
61.5	3.62	150	163	58484	0.28
62.5	3.68	132	112	46838	0.24
63.5	3.74	112	161	70672	0.23
64.5	3.79	92	218	99256	0.22
65.0	3.82	80	106	43738	0.24
65.5	3.85	69	112	50379	0.22
66.0	3.88	59	73	42526	0.27
$^{32}S+^{60}Ni$ at 60 MeV					
m	m/q	Elastic centroid	Elastic counts	Monitor counts	Normalized counts
56.5	3.77	166.7	465	22167	2.09
57.0	3.80	160.4	3655	61053	5.98
58.0	3.86	143.9	3266	49919	6.54
59.0	3.93	123.1	3367	47232	7.13
60.0	4.00	101.1	4742	69248	6.84
61.0	4.07	77.3	3852	60175	6.40
62.0	4.13	52.8	775	53238	1.45
62.1	4.14	506.7	370	41471	0.89

Table 6.12 : Results of the mass scanning for the $^{32}S+^{60,64}Ni$ systems.

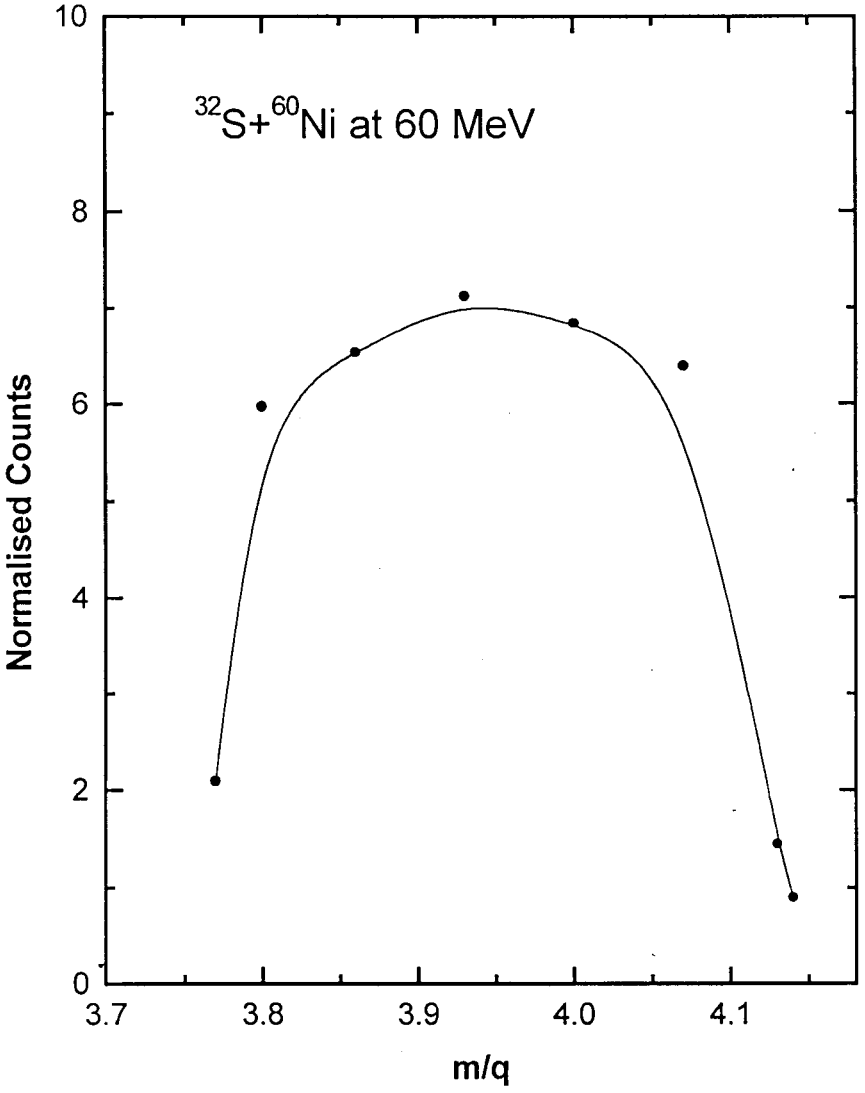

Figure 6.15 : Results of mass scanning for the $^{32}S+^{60}Ni$ at 60MeV

maximum efficiency, a correction of N_{obs} x 100/x have to be incorporated by fitting the data points where 'x' is the actual yield. Table 6.12 shows the results of the mass scanning measurements for the $^{32}S+^{60,64}Ni$ systems. Figure 6.15 shows the mass (m/q) distribution for $^{32}S+^{60}Ni$ at 60 MeV.

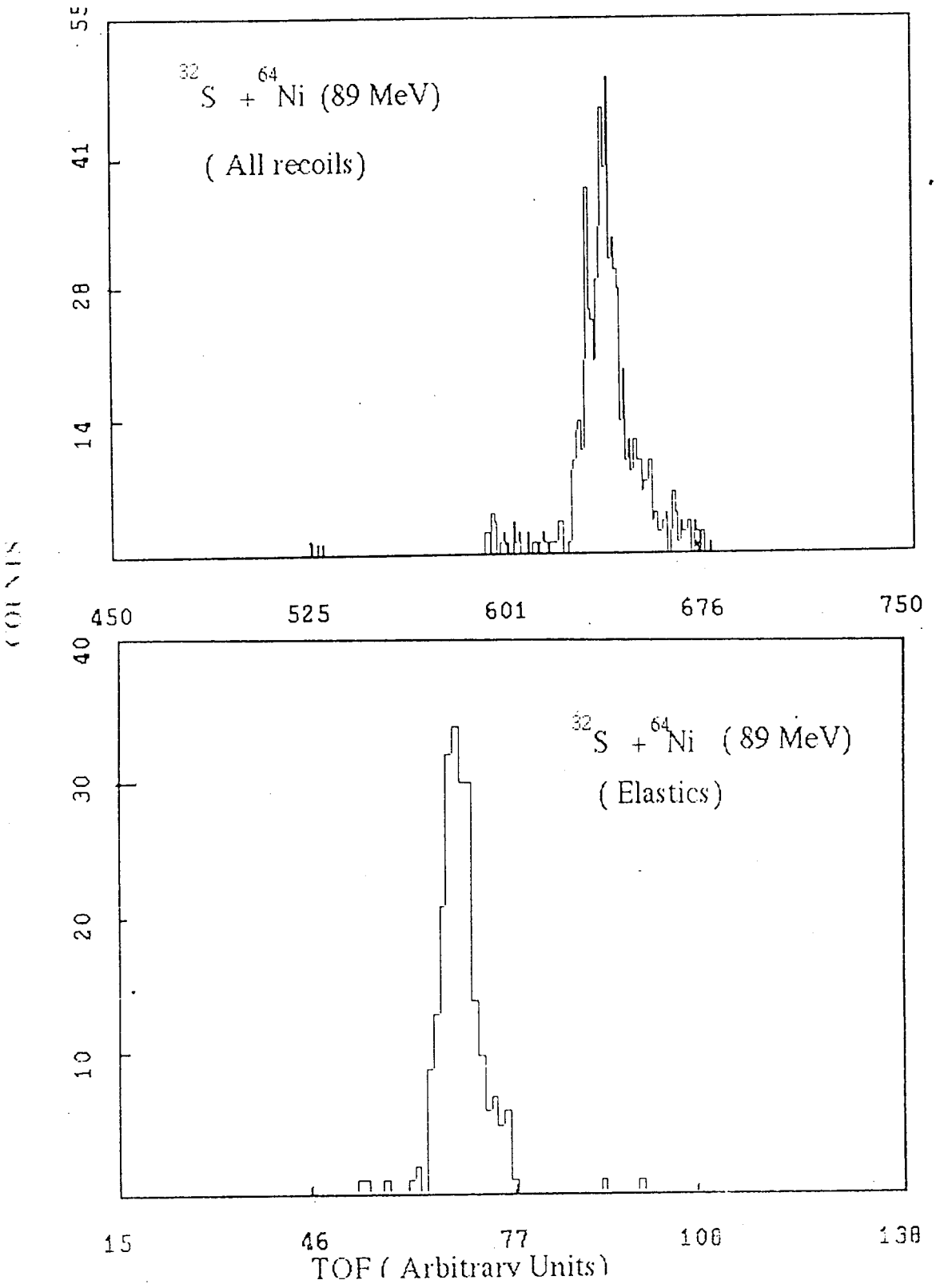

Figure 6.16 : A typical TOF spectrum for $^{32}S+^{64}Ni$ system at 89 MeV containing all recoils and elastics.

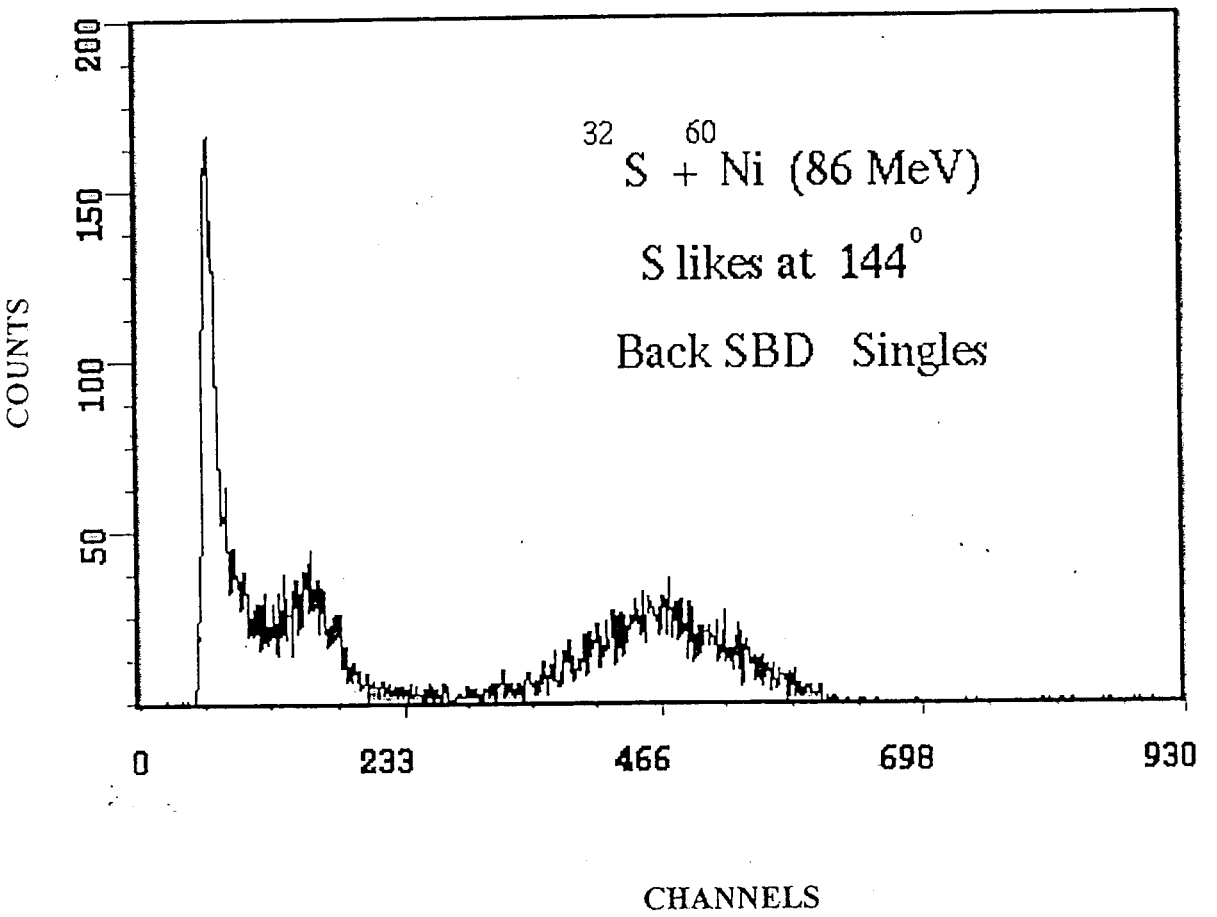

Figure 6.17 : Back SBD singles of sulphur-like particles detected at 144° for the $^{32}S+^{60}Ni$ at 86 MeV.

6.15 Back ground Subtraction

The background radiation reaching HIRA focal plane includes multiple scattering inside the electric dipoles, energy and angular straggling due to thick targets, isotopic impurity contaminations in targets etc. This can be corrected by fitting the mass peaks by assuming a linear back ground. Figure 6.16 shows the TOF spectrum for $^{32}S+^{64}Ni$ at 89 MeV containing all recoils and elastics. Figure 6.17 shows the back SBD singles of sulphur-like particles detected at 144° for $^{32}S+^{60}Ni$ at 86 MeV.

6.16 Calculation of the Back Scattered Sulphur Angles

The angles of the recoiling transfer products were determined for different back scattered angles of sulphur projectiles using the computer code 'Kinematics'. From this a quadratic relation can be deduced between θ_{Ni} and θ_S. This relation was used for the theoretical prediction of a distribution of the back scattered angles θ_S for which the counts for each angle have been determined using a computer program 'sniang.f ' by random number generation for a 10000 events. Out of θ_{Ni} calculated for a range of θ_S as mentioned above those values within the limits obtained by 'kinematics' have been used for the extraction of the counts. Each random event is weighted for the acceptance factor y/rS where r =1.93 cm and S = $\Delta\Omega_{Ni}/\Delta\Omega_S$ =1/16. The results of this calculation have been compared with the experimentally measured normalized counts for $^{32}S+^{64}Ni$ system in figure 6.18, which shows good agreement. Figure 6.19 shows a comparison of the normalized TAC counts for $^{32}S+^{60}Ni$ and $^{32}S+^{64}Ni$ system at 60 MeV as a function of sulphur SBD angle. Figure 6.20 gives the variation of yield with respect to SBD angle for $^{32}S+^{64}Ni$ system at 89 MeV (2N pickup) for different Q-values. The experimentally observed variation of the normalized counts with back SBD angle for $^{32}S+^{60}Ni$ at 60 MeV is given in figure 6.21. The back SBD set angle at E_{lab}= 89 MeV is 146° corresponding to the nickel-like recoil energy 73.2 MeV obtained by correcting for an energy loss of 2.77 MeV. The angle θ_S varies between 142° to 150° for a variation of HIRA angle θ_{Ni} between 8.3° to 9.5°.

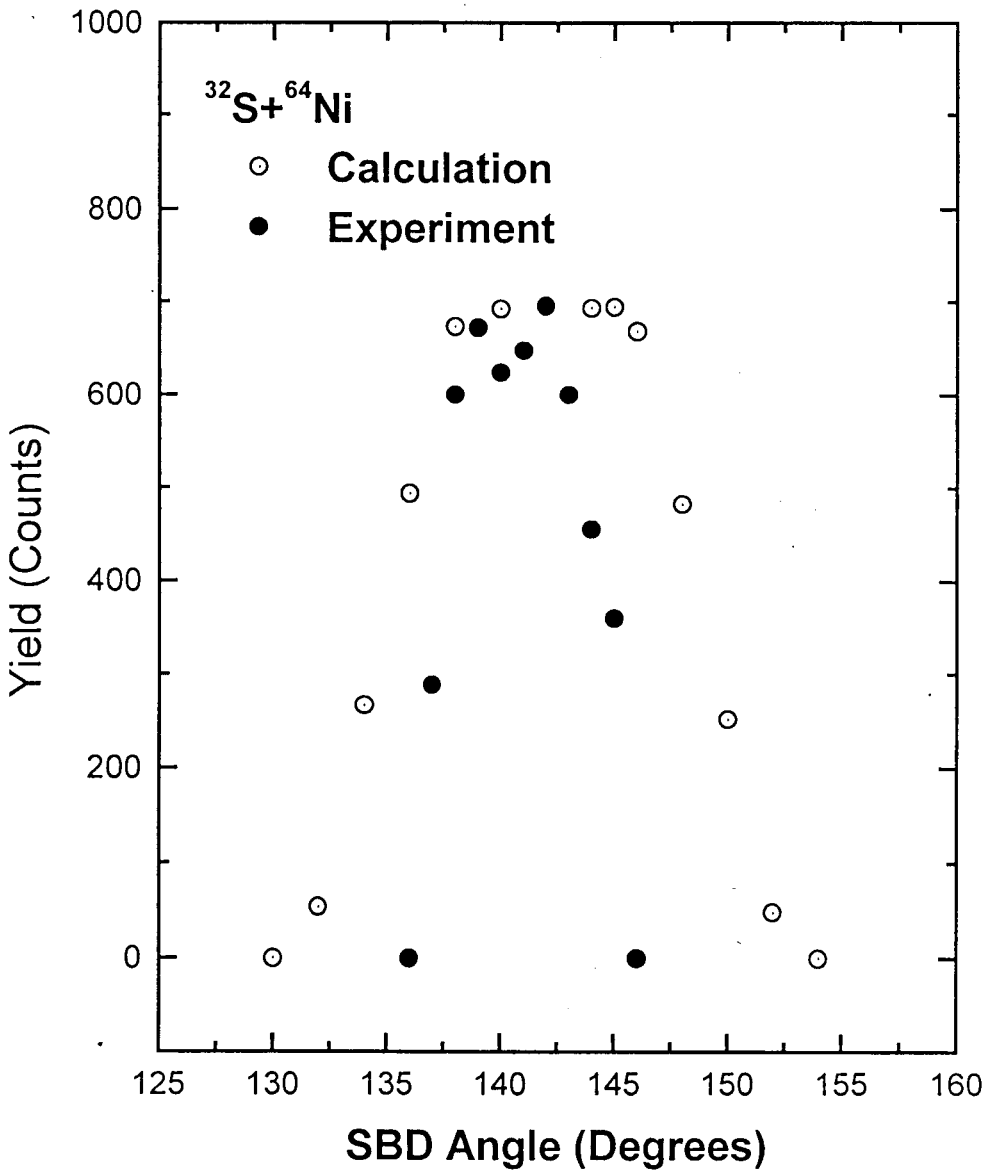

Figure 6.18 : A comparison of the yield at the back S-SBD between the theoretical calculation and the present experimental results for the ^{32}S+^{64}Ni system.

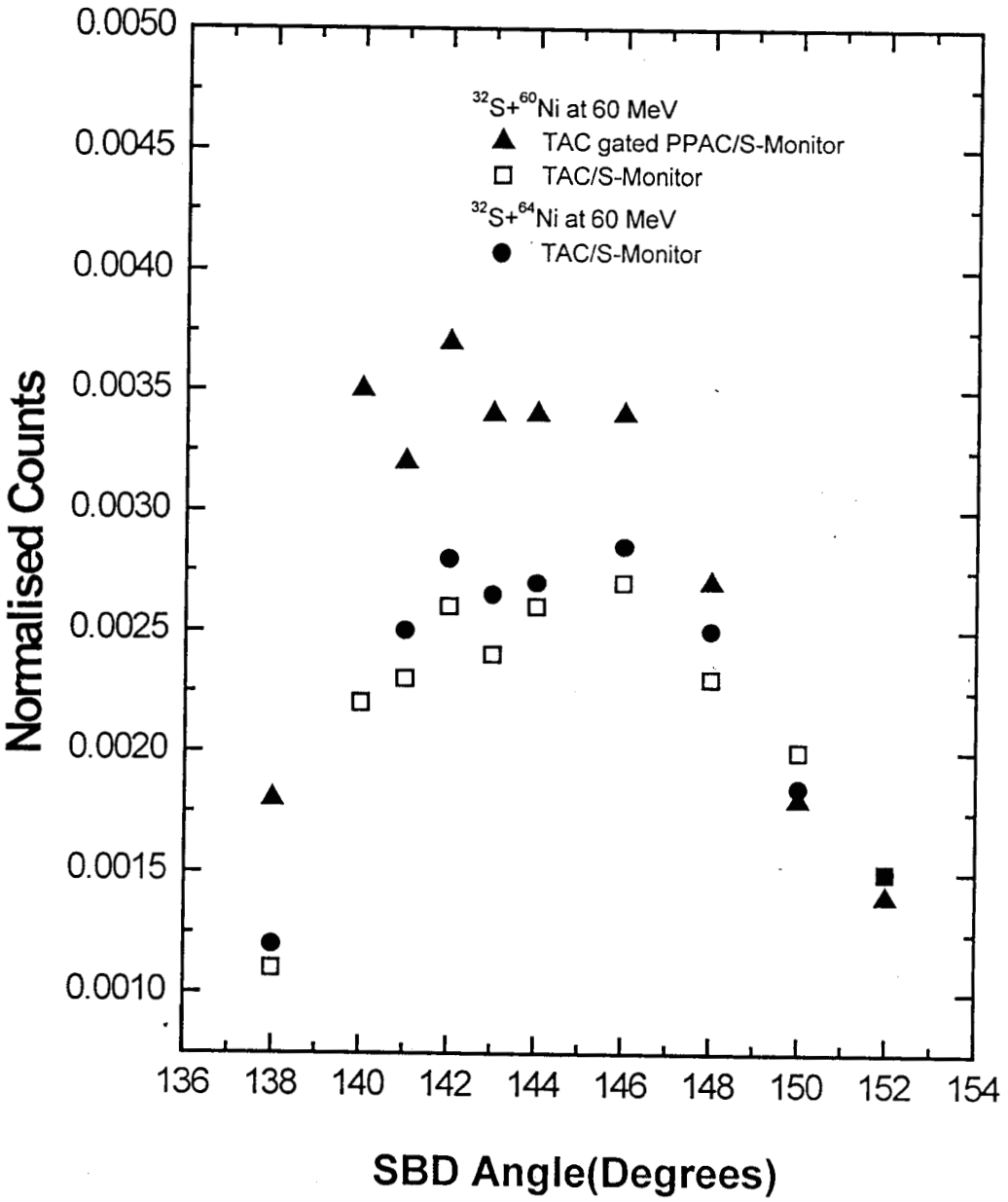

Figure 6.19 : The normalized TAC gated MWPC anode and TAC yield with the variation of back sulphur SBD angle for the $^{32}S+^{60,64}Ni$ systems at 60 MeV.

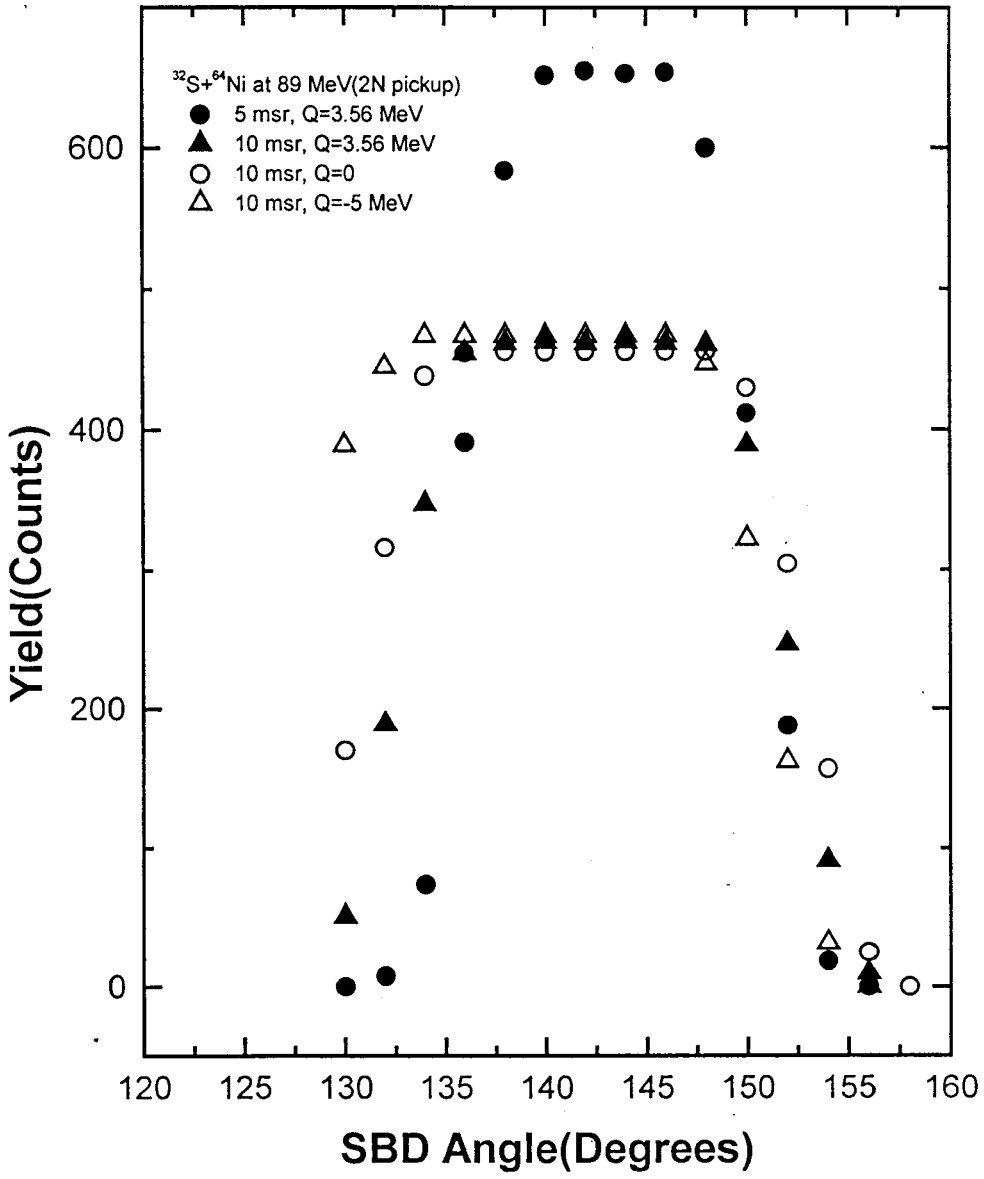

Figure 6.20 : The dependence of yield at the back SBD for the variation of solid angle corresponding to different solid angles of HIRA for different Q-values for the $^{32}S+^{64}Ni$ system at 89 MeV.

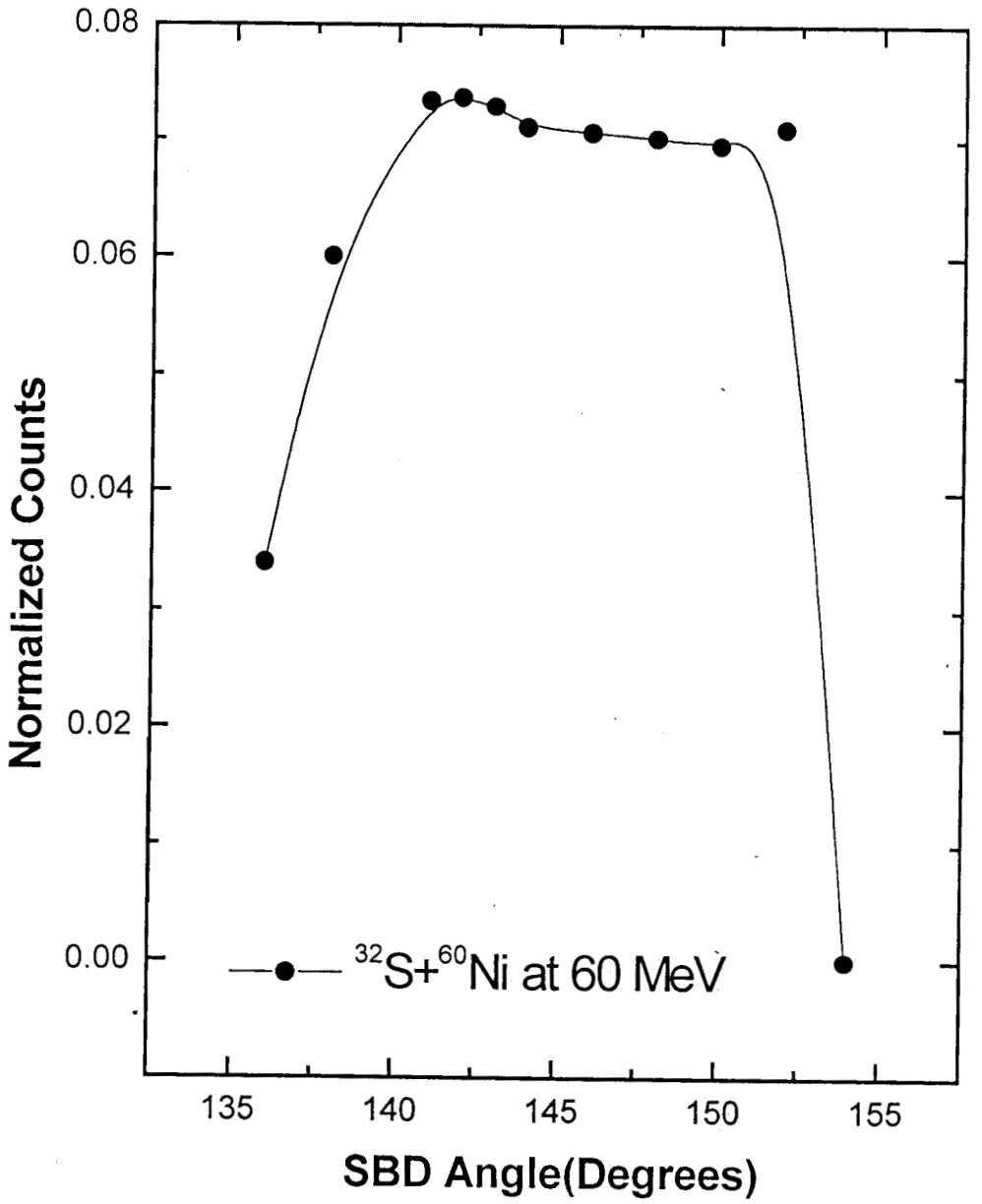

Figure 6.21 : The normalized yield as a function of the back sulphur SBD angles for $^{32}S+^{60}Ni$ system at 60 MeV.

6.17 Q-value Spectrum

The energy of the target like recoils E_{Ni} was determined from the TOF as

$$E_{Ni} = (Mc^2/2)(\ell/ct)^2 \quad (6.8)$$

where Mc^2 is equal to A×931 MeV, ℓ is the flight path length of the recoils equal to the length of HIRA (≅ 880 cm) and ct = 30T. The TOF is measured as T = α+βC. From the TOF - TAC calibration α = 60 ns, β=0.9737 ns and C is the channel number.

$$E = (A \times 931/2)(880/30T)^2 = K/T^2 \quad (6.9)$$
$$dE = -2KdT/T^3 \quad (6.10)$$
$$|dT/dE| = T^3/2K \quad (6.11)$$

From the T vs N(T) TOF spectrum of channel width β = 0.9737 ns, the E vs N(E) energy spectrum can be determined by calculating N(E) using the program 'ttoe.f ' as

$$N(E) = N(T)dT/dE = N(T)T^3/2K \quad (6.12)$$

A plot of the energy spectrum is given in figure 6.22 which shows the peaks corresponding to elastic, pickup(1N,2N) and stripping(1N,2N) channels. The variation of E_{Ni} with Q-value can be determined using the program 'kinematics' and plotted in figure 6.23. The slope of the Q vs E_{Ni} plot gives dE/dQ for different transfer channels. From the E vs N(E) plots the actual Q-value spectrum [30] Q vs N(Q) can be obtained by calculating N(Q) as

$$N(Q) = N(E)dE/dQ \quad (6.13)$$

The value of N(E) used in this calculation can be taken from the energy spectrum corresponding to the Q-values ranging from –5 to +5 MeV for each recoil energy E_{Ni}. The FWHM of the kinetic energy distribution of the elastically scattered recoils at E_{lab} = 73.2 MeV (corrected) is obtained as 1.9 MeV. By fitting the Q-value (energy) spectrum for 2-neutron transfer using a Gaussian fit at 1.9 MeV width, with expected energies at the center, the transfer form factor strength for individual states can also be extracted from the Q-value spectrum fitting. Because of the poor resolution of the individual states, accuracy in determining the strength of the individual states is less. So a correction has to be applied to the form factor for the ground state and excited states. Figure 6.24 shows a plot of the peak centroids of the converted energy spectrum obtained from TOF for different transfer products for $^{32}S+^{64}Ni$ at 89 MeV using the program 'ttoe.f '. A method of extraction of transfer form factor from the energy/Q-value spectrum was reported earlier[31].

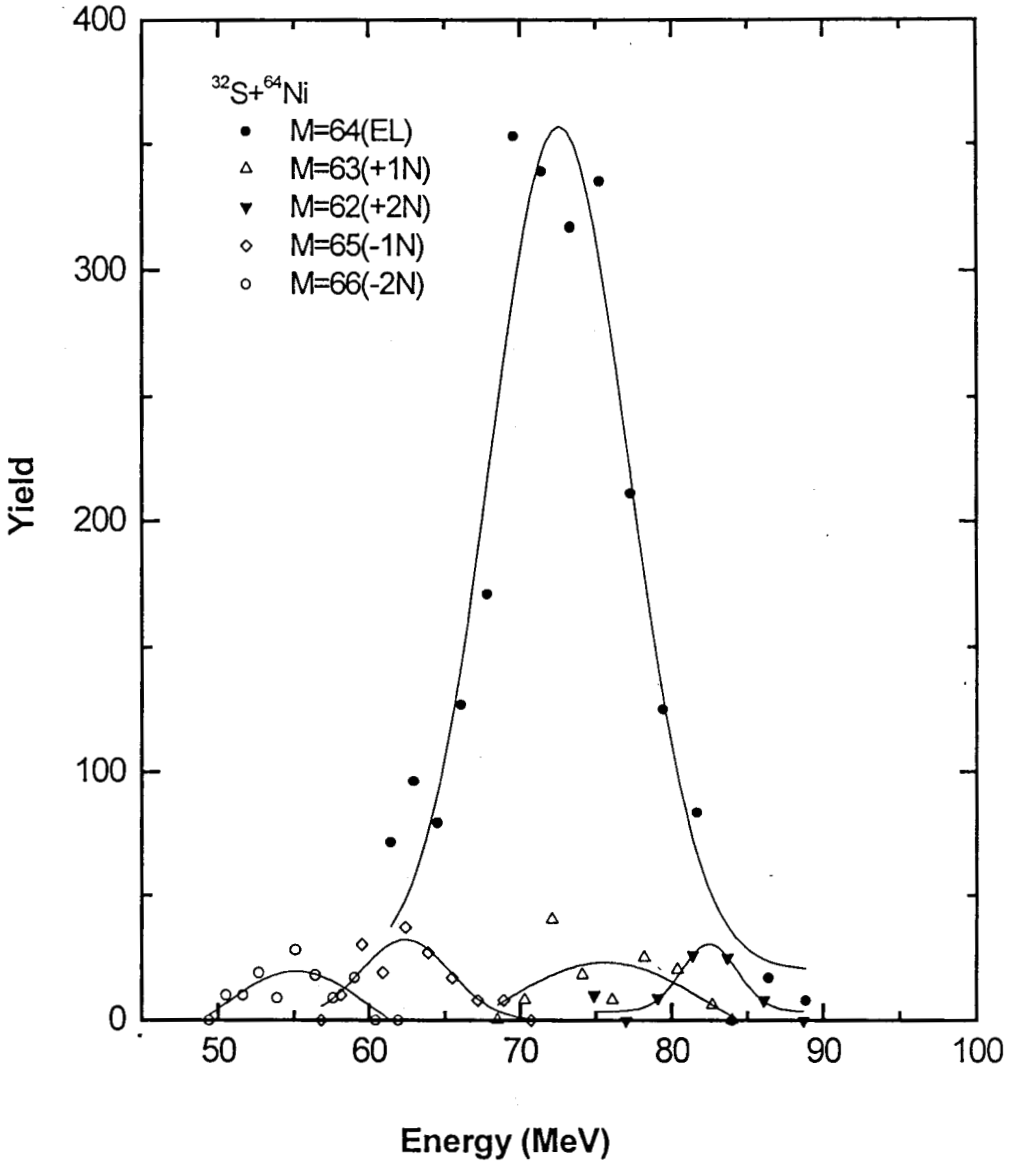

Figure 6.22 : Recoil Energy spectrum for the transfer products of $^{32}S+^{64}Ni$ experiment which shows clear peaks for 1N,2N pickup and 1N,2N stripping.

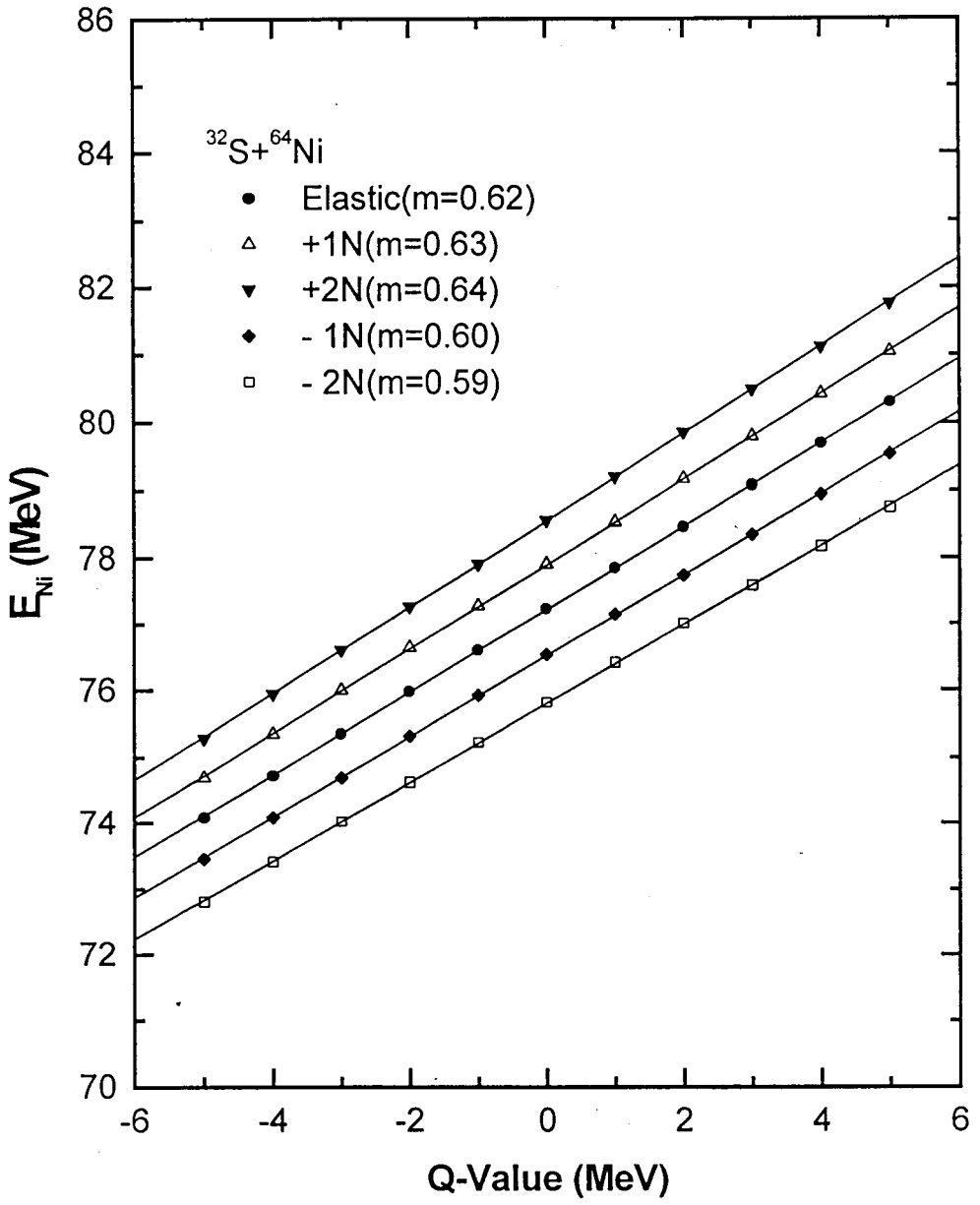

Figure 6.23 : The dependence of recoil energy on Q-value ranging from –5 to +5 MeV for $^{32}S+^{64}Ni$ system determined by the computer code 'Kinematics'. The slope (m) of this plots gives dE/dQ which can be used in determining the Q-value spectrum.

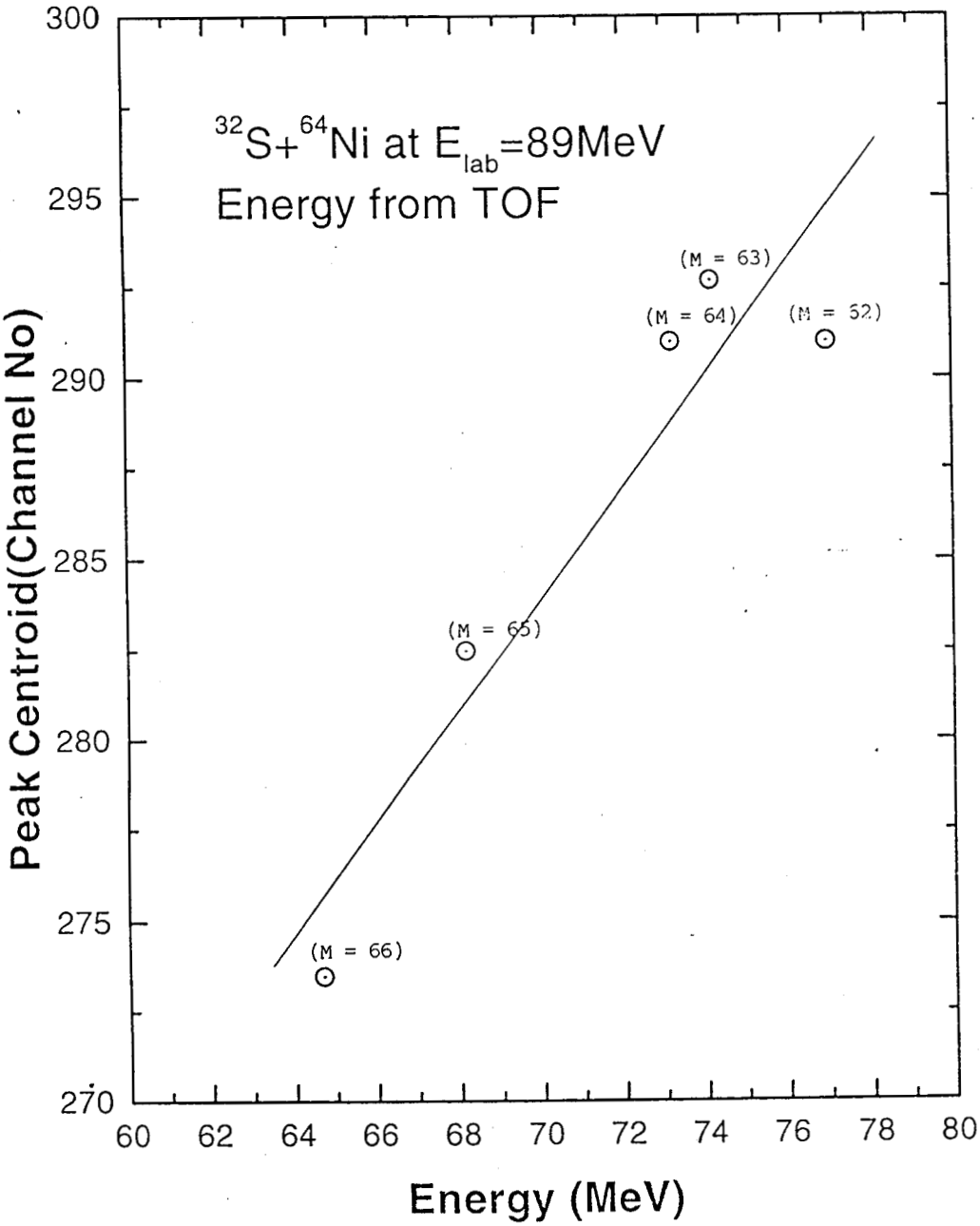

Figure 6.24 : Plot of the peak centroids of the converted energy spectrum obtained from TOF for different transfer products for $^{32}S+^{64}Ni$ at 89 MeV using the program ttoe.f

References

[1] R.R Betts, P.M. Evans, C.N. Pass, N. Poffe, A.E. Smith, L. Stuttge, J.S. Lilley, D.W. Banes, K.A. Connell, J. Simpson, J.R.H. Smith, A.N. James, B.R. Fulton, Phys.Rev. Lett. **59**(1987)978.

[2] L.Corradi, G. Montagnoli, D.R. Napoli, P. Spolaore, A.M. Stefanini, Xu Jincheng, S. Beghini, F. Scarlassara, G.F. Segato, F. Soramel and C. Signorini, Nucl. Instr. and Meth. **A297**(1990)461.

[3] R.R.Betts, Nucl. Instr. and Meth.**162**(1979)531.

[4] G.W.Butler, A.M.Poskanzer and D.A.Landis, Nucl. Instr. and Meth. **89**(1970)189

[5] D.Kanjilal, S. Chopra, M.M. Narayanan, I.S. Iyer, V. Jha, R. Joshi and S.K. Datta, Nucl. Instr. and Meth. **A328**(1993)97.

[6] G.K. Mehta and A.P. Patro, Nucl. Instr. and Meth. **A268**(1988)334.

[7] N.Madhavan, J.J. Das, P. Sugathan, D.O. Kataria, D.K. Avasthi and A. Mandal, Nucl. Instr. and Meth. **A370**(1996)315.

[8] A.Sarkar et al., Nucl. Instr. and Meth. **A371**(1996)351.

[9] R.O.Sayer, Revue de Physique Appliquëe **12**(1972)1543.

[10] A.K.Sinha, Proced. DAE Symp. on Nucl.Phys. **33A**(1990)198.

[11] A.K.Sinha, N. Madhavan, J.J. Das, P. Sugathan, D.O. Kataria, A.P. Patro and G.K. Mehta, Nucl. Instr. and Meth. **A339**(1994)543.

[12] D.O.Kataria, A.K. Sinha, J.J. Das, N. Madhavan and P. Sugathan, Proced. DAE Symp. on Nucl. Phys.(Bombay) **Vol.35B**(1992)498.

[13] I.S. Iyer and D. Kanjilal, Proced. DAE Symp. on Nucl. Phys. **35B**(1992)494.

[14] Roy Middleton, David Juenemann and Jeffrey Klein, Nucl. Instr. and Meth. **B93** (1994)39.

[15] G. Clausnitzer, H. Klinger, A. Muller and E. Salzborn, Nucl. Instr. and Meth. **128** (1975)1.

[16] R. Middleton and C.T. Adams, Nucl. Instr. and Meth. **118**(1974)329.

[17] G.T.Caskey, R.A.Douglas, H.T.Richards and H.V.Smith, Nucl. Instr. and Meth. **157** (1978)1.

[18] R.D. Rathmell and G.A. Norton, Nucl. Instr. and Meth. **B21**(1987)270.

[19] R. Middleton, Nucl. Instr. and Meth **214**(1983)139.

[20] G.D. Alton, Nucl. Instr. and Meth. **A244**(1986)133.

[21] Roy Middleton, "Treatise on Heavy Ion Science", **Vol.7**(1985)53.

[22] D.K. Avasthi, Jaipal and S. Gargari, Nucl. Instr. and Meth. **A303**(1991)43.

[23] Jaipal, D. Kabirraj and D.K. Avasthi, Nucl. Instr. and Meth. **A334**(1993)196.

[24](a) P.P. Shakkeeb, A.M. Vinod Kumar, K.M. Varier, N.V.S.V. Prasad, R. Singh, A.K. Sinha, N. Madhavan, P. Sugathan, D.O. Kataria and Lagy. T. Baby, Proced. DAE Symp. on Nucl. Phys. **38B**(1995).

(b) P.P. Shakkeeb, A.M. Vinod Kumar, K.M. Varier, N.V.S.V. Prasad, R. Singh, A.K. Sinha, N. Madhavan, P. Sugathan, D.O. Kataria and Lagy. T. Baby, Annual Report, Nuclear Science Centre,New Delhi (1995)78.

[25] A.K.Sinha, L.T. Baby, N. Badiger, J.J. Das, S.K. Hui, D.O. Kataria, R.G. Kulkarni, N. Madhavan, P.V. Madhusudhana Rao, I. Mazumdar, M.C. Radhakrishna, N.V.S.V. Prasad, N.G. Puttaswamy, P.P. Shakkeeb, R. Singh, D.L. Sastry, P. Sugathan, V. Tripathi, K.M. Varier and A.M. Vinod Kumar, J. Phys. G. Nucl. Part. Phys.**23** (1997)1331.

[26] S. Muralidhar, A.K. Sinha, N. Madhavan, P. Sugathan and J.J. Das, Proced. DAE Symp. on Nucl. Phys.(BARC) **Vol.35B**(1992)502.

[27] E.T.Subramanian, P.Sugathan, A.K.Sinha, N.Madhavan and J.J.Das, Proced. DAE Symp. on Nucl. Phys.(BARC) **Vol.35B**(1992)500.

[28] R.K.Bhowmik et al., Proced. National Symp. on Adv. Instr. for Nucl. Res.(1993) **D1-1**.

[29] R.K.Bhowmwik, D.K.Goyal, and S.naithani, Proced. DAE Symp. on Nucl. Phys. (Bombay) **34B**(1992)498.

[30] D.O.Kataria, A.K. Sinha, J.J. Das, N. Madhavan, P. Sugathan, Lagy. T. Baby, I. Mazumdar, R. Singh, C.V.K. Baba, Y.K. Agrawal, A.M. Vinod Kumar and K.M. Varier, Phys. Rev. **C56**(1997)1902.

[31] L.Corradi, S.J. Skorka, U. Lenz, K.E.G. Löbner, P.R. Pascholati, U. Quade, K. Rudolph, W. Schomburg, M. Steinmayer, H.G. Thies, G. Montagnoli, D.R. Napoli, A.M. Stefanini, A. Tivelli, S. Beghini, F. Scarlassara, C. Signorini and F. Soramel, Z. Phys. **A 334**(1990)55.

Chapter 7

Transfer Experiment - Results and Discussions

In this chapter the various results obtained by the transfer experiments discussed in the previous chapter for the $^{32}S+^{60,64}Ni$ system are given. The effective Q-values were extracted from ground state Q-values for each transfer channel for the two systems. The distance of closest approach d_0 and distance parameter D has been calculated for all centre-of-mass energies. The transfer probabilities have been extracted from the experimental data with probable errors. The variation of transfer probability P_{tr} with d_0 and D has been studied. The slope parameters and the widths of the form factors have been determined from the experimental P_{tr} directly and by fitting. The optimum Q-value have been calculated on the basis of experimental results. It is predicted by Buttle and Goldfarb [1] that the transfer is most probable when the incident and outgoing orbits at the distance of closest approach are matched. So the slope parameter(α), transfer probability (P_{tr}), coupling strength (F) and width of form factor(σ) have been calculated from the fitted values of P_{tr} at distance of closest approach d_0=1.44 fm. The extracted form factors have been used in the coupled channel calculations. The couplings have been done with 1DBPM using the inelastic excitations(2^+,3^-), transfer and higher order phonon coupling [2] through various combinations and compared with previously reported experimental results [3,4,5].

7.1 Distance Parameter and Distance of closest Approach

The specific energy loss dE/dx of the beam in the target for different beam energies for the two targets have been calculated using the computer code TRIM. The value of dE/dx was used to calculate the half thickness energy loss (HTEL). The incident energy is corrected for HTEL in centre-of-mass which was used for calculating the distance parameter D[6] using equation (3.13). From the value of D, the distance of closest approach at each incident energy was calculated for the two systems $^{32}S+^{60,64}Ni$, using equation (3.14). Table 7.1 gives the results of these calculations for the $^{32}S+^{64}Ni$ system at different incident energies at which the experiment was performed.

E_{lab} (MeV)	dE/dx MeV/μg/cm^2	HTEL (MeV)	E_{lab}(corr) (MeV)	E_{cm}(corr) (MeV)	D(Fermi)	d_0(Fermi)
60	11.80	1.433	58.56	39.04	16.65	2.32
70	11.20	1.360	74.63	49.75	13.06	1.82
79	11.50	1.354	77.64	51.76	12.56	1.75
81	11.09	1.347	79.60	53.10	12.24	1.70
83	11.03	1.340	81.65	54.44	11.94	1.66
84.5	10.98	1.334	83.16	55.44	11.72	1.63
86	10.94	1.329	84.67	56.44	11.51	1.60
87.5	10.89	1.323	86.17	57.45	11.32	1.57
89	10.85	1.318	87.68	58.45	11.12	1.55
92	10.76	1.307	90.69	60.46	10.75	1.50

Table 7.1 : Calculation of the distance parameter (D) and distance of closest approach (d_0) from E_{cm} for $^{32}S+^{64}Ni$ system.

7.2 Measurement of Transfer Probability

The mass peaks of the mass spectra shown in figure 6.9 were identified and fitted with single or multiple Gaussian. FWHM is taken as same for all peaks while fitting the multiple peaks. The counts in the elastic peak and in the mass peaks of different transfer channels were taken for all runs from the fitted results. The fitting program can search for all parameters and follows an iterative procedure to get the minimum chisquare value. The transfer channels identified were 1N,2N pickup and 1N,2N stripping channels. The other multinucleon transfer channels were not identified. The transfer probabilities [7] were determined from the fitted data for the channels for the channels such as +1N, +2N, -1N and -2N for the two systems as the ratio between the counts in the individual transfer channel to the sum of the counts in the total transfer channel and elastic peak as follows. HIRA focuses the elastically scattered recoils along with the recoiling inelastic and transfer products . Since the solid angle is same for all channels, the yield of these channels can be directly used for obtaining the transfer probability as

$$P_{tr} = N_{tr}/(N_{tr}+N_{el}) \qquad (7.1)$$

E_{lab}	d_0	$Ptr\|_{+1N}$	$Ptr\|_{+2N}$	$Ptr\|_{-1N}$	$Ptr\|_{-2N}$
			$^{32}S+^{64}Ni$		
92.0	1.50	10.02±3.28	5.6±1.53	5.61±2.4	3.74±1.27
89.0	1.55	7.6±1.58	6.53±0.63	6.52±1.49	6.27±1.37
87.5	1.58	9.3±0.77	2.93±0.26	7.91±0.7	4.46±0.36
86.0	1.60	5.0±0.63	3.55±0.36	6.2±0.67	3.25±0.38
84.5	1.63	4.21±0.4	1.46±0.13	6.19±0.46	2.24±0.2
83.0	1.66	2.97±0.32	---	4.47±0.41	1.48±0.1
81.0	1.70	1.69±0.17	0.16±0.07	2.13±0.2	1.24±0.11
79.0	1.75	0.84±0.24	0.22±0.12	0.95±0.2	0.37±0.06
76.0	1.82	0.50±0.12	0.16±0.10	0.27±0.1	---
			$^{32}S+^{60}Ni$		
89.0	1.60	1.9±0.48	1.0±0.34	2.38±0.54	1.31±0.398
86.0	1.66	0.63±0.12	0.197±0.066	0.70±0.12	0.57±0.112
84.5	1.69	0.59±0.59	---	0.59±0.59	---
83.0	1.72	0.46±0.13	0.07±0.05	0.38±0.12	0.04±0.04

Table 7.2 : The experimentally measured transfer probabilities in percentage for $^{32}S+^{60,64}Ni$ systems with probable errors.

Table 7.2 shows the measured transfer probabilities for pickup(+1N,+2N) and stripping (-1N,-2N) channels for the $^{32}S+^{60,64}Ni$ system at various incident energies with the corresponding distance of closest approach. The probable errors in the measurement is also estimated and given in the same table. Figure 7.1 shows the variation of P_{tr} with respect to the distance of closest approach d_0 for the $^{32}S+^{64}Ni$ system. Figure 7.2 shows the same for $^{32}S+^{60}Ni$ system. Figure 7.3 shows a comparison of our results of the measurement of transfer probability with the results obtained by LNL group for the $^{32}S+^{64}Ni$ system. A plot of $P_{tr}/\sin(\theta/2)$ versus distance parameter D [8] for the $^{32}S+^{64}Ni$ system is given in figure 7.4.

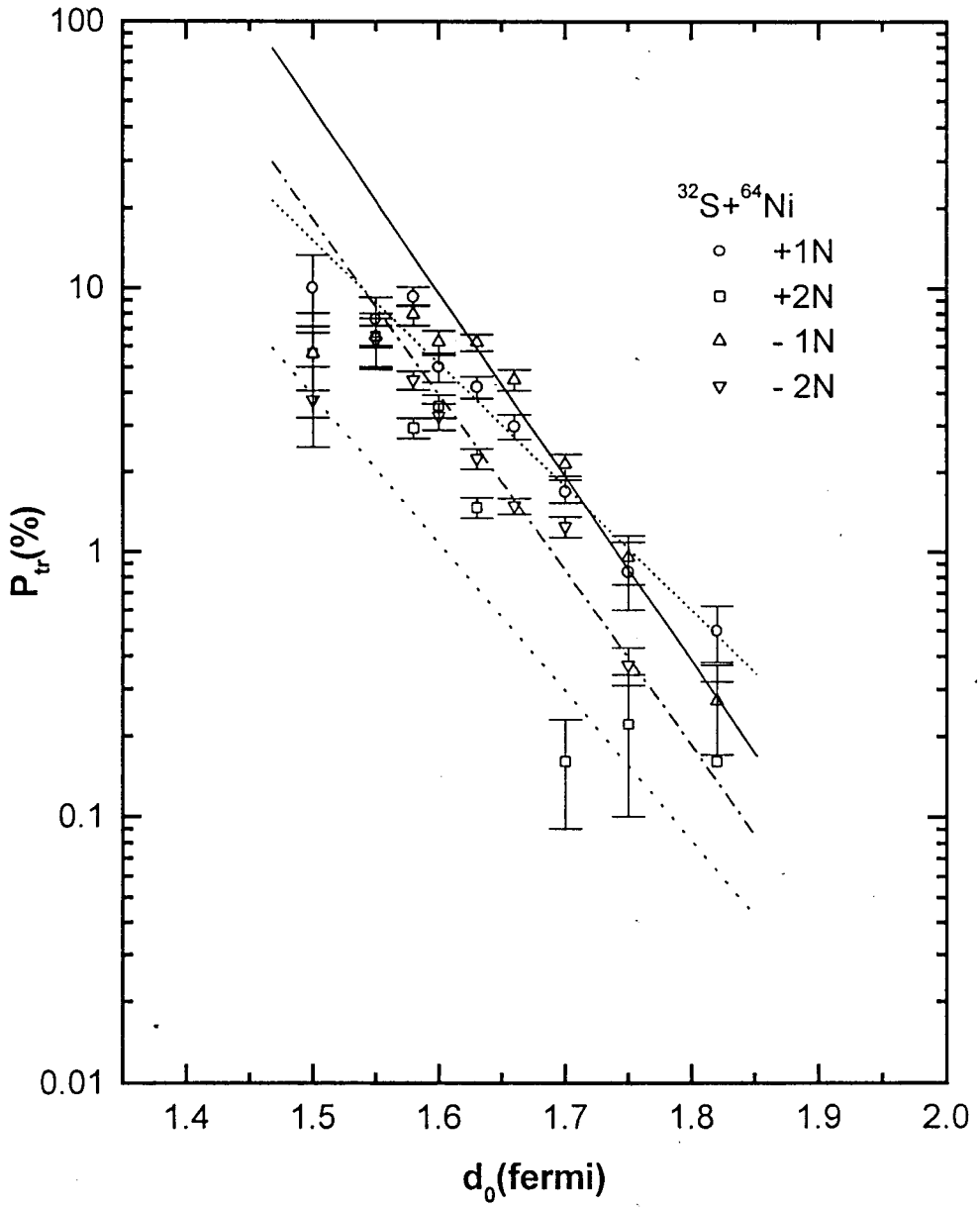

Figure 7.1 : Variation of transfer probability with distance of closest approach for the $^{32}S+^{64}Ni$ system which shows that the slope for 1N and 2N transfer channels are almost the same.

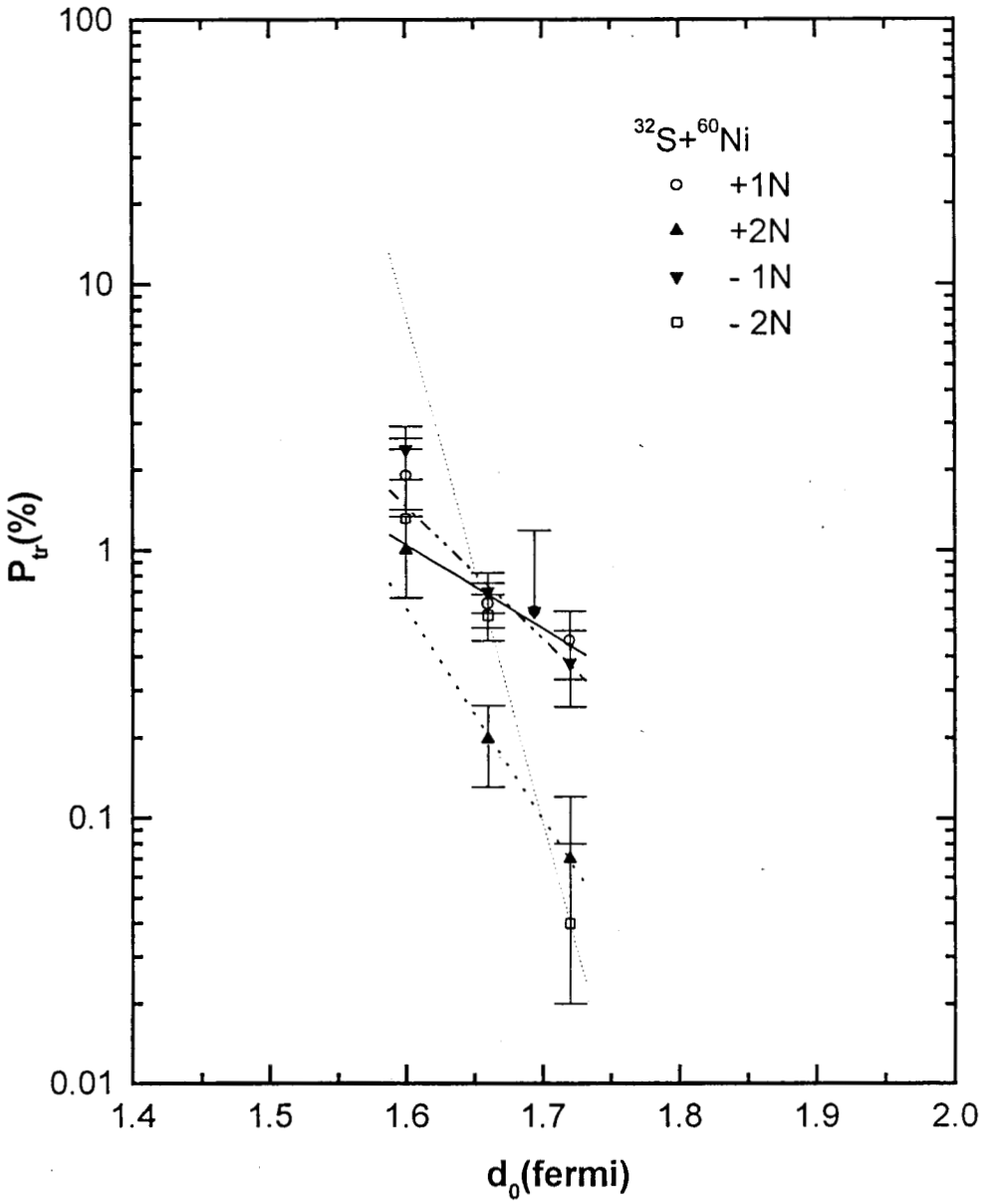

Figure 7.2 : P_{tr}-d_0 plots for $^{32}S+^{60}Ni$ system. The slopes almost shows good agreement with theoretical predictions.

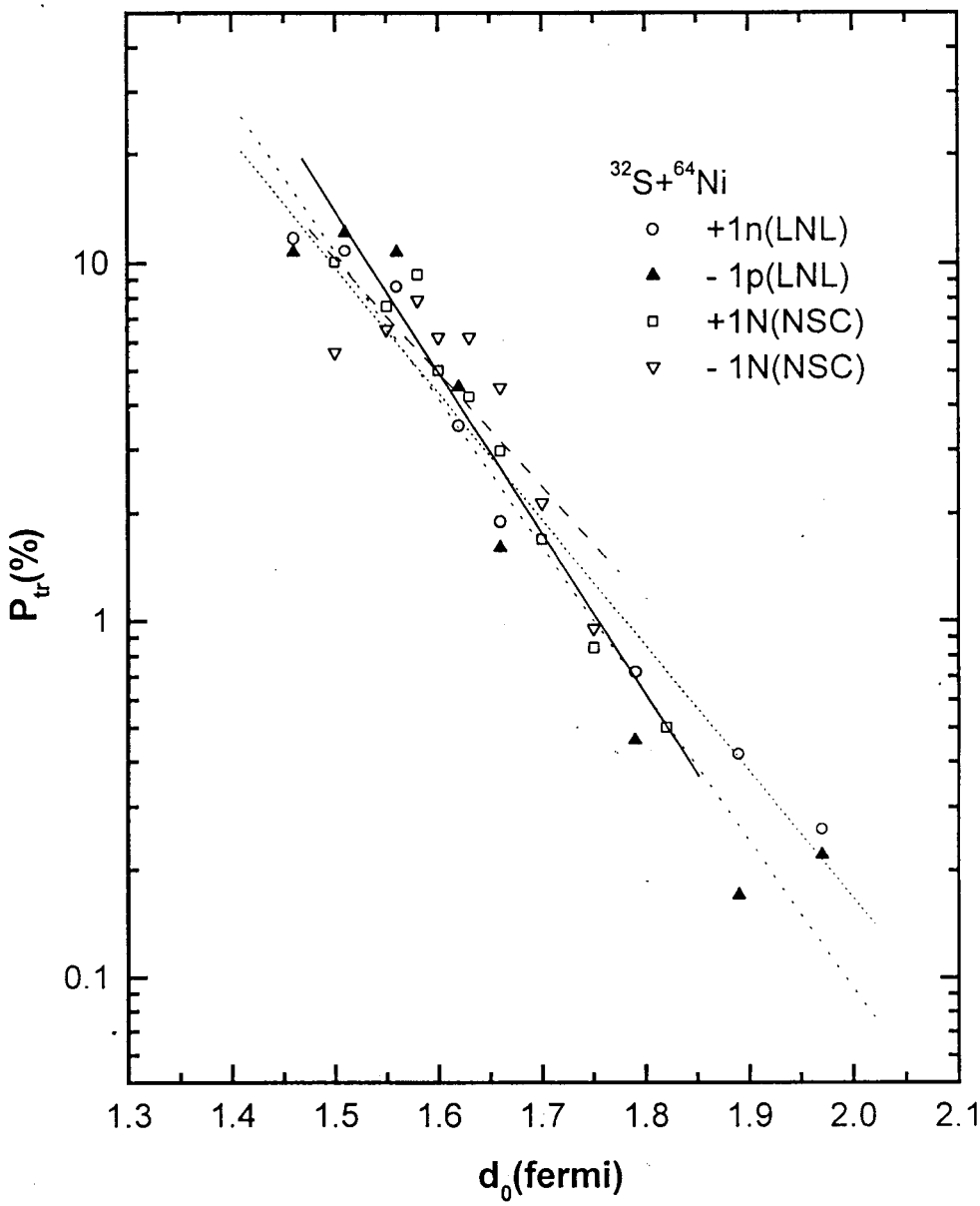

Figure 7.3 : Comparison of the transfer probabilities of our measurements for +1N, -1N channels with the measurement of LNL group for +1n and –1p channels which shows good agreement within the error limits.

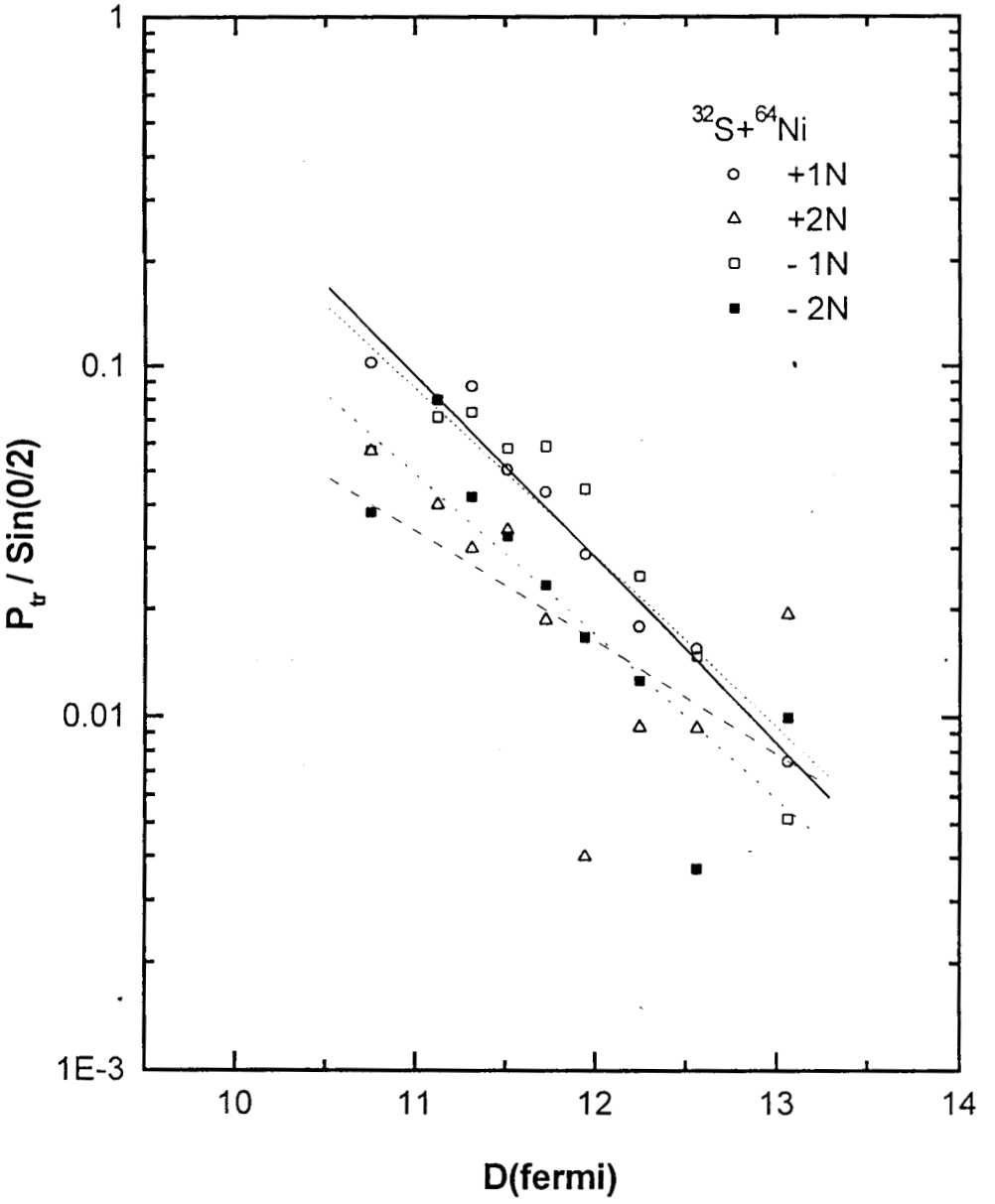

Figure 7.4 : The dependence of $P_{tr}/\sin(\theta/2)$ on the distance parameter D for the $^{32}S+^{64}Ni$ system.

7.3 Extraction of Transfer Coupling Strength

The calculation of the form factor (F) is a tedious process due to its dependence on the parameters σ, P_{tr}, Q-value and Q_{opt} for each channel . The variation in 'σ ' is due to its dependence on the slope parameter (decay constant-α) for each channel . So an average value of the form factor has to be used in Coupled Channel (CC) calculations. Even though we have performed the calculations for evaluating F for the pick-up (+1N,+2N) and stripping (-1N,-2N) channels for each incident energy in centre-of-mass we have used an average value of the form factor calculated by the expression given below in equation (7.2) in the coupled channel calculation [9].

$$F = \sigma [\sqrt{(P_{tr}/\pi)}] \exp[(Q-Q_{opt})^2/2\sigma^2]^{1/2} \qquad (7.2)$$

The value of the σ parameter was calculated at a fixed E_{cm} using the relation

$$\sigma = [\hbar E_{cm}\alpha^{1/2}] / [2Z_pZ_te^2\mu_0]^{1/2} \qquad (7.3)$$

where $\hbar = 6.58 \times 10^{-21}$, $\mu_0 = \mu \times 931/(3 \times 10^{23})^2$, μ being the reduced mass of the system. The value of α used in the calculation of σ was obtained from the fitting of P_{tr} - d_0 plots.

$$\log_{10}(100P_{tr}) = A\text{-}Bd_0 \qquad (7.4)$$

$$P_{tr} = 10^{A\text{-}B\text{-}d0} \qquad (7.5)$$

From the slope B, the parameter α was determined as

$$\alpha = B/2(A_p^{1/3}+A_t^{1/3}) \qquad (7.6)$$

The centre-of-mass energy E_{cm} was calculated at $d_0 = 1.44$ fermi as

$$E_{cm} = [Z_pZ_t/2] \frac{[1+\text{cosec}\,\theta_{cm}/2]}{(A_p^{1/3}+A_t^{1/3})} \qquad (7.7)$$

E_{cm} was obtained as 62.94 MeV for $^{32}S+^{64}Ni$ and 63.67 MeV for $^{32}S+^{60}Ni$ systems. This value of E_{cm} were used for evaluating σ and hence the form factor. The value of transfer probabilities above barrier used in the calculation of σ parameter have been extrapolated from the intercept A and slope B of the P_{tr} - d_0 plots for a value of $d_0 = 1.44$ fermi using the expression in equation (7.5). Table 7.3 shows the optimum Q-values [6]

System	$^{32}S+^{64}Ni$				$^{32}S+^{60}Ni$				
E_{cm}(MeV)	+1p	+2p	-1p	-2p	E_{cm}	+1p	+2p	-1p	-2p
49.8	1.22	2.22	-1.44	-3.11	48.6	1.19	2.16	-1.41	-3.04
51.8	1.27	2.31	-1.50	-3.24	50.6	1.24	2.26	-1.47	-3.16
53.1	1.30	2.37	-1.54	-3.32	51.9	1.27	2.31	-1.51	-3.24
54.4	1.34	2.43	-1.58	-3.40	53.2	1.31	2.37	-1.54	-3.33
55.4	1.36	2.47	-1.61	-3.47	54.2	1.33	2.41	-1.57	-3.39
56.4	1.39	2.52	-1.64	-3.53	55.2	1.36	2.46	-1.60	-3.45
57.4	1.41	2.56	-1.67	-3.59	56.2	1.38	2.51	-1.63	-3.51
58.5	1.44	2.61	-1.70	-3.66	56.9	1.39	2.54	-1.65	-3.56
60.5	1.49	2.70	-1.75	-3.78	59.1	1.45	2.64	-1.71	-3.69

Table 7.3 : Optimum Q-values for the $^{32}S+^{60,64}Ni$ systems for different proton transfer channels.

System	$^{32}S+^{64}Ni$		$^{32}S+^{60}Ni$	
Channel	Q-value (MeV)	Q-Q_{opt} (MeV)	Q-value (MeV)	Q-Q_{opt} (MeV)
+1p	-10.26	-11.69	-7.25	-5.86
-1p	-1.41	0.23	-4.06	-2.41
+1n	-1.01	-1.01	-2.74	-2.74
-1n	-8.94	-8.94	-7.22	-7.22
+2p	-15.87	-18.47	-9.95	-12.49
-2p	0.22	3.88	-4.88	-1.32
+2n	3.56	3.56	-0.33	-0.33
-2n	-13.03	-13.03	-9.68	-9.68
+n+p	-7.24	-8.68	-6.20	-7.59
-n-p	-6.65	-4.95	-7.48	-5.83
+n-p	-3.38	-1.68	-7.84	-6.19
-n+p	-19.99	-21.43	-15.51	-16.90

Table 7.4 : Ground state Q-values and Q-Q_{opt} at E_{lab} = 89 MeV

$^{32}S+^{64}Ni$					$^{32}S+^{60}Ni$				
E_{cm}	σ_{+1N}	σ_{+2N}	σ_{-1N}	σ_{-2N}	E_{cm}	σ_{+1N}	σ_{+2N}	σ_{-1N}	σ_{-2N}
49.8	1.49	1.43	1.51	1.59	50.6				
51.8	1.55	1.49	1.57	1.66	52.7				
53.1	1.58	1.53	1.61	1.70	54.0				
54.4	1.63	1.57	1.65	1.74	55.3	1.92	2.64	2.16	3.07
55.4	1.66	1.60	1.68	1.77	56.3	1.95	2.69	2.20	3.13
56.4	1.69	1.63	1.71	1.80	57.3	1.99	2.73	2.24	3.18
57.4	1.72	1.66	1.74	1.83	58.3				
58.5	1.75	1.69	1.77	1.87	59.3	2.06	2.84	2.32	3.30
60.5	1.81	1.74	1.83	1.94	61.3				

Table 7.5 : Width of form factors calculated from slope parameters.

$^{32}S+^{64}Ni$ (E_{cm} = 62.94 MeV)					$^{32}S+^{60}Ni$ (E_{cm}= 63.67 MeV)				
Transfer Channel	Q-value	α	P_{tr}	F	Q-value	α	P_{tr}	σ	F
+1n	-1.014	0.26	0.20	0.37	-2.746	0.35	0.10	1.49	0.78
+2n	3.563	0.23	0.04	1.27	-0.329	0.68	0.31	2.06	0.43
-1p	-1.412	0.25	0.18	0.31	-7.222	0.45	0.23	1.70	5.30
-2p	0.216	0.23	0.10	3.86	-9.678	0.89	1.86	2.44	7.30

Table 7.6 : Transfer parameters for $^{32}S+^{60,64}Ni$ systems extracted by fitting $P_{tr} - d_0$ plots.

for the $^{32}S+^{60,64}Ni$ systems for the proton transfer channels such as +1p, +2p, -1p and –2p. For the neutron transfer channels Q_{opt} = 0 because there is no change in atomic number due to nucleon transfer process. Table 7.4 gives the Q-values and Q-Q_{opt} at E_{lab} = 89 MeV for the $^{32}S+^{60,64}Ni$ systems.

E_{cm}	d_0	N_{el}	N_{Ruth}	$\sigma_{el}/d\sigma_{Ruth}$	$\sigma_{el}/d\Omega$
49.8	1.85	4849	1742561	0.0026	0.8424
51.8	1.75	2434	128087	0.0013	0.415
53.1	1.70	5316	697772	0.0061	1.99
54.4	1.66	2427	2355882	0.0007	0.25
55.4	1.63	2217	115884	0.0142	0.461
56.4	1.60	989	717006	0.0010	0.33
57.4	1.58	968	1678942	0.0004	0.13
58.5	1.55	746	346603	0.0014	0.46
60.5	1.50	63	82575	0.0005	0.16

Table 7.7 : Normalized elastic cross sections for the $^{32}S+^{64}Ni$ system

The extracted width of form factor is given in table 7.5 for different E_{cm} for the $^{32}S+^{60,64}Ni$ systems. Table 7.6 shows the results of the extraction of the transfer parameters such as slope parameter (α),transfer probability (P_{tr}), form factor width (σ) and form factor (F) by fitting the transfer probability vs d_0 plots for the $^{32}S+^{60,64}Ni$ systems. The extracted values are at $d_0 = 1.44$ fermi corresponding to the beam energies above barrier at $E_{cm}/V_b = 1.05$ and 1.07 respectively. Table 7.7 gives the normalized elastic cross sections [8] which is given as plot in figure 7.5.

7.4 Evaluation of Transfer Cross sections

The measurement of transfer reaction cross section at sub-barrier energies is difficult because of its backward peaking. This difficulty can overcome by using a recoil mass separator like HIRA to separate the recoiling target-like particles corresponding to back scattered projectile-like particles from the intense beam back ground by the method of beam rejection. The focal plane X position-TOF 2D was banana gated and projected to get m/q mass spectra as discussed in chapter 6. This mass peaks are identified and fitted with multiple or single Gaussian to obtain Gaussian shaped peaks. The transfer cross sections for 1N,2N pickup and 1N,2N stripping may be calculated as

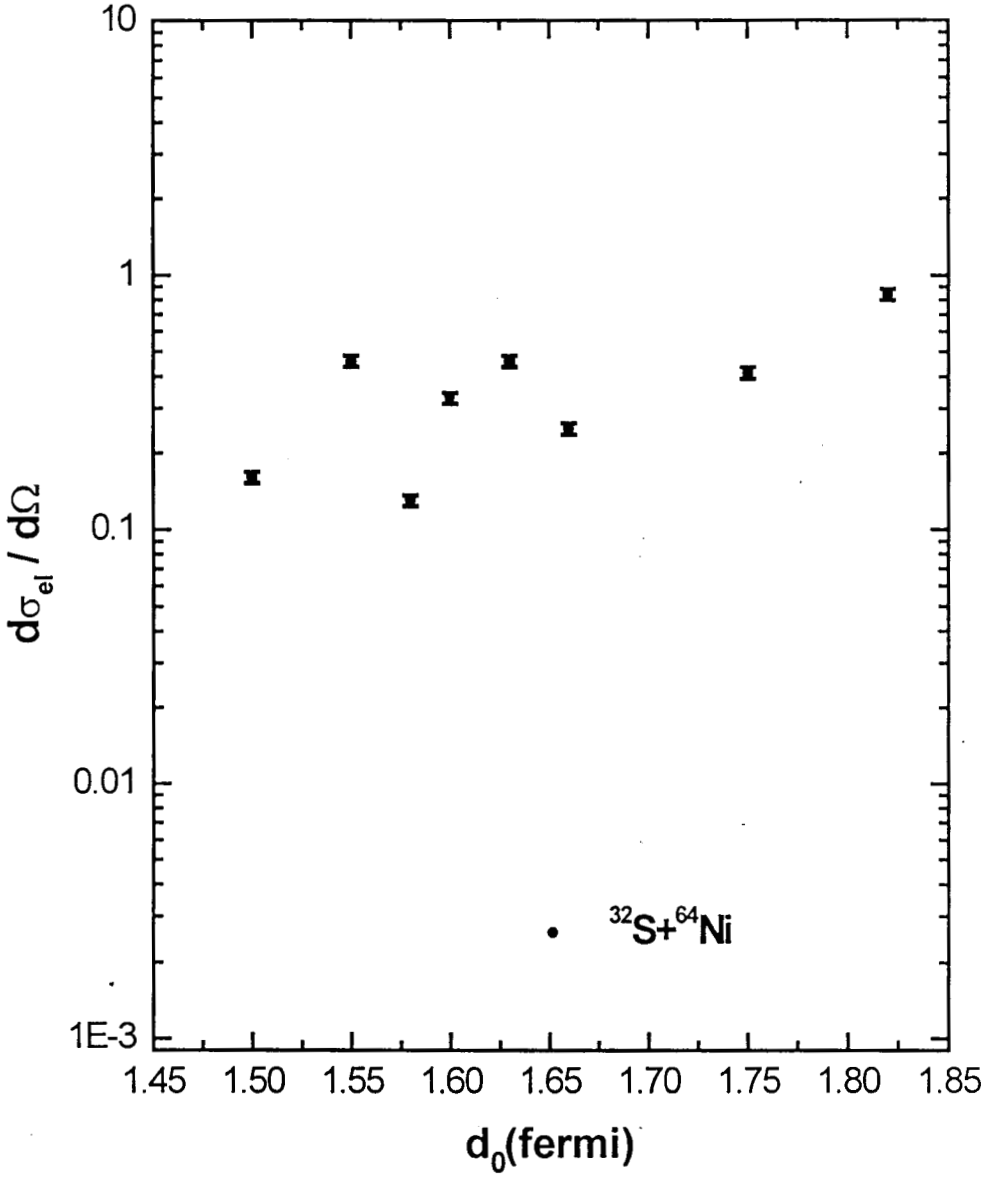

Figure 7.5 : Normalized Elastic cross section as a function of distance of closest approach.

$$\sigma_{tr} = N_{tr}/(N_p N_t \Omega) \quad (7.8)$$

where N_{tr} is the transfer yield, N_p is the counts of projectile-like ions, N_t is the counts of target-like ions and Ω is the solid angle subtended by the back SBD. Instead of measuring the solid angle subtended by the back SBD, we have indirectly calculated the transfer cross sections from the measured transfer probability as

$$d\sigma_{tr} = P_{tr} \times d\sigma_{el} \quad (7.9)$$

The evaluated transfer cross sections for the 1N, 2N pickup and stripping channels corresponding to different centre-of-mass energies is given in table 7.8 which is plotted in Figure 7.6.

E_{lab}	E_{cm}	$d\sigma_{+1N}$	$d\sigma_{+2N}$	$d\sigma_{-1N}$	$d\sigma_{-2N}$
76.0	49.8	0.0061	0.0158	0.0042	0.008
79.0	51.8	0.0063	0.0038	0.0046	0.0015
81.0	53.1	0.034	0.0185	0.049	0.025
83.0	54.4	0.0073	0.001	0.0112	0.0042
84.5	55.4	0.0197	0.0084	0.0268	0.0107
86.0	56.4	0.016	0.0106	0.0183	0.0102
87.5	57.4	0.0113	0.0038	0.009	0.0054
89.0	58.5	0.0365	0.0181	0.033	0.0366
92.0	60.5	0.0156	0.0087	0.0086	0.0059

Table 7.8 : Transfer cross sections evaluated from transfer probabilities for the $^{32}S+^{64}Ni$ system.

7.5 Inelastic Coupling

The coupling of inelastic excitations [5] to the 1DBPM was carried out using the computer code CCMOD. The 2^+, 3^- vibrational states of target and projectile were included in the calculations. The excitation energy E_x, deformation parameter 'β' for the low lying collective vibrational states, reduced transition probability S_λ used for calculating the dynamic deformation parameter in the case of surface vibrational models and ground state transition strengths $B(E\lambda)$ for the states 2^+ and 3^- for the projectile and target were

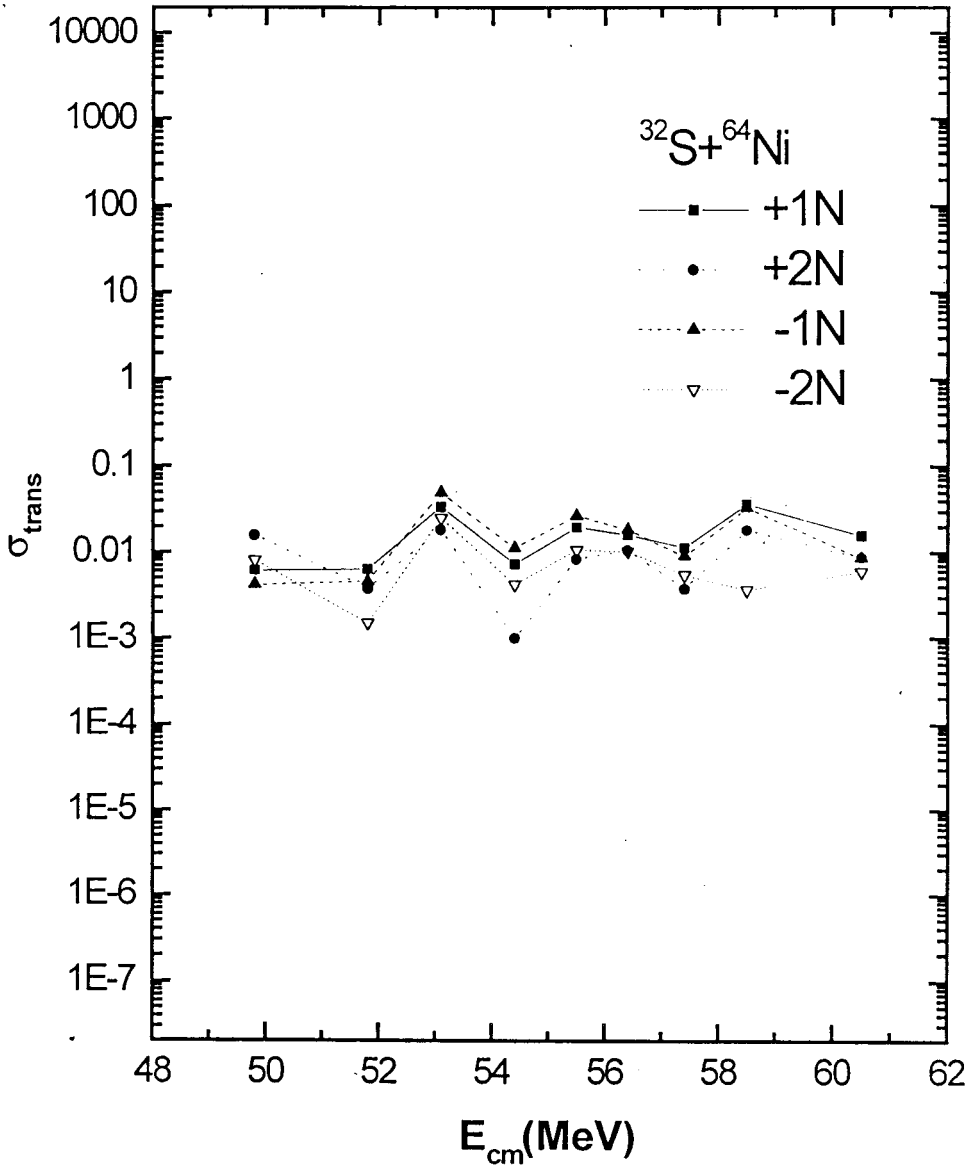

Figure 7.6 : Transfer cross sections for different transfer channels for the $^{32}S+^{64}Ni$ system.

considered. The coupling of the inelastic channel join the experimental measurement reported by Stefanini et al [5]. The enhancement in the barrier is only 43% which is not sufficient to get the reported experimental fusion cross section. So we have gone for the coupling of transfer channel and higher order phonon coupling channel. Table 7.9 gives the values of E_x, β and $B(E\lambda)$ used for the CC calculation which were taken from literature [10-14].

Nucleus	State(J^{π})	E_x(MeV)	β	B(Eλ)	S_λ
^{32}S	2^+	2.23	0.31	10.00	
	3^-	5.01	0.44	20.00	
^{64}Ni	2^+	1.35	0.19	8.60	10.3
	3^-	3.58	0.22	7.20	14.1
^{60}Ni	2^+	1.33	0.22		13.7
	3^-	4.04	0.19		10.9

Table 7.9 : The parameters of inelastic coupling used in CCNSC

7.6 Higher Order Phonon Coupling

The experimentally observed enhancement in the fusion cross section at sub-barrier energies can not be estimated by the linear coupling calculations of one phonon states of the target (2^+ and 3^-) and projectile (2^+). Coupling of this inelastic channel can not explain the observed fusion data. The surface vibrational states of the target (quadrupole and octapole) and projectile (quadrupole) nuclei is included in second order two phonon coupling. All possible states involving up to two phonons are included in second order coupling. Higher order phonon coupling [14] includes all the possible states related to more than two phonons. The second order phonon coupling is not able to describe the data at lower energies. But the higher order multiphonon coupling together with the coupling of transfer and inelastic channel shows best agreement between experimentally measured fusion data and coupled channel results within the finite range. We have carried out the coupled channel calculations for $^{32}S+^{64}Ni$ system by including higher order multiphonon coupling with 1DBPM and linear inelastic and transfer channels. The computer code CCNSC have the options for including the higher order phonon coupling within the finite range effects. The matrix elements proposed by Esbensen and Landowne [15] were used for higher order multiphonon coupling. Higher coupling effects are found to be more significant at smaller excitation energies of the surface vibration as investigated above[15].

7.7 Computer Codes

Since there are different models for nuclear fusion, standard computer codes are available for each model. The source codes are keeping on modifying according to the requirements of each research groups and available with them. Even though there are computer codes for each fusion model, we have limited our discussions to mainly one important model. It is the well known Coupled Channel codes. The important codes used for transfer measurement are kinematics, TRIM etc. Kinematics is able to predict the recoil energy, recoil angle, θ_{cm}, θ_{lab}, E_{cm}, E_{lab} etc., which can be used for the proper setting of the experimental set up. It also predicts the energy, angles etc., in which the experiment can be performed. As mentioned earlier TRIM can be used for specific energy loss calculations. Besides these programs we have developed a number of small computer codes in FORTRAN for meeting our requirements. The important of them are for predicting the SBD angle for better yield, for calculating recoil energy from TOF, for calculating Q-values etc.

7.7.1 Coupled Channel Codes

The coupled channel codes are developed on the basis of barrier passing theory of fusion. That is, the barrier is considered as a dividing line between direct reactions and compound nuclear formation (fusion). A common result of this calculation is that the barrier height varies significantly about the coulomb barrier from standard 1DBPM. This variation is due to the additional coupling or dimension used in the model. The source code of this program called CCFUS was developed by Dasso et al.[16,17]. This code was modified by Fernandez Niello et al.,[18] and Dasso et al., [19] and it is known as CCDEF by considering the static deformation of projectile and/or target. The expression for nuclear and coulomb potentials have to be modified when considering this static deformations. A simplified version of these codes are available now and it is known as CCMOD [20] which is again simplified and modified at NSC to the latest form called CCNSC. Even though these above mentioned codes differ in some aspects, the different channels such as inelastic excitations, transfer channels etc., are treated as independent modes and they are coupled to the initial ground state. We have used CCNSC and CCNSCHO2[21] for our

calculations of fusion cross sections to couple the inelastic, transfer and the higher order phonon coupling channels. CCNSC treats finite range effects more extensively. It has the provision for including higher order phonon coupling. The uncoupled barrier parameters calculated by CCNSCHO2 for the $^{32}S+^{60,64}Ni$ systems given in table 7.10. The results of the CC calculation for $^{32}S+^{60,64}Ni$ system is given in table 7.11 and 7.12 respectively. The various coupling schemes included are (a) $2^+,3^-$(b) $2^+,3^-$& transfer(c) $2^+,3^-$ & one-phonon coupling. (d) $2^+,3^-$ & transfer plus one- and two-phonon coupling. The important input parameters used in this calculation are discussed in the following sections.

System	V_b (MeV)	R_b (fermi)	$\hbar\omega$ (MeV)
$^{32}S+^{60}Ni$	59.833	10.0156	3.7942
$^{32}S+^{64}Ni$	59.108	10.1484	3.7185

Table 7.10 : Barrier parameters calculated using the code CCNSCHO2 for the two systems

1) Potential

The general consideration of the nuclear and coulomb potentials are on the basis of the deformation of the projectile and target. For deformed nuclei the nuclear and coulomb potentials have to be calculated for each orientations of target and projectile. Another important thing to be considered is the characteristic time of interaction which is short compared to the rotational motion of the deformed nuclear system. While the Christensen-Winther form of nuclear potential is used in CCDEF, the Woods-Saxon parametrisation of Akyuz-Winther potential is used in the code CCMOD. In the coulomb potential the quadrupole and hextadecupole nuclear deformations have to be considered.

2) Coupling Strength

The inelastic coupling strength to be used in the code can be calculated according to the expression used in chapter 3 (section 3.6). The transfer coupling is carried out by using the value of the form factor calculated using the expression

$$F(r) = F_0/\sqrt{4\pi}\ \{ \exp[-(r-R_p-R_t)/1.2]\} \qquad (7.10)$$

where $F_0 = 3$ is the one particle transfer coupling strength.

3) Eigen Values

The eigen values λ_α s and the weight factor $U_{0\alpha}$ can be obtained by solving the n uncoupled equations by diagonalizing the coupling matrix $M_{\alpha\beta}$ given in section 3.6. The eigen values and eigen vectors are evaluated by diagonalizing this matrix in CCMOD. But in CCDEF the eigen values and weight factors are obtained by coupling two channels at a time.

4) Finite Range Effects

The barrier position for each eigen value can be obtained by finding the value of 'r' corresponding to the maximum value of barrier height $V_\ell(r)+\lambda_\alpha(r)$. This technique is adopted in CCMOD. At the average position of eigen barriers or unperturbed barrier the weighting factor can be fixed at a convenient distance R. That is $U_{0\alpha}(r) = U_{0\alpha}(R)$ and this value can be used in the calculation of transmission coefficient $T_\ell(E)$.

5) Static Deformation

Fusion of heavy ions is enhanced or reduced according to the mutual orientation of deformed projectile and target [22]. Barrier is lowered when two prolate deformed nuclei are oriented tip-to-tip and fusion is enhanced. When two oblate deformed nuclei are oriented equator-to-equator fusion is reduced due to the increase in barrier height. Coupled channel calculations are developed by considering the above effects due to static deformation.

6) Zero Point Motion

The boundary of a nucleus is not well defined, and the nuclear radius can be considered as a Gaussian distribution due to the zero point fluctuation due to the collective vibrational motion as proposed by Esbensen [23]. This produces a distribution of barrier heights. Thus the total cross section can be obtained by averaging over all nuclear shapes for each collision. This is similar to the angle averaging in static deformation.

E_{cm}(MeV)	σ_{fus}(1DBPM) mb	σ_{fus}(coupled) mb
50.0	3.23E-06	9.79E-05
51.0	1.66E-05	4.24E-04
52.0	8.51E-05	1.84E-03
53.0	4.38E-04	7.98E-03
54.0	2.25E-03	3.46E-02
55.0	1.16E-02	0.150
56.0	5.95E-02	0.645
57.0	0.305	2.70
58.0	1.54	10.2
59.0	7.24	29.5
60.0	26.7	60.6
61.0	64.5	96.7
62.0	111	134
63.0	159	172
64.0	205	209
65.0	251	247
66.0	294	283
67.0	337	319
68.0	378	354
69.0	419	391
70.0	458	428

Table 7.11 : Fusion cross sections calculated for inelastic + transfer + one-phonon coupling using the code CCNSCHO2 for the $^{32}S+^{60}Ni$ system using the parameters extracted in the present transfer experiment. The uncoupled (1DBPM) cross section is also given.

σ_{fusion} (mb) BY CALCULATION USING THE CODES CCNSC & CCNSCHO2							EXPERIMENT	
E_{cm} MeV	IDBPM	(2+,3-)	2+,3- & transfer	2+,3- & one-phon	2+,3- & transfer + one -phon	2+,3- & transfer+ two-phon	E_{cm} (MeV)	σ_{fusion} (mb)
50.0	7.93E-06	2.11E-04	0.00712	0.000210	0.00685	0.0239	54.1	1.4
51.0	4.21E-05	9.34E-04	0.0267	0.000932	0.0257	0.0738	55.0	4
52.0	2.24E-04	4.14E-03	0.100	0.00413	0.0962	0.227	55.5	9.5
53.0	1.19E-03	1.84E-02	0.371	0.0183	0.357	0.688	56.0	17
54.0	6.33E-03	8.15E-02	1.33	0.0813	1.28	2.03	57.0	29
55.0	3.36E-02	0.360	4.25	0.360	4.10	5.50	57.5	40
56.0	0.179	1.57	10.9	1.56	10.5	12.8	58.4	55
57.0	0.940	6.39	22.3	6.38	21.6	24.7	59.6	105
58.0	4.72	21.3	41.7	21.3	40.7	42.1	60.2	130
59.0	19.7	50.2	72.5	50.1	71.4	64.9	60.8	160
60.0	54.5	87.0	109	86.9	108	91.5	61.5	180
61.0	102	126	147	126	146	121	62.5	200
62.0	151	165	184	165	183	156	63.0	220
63.0	200	204	222	204	221	196	63.4	240
64.0	247	243	260	243	258	242	64.2	260
65.0	293	281	297	281	295	288	64.8	280
66.0	338	319	333	319	331	333	65.4	300
67.0	381	356	368	356	367	377	66.1	320
68.0	423	394	405	393	404	420	66.7	350
69.0	464	433	443	432	441	462	67.6	385
70.0	503	473	481	472	480	503		

Table 7.12 : Fusion cross sections calculated for various coupling schemes for $^{32}S+^{64}Ni$ system using the computer code CCNSC/CCNSCHO2.

7.8 Experimental Fusion Cross Section

The experimental fusion cross section for the $^{32}S+^{64}Ni$ was measured by Stefanini et al.[5] They have used the following relation for measuring the fusion cross section.

$$\sigma_{fus} \mid_{ER} = 1/\varepsilon_{RMS}(Y_{ER}/Y_M)(d\sigma_R/d\Omega_M)\Omega_M \qquad (7.11)$$

where ε_{RMS} is the efficiency of the recoil mass separator, Y_{ER} is the yield of the evaporation residues, Y_M is the monitor counts, $(d\sigma_R/d\Omega M)$ is the Rutherford cross section in the laboratory system and Ω_M is the solid angle subtended by the monitor detector. The experimentally measured fusion cross section is compared with the Coupled Channel calculation results based on our transfer experiment. No experimental studies have been reported about the fusion measurements on $^{32}S+^{60}Ni$ to the best of our knowledge.

7.9 Summary and Conclusions

The transfer experiment discussed in this thesis for the $^{32}S+^{60,64}Ni$ systems was carried out [24,25,26] for an energy range 60 to 92 MeV at Nuclear Science Centre (New Delhi), using the pelletron accelerator and the RMS-Heavy Ion Reaction Analyser (HIRA). By the method of kinematic coincidence technique between the back scattered sulphur ions and the corresponding forward recoiling target-like ions, the various transfer products of pickup (1N,2N) and stripping (1N,2N) channels were identified from the mass spectrum obtained by the banana gated projection of X position –TOF 2D spectrum. The transfer probabilities (P_{tr}) were extracted from the mass spectrum (figure 6.9). From the fitting of P_{tr} - d_0 plots the slope parameter (α), width of form factor(σ) and the form factor (F) were calculated. The slope Parameter (α) for the $^{32}S+^{64}Ni$ system shows anomaly with the predictions of theory. The results show that the slope for 1N and 2N transfer channels have almost the same value. But there was no considerable anomaly observed in the case the case of $^{32}S+^{60}Ni$ in which case the slope of 2N transfer channel has a value almost equal to twice that of 1N transfer channel.

The experimentally obtained transfer form factor strength and the parameters for inelastic and higher order phonon coupling were used for performing simplified Coupled Channel calculations for $^{32}S+^{64}Ni$ system using the computer code CCNSCHO2[21]. The One Dimensional Barrier Penetration Model calculations were performed with the computer code CCNSC using the Woods-Saxon form of Akyuz-Winther (AW) nuclear potential. Figure 7.7 shows the results of our coupled channel calculations for $^{32}S+^{64}Ni$ system which shows a comparison between 1DBPM results and the calculated cross sections for different coupling schemes using the transfer coupling strength measured by our $^{32}S+^{64}Ni$ experiment. The various coupling schemes involved with 1DBPM are given in table 7.12. The table 7.13 gives the asymptotic barrier shifts at 0.1mb level calculated using the code CCNSCHO2 [21] for the $^{32}S+^{64}Ni$ system for different coupling schemes. A comparison of these parameters with experimental studies for the $^{32}S+^{64}Ni$ system is also given. Table 7.13 is also shows the results of CC calculations for the $^{32}S+^{60}Ni$ system on the basis of our transfer measurements.

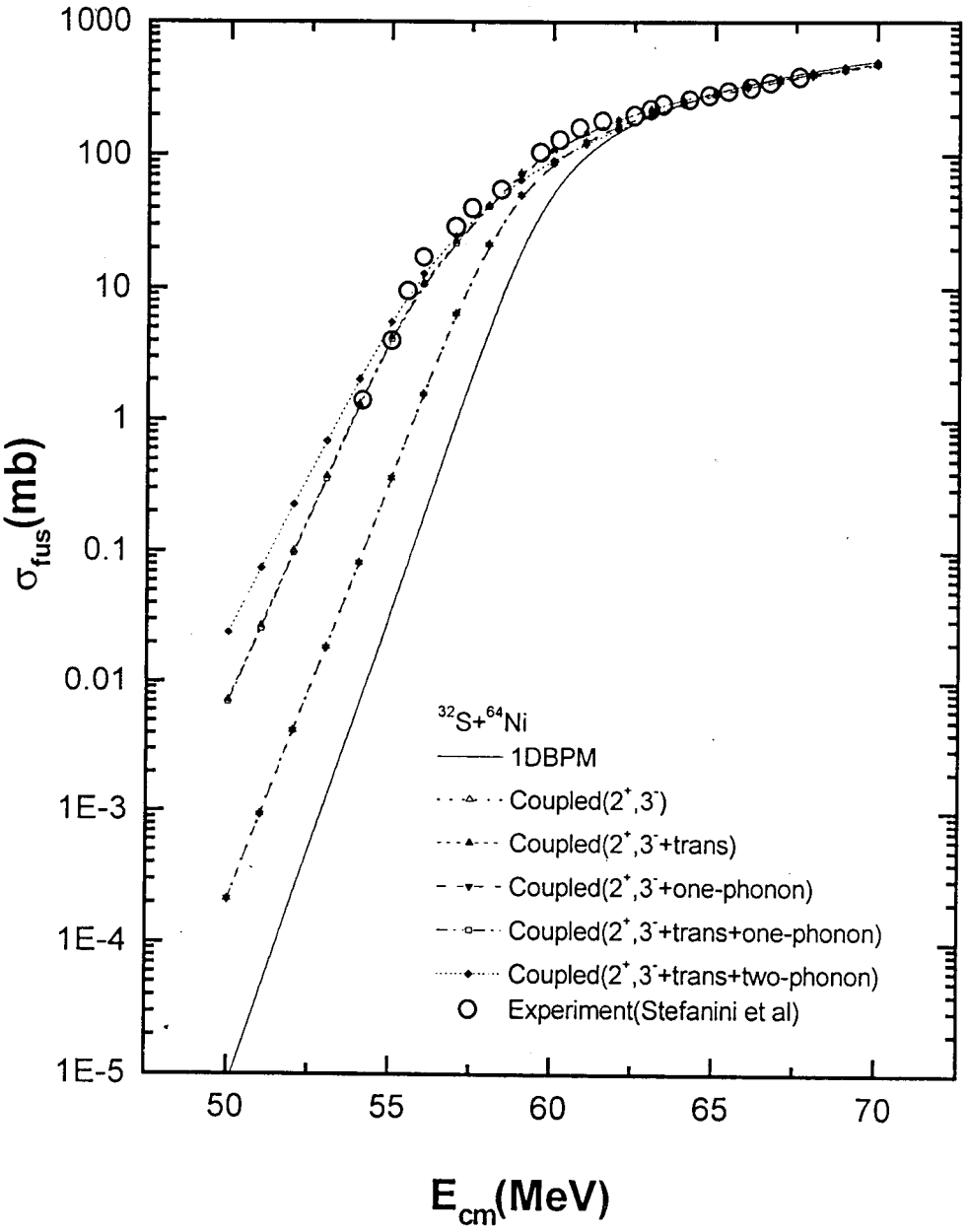

Figure 7.7 : Results of excitation function calculations for $^{32}S+^{64}Ni$ system for various coupling schemes on the basis of the present transfer experiment. A comparison with 1DBPM and the previous fusion experimental measurement reported by Stefanini et al. is also given.

It is seen from table 7.13 that the asymptotic barrier shift for $^{32}S+^{64}Ni$ system with inelastic coupling of 2^+ and 3^- states of projectile and target is obtained from the CCNSC/CCNSCHO2 [21] calculation as 1.51 MeV. The value of ΔB for the coupling of inelastic and transfer channels is 3.65 MeV, while the coupling of inelastic + transfer + one-phonon coupling gives a ΔB of 3.62 MeV, which nearly equal to the value of 3.2 to 3.6 MeV obtained by Saha et al. [9]. The experimental value of ΔB obtained by LNL group [5] was 3.39 MeV. The –1p and –2p channels enhances the barrier only by a factor of 0.3 MeV. So a major contribution to ΔB will be from neutron transfer channels and is of the order of 2.14 MeV. This gives the importance of +2n channel with positive Q-value of 3.563 MeV, which has to be included in coupled channel calculations. The coupling strength of the +2n channel is more because of its large positive Q-value.

The contribution to the barrier shift by inelastic coupling is about 42% where as transfer coupling accounts about 58% and higher order phonon coupling contributes much less. The value of coulomb barrier obtained by fitting of the data of coupled channel calculation is V_b=59.108 MeV, which shows agreement with experimental value obtained by Stefanini et al., [5] as V_b = 58.1±0.7 MeV. The barrier radius obtained by the same experiment was 8.8 ±0.5 fm. The $\hbar\omega$ parameter obtained by their experiment was 4.1 ± 0.2 MeV. We have obtained a value of $\hbar\omega$ parameter from the coupled channel calculations as 3.82 MeV for the coupling of inelastic + transfer + one-phonon coupling channels. The barrier curvature $\hbar\omega$ is an inverse measure of the barrier thickness in the parabolic approximation of the barriers.

A comparison with the experimental measurement of fusion cross section by Stefanini et al.,[5] with our results is also given in figure 7.7. The analysis suggests that the coupling of 2^+, 3^- plus transfer and one phonon coupling shows good agreement with the experiment and this coupling is best suited for explaining the experimental data. Coupling of transfer + inelastic + 2 phonon (higher order) shows agreement with the experiment within the probable error limits. The coupling of positive Q-value (2n pickup) channel contribute more to the sub-barrier fusion enhancement over 1DBPM. Figure 7.8 shows a

comparison of $\sigma_f[A_p^{1/3}+A_t^{1/3}]^{-2}$ calculated on the basis of our transfer results for the $^{32}S+^{60,64}Ni$ systems with that obtained by the experimental measurement reported by Stefanini et al.,[5] for the $^{32}S+^{64}Ni$ system, which shows good agreement. To the best of our knowledge no experimental data are available on $^{32}S+^{60}Ni$ system. However we have calculated the coupled channel results for this system also. Figure 7.9 gives the results. Figure 7.10 shows a comparison of our results of CC calculation for determining the fusion cross section for the $^{32}S+^{64}Ni$ with the previous experimental reports. Figure 7.11 shows the barrier distributions for the $^{32}S+^{60,64}Ni$ systems calculated using the code CCNSCHO2.

The value of $E_{red} = [E_{cm} - V_b]/\hbar\omega$ and $\sigma_{red} = 2\sigma_f E_{cm}/\hbar\omega R_b^2 = \ln[1 + \exp(2\pi E_{red})]$ are calculated using this expressions for the $^{32}S+^{60,64}Ni$ systems with the barrier parameters extracted by coupled channel calculations. The barrier parameters were taken from the results of our CC calculations as given in table 7.10. The experimental barrier parameters for the $^{32}S+^{64}Ni$ were taken from stefanini et al.[5]. Figure 7.12 shows a plot between the dimensionless parameters E_{red} and σ_{red} for the $^{32}S+^{60,64}Ni$ system based on the above results. The above results show good agreement between our transfer measurements and previous fusion experiment for the $^{32}S+^{64}Ni$ system. The $^{32}S+^{60}Ni$ system is also compared with $^{32}S+^{64}Ni$ system in different figures, since there is no experimental data is available for the $^{32}S+^{60}Ni$ system.

In the present studies we have succeeded in resolving the m/q ambiguity due to the focusing of same m/q to the same focal plane position by the kinematic coincidence method for TOF measurements. We were able to resolve the 1N, 2N pick up and 1N, 2N stripping channels. This is clearly evident from the X position-TOF 2D spectrum (figure 6.7) and from the recoil energy spectrum (figure 6.22). But the attempts by previously reported groups [4,7] did not succeeded in resolving m/q ambiguity for resolving one-nucleon and two-nucleon transfer channels.

$^{32}S+^{64}Ni$ SYSTEM

Uncoupled centre of mass energy for 0.1 mb cross section = 55.65 MeV		
Coupling Scheme	Coupled E_{cm} for σ = 0.1 mb (MeV)	ΔB (MeV)
Projectile(2^+,3^-)+ Target (2^+, 3^-)	54.14	1.51
Projectile(2^+,3^-) + Target (2^+, 3^-) + Transfer	52.00	3.65
Projectile(2^+,3^-)+ Target (2^+, 3^-) + One-phonon	54.14	1.51
Projectile(2^+,3^-) + Target (2^+, 3^-) + Transfer + One-phonon	52.03	3.62
Projectile(2^+,3^-) + Target (2^+, 3^-) + Transfer + Two-phonon (Higher Order)	51.27	4.38
Experiment (Stefanini et al.)	52.20	3.39

$^{32}S+^{60}Ni$ SYSTEM

Uncoupled centre of mass energy for 0.1 mb cross section = 56.32 MeV		
Projectile(2^+,3^-) + Target (2^+, 3^-) + Transfer + One-phonon	54.72	1.59

Table 7.13 : Asymptotic Barrier shifts at 0.1mb level using the computer code CCNSC/CCNSCHO2 for the $^{3\ 2}S+^{60,64}Ni$ system on the basis of our transfer results. A comparison with experimental results is also given for $^{32}S+^{64}Ni$ system.

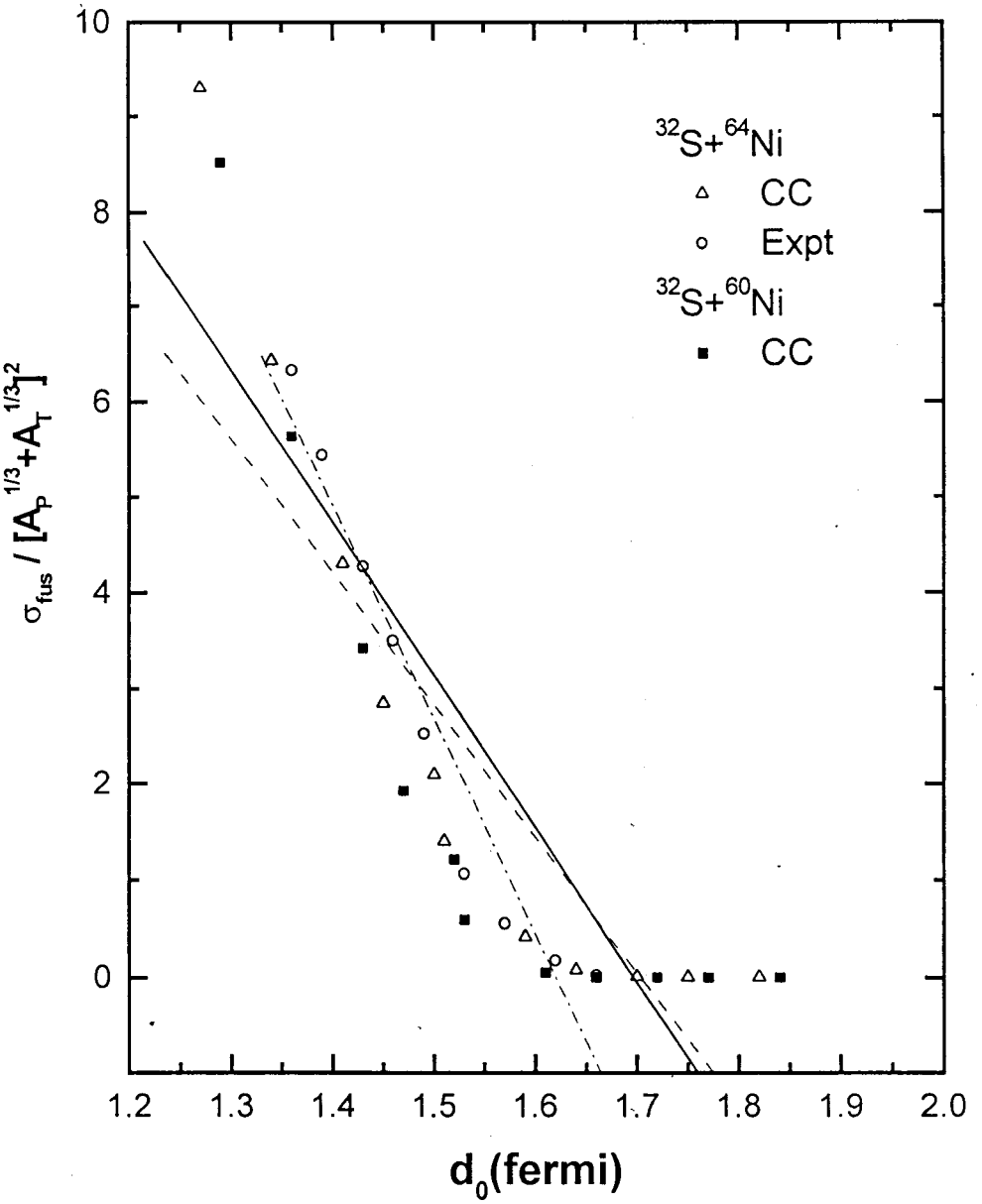

Figure 7.8 : A comparison between the present calculations of normalised fusion cross section as a function of distance of closest approach using the results of CCNSCHO2 with the experiment using ^{64}Ni target.

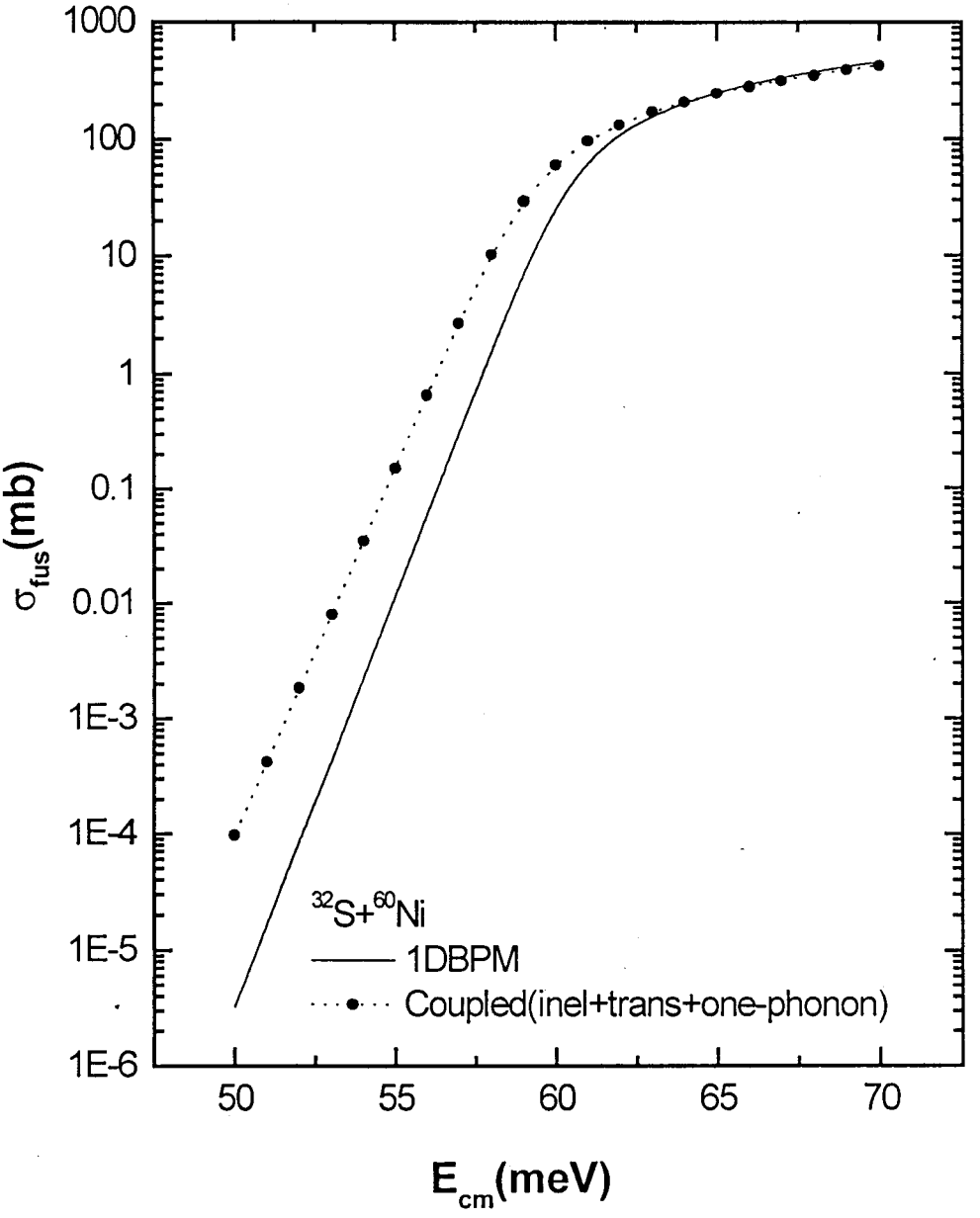

Figure 7.9 : Results of the fusion cross section calculations based on the transfer parameters extracted by the present experiment for the $^{32}S+^{60}Ni$ system. A comparison with 1DBPM predictions is also given.

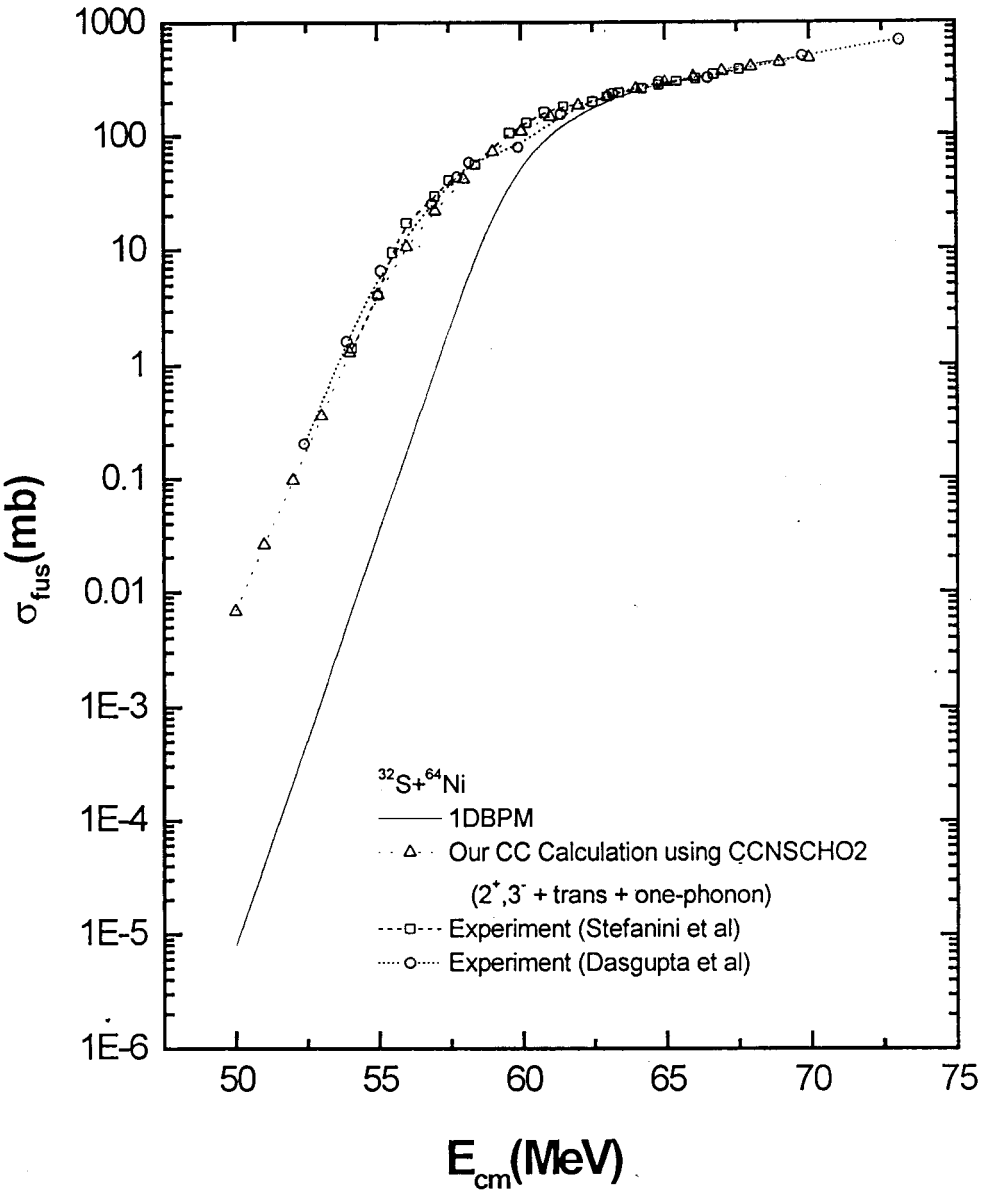

Figure 7.10 : A comparison of fusion cross sections calculated using coupled channel code CCNSCHO2 using the parameters obtained by our transfer experiment with the previous experimental results and with the 1DBPM predictions.

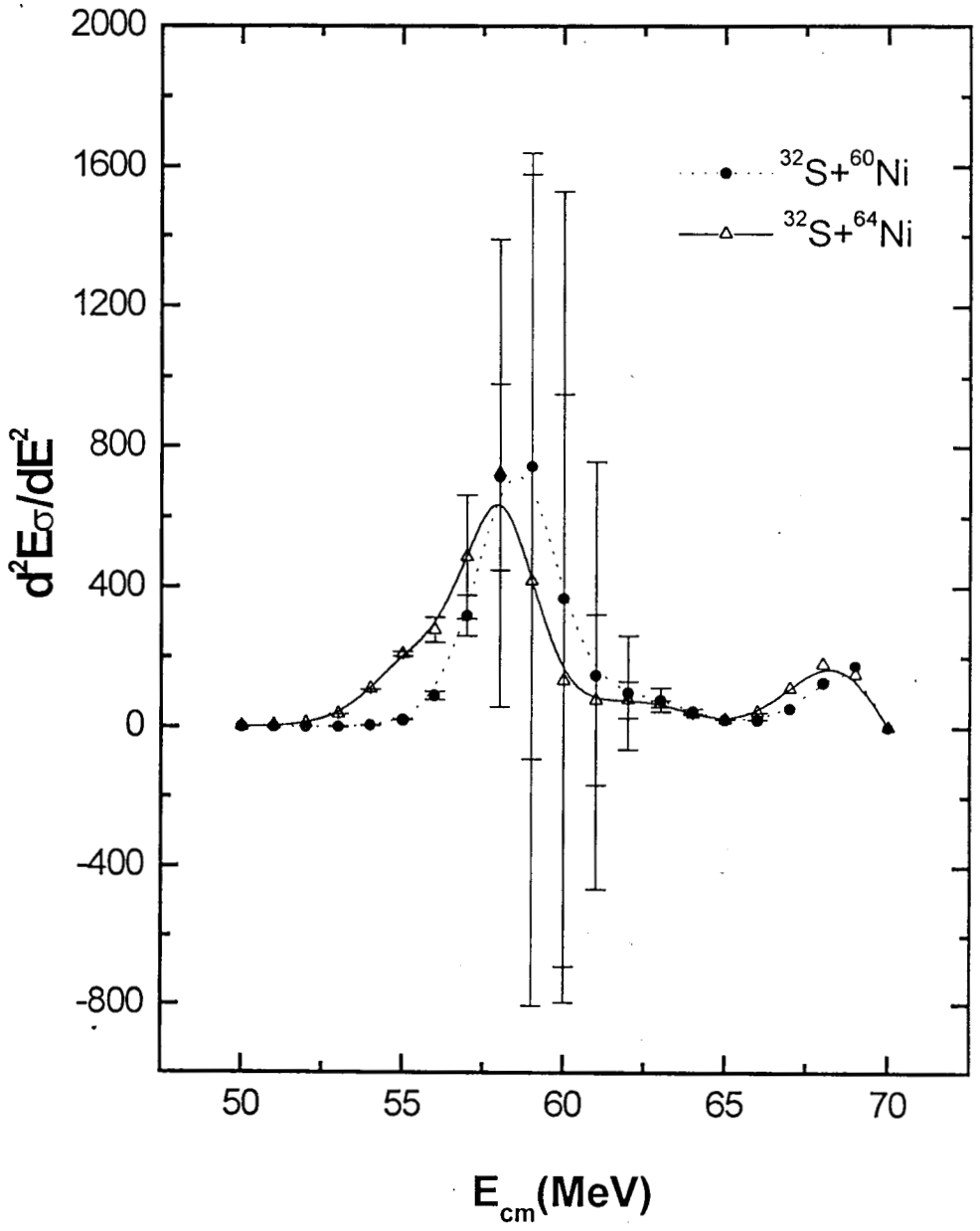

Figure 7.11 : Barrier distributions calculated using the code CCNSCHO2 for the $^{32}S+^{60,64}Ni$ systems. The coupling scheme used for this calculation is inelastic + transfer + one-phonon.

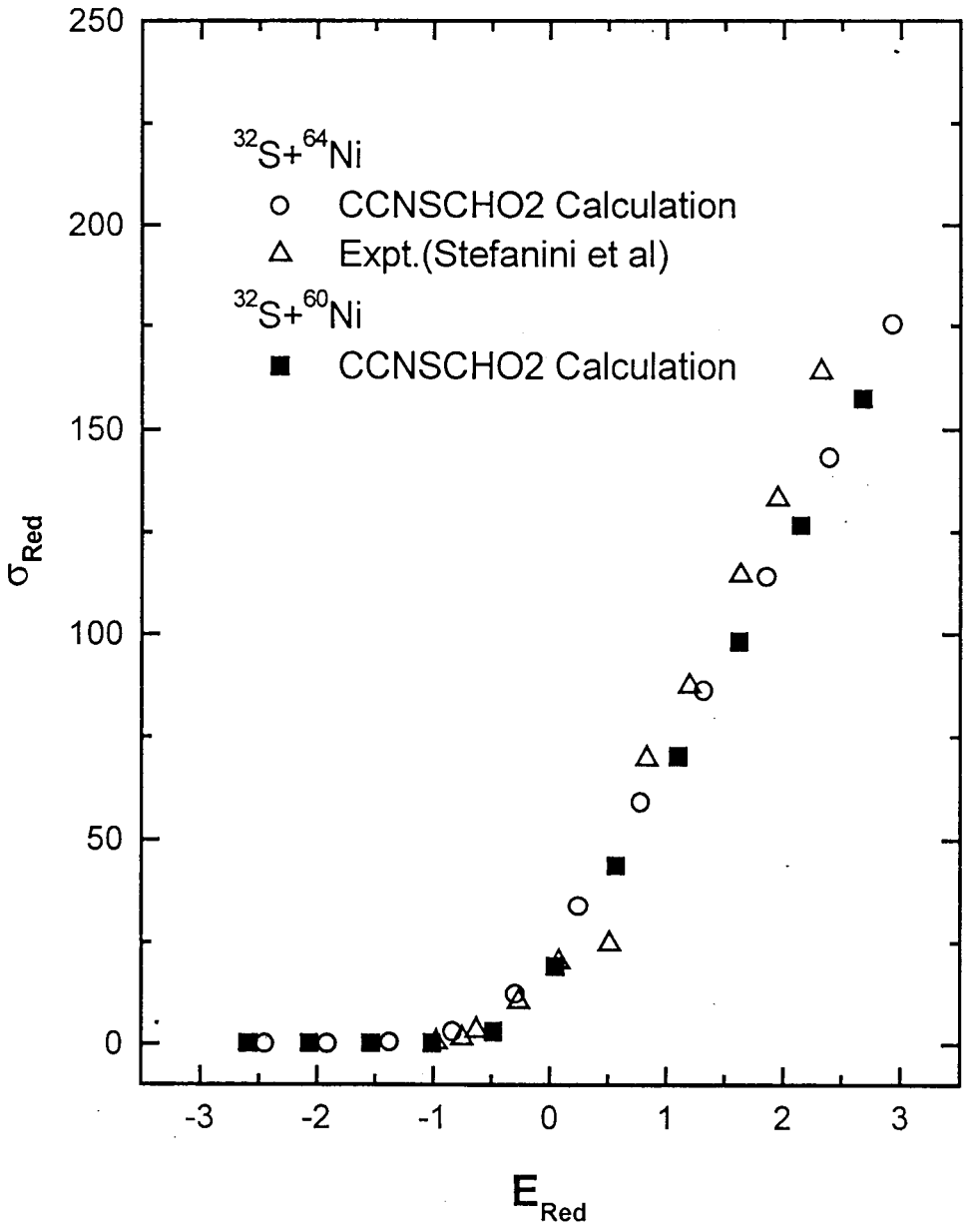

Figure 7.12 : The reduced cross section as a function of reduced energy calculated using the barrier parameters extracted from the results of Coupled Channel calculations.

In conclusion, we suggest that exhaustive studies incorporating transfer, elastic and inelastic scattering and fusion measurements should be carried out for various nuclear systems for getting a better understanding of the reaction mechanism and the interplay of the various interaction process. The various coupling schemes such as inelastic, transfer and higher order phonon coupling should be used for performing elaborate coupled channel calculations and a comparison with 1DBPM should be made. Since the spin and barrier and angular momentum distributions of the compound nucleus are sensitive to the involved coupling, a measurement of these distributions also should be carried out. This will be helpful for a detailed understanding of the reaction mechanisms which is the expected gate way to the production of super heavy elements.

References

[1] P.J.A.Buttle and J.L.B.Goldfarb, Nucl. Phys.**A176**(1971)299.

[2] A.K.Sinha, L.T. Baby, N. Badiger, J.J. Das, S.K. Hui, D.O. Kataria, R.G. Kulkarni, N. Madhavan, P.V. Madhusudhana Rao, I. Mazumdar, M.C. Radhakrishna, N.V.S.V. Prasad, N.G. Puttaswamy, P.P. Shakkeeb, R. Singh, D.L. Sastry, P. Sugathan, V. Tripathi, K.M. Varier and A.M. Vinod Kumar, J. Phys. G. Nucl. Part. Phys. **23** (1997)1331.

[3] T.udagawa, T.Tamura, B.T.Kim, Phys. Rev.**C39**(1989)1840.

[4] M.Dasgupta, A. Navin, Y.K. Agarwal, C.V.K. Baba, H.C. Jain, M.L. Jhingan and A. Roy, Nucl. Phys.**A539**(1992)351.

[5] A.M.Stefanini, G. Fortuna, R. Pengo, W. Meczynski, G. Montagnoli, L. Corradi, A. Tivelli, S. Beghini, C. Signorini, S. Lunardi, M. Morando and F. Soramel, Nucl. Phys. **A456**(1986)509.

[6] S.Saha, Y.K.Agarwal and C.V.K.Baba, Phys. Rev. **C49**(1994)2578.

[7] D.R.Napoli, A.M. Stefanini, H. Moreno Gonzalez, B. Million, G. Prete, P. Spolaore, M. Narayanasamy and Zi Chang Li, Nucl. Phys. **A559**(1993)443.

[8] J.F.Liang, L.L.Lee, Jr.,J.C.Mahon and R.J.Vojtech, Phys. Rev.**C50**(1994)1550.

[9] S.Saha and Y.K.Agarwal, Nucl. Phys.**A601**(1996)251.

[10] P.M. Endt, Atomic data and nuclear data tables **23**(1979)3 and 547.

[11] G. Bruge, J.C. Faivre, H. Faraggi and A. Bussiere, Nucl. Phys. **A146**(1970)597.

[12] J. Albinski, A. Budzanowski, H. Dabrowski, Z. Rogalska, S. wiktor, H. Rebel, D.K. Srivastawa, C. Aldeliesten, J. Bojowald, W. Oelert, C. Mayer-Böricke and P. Turek, Nucl. Phys. **A455**(1985)477.

[13] J.J. Vega, E.F. Aguilera, G. Murillo, J.J. Kolata, A. Morsad and X.J. Kong, Phys. Rev. **C42**(1990)947.

[14] Lagy.T.Baby, Vandana Tripathi, D.O. Kataria, J.J. Das, P. Sugathan, N. Madhavan, A.K. Sinha, M.C. Radhakrishna, N.M. Badiger, N.G. Puttaswamy, A.M. Vinod Kumar, N.V.S.V. Prasad, Phys. Rev.**C56**(1997)1936.

[15] H. Esbensen and S. Landowne, Phys. Rev. **C35**(1987)2090.

[16] C.H. Dasso, S.Landownw and A.Winther, Nucl. Phys.**A405**(1983)381.

[17] C.H. Dasso, S. Landowne and A. Winther, Nucl. Phys. **A407**(1983)221.

[18] J. Fernandez Niello, C.H.Dasso and S. Landowne, Comput. Phys. Comm.**54** (1989)409.

[19] C.H. Dasso and S. Landowne, Comput. Phys. Comm.**46**(1987)187.

[20] Dasgupta, A. Navin, Y.K. Agarwal, C.V.K. Baba, H.C. Jain, M.L. Jhingan and A. Roy, Nucl. Phys. **A539**(1992)351.

[21] A.K. Sinha, NSC communications (Unpublished)

[22] C.Y.Wong, Phys. Rev. Lett.**31**(1973)766.

[23] H.Esbensen, Nucl. Phys. **A352**(1981)147.

[24] P.P.Shakkeeb, A.M. Vinod Kumar, K.M. Varier, N.V.S.V. Prasad, R. Singh, A.K. Sinha, N. Madhavan, P. Sugathan, D.O. Kataria and Lagy. T. Baby, Proced. DAE Symp. on Nucl. Phys.**38B**(1995).

[25]] P.P.Shakkeeb, A.M. Vinod Kumar, K.M. Varier, N.V.S.V. Prasad, R. Singh, A.K. Sinha, N. Madhavan, P. Sugathan, D.O. Kataria and Lagy. T. Baby, Annual Report, Nuclear Science Centre, New Delhi (1995)78.

[26] A.K. Sinha, Int. Nation. Symp. on Nucl. Phys.-**INPS-95**(1995)163